A Unified Formation Scenario for the Zoo of Extended Star Clusters and Ultra-Compact Dwarf Galaxies

Dissertation

zur
Erlangung des Doktorgrades (Dr. rer. nat.)
der
Mathematisch-Naturwissenschaftlichen Fakultät
der
Rheinischen Friedrich-Wilhelms-Universität Bonn

vorgelegt von

Renate Claudia Brüns

aus
Bonn

Bonn, 2013

Angefertigt mit Genehmigung der Mathematisch-Naturwissenschaftlichen Fakultät der
Rheinischen Friedrich-Wilhelms-Universität Bonn

1. Gutachter:	Prof. Dr. P. Kroupa
2. Gutachter:	Prof. Dr. U. Klein
Tag der Promotion:	16. Juni 2014
Erscheinungsjahr:	2014

Contents

List of Figures

List of Tables

Abstract

In the last decade, very extended old stellar clusters, which cover a large mass range, have been found in various types of galaxies in different environments. Objects with masses comparable to normal globular clusters (GCs) are called extended clusters (ECs), while objects with masses in the dwarf galaxy regime are called ultra-compact dwarf galaxies (UCDs). Moreover, observations indicate that star clusters tend to form in larger conglomerations called star cluster complexes (CCs) in heavily interacting galaxies. The CCs have typical masses between $M^{\rm CC} = 10^5$ and a few 10^7 $\rm M_\odot$, radii of tens to a few hundred parsecs, and they typically consist of few to several dozens of young massive star clusters.

I have compiled a catalog of 835 ECs and UCDs with effective radii larger than 10 pc from the literature. At each magnitude objects are found with effective radii between 10 pc and an upper size limit, which increases for brighter luminosities. For objects associated with early- and late-type galaxies, the turnover of the luminosity function of the extended objects is about one magnitude fainter than that of the GC luminosity function. The extended objects and GCs form a coherent structure in the $r_{\rm eff}$ vs. $M_{\rm V}$ parameter space, while there is a clear gap between extended objects and early-type dwarf galaxies except for the high-mass end, where the most extended objects are close to the parameters of some compact elliptical galaxies. The rapidly increasing number of observed objects allows for the first time an in-depth investigation of their nature.

In this thesis I investigate the question whether CCs are the progenitors of ECs associated with galactic disks (also known as faint fuzzies, FFs), of ECs located in galactic halos, and of UCDs by performing extensive numerical simulations (in total 154). It is the first systematic research on the evolution of CCs. In this formation scenario these extended objects evolve from CCs by merging of their constituent star clusters. The basic and most important parameters of a CC are its mass and size. These two parameters were varied in all parametric studies to investigate how the structural parameters of the final merger objects correlate with the underlying CC parameter space. The third important factor is the external tidal field which has a large impact on the evolution of a CC. The influence of the external tidal field was studied by varying the orbital parameters of the CCs. These three parameters are varied systematically and the resulting merger objects are compared with specific extended objects like the faint fuzzies in the galaxy NGC 1023 and the Milky Way cluster NGC 2419 and with the overall properties of the extended objects in the catalog.

A comparison of the observed sample of extended objects of the catalog with the numerical models demonstrates that the merging star cluster scenario reproduces the structural parameters, the distribution, and the overall trends of the observed extended objects very well. Even specific features of some extended objects are well reproduced in the simulations. All extended objects can be very well explained by a star cluster origin, where they are the results of merged star clusters of cluster complexes. The distinction made between FFs, ECs, and UCDs is no longer existent in this formation scenario. They all stem from the same formation process and are therefore united under the name "extended stellar dynamical object" (EO).

1

Introduction

Globular star clusters are among the oldest radiant objects in the Universe. They were formed at the same time as the very first galaxies during the cosmological epoch of structure formation. Despite the fact that star clusters have been studied in quite some detail, the conditions and modes of their formation are still not well known. In the past decade, unusually extended old star clusters covering a mass range of more than three orders of magnitude have been found in various types of galaxies in different environments. Objects with masses comparable to normal globular clusters (GCs) are called extended clusters (ECs), while objects with masses in the dwarf galaxy regime are called ultra-compact dwarf galaxies (UCDs). The rapidly increasing number of detected extended stellar dynamical objects (EOs) allows, for the first time, an in-depth investigation of their nature.
In addition, recent observations of massively interacting galaxies have shown that young massive star cluster complexes (CCs) can reach masses of up to possibly 10^8 $M_\odot$ *spanning several hundred parsecs in extent and containing a few to several dozens or possibly even hundreds of young massive star clusters. Since galaxy-galaxy interactions are anticipated to have been more common during early cosmological structure formation it is expected that star formation in CCs has been a significant star formation mode during early cosmological epochs.*
This thesis addresses the question whether ECs and UCDs can be explained as the evolved end-products of CCs. The evolution and future fate of CCs in various environments is investigated using numerical simulations. The resulting objects are compared to the observed ECs and UCDs.

1.1 Old Star Clusters in the Local Group

Globular clusters (GCs) are self-gravitationally bound collections of stars with typical masses between a few 10^4 and 10^6 $M_\odot$ (corresponding roughly to total luminosities between $M_V = -5$ and $M_V = -10$ mag). The distribution of stars in a GC is roughly spherical with a high density of stars in the center, gradually fading out to a smaller number density of stars in the outer regions. The term "globular cluster" was introduced by Sir William Herschel in 1789 based on the visual appearance of these star clusters. The GCs of the Milky Way are rather old objects. Most of them have ages larger than 10 Gyr (e.g. Forbes & Bridges 2010; Dotter et al. 2010; Cezario et al. 2013).

The Milky Way (= the Galaxy) is a spiral galaxy with three basic components to its visible matter. It consists of a disk of stars and gas and a spherical stellar bulge at the center of the Galaxy which are embedded in an approximately spherical halo of old stars, GCs and a few satellite galaxies.

Even though the Milky Way has the best studied GC system, the total number of known Milky Way GCs has changed in recent years. In the year 2010 157 GCs were known (Harris

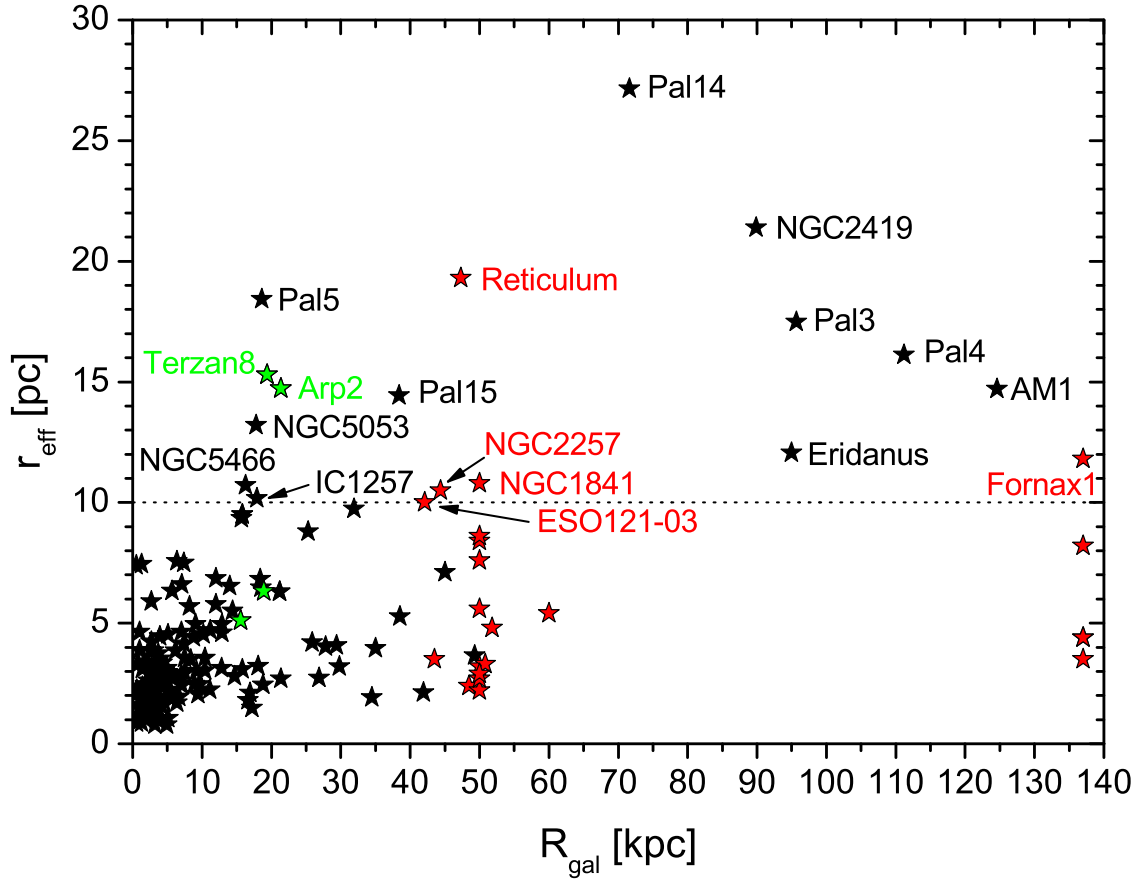

FIGURE 1.1— Effective radii, $r_{\rm eff}$, of GCs/ECs of the Milky Way (black stars), the Sag dSph (green stars), the LMC, the SMC, and the Fornax dSph (all red stars) are plotted against their distance, $R_{\rm gal}$, from the Galactic center. The dashed line indicates the separator between GCs and ECs.

1996, 2010 edition[1]). Recently, the ultra-faint Milky Way GCs Segue 3 (Belokurov et al. 2010), Muñoz 1 (Muñoz et al. 2012), and Balbinot 1 (Balbinot et al. 2013) were discovered, increasing the total number of GCs to 160. However, the proximity of the GCs M54, Terzan 7, Terzan 8, and Arp 2 to the Sagittarius dwarf spheroidal galaxy (Sag dSph) suggests that they are associated with this Milky Way satellite, and not to the Milky Way itself (Da Costa & Armandroff 1995). Consequently, the actual number of Milky Way GCs is now 156. As the Sag dSph is apparently in the process of being tidally disrupted by the Milky Way additional GCs may have been stripped and distributed across the sky. Candidates of GCs that were possibly stripped from the Sag dSph during the encounter are for example Pal 12 (Dinescu et al. 2000; Cohen 2004) and NGC 5634 (Bellazzini et al. 2002). There may be even more Milky Way GCs that may have been former members of disrupted Milky Way satellite galaxies.

Figures 1.1 and 1.2 present an overview of the GCs of the Milky Way. The majority of the GCs are compact with effective radii[2] of a few parsecs. The median effective radius of the 156 Milky Way clusters is 3.0 pc. In addition to compact GCs, there are a number of GCs which have much larger sizes and are therefore called extended clusters (ECs). As these ECs were not considered special in the past they were simply assigned to the sample of GCs. There is no unique physical size demarcation between GCs and ECs. However, an effective radius of $r_{\rm eff} = 10$ pc is currently seen as a reasonable limit (e.g. van den Bergh & Mackey 2004). The

[1] http://physwww.physics.mcmaster.ca/~harris/mwgc.dat

[2] The effective radius is defined as the projected radius wherein half of the total luminosity of the object is enclosed.

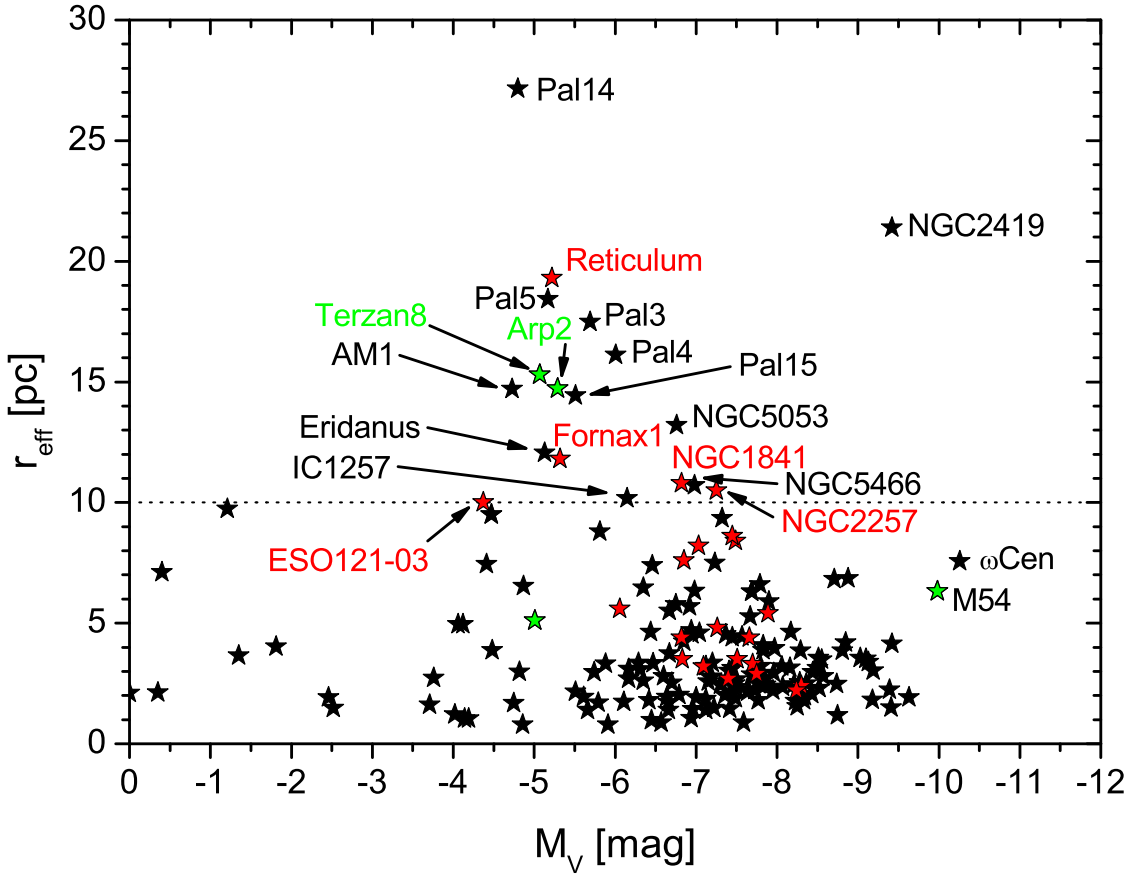

FIGURE 1.2— Effective radii, $r_{\rm eff}$, of GCs/ECs of the Milky Way (black stars), the Sag dSph (green stars), the LMC, the SMC, and the Fornax dSph (all red stars) are plotted against their total V-band luminosities, $M_{\rm V}$. The dashed line indicates the separator between GCs and ECs.

sample of 156 Milky Way GCs comprises 11 ECs, which corresponds to about 7% of the total sample. The ECs are metal-poor clusters at large Galactic radii (Fig. 1.1). While the entire GC sample has a median Galactic distance of about $R_{\rm gal,median} \approx 5$ kpc, the 11 ECs have a median distance of $R_{\rm gal,ECmedian} = 72$ kpc.

The ECs of the Milky Way are in general fainter than $M_{\rm V} = -7$ mag (Fig. 1.2) with a median value of -5.7 mag, while the median luminosity of the entire GC sample is -7.2 mag. Only the EC NGC 2419, which has an effective radius of about 20 pc, has a high luminosity of $M_{\rm V} = -9.4$ mag (Harris 1996, 2010 edition) corresponding to a mass of about $9 \cdot 10^5$ $M_\odot$ (Baumgardt et al. 2009). The most extended EC of the Milky Way is Palomar 14 (Pal 14) with an effective radius of 27 pc (Harris 1996, 2010 edition). It was discovered on photographic plates from the Palomar Sky Survey by Sidney van den Bergh and Halton Arp in 1958. The most remote star cluster AM1 (Madore & Arp 1979) is an EC at a distance of about $R_{\rm gal} = 125$ kpc (Harris 1996, 2010 edition) from the center of the Galaxy.

The Milky Way has a system of 27 satellite galaxies (McConnachie 2012, and references therein). Except for the Large and Small Magellanic Clouds (LMC & SMC), a nearby binary system of dwarf irregular galaxies (dIrrs) at galactocentric distances of about 50 kpc (LMC) and 60 kpc (SMC), all satellites are dwarf spheroidal galaxies (dSphs). Some of the satellite galaxies have been known for centuries (e.g. the LMC was first mentioned by Al Sufi (964)), while the ultra faint dwarf galaxies (UFDs), which cover the luminosity range between $M_{\rm V} = 0$ and -5 mag, were only recently discovered (e.g. Belokurov et al. 2010, and references therein). The satellite galaxies are not isotropically distributed but form a disk-like structure named

the disk-of-satellites (DoS) which lies nearly perpendicularly to the plane of the Milky Way (Kroupa et al. 2005, 2010, and references therein).

Only the four most massive Milky Way satellites (LMC, SMC, Sag dSph, Fornax dSph) possess a GC/EC system. The closest Milky Way companion, the Sag dSph, has two GCs and the two ECs Arp 2 and Terzan 8 (Da Costa & Armandroff 1995; Salinas et al. 2012). These GCs and ECs are added to Figs. 1.1 and 1.2 as green stars. The LMC has in total 16 old GCs, of which four are ECs (van den Bergh & Mackey 2004; Mackey & Gilmore 2004, and references therein). The most extended EC in the LMC is the Reticulum cluster with an effective radius of 19.3 pc (van den Bergh & Mackey 2004). The SMC has only one compact old GC, NGC 121 (van den Bergh & Mackey 2004; Glatt et al. 2008). The Fornax dSph galaxy, which is located at a distance of 138 kpc, has in total five GCs (Hodge 1961b; van den Bergh & Mackey 2004). One of them (Fornax 1) is extended with an effective radius of 11.8 pc (van den Bergh & Mackey 2004). The GCs/ECs of the LMC, the SMC and the Fornax dSph galaxy are added as red stars in Figs. 1.1 and 1.2. The Milky Way and its satellites have a combined GC system of 182 objects. In total, 18 of these objects (or ten percent) are ECs.

While the GC system of the 16 LMC GCs resembles the Milky Way GCs, the Magellanic Clouds – in contrast to the Milky Way – also contain young and intermediate-age GC-like objects with ages less than a few Gyr (e.g. Hodge 1961a; Chun 1978; da Costa 2002). The number of young and intermediate-age clusters in the Magellanic Clouds exceeds the number of old objects (e.g. da Costa 2002).

The nearest neighborhood of the Milky Way is known as the Local Group (Hubble 1936). It has decoupled from the Hubble expansion flow and is expected to be gravitationally self-bound. The Local Group consists of two more spiral galaxies, the Andromeda Galaxy (M31) and the Triangulum Galaxy (M33), and a large number of dwarf galaxies. The dwarf galaxies in the Local Group can be subdivided into dIrrs, dwarf ellipticals (dEs), compact ellipticals (cEs) and dSphs. Most dSphs, dEs and the only cE (M32) of the Local Group are satellite galaxies of the Milky Way and the Andromeda Galaxy. As for the Milky Way, a disk-of-satellites was also found in the Andromeda Galaxy which contains about half of its satellite galaxies (Conn et al. 2013; Pawlowski et al. 2013, and references therein). In contrast, the majority of dIrrs are free-floating members located at larger distances from the Milky Way and M31. However, they also appear to be not isotropically distributed but located in planes (Pawlowski et al. 2013).

The Andromeda Galaxy (M31) is the nearest spiral galaxy to the Milky Way at a distance of about 780 kpc (McConnachie et al. 2005, and references therein) and the largest member of the Local Group, being about twice as massive as the Milky Way (when comparing the total disk + bulge masses of the Milky Way and the Andromeda galaxy from Flynn et al. (2006) and Geehan et al. (2006), respectively). The detection of GCs in M31 dates back to the early work of Edwin Hubble (Hubble 1932). The M31 GC system is still an active research area, where new GCs have been found in all parts of this galaxy. Apart from old GCs, the Andromeda galaxy also hosts a population of young and intermediate-age GC-like objects (e.g. Burstein et al. 2004; Puzia et al. 2005). M31 has a larger GC system than the Milky Way. So far 625 GCs have been confirmed (Revised Bologna Catalog V5.0[3], Galleti et al. 2004). In addition, Huxor et al. (2005) found three ECs around M31, which have very large effective radii of the order of 30 pc. These clusters were detected by chance as the automatic detection algorithms of the MegaCam Survey discarded such extended objects as likely background contaminations. Follow-up observations by Mackey et al. (2006), using the ACS camera of the Hubble Space Telescope (HST), resolved the ECs into stars proving their nature as M31 clusters. They also detected a fourth EC. The M31 ECs have masses of the order of 10^5 $M_\odot$. Further observations increased the number of ECs in M31 to 20 (Huxor et al. 2008; Peacock et al. 2009) covering a range of projected distances

[3]http://www.bo.astro.it/M31/

between 4 and 73 kpc.

The Triangulum Galaxy (M33) is a rather small, low-luminosity spiral galaxy without a prominent bulge located in the vicinity of M31. M33 has a cluster population with a broad range of ages similar to the cluster populations of the Magellanic Clouds (e.g. Christian & Schommer 1982; Cohen et al. 1984). A catalog on the star clusters of M33 was compiled by Sarajedini & Mancone (2007)[4]. M33 hosts about 25 old GCs (Schommer et al. 1991; Huxor et al. 2009; Cockcroft et al. 2011) and two ECs with effective radii of $r_{\rm eff} \approx 20$ pc having projected distances of 12.5 and 28.6 kpc (Stonkutė et al. 2008; Huxor et al. 2009; Cockcroft et al. 2011).

Next to the Magellanic Clouds, the galaxies NGC 6822 and IC 1613 are the most massive dIrrs of the Local Group with comparable stellar masses. NGC 6822 is located at a distance of about 470 kpc from the Milky Way (Hwang et al. 2011) and hosts old GCs as well as young globular-type objects (e.g. Chandar et al. 2000). Out of the nine old GCs, three are ECs (Hwang et al. 2011; Huxor et al. 2013). Whereas in the dIrr IC 1613 neither old GCs nor massive young clusters were found (e.g. Georgiev et al. 1999; Wyder et al. 2000). The majority of the low-mass Local Group dwarf galaxies do not have a GC system.

The traditional definition of GCs being old stellar systems stemmed from observations of GCs in the Milky Way. Our Galaxy contains only old GCs with typical ages above 10 Gyr, whereas the other Local Group spiral galaxies and some dIrrs also host young and intermediate-age GC-like objects. It might be that the GC system of the Milky Way is rather an exception than the norm.

1.2 Old Star Clusters beyond the Local Group

The morphology and the total luminosities make GCs easily observable in external galaxies with modern telescopes. GCs have been discovered and studied in all types of galaxies ranging from dwarf to giant elliptical galaxies. The number of GCs associated with a galaxy correlates with the morphology and the luminosity of the host galaxy (e.g. Zepf et al. 1994). Dwarf galaxies host none or only a few GCs whereas giant elliptical galaxies may have GC systems with over 10 000 GCs. Excellent reviews on GCs are provided by the book of Ashman & Zepf (1998), the Saas-Fee lectures of Harris (2001)[5], and the review of Brodie & Strader (2006).

While the detection of GCs and ECs in distant galaxies is feasible with ground based telescopes, the determination of structural parameters of star clusters beyond the Local Group was made possible only with the Hubble Space Telescope (HST) launched in 1990. The HST has a superb spatial resolution and is able to measure GC sizes; e.g. at the distance of the Virgo Cluster of about 16.5 Mpc an HST ACS pixel corresponds to a linear scale of 4 pc.

Observations of dwarf galaxies revealed that a number of dwarf galaxies host ECs. ECs were mainly found in dIrr and Magellanic type dwarf galaxies (Sharina et al. 2005; van den Bergh 2006; Georgiev et al. 2009; Strader et al. 2012b). In addition, ECs were found in two dSph galaxies, KK 84 (Sharina et al. 2005; van den Bergh 2006) and IKN (Georgiev et al. 2009), and in the Sculptor Group dE galaxy Scl-dE1 (Da Costa et al. 2009).

Most extragalactic HST studies of spiral galaxies focused only on their disks and bulges and did not cover their halos. ECs were found for example in the spiral galaxies M81 (Chandar et al. 2004; Nantais et al. 2011), the Whirlpool Galaxy M51 (Chandar et al. 2004; Hwang & Lee 2008), and in the Sombrero Galaxy M104 (Larsen et al. 2001b).

In addition to ECs located in galactic halos, Larsen & Brodie (2000) and Brodie & Larsen (2002) discovered a population of extended star clusters co-rotating with the disk of the lenticular galaxy NGC 1023. These so-called faint fuzzies (FFs) have similar structural parameters as halo ECs and are therefore not easily distinguishable from halo ECs projected onto the disk

[4] http://www.mancone.net/m33_catalog/

[5] Available online at http://www.physics.mcmaster.ca/Fac_Harris/Harris_SaasFee.pdf

on the basis of imaging data alone. A fair fraction of ECs found in extragalactic surveys – especially those covering only the disk regions as in the afore mentioned galaxy M51 – might therefore be associated with the disks and not the halos of these galaxies.

Chies-Santos et al. (2007) searched for ECs in the lenticular galaxy NGC 1380 of the Fornax Cluster and found both types of objects: red objects similar to FFs in the inner part of the disk (2 kpc $\leq R_{\rm gal} \leq$ 5 kpc), and predominantly blue objects with sizes up to 13 pc at projected galactocentric radii 10 kpc $\leq R_{\rm gal} \leq$ 20 kpc.

Centaurus A (NGC 5128) of the neighboring CenA/M83 group is the closest giant elliptical galaxy, located at a distance of 3.8 Mpc (Harris et al. 2010). Centaurus A has a GC system of probably more than 1400 GCs (Harris et al. 2012). So far, 26 ECs were detected in NGC 5128 (Gómez et al. 2006; McLaughlin et al. 2008; Chattopadhyay et al. 2009; Taylor et al. 2010; Mouhcine et al. 2010). ECs were also detected in other giant elliptical galaxies, like for example the central galaxy of the Virgo Cluster M87 (Brodie et al. 2011; Chies-Santos et al. 2011) or NGC 4365 (Blom et al. 2012). In summary, ECs are associated with early- and late-type galaxies ranging from dwarf to giant elliptical galaxies.

1.3 Ultra-Compact Dwarf Galaxies

Ultra-compact dwarf galaxies (UCDs) were discovered in the Fornax cluster by Hilker et al. (1999) and Drinkwater et al. (2000). UCDs were defined as compact objects – not resolved by ground based observations – with luminosities *above* the brightest known GCs. They are significantly more compact than typical dwarf galaxies of comparable luminosity, but compared to GCs they are larger, brighter and more massive. Phillipps et al. (2001) interpreted these objects as a new type of galaxy and transported this interpretation in the name "ultra-compact dwarf galaxy". It is still the most common name for this kind of object, even though the interpretation as a new type of dwarf galaxy is discussed controversially. As UCDs could also be related to GCs, Kissler-Patig (2004) proposed the name "ultra-diffuse star cluster". A more neutral denomination was introduced by Haşegan et al. (2005) who introduced the term "dwarf-globular transition object" (DGTO).

There is no universally accepted definition of a UCD. Many observers apply a lower mass limit of $2 \cdot 10^6$ M$_\odot$ (e.g. Haşegan et al. 2005; Mieske et al. 2008). A range of effective radii between 10 and 100 pc is frequently adopted (e.g. Blakeslee & Barber DeGraaff 2008; Brodie et al. 2011). The most extended UCD (VUCD7) discovered in the outer halo of the elliptical galaxy M87 of the Virgo Cluster has an effective radius of 93.2 pc (Evstigneeva et al. 2008) and a mass of $8.8 \cdot 10^7$ M$_\odot$ (Evstigneeva et al. 2007).

Apart from the Fornax Cluster and the Virgo Cluster, UCDs have also been detected in a number of other galaxy clusters like for example the Centaurus Cluster (Mieske et al. 2007), the Coma Cluster (Madrid et al. 2010), and the Hydra Cluster (Misgeld et al. 2011). While most known UCDs belong to giant elliptical galaxies in cluster environments, they have also been observed in rather isolated objects like the Sombrero galaxy M104 (Hau et al. 2009) or the group elliptical NGC 3923 (Norris & Kannappan 2011).

UCDs are typically rather old objects. Most of them have ages larger than 8 Gyr (e.g. Evstigneeva et al. 2007; Hau et al. 2009; Chilingarian et al. 2011; Norris & Kannappan 2011). However, there are examples of young and intermediate-age UCDs. Maraston et al. (2004) discovered a very massive star cluster (W3) with an age between 300 and 500 Myr in the galaxy NGC 7252. W3 has a mass of about $8 \cdot 10^7$ M$_\odot$ and an effective radius of $r_{\rm eff} = 17.5$ pc and may thus be classified as a young version of a UCD. Norris & Kannappan (2011) discovered a UCD with an intermediate-age of about 3.4 Gyr in the galaxy NGC 4546. It has a mass of about $3 \cdot 10^7$ M$_\odot$ and an effective radius of $r_{\rm eff} = 25.5$ pc.

The origin and nature of UCDs has not been clarified yet and is still hotly debated. The

effective radii and total luminosities of UCDs place them between the parameters of GCs and dwarf galaxies. As there is no unique and unambiguous definition of a "galaxy", UCDs can be taken to be both depending on the favored definition. Forbes & Kroupa (2011) proposed that a galaxy is a gravitationally bound stellar system where the internal stellar dynamics can be approximated by the collisionless Boltzmann equation, i.e. systems with a two-body relaxation time longer than a Hubble time. In this definition UCDs are galaxies – along with a couple of ECs like the Milky Way EC NGC 2419 and the M31 ECs detected by Huxor et al. (2005). On the other hand, four UFDs of the Milky Way like Segue 1 and 2 would not be galaxies but star clusters. Alternatively, Willman & Strader (2012) defined a galaxy as a gravitationally bound collection of stars whose properties cannot be explained by a combination of baryons and Newton's laws of gravity. In this definition, UCDs and ECs are star clusters, while all UFDs are galaxies.

The formation scenarios for UCDs can be subdivided into scenarios with a galaxy origin and scenarios with a star cluster origin. The simplest interpretation for both scenarios is a new type of dwarf galaxy (Phillipps et al. 2001) or that UCDs are an extension of the GC sequence to higher masses (Mieske et al. 2002). More complex formation scenarios propose the origin of UCDs as the remnant nucleus of a stripped dwarf galaxy (e.g. Bekki et al. 2001; Drinkwater et al. 2003; Bekki et al. 2003; Pfeffer & Baumgardt 2013) or as a merger of young massive star clusters (e.g. Fellhauer & Kroupa 2002a).

Forbes et al. (2008) and Mieske et al. (2008) analyzed larger samples of UCDs. They find that GCs and UCDs form a coherent data set where size and mass-to-light ratio increase continuously with their total mass and concluded that UCDs are more likely bright extended clusters than naked cores of stripped dwarf galaxies. The marginally enhanced mass-to-light ratios of UCDs can be explained by slightly modified initial stellar mass functions as either a surplus of faint low-mass stars, i.e. a bottom-heavy IMF (Mieske & Kroupa 2008), or through a top-heavy IMF which would yield a surplus of dark stellar remnants (Dabringhausen et al. 2009; Marks et al. 2012).

1.4 Young Massive Star Clusters and Star Cluster Complexes

GC formation had been thought to occur only in the early Universe (e.g. Peebles & Dicke 1968). A few decades ago "young massive star clusters" (YMCs) were found with the HST with GC-like properties. YMCs are found in all types of gas-rich galaxies and constitute a common class of star clusters. They are particularly abundant in starburst and interacting galaxies, but are also present in some apparently unperturbed disk galaxies (Larsen & Richtler 1999). Although YMCs are quite common in gas-rich galaxies there are some that do not host any YMCs. Larsen & Richtler (1999) searched for YMCs in 21 nearby spiral galaxies. Two galaxies (NGC 1493 and NGC 7741) did not contain any YMCs at all and some galaxies (e.g. NGC 300, NGC 4395) had only very poor YMC systems. It is not yet understood why some galaxies host YMCs whereas others do not.

There is a consensus in the GC community that YMCs are GC progenitors. However, there is no unique definition of YMCs. The definition is rather author dependent. I adopt the definition of Whitmore (2003) who defined "young" as having an age less than 500 Myr and "massive" as having masses ranging from 10^3 to 10^8 $M_\odot$. Individual YMCs were analyzed in detail by Bastian et al. (2006b), Mengel et al. (2008), and Bastian et al. (2009). The combined data set of the three publications demonstrates that the median size of YMCs in the mass range between 10^5 and 10^6 $M_\odot$ is about 4 pc. YMCs with masses of a few times 10^7 $M_\odot$ have only been observed in strong starburst environments like for example in the strongly interacting galaxies NGC 6745 (de Grijs et al. 2003), NGC 7252 (Maraston et al. 2004; Bastian et al. 2006b), and Arp 220 (Wilson et al. 2006).

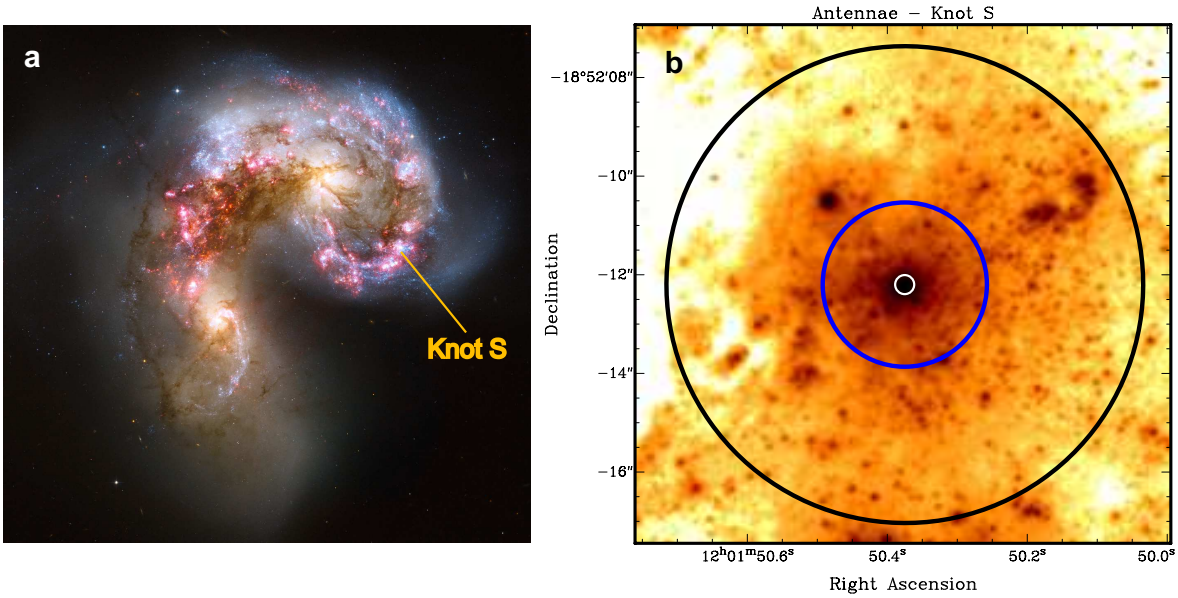

FIGURE 1.3— The Antennae (NGC 4038 + NGC 4039) – an interacting pair of galaxies at a distance of about 20 Mpc. **a:** Image of the central region of the Antennae galaxies showing the cores of the two galaxies and the inner tidal arms with complexes of young massive star clusters. The figure is a slightly modified version of Fig. 1 of Whitmore et al. (2010). **b:** HST ACS image in the F435W band of knot S, a CC with a dense object already formed in its center. The white circle indicates the effective radius of 18 pc of the central object of knot S, the blue circle the effective radius of 155 pc of the entire CC and the black circle a radius of 450 pc that was used by Whitmore et al. (1999) to derive the total luminosity. This plot is based on data taken from the Hubble Legacy Archive, see http://hla.stsci.edu/hlaview.html.

Observations have shown that YMCs are often not isolated, but are part of larger structures called cluster complexes (e.g. Whitmore & Schweizer 1995; Bastian et al. 2005, 2006a), abbreviated as CCs. The CCs contain a few to several dozens or possibly even hundreds of YMCs spanning up to a few hundred parsecs in diameter. The mass of a CC is the sum of its YMC constituents. Little is known about the detailed distribution of the YMCs in a CC and about their velocity distribution, largely because the existence of CCs had not been realized fully until only very recently. However, the observations show that most CCs have a massive concentration of star clusters in their centers and few to several dozens or possibly even hundreds of isolated star clusters in their vicinity (e.g. Bastian et al. 2005; Whitmore et al. 2010).

One well studied example of a galaxy interaction leading to the formation of CCs are the Antennae galaxies (NGC 4038 + NGC 4039), which are two colliding spiral galaxies at a distance of about 20 Mpc (Fig. 1.3a). The two interacting galaxies are currently going trough a phase of starburst. In the process of the encounter, two long tidal tails of stars and gas are thrown out of the galaxies which resemble the antennae of an insect. The CCs in the Antennae (Whitmore & Schweizer 1995; Whitmore et al. 1999) are often referred to as knots. They are located in the outskirts of the interacting galaxies. The knots of the Antennae have typical masses of the order of $M_{\rm knot} = 10^6$ to 10^7 $M_\odot$ and sizes of up to a few hundred parsecs (Whitmore et al. 2005; Bastian et al. 2006a). The knots typically consist of a few YMCs more massive than 10^5 $M_\odot$, about 25 YMCs with masses greater than 10^4 $M_\odot$ and about 60 lower-mass clusters (Whitmore et al. 2005, 2010).

One prominent example is knot S (Fig. 1.3b), which is the second brightest knot of the Antennae. Whitmore et al. (1999) used a radius of 450 pc (black circle in Fig. 1.3b) to derive a total luminosity of knot S of $M_{\rm V} = -15.8$ mag. The very young age of knot S of about 7 Myr (Whitmore et al. 1999) involves a mass-to-light ratio of only $\log_{10}(M/L_{\rm V}) = -1.6$ (Bruzual & Charlot 2003). This low mass-to-light ratio leads to a total mass of knot S of $4.5 \cdot 10^6$ $M_\odot$. Knot S has a

bright central object, which contains approximately one-third of the total mass of knot S. The entire knot S has an effective radius of 155 pc (blue circle[6] in Fig. 1.3b), while the central object has an effective radius of 18 pc (Bastian et al. 2013, white circle in Fig. 1.3b). Next to the central object, knot S comprises further 95 objects, 33 objects thereof are brighter than $M_{\rm V} = -9$ mag or more massive than $3.8 \cdot 10^3$ $M_\odot$ (Whitmore et al. 2010).

Inspired by the observations in the Antennae galaxies Kroupa (1998) studied for the first time the dynamical evolution of CCs for the duration of 95 Myr. Kroupa (1998) showed that in CCs with a high density of star clusters significant merging of star clusters is likely. The merging process leads to a massive star cluster – the merger object – in the central part of a CC. The scenario is therefore called the "merging star cluster scenario". In this scenario the bright central object in knot S could be interpreted as an early merger object.

Whitmore et al. (2005) found that the cluster-to-cluster velocity dispersion in the knots of the Antennae galaxies is small enough to keep them gravitationally bound leading to merging of star clusters in the central region of the knots, confirming the prior suggestion by Kroupa (1998). Mengel et al. (2008) observed individual young (≈ 10 Myr) clusters associated with CCs in the Antennae and NGC 1487. They compared dynamical mass estimates with derived photometric masses and found them in excellent agreement, implying that most of the star clusters survived the gas removal phase and are bound stellar objects. Bastian et al. (2009) found three 200 to 500 Myr old, apparently stable clusters in the Antennae with very high radial velocities relative to the galactic disk, indicating that these star clusters will most likely become future halo objects. One cluster is surrounded by so far unmerged stellar features in its vicinity.

The collision between the two gas-rich Antennae galaxies triggered the formation of super giant molecular complexes with masses up to $9 \cdot 10^8$ $M_\odot$ (Wilson et al. 2003). It is expected that these super massive complexes of gas clouds will lead to CCs even more massive than the currently observed ones. Some starburst galaxies like for example Arp 220 at a distance of 77 Mpc hosts YMCs/CCs as massive as 10^7 $M_\odot$ with ages less than 10 Myr (Wilson et al. 2006). Arp 220 also represents two colliding spiral galaxies. In contrast to the Antennae galaxies the cores of the individual galaxies can hardly be separated. In addition to the very massive YMCs/CCs mentioned before, Arp 220 also hosts somewhat older YMCs with ages between 70 and 500 Myr and masses of the order of 10^6 $M_\odot$ comparable to those of the Antennae. The data suggest that in a heavily interacting system very massive CCs form at considerably later phases of the encounter.

The galaxy NGC 7252 hosts a very massive star cluster (W3) with an age between 300 and 500 Myr. W3 has a mass of about $8 \cdot 10^7$ $M_\odot$ and an effective radius of $r_{\rm eff} = 17.5$ pc (Maraston et al. 2004). From its structural parameters W3 may be classified as a young version of a UCD. The young age of W3 rules out an origin as a remnant nucleus of a stripped dwarf galaxy. W3 may instead have evolved from a CC by merging of its constituent star clusters. This formation scenario for W3 has been studied by Fellhauer & Kroupa (2005a).

An example for the formation of CCs in a spiral galaxy formed during an interaction with a small companion galaxy is the so-called Whirlpool Galaxy (M51, Fig. 1.4). M51 is a spectacular grand-design spiral galaxy at a distance of about 9 Mpc seen nearly face-on. The galaxy has a close galactic neighbor, NGC 5195. Bastian et al. (2005) found eleven CCs in the disk of M51. The spatial distribution of the CCs is connected to the spiral arms of the disk. Most complexes are found at the outer edges of the spiral arms. An example of such a CC is shown in the blow-up picture of Fig. 1.4. The CCs in M51 are all less than 10 Myr old, have radii[7] between

[6] No effective radius of the entire knot S has been published so far. I determined $r_{\rm eff}$ using HST data (Fig. 1.3b).

[7] The radius of the CCs in M51 was defined by Bastian et al. (2005) as the radius of a circle around a CC where the color, as a function of radius, becomes constant. Note that these radii are completely independent of the effective radii, $r_{\rm eff}$, and correspond rather to a cutoff radius.

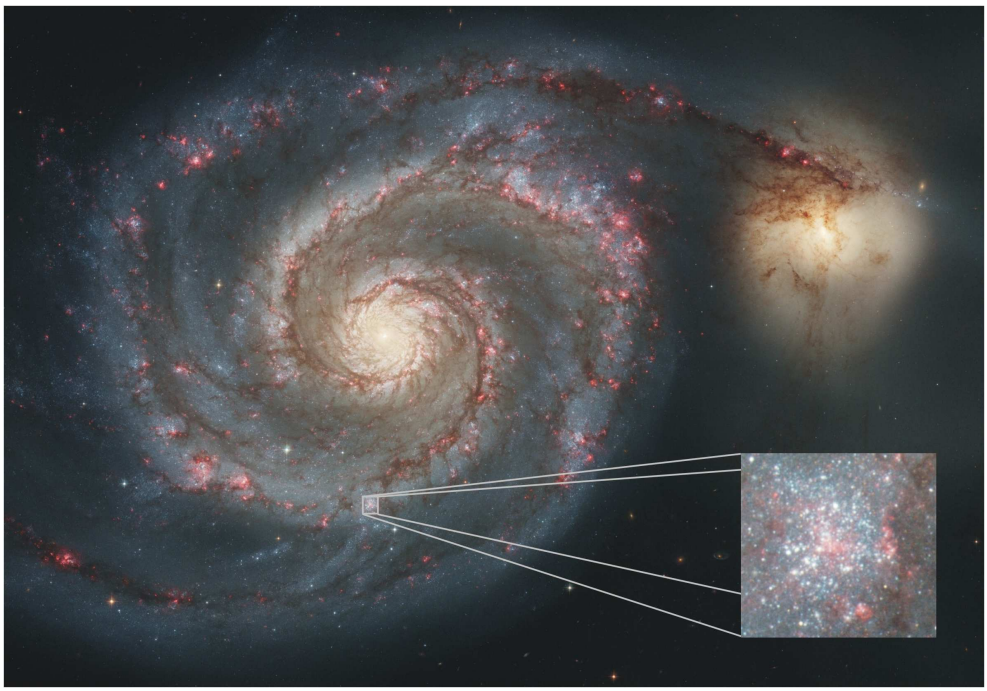

FIGURE 1.4— The Whirlpool galaxy (M51 or NGC 5194) – a grand-design spiral galaxy interacting with its small companion NGC 5195. The system is located at a distance of about 9 Mpc. Bastian et al. (2005) found eleven young massive star cluster complexes with ages younger than 10 Myr in the disk of M51 which have sizes between 85 and 240 pc, and cover a mass range of $0.3 - 3 \cdot 10^5$ $M_\odot$. An example of one of the CCs is shown in the blow-up picture. The figure is based on images taken from the HST public picture database.

$R_{\rm cut} \approx 85$ and ≈ 240 pc, and cover a mass range of $M^{\rm CC} = 0.3 - 3 \cdot 10^5$ $M_\odot$. For the eleven CCs of M51 Bastian et al. (2005) found a power law correlation between the mass and the size. This CC mass-radius relation is comparable to the one of the progenitor giant molecular clouds.

The Tadpole galaxy (UGC 10214) is an example for CC formation in a tidal tail. It is a disrupted barred spiral galaxy at a distance of about 125 Mpc. The galaxy shows a long tidal tail of stars and some CCs. The long tidal tail stems from a previous interaction which makes the galaxy look like a tadpole. The enlargement in Fig. 1.5 shows the most luminous and largest CC in the tail, which has an age of about 4.5 Myr, an effective radius of $r_{\rm eff} = 160$ pc, and a total luminosity of $M_{\rm V} = -14.45$ mag (Tran et al. 2003). The very young age of 4.5 Myr involves a mass-to-light ratio of only $\log_{10}(M/L_{\rm V}) = -1.6$ (Bruzual & Charlot 2003) and therefore a total mass of $M^{\rm CC} = 1.3 \cdot 10^6$ $M_\odot$ (Tran et al. 2003). The relatively large projected distance of approximately 60 kpc from the center of the galaxy and the young age of 4.5 Myr would imply an unrealistically high velocity of at least 13 000 km s^{-1} relative to the Tadpole galaxy, if the CC was formed within this galaxy. Consequently, the CC needs to be formed within the tidal tail (Tran et al. 2003), demonstrating that CCs can be generated outside galaxies.

Further examples for galaxies with CCs are Arp 24 (Cao & Wu 2007), NGC 6946 (Larsen et al. 2002), NGC 3256 (Trancho et al. 2007), Stephan's Quintet (Trancho et al. 2012), the dwarf galaxies Mrk 36, UM 408, and UM 461 (Lagos et al. 2011) and several nearby spiral galaxies (Larsen 2004). There are many more examples of YMCs/CCs, however, in distant galaxies the spatial resolution of the observations is not high enough to identify individual YMCs, so a CC would look like one big YMC. In the interacting galaxy Stephan's Quintet, where individual YMCs were resolved, the objects associated with recent star formation appeared to be complexes of YMCs rather than single YMCs, whereas the older sources seemed to be single star clusters (Trancho et al. 2012).

The preponderance of clumpy galaxies at high redshifts (Elmegreen 2007, and references

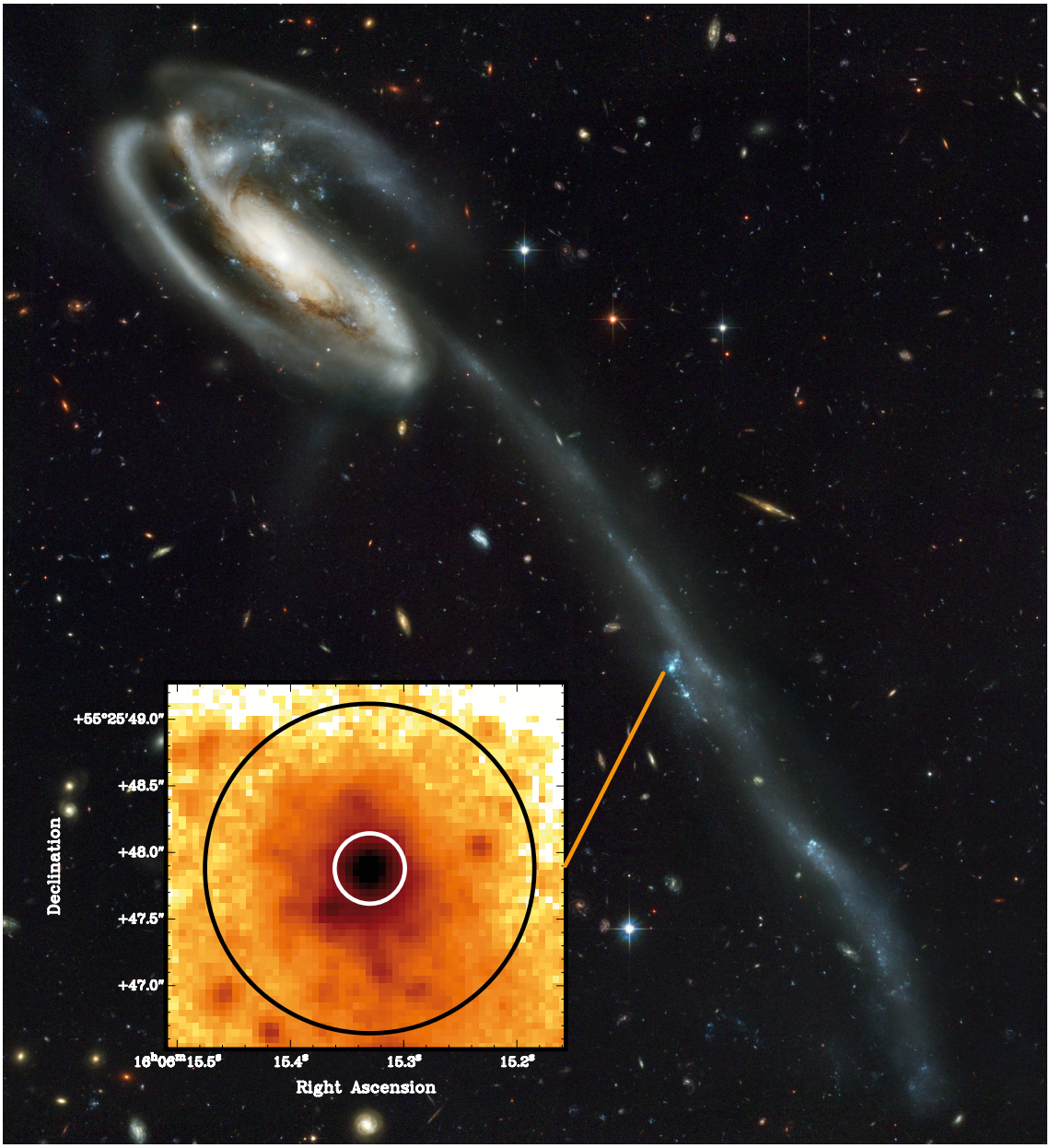

FIGURE 1.5— The Tadpole galaxy (UGC 10214) – a disrupted barred spiral galaxy at a distance of about 125 Mpc. The galaxy shows a long tidal tail of stars and complexes of young massive star clusters stemming from a previous interaction. The most massive CC in the tail (blow-up picture) has a mass of the order of 10^6 $M_\odot$, an effective radius of about 160 pc and is located at approximately 60 kpc from the center of the galaxy (Tran et al. 2003; Jarrett et al. 2006). The white circle in the blow-up picture indicates the effective radius of 160 pc of the CC and the black circle a radius of 750 pc, illustrating the total extent of the CC. The main figure is taken from the HST public picture database and the blow-up picture is based on HST ACS data in the F435W band, taken from the Hubble Legacy Archive, see http://hla.stsci.edu/hlaview.html.

therein) indicates that early gas-rich galaxies went through an epoch of profuse CC formation. Bournaud et al. (2008a) performed high-resolution modeling of a galaxy interaction that lead to a merger remnant comparable to an elliptical galaxy. In these models, super star clusters with masses of a few 10^7 $M_\odot$ and sizes up to about 150 pc formed in the halo of this merger remnant. Bournaud et al. (2008b) demonstrated that these star clusters are gravitationally stable.

The wide occurrence of CCs in various physical environments ranging from disk galaxies through interacting galaxies to tidal tails is prompting the realization that CCs are likely a very

important mode of star formation. Since galaxy-galaxy interactions are anticipated to have been more common during early cosmological structure formation CCs are probably the main mode of star-burst activity at high redshift.

An important question about these CCs concerns their future evolution over several gigayears. As already mentioned before, Kroupa (1998) showed that in CCs with a high density of star clusters, significant merging of star clusters is likely within a timescale of less than 100 Myr. The merging leads to massive star clusters in the central part of the CCs. Fellhauer & Kroupa (2002a) and Fellhauer & Kroupa (2002b) demonstrated that the merging star cluster scenario is able to produce merger objects with structural parameters similar to FFs and UCDs after a dynamical evolution of several gigayears. On the foundation of this proof of concept, my thesis presents for the first time systematic parameter studies covering the CC parameter space.

1.5 Outline of Thesis

In this thesis, I propose a unified formation scenario for the different types of extended stellar dynamical objects (EOs), i.e. faint fuzzies (FFs), extended star clusters (ECs) in the halo, and ultra-compact dwarf galaxies (UCDs). I suggest that the merging of star clusters in CCs is a suitable formation mechanism to explain all types of EOs as remnants of merged CCs. In my simulations, I start with newly born complexes of star clusters formed during a past interaction of galaxies and model the dynamical evolution of the CCs in different gravitational environments leading to merger objects.

The thesis comprises five extensive parameter studies of the merging star cluster scenario. The first two projects focus on well observed examples for EOs in the disk and the outer halo of galaxies (Chapter 4). The remaining three studies treat the subject more generally by covering the entire range of observed objects located in a galactic halo (Chapter 5). To compare the results of the simulations with observations, I compiled the first comprehensive catalog of ECs and UCDs with effective radii larger than 10 pc from the literature (Chapter 3). A brief description of the contents of the chapters is given below.

Chapter 2 introduces the numerical method used for the parameter studies of this thesis. I used the particle-mesh code SUPERBOX which had already been successfully employed by M. Fellhauer for studies of the merging star cluster scenario (e.g. Fellhauer & Kroupa 2002a,b). The first parameter study on FFs used the Fortran version of SUPERBOX (Bien et al. 1990, 1991; Fellhauer et al. 2000), the later projects profited from a new version called SUPERBOX++ (Metz 2008), which was developed by M. Metz between 2006 and 2009 at the Argelander-Institut (AIFA) in Bonn. It is a new C++ implementation of the FORTRAN particle-mesh code SUPERBOX using object oriented programming techniques and modern multi-core processor technologies. The simulations presented in the different parameter studies below are all very time-consuming. Even on the AIfA compute servers with 16 and 32 CPU cores the computing time for a simulation typically ranged between two weeks and two months depending on the individual simulation.

Chapter 3 presents a comprehensive catalog of observed EOs, i.e. FFs, halo ECs, and UCDs with effective radii larger than 10 pc compiled from the literature. At the moment, the catalog contains 835 EOs. The data of the EO catalog is presented in Appendix A. The number of discovered EOs has increased continuously especially in the past few years. The EOs have been found in all types of galaxies in different environments. The catalog contains information on the structural parameters of the EOs, their projected distances to the host galaxies as well as information on the basic parameters of the host galaxies. The various parameters are analyzed in

detail, expecially with respect to overall trends and correlations. The results are also discussed in terms of possible selection effects.

Chapter 4 investigates the merging star cluster formation scenario for special examples of EOs. The first part deals with the evolution of CCs in galactic disks and the second part gives an insight into the evolution of a CC in a galactic halo.

In the first part, I tackle the question whether CCs associated with galactic disks could be the progenitors of FFs, which are a type of EO first observed by Larsen & Brodie (2000) in the disk of the galaxy NGC 1023. The parameters of the CCs are chosen such that the models cover the entire range of the mass-radius relation of Bastian et al. (2005). I performed simulations on different circular orbits between 2 and 12 kpc, on an eccentric orbit between 3 and 8 kpc and without an external gravitational field. In addition, I varied the number and the initial configuration of the star clusters in the CC. The total number of simulations amounts to 25.

In the second part, I investigate in detail the possibility that the exceptional Milky Way EC NGC 2419 is the remnant of a merged CC. NGC 2419 is one of the most luminous, one of the most distant ($R_{\rm gal} = 92.5$ kpc), and as well one of the most extended GCs of the Milky Way. Comprehensive observational data are available to allow for a detailed comparison of simulations and observations. It is therefore an ideal object to study the future fate of CCs in low gravitational field environments. I traced back a suitable orbit in time and performed 27 different numerical simulations with varying CC masses, CC sizes, and initial distributions of star clusters in the CC.

The total number of simulations in the two parameter studies to model specific EOs amounts to 52 simulations.

Chapter 5 analyzes in general how the structural parameters of the final merger objects correlate with the underlying CC parameter space.

In the first part, I study the dependence of the initial CC sizes and masses on the evolution of the CCs keeping the orbit fixed. The varied sizes and masses of the initial CCs cover a matrix of 5×6 values with CC Plummer radii between 10 and 160 pc and CC masses between $10^{5.5}$ and 10^8 $\mathrm{M}_\odot$, which are consistent with the observed range of CC parameters. The CCs are placed on a polar eccentric orbit with galactocentric distances between 20 and 60 kpc in an analytical Milky-Way-like potential. I also recalculated some CC models on an eccentric inclined orbit to study whether the inclination of the orbit has a measurable effect on the structural parameters of the final merger objects. The parameter study on initial CC conditions consists of 52 simulations.

In the second part, I investigate the influence of the orbit on the low-mass CC models which are most vulnerable to a tidal field. First, I consider circular orbits for CC models with a fixed mass of $M^{\rm CC} = 10^{5.5}$ $\mathrm{M}_\odot$. The initial CC sizes and the galactic distances of the CC orbits cover a matrix of 4×4 values with CC Plummer radii between 20 and 160 pc and galactic distances between 20 and 120 kpc. For comparison, I also include simulations without a tidal field. In addition, I extend the orbital parameter study to different eccentric orbits to investigate also the influence of varying apo- and perigalactic distances and the choice of the CC starting point (peri- or apocenter) on the evolution of the CCs. The total number of simulations of the orbital parameter study amounts to 28 simulations.

In the third part, I discuss the conditions for the formation of extremely extended EOs. The study focuses on low-mass CC models with masses between $M^{\rm CC} = 10^5$ and 10^6 $\mathrm{M}_\odot$ which are studied on different orbits. Moreover, for the most extended CC models I extend the simulations on circular orbits at 60 and 120 kpc to CC masses up to $M^{\rm CC} = 10^8$ $\mathrm{M}_\odot$ and $M^{\rm CC} = 10^7$ $\mathrm{M}_\odot$, respectively. The study of extreme EOs leads to 22 additional simulations.

In all three parameter studies, the results of the models are analyzed with respect to overall

trends and the structural parameters of the merger objects are compared with the corresponding data from the EO catalog. The total number of simulations from the three parameter studies of this chapter amounts to 102 simulations.

Chapter 6 summarizes the main results of the 154 simulations presented in Chapters 4 and 5 and the EO catalog of Chapter 3.

Chapter 7 provides an outlook to future numerical and observational work that should be done to shed additional light on the origin of EOs.

The thesis has three appendices. Appendix A contains the data of the EO catalog presented in Chapter 3. Appendix B provides a short manual on SUPERBOX with a focus on the merging star cluster scenario. It describes the set-up procedure of the CC models and the computation of their evolution. The simulations require a high level of maintenance. Appendix C contains the tables with the results of the simulations of Chapters 4 and 5.

A large part of this thesis has been published in the Journals *Astrophysical Journal* and *Astronomy & Astrophysics*:

Brüns, R. C., Kroupa, P., & Fellhauer, M. 2009, ApJ, 702, 1268, 7 pages
Faint Fuzzy Star Clusters in NGC 1023 as Remnants of Merged Star Cluster Complexes

Brüns, R. C., & Kroupa, P. 2011, ApJ, 729, 69, 12 pages
A New Formation Scenario for the Milky Way Cluster NGC 2419

Brüns, R. C., Kroupa, P., Fellhauer, M., Metz, M., & Assmann, P. 2011, A&A, 529, 138, 12 pages
A Parametric Study on the Formation of Extended Star Clusters and Ultra-Compact Dwarf Galaxies

Brüns, R. C., & Kroupa, P. 2012, A&A, 547, 65, 17 pages
A Catalog of Extended Clusters and Ultra-Compact Dwarf Galaxies. An Analysis of their Parameters in Early- and Late-type Galaxies

2

Numerical Method

Observations of stellar systems like star clusters (SCs) and galaxies represent only snapshots of these objects. To study the dynamical evolution of stellar systems which takes billions of years and to find relations between astronomical objects in different evolutionary states computer simulations are required. In this thesis I study the fate of star cluster complexes (CCs). The SCs in a CC merge and form a larger object, called the merger object. The formation scenario is therefore called the "merging star cluster scenario". In this chapter I describe the setup of the CCs and the numerical method used for the simulations.

2.1 N-Body Codes

N-body codes calculate the time evolution of multi-body systems. In simulations the matter distribution of a stellar system is discretized into a collection of N point masses called particles. In stellar systems with a small number of stars the particles may represent real stars whereas in large stellar systems like for example galaxies, which contain several hundred billions of stars, it is impossible to cope with such a large number of particles. The particles in these simulations have masses several orders of magnitude above the mass of a single star. In N-body simulations the particles move according to the Newtonian equations of motion

$$\begin{aligned} \frac{d\vec{r}_i}{dt} &= \vec{v}_i, \\ \frac{d\vec{v}_i}{dt} &= \vec{a}_i = \frac{\vec{F}_i}{m_i} = -\vec{\nabla}_i \Phi, \end{aligned} \qquad i = 1, \ldots, N \tag{2.1}$$

where $\vec{r}_i$, $\vec{v}_i$, and $\vec{a}_i$ are the position, velocity, and acceleration vectors of particle i at time t, m_i the particle mass, $\vec{F}_i$ the total force acting on a particle i and Φ is the gravitational potential. The equations describe the change in particle position and velocity over time.

Figure 2.1 illustrates the basic structure of an N-body code. To start a simulation, the initial state ($t = t_0$) of the stellar system has to be specified (step 1), i.e. the initial positions $\vec{r}_{i,0}$ and initial velocities $\vec{v}_{i,0}$ have to be set for every particle i. From the initial state the positions and velocities of the particles are evolved over time according to Eq. 2.1. To integrate Eq. 2.1 numerically the continuous functions $\vec{r}_i$ and $\vec{v}_i$ have to be replaced by values at discrete time intervals (step 2). The integrator estimates the new position and velocity of a particle for the next time step. Therefore the acceleration has to be computed for every time step. The simulation is stopped when the user-defined integration time, t_{int}, is reached and the resulting stellar dynamical object is analyzed or processed further (step 3).

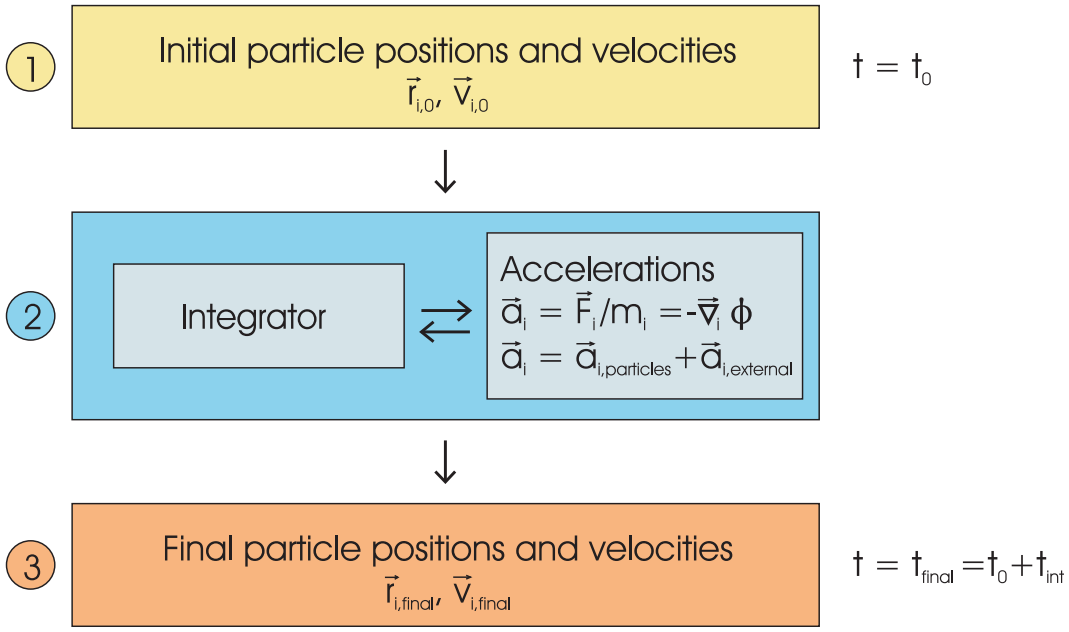

FIGURE 2.1— Basic programming structure of an N-body code. The initial particle positions and velocities, $\vec{r}_{i,0}$ and $\vec{v}_{i,0}$, are needed as an input for the numerical integrator (step 1). The integrator determines the orbital evolution of the particles with respect to the potential (step 2). After the integration time, $t_{\rm int}$, the final particle positions and velocities, $\vec{r}_{i,\rm final}$ and $\vec{v}_{i,\rm final}$, are reached and the resulting stellar dynamical object can be analyzed or processed further (step 3).

2.1.1 Set-Up of the Initial Conditions

To start a simulation the initial conditions of the particles building up the SCs and of the distribution of SCs in a CC have to be specified (step 1 in Fig. 2.1). Sections 2.1.1.1 and 2.1.1.2 describe, respectively, the setup of a CC model and the initial conditions for the individual SCs in the CC. Section 2.1.1.3 introduces an important parameter to describe how densely a CC is filled with SCs.

2.1.1.1 The CC Model

CCs are observed to have a massive concentration of SCs in their centers and a few to several dozens or possibly even hundreds of isolated SCs in their vicinity (e.g. Bastian et al. 2005; Whitmore et al. 2010). As the exact mass distribution of SCs within CCs is not known I adopt a Plummer model (Plummer 1911) to create the initial distribution of SCs in the CCs, which is a good approximation to the observed distribution and also constitutes the simplest solution of the collisionless Boltzmann equation. The Plummer model is defined by only two free parameters, the total mass, M, and the Plummer radius, $R_{\rm pl}$. In addition, every important quantity can be derived analytically. As a starting point for my simulations I distribute $N_0^{\rm CC}$ equal-mass SCs according to a spherical Plummer distribution. The initial position and velocity of a SC in the Plummer sphere are generated with seven random numbers $X_1 ... X_7$ according to the recipe of Aarseth et al. (1974). I will summarize the basic steps of the procedure below. For additional lectures on this topic the reader is referred to the "The Cambridge N-Body Lectures" (Kroupa 2008) and the excellent website[1] "The Art of Computational Science" developed by Hut & Makino (2003).

I start with the initial spatial distribution of SCs of the CC, i.e. the positions of the SCs, $\vec{r}_{i,0} = (x_{i,0}, y_{i,0}, z_{i,0})$ with $i = 1 \ldots N_0^{\rm CC}$, at time $t = t_0$. The mass enclosed within a distance $r = |\vec{r}|$

[1]The lecture on Plummer models is available at http://www.artcompsci.org/kali/vol/plummer/volume9.pdf

from the center of the CC is given by

$$M(r) = \int_0^r 4\,\pi\,r'^2\,\rho(r')\,dr' = M^{\rm CC}\,\left(1+\left(\frac{R_{\rm pl}^{\rm CC}}{r}\right)^2\right)^{-3/2}, \tag{2.2}$$

where $\rho(r)$ is the mass density, and $M^{\rm CC}$ and $R_{\rm pl}^{\rm CC}$ are the total mass and the Plummer radius of the CC. Equation 2.2 can be rewritten as

$$X_1(r) \equiv \frac{M(r)}{M^{\rm CC}} = \left(1+\left(\frac{R_{\rm pl}^{\rm CC}}{r}\right)^2\right)^{-3/2}. \tag{2.3}$$

The function $X_1(r)$ is the fraction of the total CC mass inside the radial position r. If an object is placed at the center of the CC, this fraction is zero, i.e. $X_1(r=0)=0$. Placing an object very far away from the CC center yields $M(r)\approx M^{\rm CC}$ and $X_1(r\to\infty)=1$. Thus the function $X_1(r)$ yields values between 0 and 1. Solving Eq. 2.3 for r gives the radial position as a function of X_1,

$$r(X_1) = R_{\rm pl}^{\rm CC}\,\left(X_1^{-2/3}-1\right)^{-1/2}. \tag{2.4}$$

The radial position, r_i, of a SC i can therefore be obtained from its position in the mass distribution, X_1. For each SC a value for X_1 is diced and its radial position, r_i, is determined via Eq. 2.4. Since the Plummer distribution extends infinitely it has to be truncated at some radius known as the cutoff radius $R_{\rm cut}^{\rm CC}$. SCs are only placed within the user-defined cutoff radius. This cutoff radius should be chosen large enough to prevent a clear break or edge in the spatial distribution and small enough to avoid single SCs at very large distances that would be stripped away immediately.

As the distance r_i of a SC i from the center of the CC is already determined from Eq. 2.4 and therefore fixed, two additional random numbers, X_2 and X_3, are necessary to determine the initial position $\vec{r}_{i,0}=(x_{i,0},y_{i,0},z_{i,0})$ of the SC on the surface of the sphere with radius r_i.

$$z_{i,0} = (1-2\,X_2)\,r_i, \tag{2.5a}$$

$$x_{i,0} = \sqrt{r_i^2-z_{i,0}^2}\,\cos\theta_i = \sqrt{r_i^2-z_{i,0}^2}\,\cos(2\,\pi\,X_3), \tag{2.5b}$$

$$y_{i,0} = \sqrt{r_i^2-z_{i,0}^2}\,\sin\theta_i = \sqrt{r_i^2-z_{i,0}^2}\,\sin(2\,\pi\,X_3), \tag{2.5c}$$

where X_2 and X_3 are random numbers between 0 and 1. The coordinate $z_{i,0}$ covers the range from $-r_i$ up to r_i uniformly and the angles θ_i cover uniformly the range $0\le\theta_i\le 2\pi$. The procedure has to be repeated for all $N_0^{\rm CC}$ SCs to determine their positions in the CC.

In addition to spherical symmetry in position space the Plummer model has an isotropic velocity distribution. The initial velocities $\vec{v}_{i,0}=(v_{x,i,0},v_{y,i,0},v_{z,i,0})$ of the SCs are obtained from the velocity distribution function $f(r,v)=f(E)$ that generates the Plummer's density law, i.e.

$$f(E) = \begin{cases} \left(\frac{24\,\sqrt{2}}{7\,\pi^3}\frac{(R_{\rm pl}^{\rm CC})^2}{G^5\,(M^{\rm CC})^4}\right)(-E)^{7/2} & \text{if } E\le 0,\\ 0 & \text{if } E>0, \end{cases} \tag{2.6}$$

where E is the total energy per SC. The distribution function is zero for escapers, i.e. for $E>0$. The total energy E_i of an individual SC i with mass $M^{\rm SC}$ and velocity $\vec{v}_i$ is calculated by

$$E_i = \tfrac{1}{2}\,M^{\rm SC}\,v_i^2 + M^{\rm SC}\,\Phi_{\rm pl}^{\rm CC}(r_i) \tag{2.7}$$

where $\Phi_{\rm pl}^{\rm CC}(r_i)$ is the Plummer potential at the location r_i of the SC, i.e.

$$\Phi_{\rm pl}^{\rm CC}(r_i) = -\frac{G\,M^{\rm CC}}{\sqrt{r_i^2 + \left(R_{\rm pl}^{\rm CC}\right)^2}}. \tag{2.8}$$

At a particular distance r_i from the center of the CC the minimum possible velocity of a SC is $v_i = 0$. It occurs when a SC is moving on a radial orbit and has reached its maximum distance. For a SC to be bound its maximum velocity v_i has to be smaller than the escape velocity, $v_{\rm esc}(r_i)$. Thus the maximum velocity allowed at a radius r_i is the point where the total energy E_i of a SC is zero. The values of the escape velocity at a given distance r_i are calculated by Eq. 2.10:

$$\frac{1}{2}\,M^{\rm SC}\,(v_{\rm esc}(r_i))^2 + M^{\rm SC}\,\Phi_{\rm pl}^{\rm CC}(r_i) = 0 \Longrightarrow v_{\rm esc}(r_i) = \sqrt{-2\,\Phi_{\rm pl}^{\rm CC}(r_i)} \tag{2.9}$$

$$\overset{(2.8)}{\Longleftrightarrow} v_{\rm esc}(r_i) = \sqrt{2\,G\,M^{\rm CC}}\,\left(r_i^2 + \left(R_{\rm pl}^{\rm CC}\right)^2\right)^{-1/4}. \tag{2.10}$$

At a given radial position r, the probability to obtain velocities between v and $v + dv$ is obtained from the distribution function $f(E)$ presented in Eq. 2.6,

$$\begin{aligned} 4\,\pi\,f(E)\,v^2\,dv &\overset{(2.6)}{=} const.\,(-E)^{7/2}\,v^2\,dv \\ &\overset{(2.7)}{=} const.\left(-\frac{1}{2}\,v^2 - \Phi_{\rm pl}^{\rm CC}(r)\right)^{7/2} v^2\,dv \\ &\overset{(2.9)}{=} const.\left(1 - \frac{v^2}{v_{\rm esc}^2}\right)^{7/2} v^2\,dv \\ &\equiv g(v)\,dv. \end{aligned} \tag{2.11}$$

Introducing the variable $q = \frac{v}{v_{\rm esc}}$ yields

$$g(q)\,dq \propto q^2\,\left(1-q^2\right)^{7/2}\,dq \Rightarrow g(q) = g_0\,q^2\,\left(1-q^2\right)^{7/2}, \tag{2.12}$$

where g_0 is a normalization constant. A SC can have a minimum velocity of zero and a maximum velocity of $v_{\rm esc}$. Thus the variable q has values between 0 and 1. To determine the absolute value for the velocity v_i of a SC for a fixed position r_i, the values of q_i are diced according to the function $g(q_i)$. Therefore the Neumann acceptance-rejection method is used which needs two random numbers X_4 and X_5 between 0 and 1. The random number X_4 stands for q_i. For each random value of q_i the corresponding value $g(q_i) = q_i^2\,\left(1-q_i^2\right)^{7/2}$ is calculated[2] and compared to the random number X_5. In case X_5 lies below or is equal to $g(q_i)$ the value is accepted. Otherwise the values of X_4 and X_5 are diced anew. To make the acceptance-rejection technique more efficient, the maximum value of the function $g(q)$ is calculated. The derivative of the function $g(q)$ is

$$\begin{aligned} \frac{d\,g(q)}{dq} &= \frac{d}{dq}\left(q^2\,\left(1-q^2\right)^{7/2}\right) \\ &= 2\,q\,\left(1-q^2\right)^{7/2} - 7\,q^3\,\left(1-q^2\right)^{5/2} \\ &= q\,\left(2-9\,q^2\right)\,\left(1-q^2\right)^{5/2} \end{aligned} \tag{2.13}$$

[2]The determination of the normalization constant g_0 is not necessary in this method. Scaling the function $g(q)$ by any constant has no effect on the sampled q-values.

The function $g(q)$ has two minima and one maximum. The value of $g(q)$ at the maximum is

$$q^2 = \frac{2}{9} \Rightarrow g(q) = \frac{2}{9}\left(1 - \frac{2}{9}\right)^{7/2} \approx 0.092 \tag{2.14}$$

Scaling X_5 with 0.1 thus reduces the number of rejections in the dicing process making the procedure more efficient:

$$\begin{array}{llll} \text{if} & 0.1\ X_5 \leq g(X_4) & \text{accept:} & q = X_4, \\ \text{if} & 0.1\ X_5 > g(X_4) & \text{reject:} & \text{dice } X_4,\ X_5 \text{ anew.} \end{array} \tag{2.15}$$

As the absolute value for the velocity $v_i = q_i\ v_{\text{esc}}$ of the SC has been diced according to the velocity distribution function and is therefore fixed, two random numbers, X_6 and X_7, are necessary to determine the initial velocity $\vec{v}_{i,0} = (v_{x,i,0}, v_{y,i,0}, v_{z,i,0})$ of SC i. The algorithm is similar to the algorithm used to obtain the initial position $\vec{r}_{i,0}$ of a SC.

$$v_{z,i,0} = (1 - 2\ X_6)\ v_i, \tag{2.16a}$$

$$v_{x,i,0} = \sqrt{v_i^2 - v_{z,i,0}^2}\ \cos\theta_i = \sqrt{v_i^2 - v_{z,i,0}^2}\ \cos(2\ \pi\ X_7), \tag{2.16b}$$

$$v_{y,i,0} = \sqrt{v_i^2 - v_{z,i,0}^2}\ \sin\theta_i = \sqrt{v_i^2 - v_{z,i,0}^2}\ \sin(2\ \pi\ X_7), \tag{2.16c}$$

where X_6 and X_7 are random numbers between 0 and 1. The coordinate $v_{z,i,0}$ covers the range from $-v_i$ up to v_i uniformly and the angles θ_i are uniformly distributed over the range $0 \leq \theta_i \leq 2\pi$. The procedure has to be repeated for all N_0^{CC} SCs to determine their velocities at a fixed radial position r_i.
In my simulations, I mainly use CCs comprising 20 or 32 SCs. These numbers are too low to sample an exact Plummer distribution. However, the above procedure will generate a SC distribution with a high concentration of SCs close to the CC center and few SCs at larger distances and thus gives a good first order approximation of the observed distribution of SCs in CCs.

2.1.1.2 The SC Model

SCs are modeled as aggregations of large numbers of particles. In my simulations the SCs typically consist of $N_0^{\text{SC}} = 100\,000$ particles. To mimic the potential of real SCs I use Plummer models (Plummer 1911). The Plummer model fits the light distribution of globular clusters (e.g. Plummer 1911; Spitzer 1987) and is frequently used to model SCs. The initial position and velocity, $\vec{r}_{i,0}$ and $\vec{v}_{i,0}$, of a particle i ($i = 1 \ldots N_0^{\text{SC}}$) are calculated according to the same method as described in Sect. 2.1.1.1. A short description how to set up the SCs and the CCs is presented in Appendix B.

2.1.1.3 The Parameter α

The formation of the merger object depends on the compactness of the initial CC. A measure of how densely a CC is filled with SCs for an equal number N_0^{CC} of SCs is given by the parameter α (Fellhauer et al. 2002),

$$\alpha = \frac{R_{\text{pl}}^{\text{SC}}}{R_{\text{pl}}^{\text{CC}}}, \tag{2.17}$$

where $R_{\text{pl}}^{\text{SC}}$ and $R_{\text{pl}}^{\text{CC}}$ are the Plummer radii of a SC and of the CC, respectively. In general high values of α accelerate the merging process because the SCs already overlap in the center of the CC, whereas low values of α hamper the merging process. For example a very compact

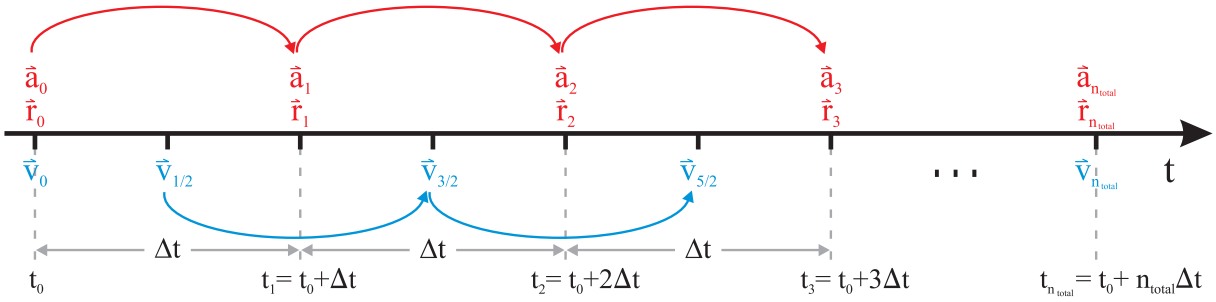

FIGURE 2.2— Illustration of the structure of the leapfrog method. The positions $\vec{r}$ and velocities $\vec{v}$ are specified at alternating points in time: the positions $\vec{r}$ and accelerations $\vec{a}$ are updated at integer times whereas the velocities $\vec{v}$ are updated at half-integer times. The method starts with $\vec{r}_0$ and $\vec{v}_{\frac{1}{2}}$ and continues with $\vec{r}$ and $\vec{v}$ leapfrogging over each other as indicated by the red and blue arrows. The simulation stops when the last integration step, $n_{\rm total}$, is reached where the values of the positions and the velocities are synchronized again.

CC consisting of SCs with SC Plummer radii of $R_{\rm pl}^{\rm SC} = 4$ pc and a CC Plummer radius of only $R_{\rm pl}^{\rm CC} = 10$ pc has an α value of $\alpha = 0.4$. Whereas an extended CC with a Plummer radius of $R_{\rm pl}^{\rm CC} = 160$ pc and the same value for the SC Plummer radius has a much smaller α value of $\alpha = 0.025$.

2.1.2 The Integrator

The integrator determines the orbital evolution of the particles in the gravitational potential (step 2 in Fig. 2.1). To integrate the Newtonian equations of motion (Eq. 2.1) numerically the continuous functions $\vec{r}_i$ and $\vec{v}_i$ for every particle need to be replaced by values at discrete time intervals. A very popular integration scheme is the leapfrog integrator. It is implemented in the particle-mesh code SUPERBOX which I used to study the merging of SCs. The discretization of Eq. 2.1 in the leapfrog scheme is given by

$$\vec{r}_{i,n+1} = \vec{r}_{i,n} + \vec{v}_{i,n+\frac{1}{2}}\,\Delta t \qquad i = 1,\ldots,N;\, n = 0,\ldots,n_{\rm total}-1 \tag{2.18a}$$

$$\vec{v}_{i,n+\frac{3}{2}} = \vec{v}_{i,n+\frac{1}{2}} + \vec{a}_{i,n+1}\,\Delta t, \tag{2.18b}$$

where $\vec{r}_{i,n}$ and $\vec{r}_{i,n+1}$ are the positions of particle i at the integration steps n and $n+1$, $\vec{v}_{i,n+\frac{1}{2}}$ and $\vec{v}_{i,n+\frac{3}{2}}$ its velocities at the integration steps $n+\frac{1}{2}$ and $n+\frac{3}{2}$, $\vec{a}_{i,n+1}$ its acceleration at integration step $n+1$, and Δt denotes the chosen time step. For each integration step n the integrator determines the new positions and velocities of all $N = N_0^{\rm CC}\, N_0^{\rm SC}$ particles until the total number of integration steps, $n_{\rm total}$, is reached.[3] In SUPERBOX all particles have the same time step which is fixed during the whole simulation. The total number of integration steps, $n_{\rm total}$, in a simulation is given by

$$n_{\rm total} = \frac{t_{\rm int}}{\Delta t}, \tag{2.19}$$

where $t_{\rm int}$ is the integration time and Δt the time step.

In the leapfrog scheme, the positions and velocities are "leapfrogged" over each other as illustrated in Fig. 2.2. The positions and accelerations are defined at integer times whereas the velocities are defined at half-integer times. Taking the velocity vector at the midpoint between the old and new particle position as in Eq. 2.18a makes the method more accurate than taking it at either end. In addition, the two equations Eq. 2.18a and Eq. 2.18b are time-reversible. Integrating backwards after integrating forward will return precisely to the starting point. Thus

[3] The subscripts n, $n+\frac{1}{2}$, $n+1$ etc. indicate the values at times $t_n = t_0 + n\,\Delta t$, $t_{n+\frac{1}{2}} = t_n + \frac{\Delta t}{2} = t_0 + (n+\frac{1}{2})\,\Delta t$, $t_{n+1} = t_n + \Delta t = t_0 + (n+1)\,\Delta t$ etc.

the leapfrog integrator allows to calculate orbits back in time. Another property of the leapfrog method is that it very well conserves the total energy.

The easiest way to derive $\vec{v}_{i,\frac{1}{2}}$ from the initial particle velocity $\vec{v}_{i,0}$ is by taking the first term of a Taylor series expansion, i.e. $\vec{v}_{i,\frac{1}{2}} = \vec{v}_{i,0} + \frac{1}{2}\,\vec{a}_{i,0}\,\Delta t$. To synchronize the values of the position and the velocity at the end of the simulation the same procedure can be applied.

The computation of the accelerations, which is needed to update the velocities of the particles (Eq. 2.18b), is described in the next section.

2.1.3 Determination of Accelerations from the N Particles

The total acceleration $\vec{a}_i$ of a particle i is composed of two parts: the acceleration $\vec{a}_{i,\text{particles}}$ stemming from the interaction with the $N-1$ particles of the model system and the acceleration $\vec{a}_{i,\text{external}}$ due to an external tidal field, i.e.

$$\vec{a}_i = \vec{a}_{i,\text{particles}} + \vec{a}_{i,\text{external}} \quad i = 1, \ldots, N. \tag{2.20}$$

The total acceleration $\vec{a}_i$ is needed to update the position $\vec{x}_i$ and velocity $\vec{v}_i$ of particle i (Sect. 2.1.2). The determination of the accelerations $\vec{a}_{i,\text{particles}}$ is discussed below in this section whereas the accelerations due to the tidal field of a host galaxy, $\vec{a}_{i,\text{external}}$, is treated in Sect. 2.1.4.

The acceleration $\vec{a}_{i,\text{particles}}$ of particle i is given by Newton's law of universal gravitation:

$$\vec{a}_{i,\text{particles}} = \frac{\vec{F}_{i,\text{particles}}}{m_i} = -\,G \sum_{j=1, j\neq i}^{N} m_j \,\frac{\vec{r}_i - \vec{r}_j}{|\vec{r}_i - \vec{r}_j|^3} \quad , \quad i = 1, \ldots, N \tag{2.21}$$

where $\vec{a}_{i,\text{particles}}$ is the acceleration vector of particle i, G the gravitational constant, m_j the mass of the jth particle and $\vec{r}_i$, $\vec{r}_j$ the position vectors of particle i and j at time t.[4]

The total acceleration $\vec{a}_{i,\text{particles}}$ of particle i due to its interactions with the other $N-1$ particles, is obtained by summing all the pair-wise interactions. This method is known as direct N-body. It has the highest level of accuracy in the evaluation of the acceleration. However, evaluating all pair-wise interactions between the particles requires on the order of $O(N^2)$ operations for each integration time step and is thus computationally very expensive. This type of simulation is reasonable only for systems with a relatively small number of particles ($N < 10^4$) (Makino & Saitoh 2012), e.g. individual SCs. For larger stellar systems, e.g. galaxies and the final objects of the merging of SCs in CCs, efficient approximation techniques and special purpose hardware have been developed to speed up the force calculations and thus reduce the computing time.

The numerical approximation techniques and special-purpose hardware, which were used to study the merging of SCs, are tree codes, GRAPEs, and particle-mesh (PM) codes. They are shortly presented below with focus on the merging of star clusters.

2.1.3.1 Tree Code & Grapes

The tree code method (Barnes & Hut 1986) modifies the direct N-body approach such that direct summation is only used for particles nearby, whereas the forces between distant particles are approximated by grouping particles together and considering particle-group interactions instead of particle-particle interactions. The method is based on the assumption that a distant group of particles may be replaced by a single point mass whose mass is the sum of the masses in the group, and whose position is the center of mass of the group. To improve accuracy,

[4] To avoid the problem that the force diverges when the distance between two particles approaches zero the denominator $|\vec{r}_i - \vec{r}_j|^3$ is often replaced by $(|\vec{r}_i - \vec{r}_j|^2 + \epsilon^2)^{3/2}$ where ϵ is called the softening length. The parameter ϵ is a typical distance below which the gravitational interaction is suppressed.

the (higher-order) multipole moments of the group of particles can be included. A tree code recursively divides the N particles into groups by storing them in a tree-shaped data structure. The number of force calculations reduces to $O(N \log N)$. For further information the reader is referred to the book of Pfalzner & Gibbon (2005). Miocchi et al. (2009) investigated the merging of massive globular clusters in the central regions of galaxies to explain the formation of stellar galactic nuclei with an efficient parallel tree code (Miocchi & Capuzzo-Dolcetta 2002). The SCs start close to the galactic center and decay into the center due to dynamical friction where they merge to form a nucleus. Miocchi et al. (2009) considered four SCs, each consisting of $N_0^{\rm SC} = 2.5 \cdot 10^5$ particles, leading to a total number of particles of $N = 10^6$ and studied their evolution for the duration of $t_{\rm int} \approx 35$ Myr.

GRAPEs (GRAvity PipEs) are special-purpose hardware developed by Sugimoto et al. (1990) optimized to perform only one specific task, i.e. to calculate the gravitational forces. All remaining computational tasks, like for example the time integration of the particles, are processed by a host computer. GRAPEs provide an efficient use of the direct N-body method for larger number of particles. For further information the reader is referred to the book of Makino & Taiji (1998). Bekki et al. (2004) used GRAPE boards to study the merging of high-mass SCs in uniform disk distributions and uniform spherical distributions without an external tidal field to explain the formation of stellar galactic nuclei. They performed simulations with equal-mass SCs consisting of $N_0^{\rm CC} = 2$ to 20 SCs with a mass of $M^{\rm SC} = 2 \cdot 10^6$ $M_\odot$ and simulations with a bell-shaped mass spectrum with $N_0^{\rm CC} = 2$ to 200 SCs. The particles building up the SCs all have the same mass. Thus the total number of particles in the simulations depended on the number of SCs. For the largest simulation with 200 SCs the total number of particles in the simulation was $N = 214\,858$. The evolution of the SCs was modeled for the duration of $t_{\rm int} \approx 70$ Myr.

2.1.3.2 The Particle-Mesh (PM) Method

The particle-mesh (PM) or grid methods are based on a different approach to model the dynamics of stellar systems: The particles do not interact directly with each other as in the N-body approach, but through a field generated by the particles. The particles can be thought of as test particles which move within the potential Φ generated by the individual particles of the system. The acceleration $\vec{a}_{i,\rm particles}$ of a particle i at a position $\vec{r}_i$ is given by

$$\vec{a}_{i,\rm particles} = -\vec{\nabla}_i \Phi. \tag{2.22}$$

The potential $\Phi(\vec{r})$ is calculated from the density distribution via the Poisson equation,

$$\triangle \Phi\big(\vec{r}\big) \;\; = \;\; 4\,\pi\,G\,\rho\big(\vec{r}\big). \tag{2.23}$$

The Poisson equation relates the mass density $\rho\big(\vec{r}\big)$ to the gravitational potential $\Phi\big(\vec{r}\big)$. The solution to Eq. 2.23 can be written as a convolution in terms of the Greens function $H\big(\vec{r}-\vec{r}\,'\big)$,

$$\Phi\big(\vec{r}\big) \;\; = \;\; G \int d^{\,3} r'\; H\big(\vec{r}-\vec{r}\,'\big)\;\rho\big(\vec{r}\,'\big). \tag{2.24}$$

The basic idea of grid codes is to set up a grid covering the whole simulation volume, determine the grid-based density and obtain the grid-based potential by solving the Poisson equation on the grid. The acceleration of each particle i is derived from the grid-based potential by numerical differentiation. The individual steps are:

1. Determination of the grid-based density: The PM code SUPERBOX, which I use in this thesis (Sect. 2.2), has implemented the nearest-grid-point scheme (NGP) to compute the mass density ρ on the grid. The NGP scheme assigns a particle mass to the grid point nearest to the particle. This operation scales with the number of particles.

2. Solving the Poisson equation: The PM code solves the Poisson equation (Eq. 2.23) on the grid to obtain the potential Φ. Applying a Fourier transform (FT) to Eq. 2.24 reduces the convolution to the product of two Fourier transforms: $FT\{\Phi\} = FT\{H\}\ FT\{\rho\}$. Applying a Fast Fourier Transform algorithm (FFT) computes the discrete Fourier transform in $O(N_{GC} \log N_{GC})$ operations where N_{GC} is the number of grid cells.

3. Determination of the accelerations of the particles: The acceleration on the grid can be computed in principle via Eq. 2.22 by replacing the gradient with a finite-difference approximation. The operation scales with the number of grid cells. The accelerations at the exact positions $\vec{r}_i$ of the particles are obtained by interpolation from the grid-based accelerations. This procedure is the inverse of the assignment of particle mass to the grid. In the NGP interpolation scheme the acceleration of a particle is simply the grid acceleration at the nearest grid point. This operation scales with the number of particles.

PM codes are suitable for systems in which the potential varies predominantly on large scales. Particle interactions at length scales shorter than the cell size cannot be modeled accurately. Therefore PM methods are mainly applied to large stellar systems where the motion of the stars is governed by the overall potential of the system rather than by individual interactions between the stars. In galaxies direct collisions between stars are completely negligible. The stars only very slightly perturb the orbits of other stars leading to deflections which are negligible. These stellar systems are therefore called collisionless. However, over several gigayears the cumulative effect of these small pairwise perturbations might not be negligible any longer. A timescale at which these perturbations are starting to affect the dynamics of a stellar system is given by the two-body relaxation time. According to Spitzer & Hart (1971) the half-mass relaxation time, $t_{\rm relax}$, can be estimated by

$$t_{\rm relax} = \frac{0.06\ \sqrt{M}\ r_{\rm h}^{\frac{3}{2}}}{\langle m \rangle\ \sqrt{G}\ \log_{10}(0.4\ N)}, \tag{2.25}$$

where M and $r_{\rm h}$ denote the mass and the half-mass radius (the radius containing half the total mass) of the stellar object, $\langle m \rangle$ is the average stellar mass, $N = \frac{M}{\langle m \rangle}$ is the number of stars, and G is the gravitational constant. A PM code can be used to accurately compute the time evolution of a stellar system if the relaxation time is larger than the integration time, $t_{\rm int}$, of a simulation. For example an object with a mass of $M = 10^6$ $M_\odot$ and a half-mass radius of $r_{\rm h} = 20$ pc has a relaxation time of $t_{\rm relax} = 33$ Gyr when using an average stellar mass of $\langle m \rangle = 0.4$ $M_\odot$ (Kroupa 2001). The relaxation time of this object is much longer than a Hubble time and it can therefore be modeled with a collisionless code. Even though PM codes are mainly applied to large and massive stellar systems they can in principle be applied to every stellar system if the integration time, $t_{\rm int}$, is short compared to the relaxation time, $t_{\rm relax}$, of the object.

The PM code SUPERBOX (Bien et al. 1990, 1991) was used to study the merging of SCs in CCs (Fellhauer & Kroupa 2002a,b; Fellhauer 2004; Fellhauer & Kroupa 2005b). They performed early simulations of CCs with centrally concentrated SCs in different mass regimes in order to prove the concept of forming objects comparable to FFs and UCDs from evolved CCs. The CCs were exposed to external tidal fields. They performed simulations with equal-mass SCs consisting typically of $N_0^{\rm CC} = 20$ SCs. Each SC consisted of $N_0^{\rm SC} = 10\,000$ to $N_0^{\rm SC} = 100\,000$ particles. The evolution of the CCs was modeled up to $t_{\rm int} = 10$ Gyr.

For the simulations presented in this thesis, I used SUPERBOX for all projects. A detailed description of SUPERBOX is presented in Sect. 2.2.

2.1.4 The Analytical External Tidal Field

CCs are formed during a heavy interaction between gas-rich galaxies and are therefore exposed to the tidal fields of their host galaxies. The CCs orbit within an external potential which results in an additional acceleration $\vec{a}_{i,\text{external}}$ on the particles. For each particle the acceleration $\vec{a}_{i,\text{external}}$ from the external potential is added as an analytical formula to the grid-based acceleration computed by solving the Poisson equation as described in Sect. 2.1.3.2.

2.1.4.1 The Analytical Potential

In all my simulations I used the same set of analytical potentials consisting of a disk, a bulge, and a halo component to keep the simulations comparable. The coordinate system is chosen such that the disk of the host galaxy lies in the x-y-plane. The disk is modeled by a Miyamoto-Nagai potential (Miyamoto & Nagai 1975),

$$\Phi_{\text{disk}}(R,z) = -\frac{G\,M_{\text{d}}}{\sqrt{R^2+\left(a_{\text{d}}+\sqrt{z^2+b_{\text{d}}^2}\right)^2}}, \tag{2.26}$$

where the two variables R and z are cylindrical coordinates and the parameters M_{d}, a_{d}, and b_{d} are the mass of the disk, the disk scale length, and the spherical scale length, respectively. The bulge is represented by a Hernquist potential (Hernquist 1990),

$$\Phi_{\text{bulge}}(r) = -\frac{G\,M_{\text{b}}}{r+a_{\text{b}}}, \tag{2.27}$$

where the variable r is the distance from the center of the bulge ($r^2 = R^2 + z^2$) and the parameters M_{b} and a_{b} are the mass of the bulge and a characteristic length scale of the system, respectively. The dark matter halo is a logarithmic potential,

$$\Phi_{\text{halo}}(r) = \frac{1}{2}\,v_0^2\,\ln(r^2+r_{\text{halo}}^2), \tag{2.28}$$

where the variable r is the galactrocentric radius and the parameters v_0 and r_{halo} are, respectively, the circular velocity at large r and the core radius.

The total gravitational potential is modelled by the sum of the potentials of the different components, i.e.

$$\Phi_{\text{external}} = \Phi_{\text{disk}} + \Phi_{\text{bulge}} + \Phi_{\text{halo}}. \tag{2.29}$$

The acceleration, $\vec{a}_{i,\text{external}}$, of a particle i at a position $\vec{r}_i$ is given by

$$\vec{a}_{i,\text{external}}(\vec{r}_i) = -\vec{\nabla}_i\Phi_{\text{external}}(\vec{r}_i). \tag{2.30}$$

2.1.4.2 The Parameter β

An external tidal field is expected to have a considerable impact on the evolution of a CC as it counteracts the merging process and potentially leads to significant mass loss. To estimate the influence of the tidal field on a CC, Fellhauer et al. (2002) introduced a parameter β which is defined as the ratio of the cutoff radius, $R_{\text{cut}}^{\text{CC}}$, of the CC and its tidal radius, r_{t}^{CC}, i.e.

$$\beta = \frac{R_{\text{cut}}^{\text{CC}}}{r_{\text{t}}^{\text{CC}}}. \tag{2.31}$$

The cutoff radius, $R_{\text{cut}}^{\text{CC}}$, is the radius where the Plummer distribution is truncated (Sect. 2.1.1.1). In my simulations I chose the cutoff radius to be four to five times the CC Plummer radius. The

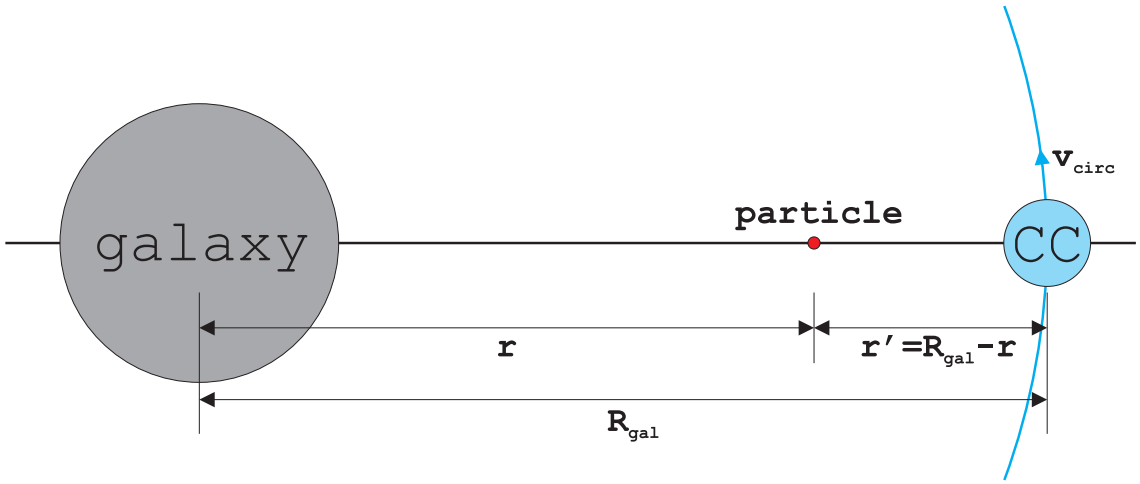

FIGURE 2.3— Geometry of the determination of the effective potential, $\Phi_{\rm eff}$. The CC and the particle move on circular orbits at distances of $R_{\rm gal}$ and r around the center of their host galaxy. The angular speed, ω, is constant and is determined by the ratio of the circular velocity, $v_{\rm circ}$, and the distance, $R_{\rm gal}$, of the CC. The particle has a distance of $r' = R_{\rm gal} - r$ from the center of the CC. It is bound to the CC if its distance r' is smaller than the tidal radius of the CC. The tidal radius is the point where the gravitational and centrifugal forces balance each other or, in other words, where the effective potential has its maximum.

tidal radius, $r_{\rm t}^{\rm CC}$, is defined as the radius where the attractive force of the CC on a particle equals the pulling force of the external analytical potential. Figure 2.3 illustrates the geometry: The CC and the particle move on circular orbits at distances of, respectively, $R_{\rm gal}$ and r around the center of their host galaxy. The angular speed, ω, is constant and is calculated by the ratio of the circular velocity, $v_{\rm circ}$, and the galactic distance, $R_{\rm gal}$, of the CC. The particle is located at a distance of $r' = R_{\rm gal} - r$ from the center of the CC and is bound to the CC if its distance, r', is smaller than the tidal radius of the CC. The total force felt by the particle is the sum of the gravitational forces of the galaxy and the CC and the centrifugal force. The tidal radius of a CC is the point where the gravitational forces and the centrifugal force compensate which corresponds to the local maxima of the effective potential, $\Phi_{\rm eff}$. The effective potential is given by the sum of the external galactic potential, $\Phi_{\rm external}$, the CC potential, $\Phi_{\rm pl}^{\rm CC}$, and the centrifugal potential, $\Phi_{\rm cf}$, i.e.

$$\Phi_{\rm eff} = \Phi_{\rm external} + \Phi_{\rm pl}^{\rm CC} + \Phi_{\rm cf}. \tag{2.32}$$

The analytical external potential, $\Phi_{\rm external}$, is given by Eq. 2.29 in Sect. 2.1.4.1, the CC potential is represented by a Plummer potential,

$$\Phi_{\rm pl}^{\rm CC}(r) = -\frac{G\,M^{\rm CC}}{R_{\rm pl}^{\rm CC}\sqrt{1+\left(\frac{R_{\rm gal}-r}{R_{\rm pl}^{\rm CC}}\right)^2}}, \tag{2.33}$$

where $M^{\rm CC}$ is the total CC mass, $R_{\rm pl}^{\rm CC}$ is the Plummer radius of the CC, and $R_{\rm gal}$ is the galactic distance at which the CC orbits around the parent galaxy. The centrifugal potential is calculated by

$$\Phi_{\rm cf} = -\frac{1}{2}\,\omega^2\,r^2 = -\frac{1}{2}\left(\frac{v_{\rm circ}}{R_{\rm gal}}\,r\right)^2. \tag{2.34}$$

Figure 2.4 shows the effective potential, $\Phi_{\rm eff}$, centered on the position of the CC. The CC orbits the host galaxy at a distance of $R_{\rm gal} = 20$ kpc. I considered four different initial CC models

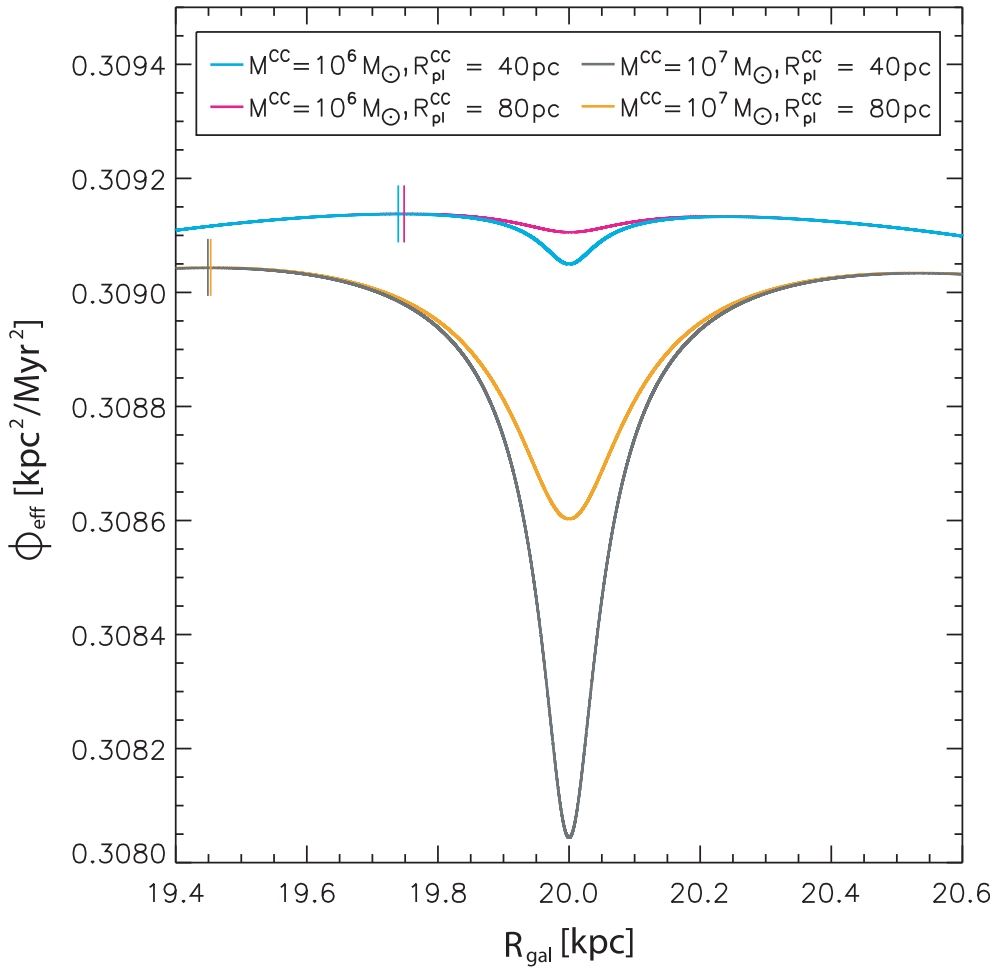

FIGURE 2.4— The effective potential, $\Phi_{\rm eff}$, is plotted versus the galactic distance, $R_{\rm gal}$, for four different initial CC models with CC masses of $M^{\rm CC} = 10^6$ and 10^7 $M_\odot$ and CC Plummer radii of $R_{\rm pl}^{\rm CC} = 40$ and 80 pc. The dents in the potentials stem from the different CC models which orbit the parent galaxy at a distance of $R_{\rm gal} = 20$ kpc. The vertical lines mark the position of the maxima on the left side of the CC center. The distance of a local maximum in the effective potential to the CC center corresponds to the tidal radius.

with CC masses of $M^{\rm CC} = 10^6$ and 10^7 $M_\odot$ and CC Plummer radii of $R_{\rm pl}^{\rm CC} = 40$ and 80 pc. The vertical lines mark the position of the maximum on the left side of the CC center. The distance of a maximum to the CC center corresponds to the tidal radius. The tidal radii depend on the CC mass as well as on the CC size. CCs with larger masses have larger tidal radii. The CCs with masses of $M^{\rm CC} = 10^6$ $M_\odot$ have tidal radii of the order of 250 pc whereas the CCs with masses of $M^{\rm CC} = 10^7$ $M_\odot$ show larger tidal radii of about 550 pc. Extended CCs models have smaller tidal radii than more compact CC models. The CCs with Plummer radii of $R_{\rm pl}^{\rm CC} = 80$ pc show slightly smaller tidal radii than the CCs with smaller Plummer radii of $R_{\rm pl}^{\rm CC} = 40$ pc. The discrepancy becomes more evident for smaller initial CC masses.

If the SC distribution lies within the tidal radius of the CC, i.e. $R_{\rm cut}^{\rm CC} < r_{\rm t}^{\rm CC}$, leading to a β-value of $\beta < 1$, the influence of the tidal field on the merging process is small. Almost all SCs will merge and only a few are able to escape by chance. However, in case of $\beta > 1$, a considerable fraction of SCs are able to leave the CC. The larger the value of β, the larger the impact of the tidal field on the formation process of the merger object.

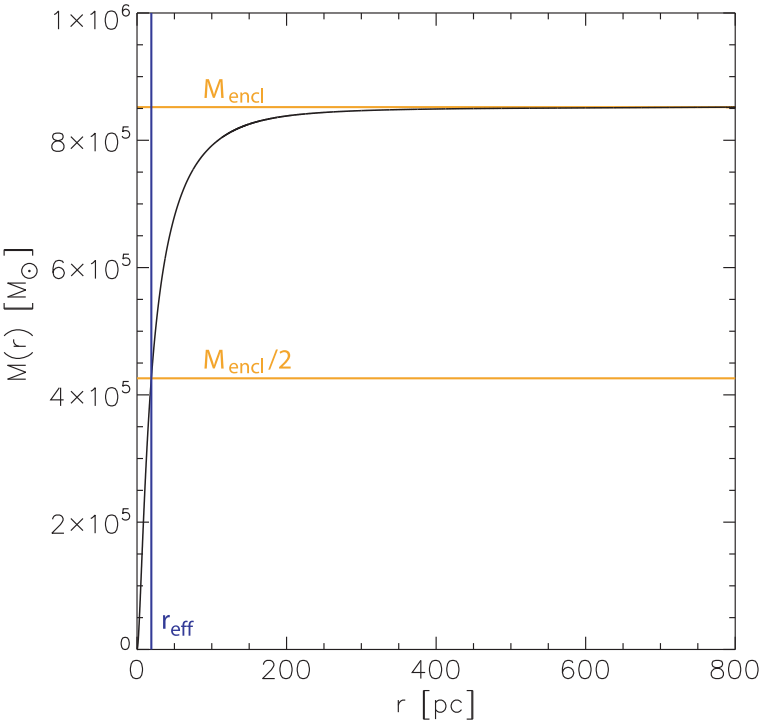

FIGURE 2.5— Determination of the enclosed mass, $M_{\rm encl}$, and the effective radius, $r_{\rm eff}$. The effective radius corresponds to the projected half-mass radius, which is the radius within which half of the mass is included when projecting the merger object on the sky.

2.1.5 Determination of the Enclosed Mass and the Effective Radius

The simulation is stopped when the user-defined integration time, $t_{\rm int}$, is reached and the resulting stellar dynamical object is analyzed or processed further (step 3 in Fig. 2.1). In my simulations the basic structural parameters of the merger object are its size and mass. The simulations provide more information on an object than observers have access to. While observations are limited to 2D projections on the sky, simulations contain the full 3D information of an object. However, in order to allow for a reasonable comparison with the observations, 2D projections are also used for analyzing the merger objects.

The size of a stellar dynamical object is difficult to define since it does not possess a clear border. The object gets fainter and fainter at larger distances from the center. Thus the apparent size depends on the sensitivity of the telescope and the exposure time. To define a more meaningful quantity allowing to compare the sizes of different objects observers introduced the "half-light radius" also known as the "effective radius", $r_{\rm eff}$, which contains half of the object's total luminosity. Under the assumption that mass follows light, the effective radius is also the projected half-mass radius. Figure 2.5 shows the cumulative mass, $M(r)$, of a merger object projected onto the sky as a function of the projected radius, r. As the object fades out at larger distances the contribution from the outer parts of the object are only marginal and the curve becomes almost constant. In the example the merger object has a total mass of $M_{\rm encl} = 8.5 \cdot 10^5$ M$_\odot$. The radius r from the center of the SC that contains half of its total mass is $r_{\rm eff} = 19.2$ pc.

2.2 The Particle-Mesh Code SUPERBOX

SUPERBOX (Bien et al. 1990, 1991; Fellhauer et al. 2000) is the code I used to study the merging of SCs in CCs. The basic ideas of PM codes have already been outlined in Sect. 2.1.3.2. Here, I

will only discuss the specifics of SUPERBOX with the focus on the merging star cluster scenario. For a detailed description of SUPERBOX and additional information the reader is referred to Fellhauer et al. (2000), Fellhauer (2001), and Warnick (2004). A short manual on how to use SUPERBOX to model the merging of SCs is given in Appendix B.

2.2.1 Definition of the Grids and the Determination of Accelerations

SUPERBOX is an enhanced PM code (Sect. 2.1.3.2) solving the Poisson equation (Eq. 2.23) on a system of Cartesian grids of three different resolutions. Besides a fixed coarse grid which covers the whole simulation area or local universe, SUPERBOX provides a set of co-moving grids of intermediate and high resolution for each stellar dynamical object. The two grids on each object allow to achieve intermediate resolution for the entire object and high resolution in the central part where the potential varies on short scales. Increasing the resolution only at places where it is necessary reduces computing time while maintaining adequate resolution of the entire object. All grids in SUPERBOX have the same number of cells per dimension $N_{\rm c} = 2^m$, where m is a positive integer. Therefore the sizes of the grids ($R_{\rm hres}, R_{\rm mres}, R_{\rm lres}$) determine the three different resolutions. The grid architecture is presented in more detail below and is visualized in Fig. 2.6.

1. Grid 1: high resolution grid. The co-moving high resolution grid treats the region of highest density of an object. It has a length of $2\,R_{\rm hres}$ in each dimension. All particles of a stellar object with a radial distance of $r \leq R_{\rm hres}$ are considered to calculate the grid-based density ρ_1 required to derive the grid-based potential Φ_1.

2. Grid 2: intermediate resolution grid. The co-moving intermediate resolution grid covers the entire stellar dynamical object. It has a length of $2\,R_{\rm mres}$ in each dimension. All particles of a stellar dynamical object within a sphere of radius $R_{\rm mres}$ are considered to derive the grid-based potentials. However, this time two grid-based densities, ρ_2 and ρ_3, are obtained. Particles with a radial distance of $r \leq R_{\rm hres}$ contribute to the grid-based density ρ_2 (the same particles as considered for grid 1), whereas the particles with $R_{\rm hres} < r \leq R_{\rm mres}$ constitute the density ρ_3. The corresponding grid-based potentials are Φ_2 and Φ_3.

3. Grid 3: low resolution grid. The low resolution grid has the size of the local universe and is fixed. It has a length of $2\,R_{\rm lres}$ in each dimension. As for grid 2, two grid-based densities, ρ_4 and ρ_5, are obtained. Particles inside the stellar dynamical object, i.e. with a radial distance of $r \leq R_{\rm mres}$ contribute to the grid-based density ρ_4 (the same particles as considered for grid 2), whereas the particles with $r > R_{\rm mres}$ constitute the density ρ_5. The corresponding grid-based potentials are Φ_4 and Φ_5.

Consider a system of $N_0^{\rm CC}$ SCs in a CC. Each SC i is covered by three grids as illustrated in Fig. 2.6. The particles $N_0^{\rm SC}$ of each SC i ($i = 1 \ldots N_0^{\rm CC}$) are assigned to the three grids as described above to obtain the grid-based densities $\rho_1^{(i)}$, $\rho_2^{(i)}$, $\rho_3^{(i)}$, $\rho_4^{(i)}$, and $\rho_5^{(i)}$. The corresponding grid-based potentials $\Phi_1^{(i)}$, $\Phi_2^{(i)}$, $\Phi_3^{(i)}$, $\Phi_4^{(i)}$, and $\Phi_5^{(i)}$ are derived by solving the Poisson equation (Eq. 2.23). The accelerations of all $N = N_0^{\rm CC}\, N_0^{\rm SC}$ particles due to SC i are determined by the following procedure:

1. Calculate the distance, $r_j^{(i)}$, of a particle j ($j = 1 \ldots N$) to the center of SC i.

2. Depending on its distance, $r_j^{(i)}$, to the center of the SC i the total potential, $\Phi^{(i)}(r_{\rm j})$, felt by

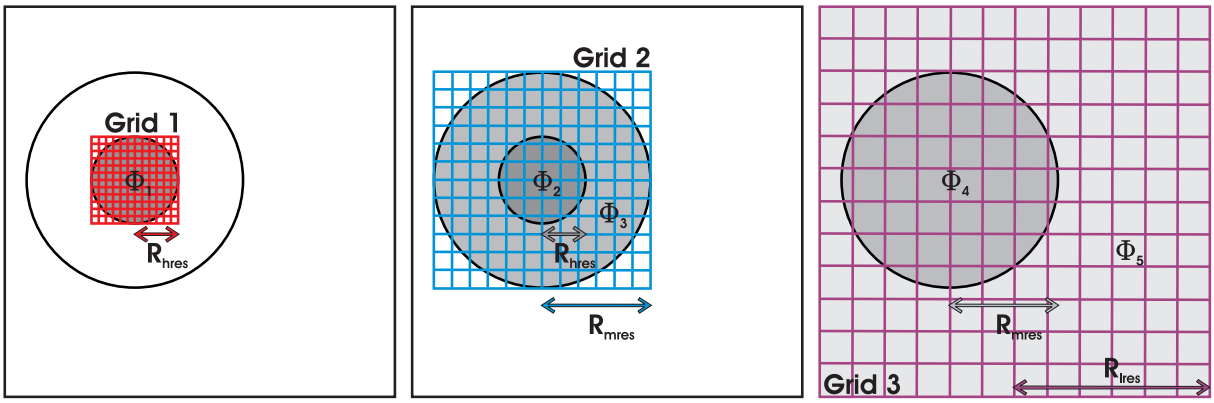

FIGURE 2.6— Illustration of the three grids used in SUPERBOX. The large circle denotes the extent of the stellar dynamical object and the small circle its central region. The object moves within a large cube which represents the local universe. The left panel shows the high resolution grid 1 with a length of $2\,R_{\rm hres}$. All particles within the central region, i.e. with $r \leq R_{\rm hres}$ (small dark grey circle), are used to derive the grid-based potential Φ_1. The middle panel displays the intermediate resolution grid 2 which covers the entire stellar dynamical object. It has a length of $2\,R_{\rm mres}$. Particles in the central region of the object, i.e. with $r \leq R_{\rm hres}$ (small dark grey circle), are considered to calculate the grid-based potential Φ_2, whereas the particles in the outer parts of the object, i.e. with $R_{\rm hres} < r \leq R_{\rm mres}$ (grey concentric ring), lead to the grid-based potential Φ_3. The right panel visualizes the low resolution grid 3. The low resolution grid covers the whole local universe and has a length of $2\,R_{\rm lres}$. Particles inside the stellar object, i.e. $r \leq R_{\rm mres}$ (grey circle) are used to obtain the grid-based potential Φ_4 whereas all other particles, i.e. with $r > R_{\rm mres}$ (light grey area), are taken for the computation of the grid-based potential Φ_5.

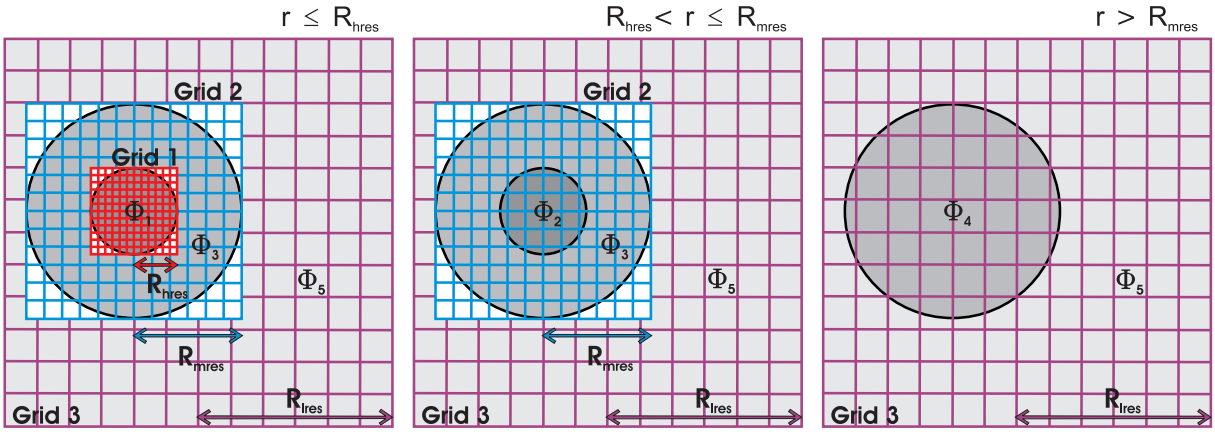

FIGURE 2.7— Total potential felt by a particle at different distances r to the center of a SC/merger object. A particle needs high resolution ($\Phi(r) = \Phi_1 + \Phi_3 + \Phi_5$) in the dense central region of a SC/merger object, i.e. for $r \leq R_{\rm hres}$. Medium resolution ($\Phi(r) = \Phi_2 + \Phi_3 + \Phi_5$) is sufficient for particles located in the outer parts of the SC/merger object, i.e. $R_{\rm hres} < r \leq R_{\rm mres}$, and low resolution ($\Phi(r) = \Phi_4 + \Phi_5$) is adopted for particles that escape from the SC/merger object, i.e. for $r > R_{\rm mres}$.

the particle j is a combination of the different grid potentials $\Phi_1^{(i)}$, $\Phi_2^{(i)}$, $\Phi_3^{(i)}$, $\Phi_4^{(i)}$, and $\Phi_5^{(i)}$:

$$\Phi^{(i)}(r_j^{(i)}) = \begin{cases} \Phi_1^{(i)} + \Phi_3^{(i)} + \Phi_5^{(i)} & r_j^{(i)} \leq R_{\rm hres}, \\ \Phi_2^{(i)} + \Phi_3^{(i)} + \Phi_5^{(i)} & R_{\rm hres} < r_j^{(i)} \leq R_{\rm mres}, \\ \Phi_4^{(i)} + \Phi_5^{(i)} & r_j^{(i)} > R_{\rm mres}. \end{cases} \tag{2.35}$$

This is illustrated in Fig. 2.7. A particle located in the central region of a SC does need high resolution in its vicinity to feel the strong variation of the potential correctly, but it does not need the same resolution in the outer parts of the SC as the potential is sufficiently resolved by the intermediate grid. For the contribution of escaping particles to the total potential the low resolution grid is entirely adequate. Therefore the

total potential generated by SC i felt by a particle in the central region is composed of $\Phi^{(i)}(r_j^{(i)}) = \Phi_1^{(i)} + \Phi_3^{(i)} + \Phi_5^{(i)}$. A particle located in the outer regions of a SC does not need the potential of the central region to be resolved with high resolution. The intermediate resolution is used for the entire SC and the low resolution grid for the regions outside the SC. Thus the total potential felt by a particle j in the outer parts of SC i is given by $\Phi^{(i)}(r_j^{(i)}) = \Phi_2^{(i)} + \Phi_3^{(i)} + \Phi_5^{(i)}$. Particles outside of SC i feel the potential only on the low resolution grid, i.e. $\Phi^{(i)}(r_j^{(i)}) = \Phi_4^{(i)} + \Phi_5^{(i)}$.

3. To obtain the accelerations $\vec{a}_{j,\text{particles}}^{(i)}$ of particle j due to SC i the potential has to be differentiated numerically and interpolated to the particle position inside the cell. SUPERBOX uses an interpolation scheme similar to the NGP interpolation scheme, but additionally accounts for the particle position inside a grid cell by adding the next term of a Taylor series of the acceleration around the grid cell. For example the acceleration in x-direction is computed as

$$\begin{aligned} a_{klm,x}(dx,dy,dz) &= \frac{\Phi_{k+1,lm} - \Phi_{k-1,lm}}{2\triangle x} + \frac{\Phi_{k+1,lm} + \Phi_{k-1,lm} - 2\Phi_{klm}}{(\triangle x)^2}\, dx \\ &+ \frac{\Phi_{k+1,l+1,m} - \Phi_{k-1,l+1,m} + \Phi_{k-1,l-1,m} - \Phi_{k+1,l-1,m}}{4\triangle x \triangle y}\, dy \\ &+ \frac{\Phi_{k+1,l,m+1} - \Phi_{k-1,l,m+1} + \Phi_{k-1,l,m-1} - \Phi_{k+1,l,m-1}}{4\triangle x \triangle z}\, dz, \end{aligned} \quad (2.36)$$

where the triple (k,l,m) denotes the cell indices of the grid cell the particle is located in, (dx,dy,dz) the deviations of the particle from the center of the grid cell and $\Delta x = \Delta y = \Delta z$ is the cell-length of the grid cells. The accelerations in y- and z-direction are computed in the same manner (Fellhauer et al. 2000).

This procedure has to be repeated for all $N = N_0^{\text{CC}}\, N_0^{\text{SC}}$ particles in the simulation to obtain the accelerations of all the particles due to SC i. The total acceleration of a particle j on account of all N_0^{CC} SCs is obtained by the sum of the individual accelerations $\vec{a}_{j,\text{particles}}^{(i)}$ ($i = 1 \ldots N_0^{\text{CC}}$), i.e. $\vec{a}_{j,\text{particles}} = \vec{a}_{j,\text{particles}}^{(1)} + \cdots + \vec{a}_{j,\text{particles}}^{(N_0^{\text{CC}})}$. The positions and velocities of the particles are integrated by a leapfrog integrator (Sect. 2.1.2) and the whole procedure is repeated for the next time step.

2.2.2 Illustration of the Combination of the Grid Potentials

Figure 2.8 illustrates the determination of the combinations of the different grid potentials for two particles, j and k, due to two SCs, SC_1 and SC_2. Let us assume that the two particles belong to SC_1. Example (a) describes the determination of the total potential for particle j, and example (b) computes the potential for particle k. Particle j is located outside of SC_1 and close to the central region of SC_2. As it is located sufficiently far away from the central region of SC_1 the potential $\Phi^{(1)}(r_j^{(1)})$ is calculated on the low resolution grid whereas it needs high resolution for the calculation of the potential $\Phi^{(2)}(r_j^{(2)})$ due to its proximity to the center of SC_2. Compared to example (a) particle k in example (b) needs a better resolution for the potential $\Phi^{(1)}(r_k^{(1)})$ because particle k is located closer to the center of SC_1 than particle j whereas a medium resolution of the potential $\Phi^{(2)}(r_k^{(2)})$ is sufficient as particle k is located further away from the center of SC_2 than particle j.

In order to calculate the forces in example (a) on particle j exerted by the two SCs, the distances of the particle to the centers of the two SCs, $r_j^{(1)}$ and $r_j^{(2)}$, have to be determined.

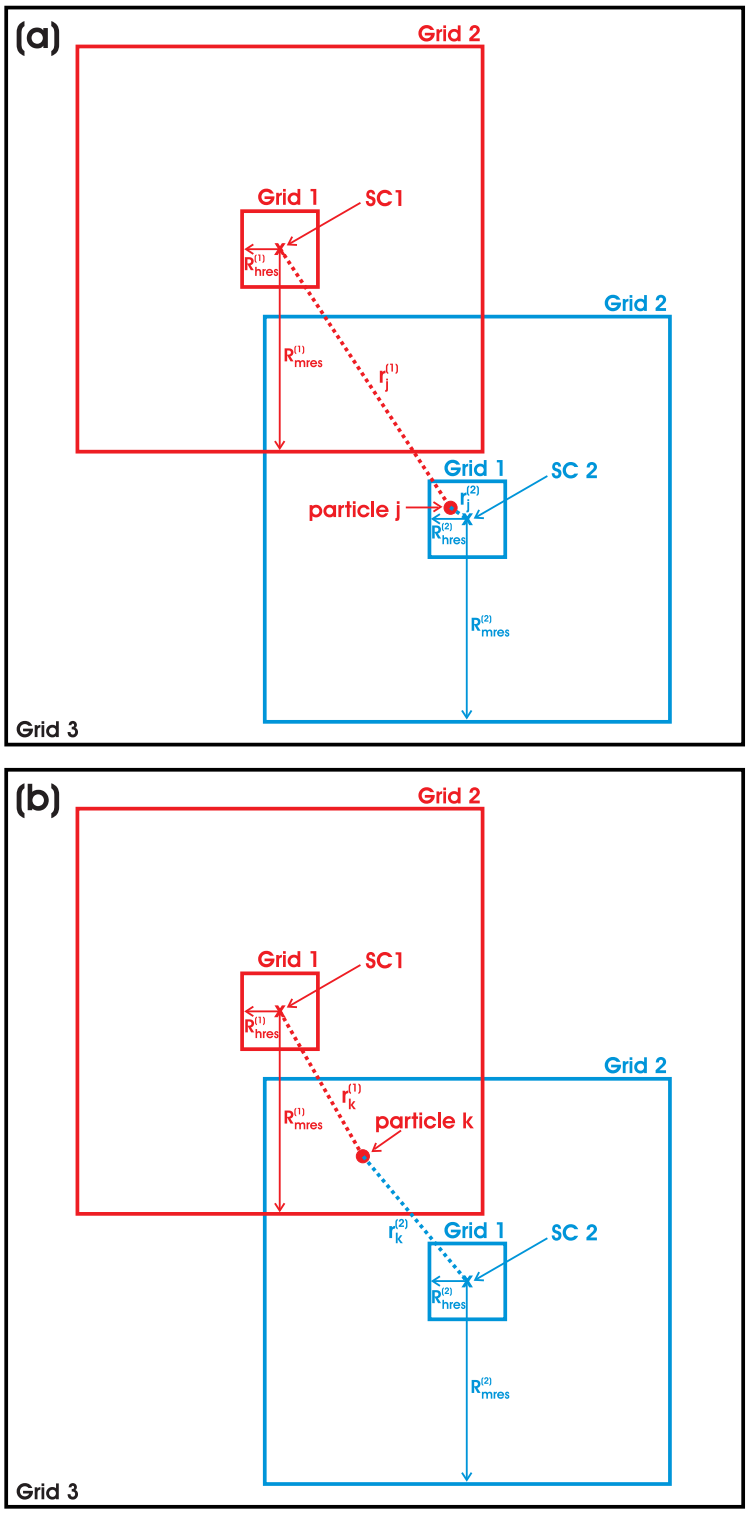

FIGURE 2.8— Example of the determination of the combinations of the different grid potentials. For convenience only two particles, j and k, and two SCs, SC_1 (red) and SC_2 (blue), are considered and both particles are assumed to belong to SC_1. The crosses mark the centers of density of the SCs. Example (a) shows particle j located outside of SC_1 and close to the central region of SC_2. It is therefore covered by the low-resolution grid of SC_1 and the high resolution grid of SC_2. In example (b) particle k is located in the outer parts of the two SCs and is therefore covered by the medium resolution grids of SC_1 and SC_2. The combination of potentials felt by the two particles, j and k, is evaluated via Eq. 2.35.

Particle j is located outside SC_1, i.e. $r_j^{(1)} > R_{\text{mres}}^{(1)}$, and close to the central region of SC_2, i.e. $r_j^{(2)} \leq R_{\text{hres}}^{(2)}$. According to Eq. 2.35 the combination of potentials, $\Phi^{(1)}(r_j^{(1)})$ and $\Phi^{(2)}(r_j^{(2)})$, is:

$$\begin{aligned} \Phi^{(1)}(r_j^{(1)}) &= \Phi_4^{(1)} + \Phi_5^{(1)}, \\ \Phi^{(2)}(r_j^{(2)}) &= \Phi_1^{(2)} + \Phi_3^{(2)} + \Phi_5^{(2)}. \end{aligned} \tag{2.37}$$

Differentiating the potential numerically yields the two accelerations, $\vec{a}_{j,\text{particles}}^{(1)}$ and $\vec{a}_{j,\text{particles}}^{(2)}$. The total acceleration of particle j due to both SCs, SC_1 and SC_2, is the sum the accelerations, i.e. $\vec{a}_{j,\text{particles}} = \vec{a}_{j,\text{particles}}^{(1)} + \vec{a}_{j,\text{particles}}^{(2)}$.

In example (b) particle k is located in the outer part of SC_1, i.e. $R_{\text{hres}}^{(1)} < r_k^{(1)} \leq R_{\text{mres}}^{(1)}$ as well as in the outer part of SC_2, i.e. $R_{\text{hres}}^{(2)} < r_k^{(2)} \leq R_{\text{mres}}^{(2)}$. According to Eq. 2.35 the total potentials, $\Phi^{(1)}(r_k^{(1)})$ and $\Phi^{(2)}(r_k^{(2)})$, felt by particle k due to the two SCs, are determined by the following combination of potentials:

$$\begin{aligned} \Phi^{(1)}(r_k^{(1)}) &= \Phi_2^{(1)} + \Phi_3^{(1)} + \Phi_5^{(1)}, \\ \Phi^{(2)}(r_k^{(2)}) &= \Phi_2^{(2)} + \Phi_3^{(2)} + \Phi_5^{(2)}. \end{aligned} \tag{2.38}$$

The total acceleration of particle k due to both SCs is again the sum of the two accelerations, i.e. $\vec{a}_{k,\text{particles}} = \vec{a}_{k,\text{particles}}^{(1)} + \vec{a}_{k,\text{particles}}^{(2)}$.

2.2.3 General Framework for the Choice of Parameters for the Simulations

In the merging star cluster scenario the low resolution grid contains the orbit of the CC around the center of a galaxy (Fig. 2.9). The CC orbits in the analytical galactic potential of Sect. 2.1.4.1. In order to get good resolution of the SCs the two grids with high and medium resolution are focused on each SC following their trajectories. The individual high resolution grids cover an entire SC, whereas the medium resolution grids of every SC embed the whole initial CC.

All grids have the same number of cells per dimension $N_\text{c} = 2^m$, where m is a positive integer. The choice of the sizes of the three grids, i.e. R_{hres}, R_{mres}, and R_{lres} and the number of grid cells determine the different spatial resolutions. For the simulations of the projects in Chapters 4 and 5, I used grids with $N_\text{c} = 64$ ($m = 6$) and $N_\text{c} = 128$ ($m = 7$). For a fixed grid size, a larger number of grid cells yields smaller cell sizes and therefore increases the spatial resolution. The size of a grid cell, i.e. the cell length l_{grid}, is calculated by

$$l_{\text{grid}} = \frac{2\,R_{\text{grid}}}{N_\text{c} - 4}, \tag{2.39}$$

where $2\,R_{\text{grid}}$ is the size of the considered grid and N_c the number of cells per dimension. Four cells per dimension have to be subtracted because they are used for boundary conditions.

The outer grid represents the local universe. It should be chosen large enough to keep the particles in the simulation. In the merging star cluster scenario the outer grid has to cover the entire CC orbit and has therefore only a poor resolution. For example for the simulations of the Milky Way EC NGC 2419 (Chapter 4), which has a maximum distance of about $R_{\text{gal}} = 90$ kpc, I chose a radius of $R_{\text{lres}} = 105$ kpc for the outer grid. According to Eq. 2.39 the cell length of a grid cell amounts to $l_{\text{lres}} = 1.7$ kpc for $N_\text{c} = 128$ grid cells per dimension. Because the resolution of the outer grid is very poor the intermediate resolution grids need to be chosen as large as possible to guarantee that the vast majority of particles moves within the intermediate resolution grids. However, the intermediate resolution grids should also be small enough to provide an adequate resolution. Even though the exact choice of the high- and intermediate resolution grids allows for some freedom, the following factors should be considered:

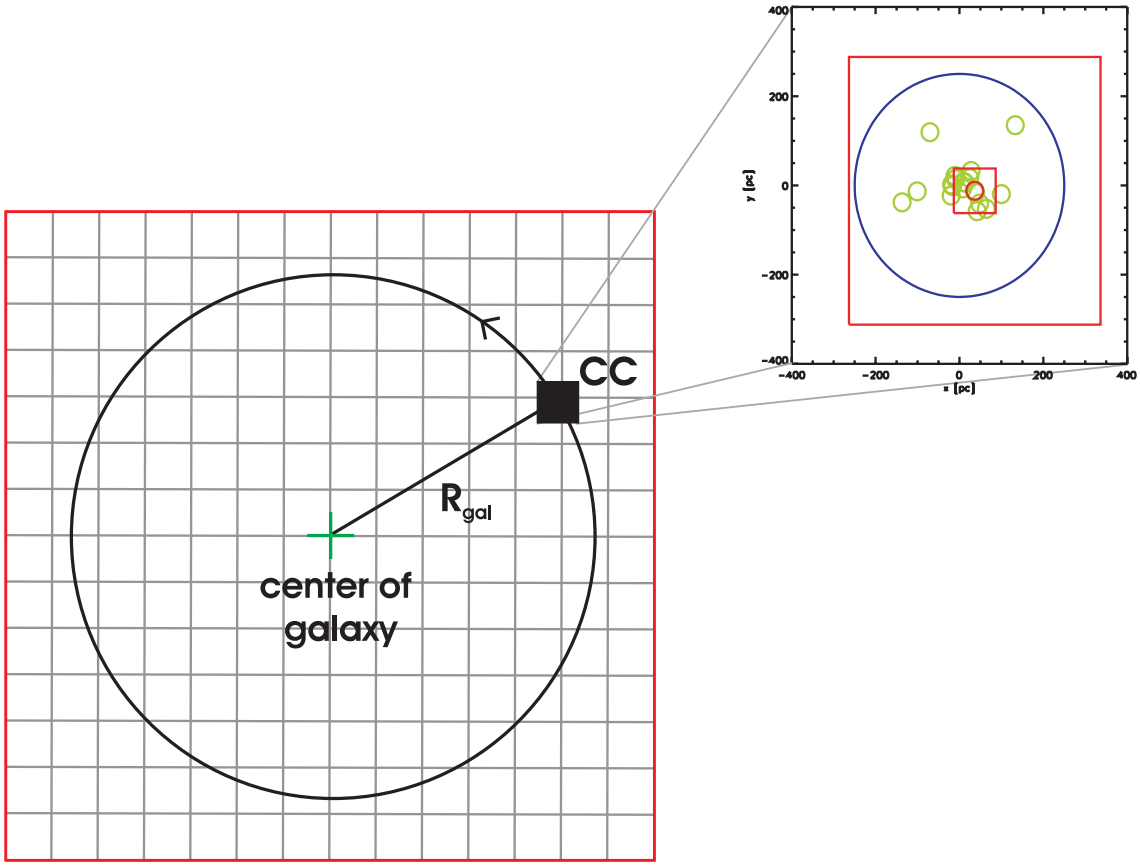

FIGURE 2.9— Illustration of the different grids of SUPERBOX: the red squares represent the different grids. The CC orbit is covered by a low resolution grid whereas each SC is embedded in a high and medium resolution grid. The SCs are marked by small green circles and are placed within the CC (big blue circle). One exemplary set of grids is plotted on one of the SCs indicated by the red circle.

- The high-resolution grids need to be small enough to resolve the central regions of the objects.
- The vast majority of bound particles should be located inside the intermediate-resolution grids.
- The difference in resolution between the high-resolution and intermediate-resolution grid of an object should not be too extreme. The intermediate-resolution grid needs to be small enough to resolve the region covered by the high-resolution grid with sufficient resolution.
- As SUPERBOX has only two grids placed on each SC, a trade-off between coverage, spatial resolution, and computing time needs to be done. Large grid sizes provide a good coverage but decrease the spatial resolution on an object. The resolution can be reestablished by increasing the number of grid cells. However using grids with a larger number of grid cells greatly increases the computing time.

The choice of the grids strongly depends on the specific simulation project and on the available computing power. There is no general recipe for finding the perfect grids.

To illustrate the impact of the grid resolution on the final merger object I performed three simulations of the NGC 2419 model M_1_1.0_50 of Chapter 4 with different grid resolutions. The grids in all three simulations have the same overall sizes, but differ in the number of grid

TABLE 2.1— Grid parameters for three different resolutions

N_c [a]	R_{hres} [b] (pc)	l_{hres} [c] (pc)	R_{mres} [d] (pc)	l_{mres} [e] (pc)
32	80	5.7	800	57
64	80	2.7	800	27
128	80	1.3	800	13

[a] Number of cells per dimension: $N_c = 2^m$, where m is a positive integer.
[b] Size of the inner grid.
[c] Cell length of the inner grid.
[d] Size of the middle grid.
[e] Cell length of the middle grid.

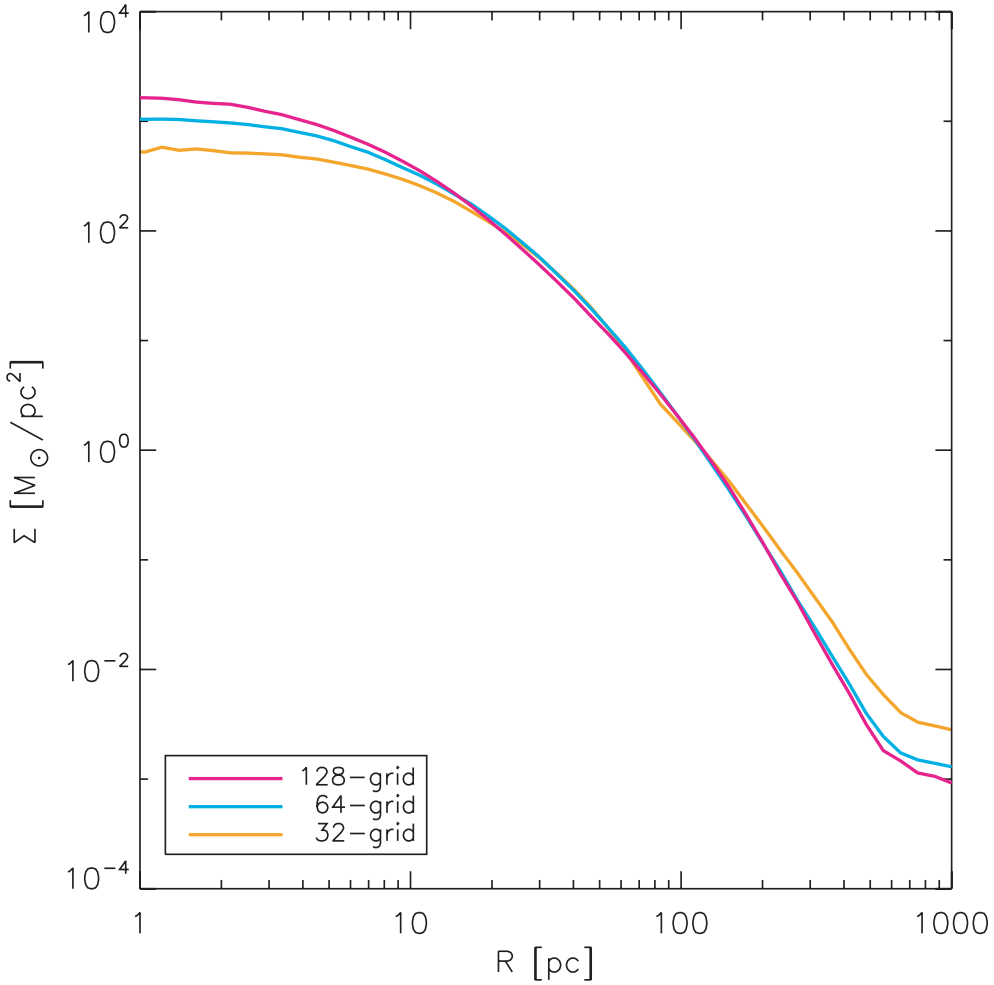

FIGURE 2.10— Illustration of the influence of the number of grid cells on the surface density profile of a merger object. The curves represent the surface density profiles of model M_1_1.0_50 of Chapter 4 after $t_{int} = 9.568$ Gyr of evolution for different grids with $N_c = 32$, 64, and 128 cells per dimension.

TABLE 2.2— Results for Model M_1_1.0_50 for different numerical setups.

Code [a]	N_c [b]	N_0^{SC} [c]	N_M [d]	M_{encl} [e] (10^6 $M_\odot$)	r_{eff} [f] (pc)
SUPERBOX++	32	10^5	20	0.76	25.9
SUPERBOX++	64	10^5	20	0.85	22.1
SUPERBOX++	128	10^5	20	0.85	19.2
SUPERBOX++	128	10^6	20	0.85	19.3
Fortran SUPERBOX	128	10^5	20	0.85	19.2

[a] Code used for simulation.
[b] Number of cells per dimension: $N_c = 2^m$, where m is a positive integer.
[c] Number of particles for a single SC.
[d] Number of merged SCs.
[e] Enclosed mass of merger object.
[f] Effective radius, i.e. the projected half-mass radius of the merger object.

cells and therefore in the spatial resolution. In this example I consider grids with $N_c = 32$, 64, and 128 grid cells per dimension. In model M_1_1.0_50 the CC consists of 20 SCs each with a Plummer radius of $R_{pl}^{SC} = 4$ pc and a cutoff radius of $R_{cut}^{SC} = 20$ pc. The CC has a Plummer radius of $R_{pl}^{CC} = 50$ pc and a cutoff radius of $R_{cut}^{CC} = 200$ pc. The high- and medium resolution grids for this model all have the same size of $R_{hres} = 80$ pc and $R_{mres} = 800$ pc. The size of the middle grid is chosen rather large to ensure that the majority of particles are located within most of the intermediate-resolution grids during the merging event and to be able to maintain the grid choice for the whole parameter study of NGC 2419. The size of the high-resolution grid is chosen such that $R_{mres} = 10\,R_{hres}$. This choice of grid dimensions gives a reasonable resolution for grids with $N_c = 128$ cells per dimension (Table 2.1). According to Eq. 2.39 the length of the grid cells on the high- and intermediate resolution grids amounts to $l_{hres} = 1.3$ pc and $l_{mres} = 13$ pc, respectively. In the extreme case of grids with only $N_c = 32$ cells per dimension, the corresponding cell lengths are $l_{hres} = 5.7$ pc and $l_{mres} = 57$ pc which is far too coarse to resolve the inner regions of the SCs. Therefore the simulation using grids with $N_c = 32$ is not expected to give reliable results for the merger object. The particles are expected to leave the central region and move to larger distances thereby increasing the effective radius of the merger object. The grids with $N_c = 64$ cells per dimension which have cell sizes of $l_{hres} = 2.7$ pc and $l_{mres} = 27$ pc resolve the SCs better than the 32-grid but still only insufficiently.

Figure 2.10 shows the surface density profiles of the merger object of model M_1_1.0_50 for the three different grid resolutions. The simulation on the 128-grid yields the highest value of the central surface density whereas the simulation on the 32-grid has the lowest value. In the middle and outer parts of the profile the situation is reversed. As the 32-grid has only a poor resolution, the particles in the inner part move outwards to larger radii thereby increasing the surface densities at intermediate and large radii. This leads to lower values of the central surface density, smaller enclosed masses and larger effective radii of the merger objects. In case of the 64-grid the effect is not so pronounced as in the simulation with a 32-grid. Table 2.2 shows the number of merged SCs, the enclosed mass, and the effective radius of the merger object for the different grid resolutions. The number of merged SCs is the same for all three simulations, i.e. all 20 SCs merge to form a merger object, whereas the structural parameters of the merger object vary with the chosen resolution. The simulation on the 128-grid gives a mass

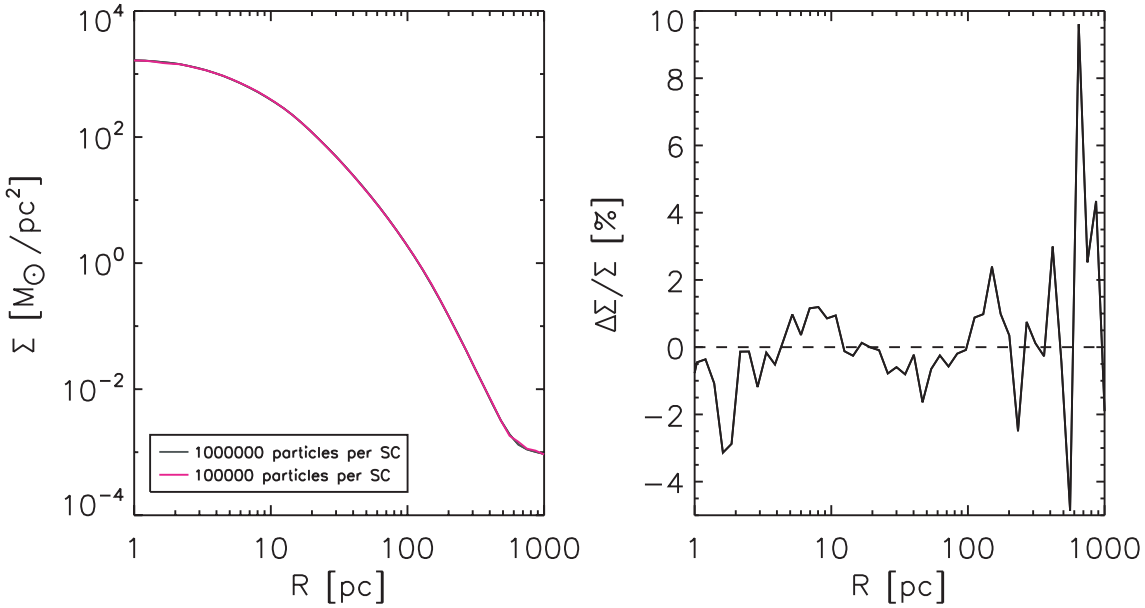

FIGURE 2.11— Illustration of the influence of the number of particles, N, on the surface density profile of a merger object computed on a grid with $N_c = 128$ cells per dimension. **Left:** The two curves represent the surface density profiles of model M_1_1.0_50 of Chapter 4 after $t_{\rm int} = 9.568$ Gyr of evolution for different number of particles of $N_0^{\rm SC} = 100\,000$ and $1\,000\,000$ per SC. **Right:** The relative deviations of the two curves as a function of distance R.

of $M_{\rm encl} = 8.5 \cdot 10^5$ M$_\odot$ and an effective radius of $r_{\rm eff} = 19.2$ pc. Reducing the number of grid cells to $N_c = 64$ cells per dimension, yields the same value for the enclosed mass, but leads to a larger effective radius of $r_{\rm eff} = 22.1$ pc. Making the resolution worse by using a 32-grid affects both, the enclosed mass and the effective radius of the merger object, resulting, respectively, in values of $M_{\rm encl} = 7.6 \cdot 10^5$ M$_\odot$ and $r_{\rm eff} = 25.9$ pc for the final merger object. In this example the resolutions of the grids were intentionally chosen such that the effects of the grid resolution become clearly evident. For the chosen grid sizes of $R_{\rm hres} = 80$ pc and $R_{\rm mres} = 800$ pc the use of the 128-grid is inevitable to get reliable results. However, increasing the number of grid cells is at the expense of computing time. The simulation on the 64-grid takes about three times longer and the simulation on the 128-grid even about 21 times longer than the simulation on the 32-grid. Therefore increasing the number of grid cells should only be done if necessary. Increasing the grid resolution further is not expected to have an influence on the enclosed mass, but could lead to a slight improvement in the accuracy of the effective radii. For my purpose of scanning large parameter spaces to verify overall trends of EOs it is not justifiable to increase the computing time any further just to slightly enhance the accuracy of the effective radius. A 128-grid is the current limit set by the computational infrastructure at the Argelander-Institut (AIfA) for performing the parametric studies presented in this thesis on an acceptable timescale.

Besides the grid parameters the number of particles N in the simulation and the time step Δt further determine the accuracy and duration of the simulation. The exact number of particles in a simulation is not so important as long as it is a suitable number to ensure a smooth density distribution on the grids. Figure 2.11 shows the surface density profiles of the merger object of model M_1_1.0_50 for two different numbers of particles N and the relative deviations of the two curves as a function of distance R. The number of particles is increased tenfold from $N = 2 \cdot 10^6$ to $2 \cdot 10^7$ particles which corresponds to a number of particles per SC of $N_0^{\rm SC} = 10^5$ and 10^6, respectively. The two curves agree quite well. In the inner part and at intermediate radii the deviations are in general well below 3%. In the outer parts of the profile, where the number of particles is low, the deviations reach a maximal value of about 10%. The values for

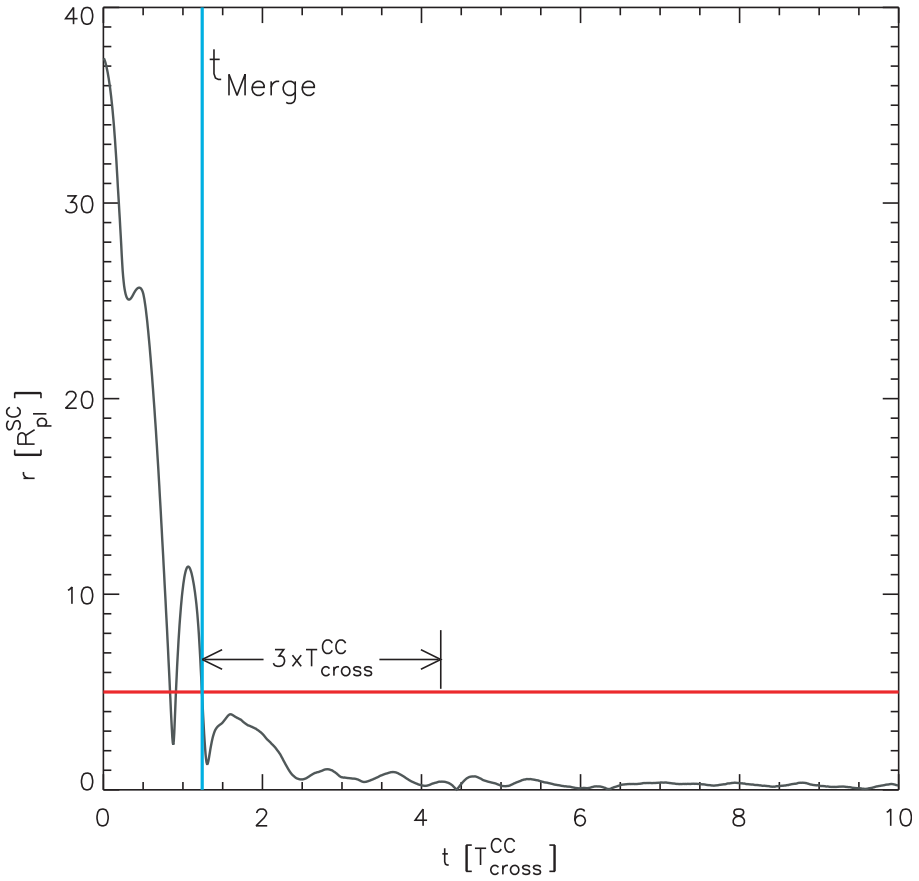

FIGURE 2.12— Illustration of the merging of two SCs. The curve represents the distance between the two SCs in terms of the SC Plummer radius, $R_{\rm pl}^{\rm SC}$, as a function of time given in terms of the CC crossing time, $T_{\rm cross}^{\rm CC}$. The SCs are considered as merged if their distance stays below the horizontal red line. The timescale on which the two SCs merge, $t_{\rm Merge}$, is indicated by the vertical blue line.

the enclosed mass and the effective radius of the merger object are displayed in Table 2.2. I performed two simulations on a 128-grid with 10^5 and 10^6 particles per SC. The enclosed mass is the same for both simulations. Only the effective radius differs by about 0.1 pc which is negligible for these kind of simulations. Even though the increase in computing time is "only" about a factor of two I decided in favor of the lower particle number, because the results only differ slightly and the computing time for the lower particle number already ranges between two weeks and two months depending on the individual simulation.

All particles in a SUPERBOX simulation have the same time step Δt which is fixed throughout the whole simulation. As a rule of thumb the time step should be smaller than the crossing time $T_{\rm cross}^{\rm SC}$ of a SC divided by 10 (Fellhauer priv. communication). The crossing time $T_{\rm cross}^{\rm SC}$ is a typical timescale for a particle to cross the SC. As all SCs in the CC are identical they all have the same crossing time which can be calculated via

$$T_{\rm cross}^{\rm SC} = \left(\frac{3\pi}{32}\right)^{-1.5} \sqrt{\frac{(R_{\rm pl}^{\rm SC})^3}{GM^{\rm SC}}}, \tag{2.40}$$

where $R_{\rm pl}^{\rm SC}$ is the Plummer radius of the SC and $M^{\rm SC}$ is the initial SC mass (for details see Fellhauer 2001). Model M_1_1.0_50 of our example has a Plummer radius of $R_{\rm pl}^{\rm SC} = 4$ pc and a SC mass of $M^{\rm SC} = 5.0 \cdot 10^4$ M$_\odot$. According to Eq. 2.40 the crossing time of this model is $T_{\rm cross}^{\rm SC} = 3.35$ Myr. I chose a time step of $\Delta t = 0.2$ Myr which is well below the rule of thumb

estimate.

In SUPERBOX there is always a tradeoff between simulation speed and accuracy. The grid resolution, the number of particles in the simulation and the time step have to be adapted to the level of accuracy required for a specific simulation project. To additionally save computing time the simulations are checked every 10 CC crossing times for merger events. The CC crossing time, $T_{\rm cross}^{\rm CC}$, can be calculated in the same manner as in Eq. 2.40 for the crossing time of the SCs. Inserting a CC Plummer radius of $R_{\rm pl}^{\rm CC} = 50$ pc and a CC mass of $M^{\rm CC} = 1.0 \cdot 10^6$ M$_\odot$ into Eq. 2.40 yields a CC crossing time of $T_{\rm cross}^{\rm CC} = 33$ Myr for the exemplary model M_1_1.0_50. In general the first 10 CC crossing times lead to the major merger events and the number of grids can thus be reduced by combining all merged SCs to a new object – the merger object – with its own set of grids. This procedure has also the advantage that the number of particles per grid cell in the outer parts of the merger object increases which reduces the statistical noise and therefore improves the force calculation.

The merging criterion is a simple distance criterion: Two objects are considered as merged if their mutual distance stays below five Plummer radii of a single SC (Fellhauer et al. 2002) for more than three crossing times of the CC. Figure 2.12 illustrates the merging of two SCs. The curve represents the distance between the two SCs in units of a SC Plummer radius, $R_{\rm pl}^{\rm SC}$, as a function of time given in units of the CC crossing time, $T_{\rm cross}^{\rm CC}$. The SCs are separated in the beginning but come close to each other within a few CC crossing times. The distance criterion by Fellhauer et al. (2002) is indicated by the horizontal red line. The timescale, $t_{\rm Merge}$, on which the two SCs have merged is indicated by the vertical blue line. After about 1.2 times the CC crossing time, i.e. after 41 Myr, the two SCs are regarded to be merged as their mutual distance is well below the horizontal line afterwards.

When it becomes apparent that no further SCs will merge into the merger object, the simulation can be run continuously to the end. Thus a computation can be roughly divided into two phases: a merging phase in the first 1–2 Gyr followed by an evolution phase of the merger object. For a detailed description of merging process and additional information the reader is referred to Fellhauer (2001) and Fellhauer et al. (2002).

2.2.4 SUPERBOX++ versus Fortran SUPERBOX

The Fortran version of SUPERBOX was developed in the early 1990s at the Astronomisches Recheninstitut (ARI) in Heidelberg (Bien et al. 1990, 1991) and has been extensively tested and compared to other numerical techniques (e.g. Klessen & Kroupa 1998; Fellhauer et al. 2000; Spinnato et al. 2003). Manuel Metz at the AIfA in Bonn re-implemented SUPERBOX in the C++ programming language (Metz 2008) between 2006 and 2009 making use of object oriented programming techniques. The new implementation of SUPERBOX, SUPERBOX++, makes use of modern multi-core processor technologies and is much more efficient than the original FORTRAN code. Only very recently there have been further developments on SUPERBOX. Bien et al. (2013) at the ARI introduced flattened grids to SUPERBOX to model disk galaxies more accurately. Pfeffer & Baumgardt (2013) at the University of Queensland increased the number of co-moving grids from two to four in a graphics processing unit (GPU) enabled version of SUPERBOX++. The additional two co-moving grids would be very useful for simulations of merging star clusters in the future as it would allow to use 64-grids instead of 128-grids while still maintaining a good coverage of the objects.

I used the FORTRAN version of SUPERBOX only for the simulations of FFs in Chapter 4 as the C++ version was not yet available at that time. The simulations of the Milky Way EO NGC 2419 in Chapter 4 and the parameter studies of EOs in Chapter 5 were performed with the new code SUPERBOX++ on compute servers with 16 and 32 CPU cores to fully benefit from the parallelization.

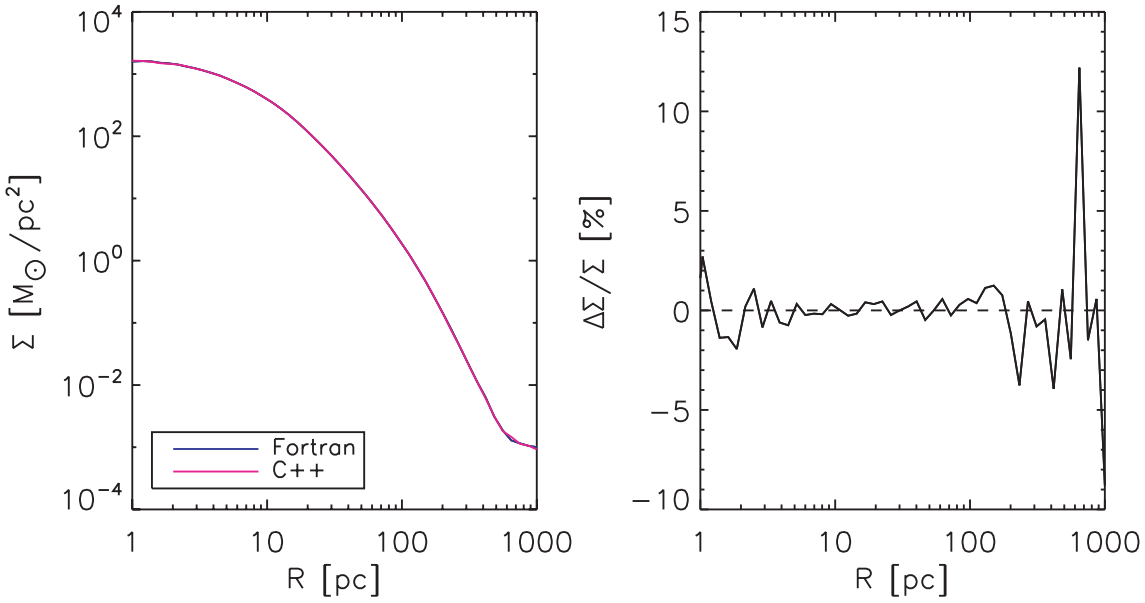

FIGURE 2.13— Comparison of the results of the simulations of M_1_1.0_50 with the two codes SUPERBOX and SUPERBOX++. **Left:** The two curves represent the surface density profiles of the final merger objects after $t_{\rm int} = 9.568$ Gyr of evolution. **Right:** The relative deviations of the two curves as a function of distance R.

As a test for the new code SUPERBOX++ I performed the example simulation M_1_1.0_50 with both codes. Figure 2.13 shows the surface density profiles of the final merger objects of model M_1_1.0_50 after $t_{\rm int} = 9.568$ Gyr of evolution obtained from the simulations with the two codes SUPERBOX and SUPERBOX++. The profiles are almost identical. They differ slightly in the inner most region and the outer parts of the profiles. In the outer parts, where the number of particles is low, the deviations reach a maximal value of about 13%. Table 2.2 displays the values of the enclosed mass and the effective radius of the merger object which are exactly the same. Further tests of the SUPERBOX++ code are presented in the PhD thesis of Manuel Metz (Metz 2008).

3

A Catalog of ECs and UCDs in Various Environments

This chapter analyzes the observational parameters total luminosity, M_V, effective radius, r_{eff}, and projected distance to the host galaxy, R_{proj}, of all known ECs and UCDs and the dependence of these parameters on the type and the total luminosity, $M_{V,gal}$, of their host galaxy. I searched the available literature to compile a catalog of star clusters with effective radii larger than 10 pc. As there is no clear distinction between ECs and UCDs, both types of objects will be called "extended stellar dynamical objects" – abbreviated "EOs". In total, I found 835 EOs of which 171 are associated with late-type galaxies and 664 EOs associated with early-type galaxies. EOs cover a luminosity range from about $M_V = -4$ to -14 mag. However, the vast majority of EOs brighter than $M_V = -10$ mag are associated with giant elliptical galaxies. At each magnitude extended objects are found with effective radii between 10 pc and an upper size limit, which shows a clear trend: the higher the luminosity the larger is the upper size limit. For EOs associated with early- and late-type galaxies, the EO luminosity functions peak at -6.34 and -6.47 mag, respectively, which is about one magnitude fainter than the peak of the GC luminosity function. EOs and GCs form a coherent structure in the r_{eff} vs. M_V parameter space, while there is a clear gap between EOs and early-type dwarf galaxies. However, there is a small potential overlap at the high-mass end, where the most extended EOs are close to the parameters of some compact elliptical galaxies.

3.1 Introduction

As already indicated in Chapter 1, GC-like objects with effective radii above 10 pc, which cover a large luminosity range, have been found in various environments from dwarf to giant elliptical galaxies. In recent years, the number of observed ECs and UCDs has rapidly increased for all types of galaxies in various environments. As there is no clear distinction between ECs and UCDs, both types of objects will be called "extended stellar dynamical objects" – abbreviated "EOs" – in this thesis. The high number of EOs known today, allows for the first time for a detailed analysis of the properties of EOs to disclose commonalities and distinctions of objects from early- and late-type galaxies. To allow for an analysis of their parameters, I compiled a catalog of effective radii, absolute V-band luminosities, and projected distances of EOs to their host galaxies as well as the absolute V-band luminosities of these galaxies and their distance to the Milky Way. I distinguish between EOs found in late-type galaxies, i.e. spiral and irregular galaxies, and early-type galaxies, i.e. elliptical, lenticular, and dwarf spheroidal galaxies.

The chapter is structured as follows: In Sect. 3.2 I compile a catalog of ECs and UCDs on the basis of the available publications containing structural parameters of ECs and UCDs. In Sect. 3.3 I present the results of the catalog that are discussed in Sect. 3.4. Section 3.5 provides

a summary and conclusions. In Appendix A, I present the catalog of the 835 EOs used in this study (Table A.1). Table A.2 of Appendix A provides an overview on the galaxies, where EOs were detected, the number of EOs per galaxy and the luminosity range of the detected EOs.

3.2 The Observational Basis of the EO Catalog

The following two sections summarize the publications used for compiling the EO catalog.

3.2.1 EOs in Late-Type Galaxies

According to the 2010 edition of the GC catalog of Harris (1996) and considering that Arp 2 and Terzan 8 are associated with the Sagittarius dwarf spheroidal galaxy (Da Costa & Armandroff 1995; Salinas et al. 2012), the Milky Way has 11 EOs. The other two Local Group spiral galaxies M31 and M33 have 20 (Huxor et al. 2008; Peacock et al. 2009; Huxor et al. 2011a) and 2 (Stonkutė et al. 2008; Huxor et al. 2009; Cockcroft et al. 2011) EOs, respectively. EOs were also found in the LMC (van den Bergh & Mackey 2004), and the dwarf irregular galaxy NGC 6822 (Hwang et al. 2011).

Outside the Local Group, EOs were detected in the spiral galaxies M81 (Chandar et al. 2004; Nantais et al. 2011), M83 (Chandar et al. 2004), M51 (Chandar et al. 2004; Hwang & Lee 2008), NGC 891 (Harris et al. 2009), NGC 3370 (Cantiello et al. 2009), and in the Sombrero Galaxy M104 (Larsen et al. 2001b; Hau et al. 2009). In addition, EOs were found in the dwarf irregular and the Magellanic type dwarf galaxies UGCA 86, UGC 8638, NGC 247, NGC 5237, ESO 269-58, NGC 784, NGC 4605, UGC 3974, and NGC 1311 (Georgiev et al. 2009), UGC 7605, KK 065, UGC 3755, KK 112, and UGC 4115 (Sharina et al. 2005; van den Bergh 2006), and NGC 4449 (Strader et al. 2012b).

In total, the EO catalog contains 171 EOs associated with late-type galaxies.

3.2.2 EOs in Early-Type Galaxies

EOs were detected in a large number of elliptical galaxies: NGC 5128 (Gómez et al. 2006; McLaughlin et al. 2008; Chattopadhyay et al. 2009; Taylor et al. 2010; Mouhcine et al. 2010), NGC 4660 (Chies-Santos et al. 2011), IC 3652 (Haşegan et al. 2005), NGC 4278 (Chies-Santos et al. 2011), NGC 4486B (Haşegan et al. 2005), M89 (Haşegan et al. 2005; Chies-Santos et al. 2011), M59 (Chilingarian & Mamon 2008), M49 (Haşegan et al. 2005), M86 (Chies-Santos et al. 2011), the central galaxy of the Virgo Cluster M87 (Haşegan et al. 2005; Evstigneeva et al. 2008; Brodie et al. 2011; Chies-Santos et al. 2011), M84 (Chies-Santos et al. 2011), the central galaxy of the Fornax Cluster NGC 1399 (Richtler et al. 2005; Evstigneeva et al. 2007; Hilker et al. 2007; Evstigneeva et al. 2008; Mieske et al. 2008; Chilingarian et al. 2011), NGC3923 (Norris & Kannappan 2011), NGC 4476 (Haşegan et al. 2005), NGC 5846 (Chies-Santos et al. 2006), NGC 4696 (Mieske et al. 2007), NGC 3311 (Misgeld et al. 2011), IC 4041, NGC 4889, IC 3998, IC 4030, IC 4041, and NGC 4908 (Chiboucas et al. 2011), NGC 4874 (Madrid et al. 2010; Chiboucas et al. 2011), NGC 1132 (Madrid 2011), NGC 1275 (Penny et al. 2012), NGC 4365 (Blom et al. 2012), NGC 1316 (Goudfrooij 2012), NGC 1199 (Da Rocha et al. 2011), M60 Strader et al. (2012a), and ESO 325-G004 (Blakeslee & Barber DeGraaff 2008).

In five lenticular galaxies, EOs were detected: in NGC 1023 (Larsen & Brodie 2000; Brodie & Larsen 2002) and NGC 1380 (Chies-Santos et al. 2007), 15 and 13 EOs were found, respectively. One EO was discovered in NGC 4546 (Norris & Kannappan 2011), three EOs in NGC 1533 (DeGraaff et al. 2007), and four EOs were found in M85 (Haşegan et al. 2005; Chies-Santos et al. 2011).

The EO of the dwarf elliptical Scl-dE1 (Da Costa et al. 2009), the two EOs of the Sagittarius dSph galaxy (Salinas et al. 2012), the EO of the Fornax dSph galaxy (van den Bergh & Mackey 2004), the 6 EOs of the dSph galaxy KK84 (Sharina et al. 2005; van den Bergh 2006), and the EO

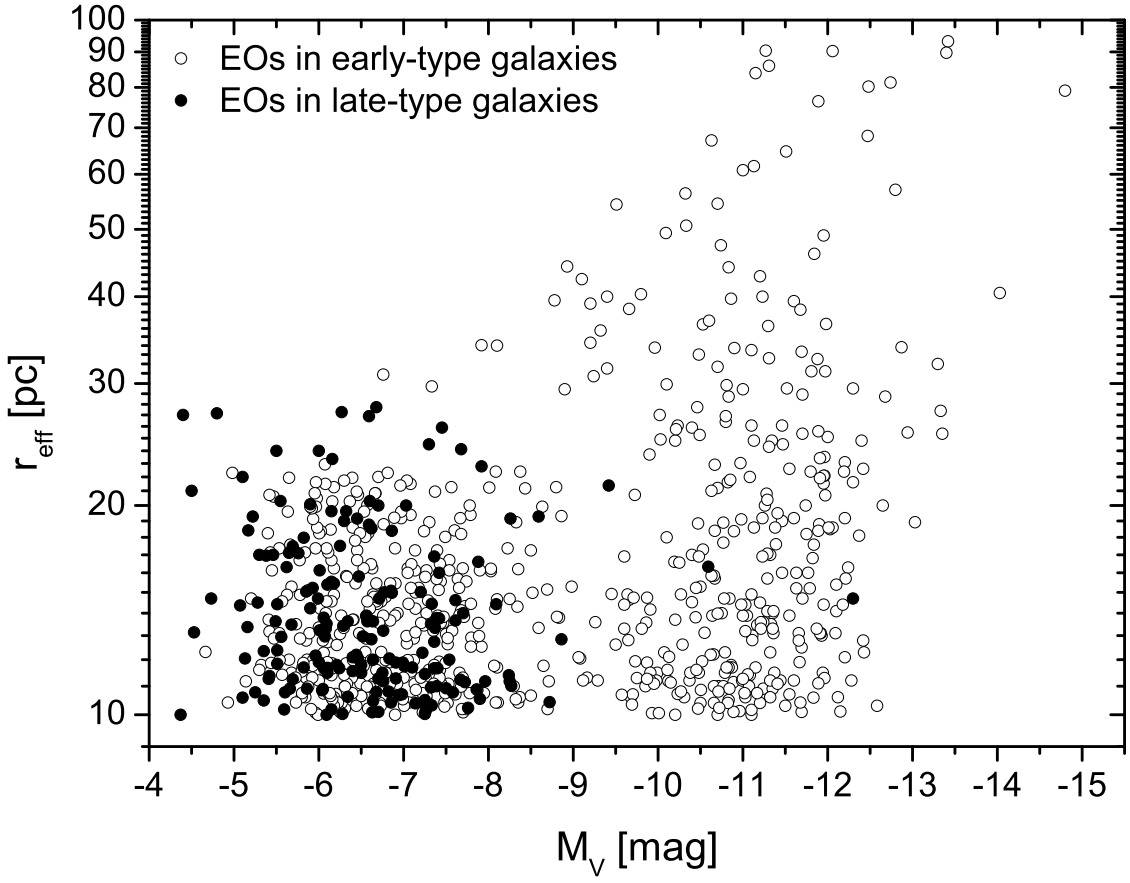

FIGURE 3.1— Effective radii, $r_{\rm eff}$, of EOs are plotted against their absolute V-band luminosities, $M_{\rm V}$. EOs associated with early-type galaxies are plotted as open circles, EOs associated with late-type galaxies are plotted as black circles.

of the dSph galaxy IKN (Georgiev et al. 2009) are contributing to the list of EOs associated with early-type galaxies.

In total, 664 EOs were found in early-type galaxies, 617 thereof are associated with elliptical galaxies. The EO sample of the elliptical galaxies is dominated by the two galaxies NGC 4365 and NGC 1275, which have 217 and 84 EO candidates, respectively.

3.3 Results

3.3.1 Trends and Correlations of the EO Parameters

Figure 3.1 shows the effective radii, $r_{\rm eff}$, of the 835 EOs of my catalog as a function of their total V-band luminosities, $M_{\rm V}$. The vast majority of EOs associated with late-type galaxies have magnitudes between $M_{\rm V} = -4$ to -9 mag. Only three EOs, the Milky Way cluster NGC 2419 and two EOs associated with the Sombrero Galaxy (M104), have absolute V-band luminosities brighter than $M_{\rm V} = -9$ mag. EOs associated with early-type galaxies cover a significantly larger range of V-band luminosities. The majority of objects are found in the magnitude range of about $M_{\rm V} = -5$ to -13 mag. At $M_{\rm V} = -8.5$ mag the number of objects is much smaller than for lower and higher luminosities.

At each magnitude EOs are found with effective radii between 10 pc and an upper size limit, which shows – at least for EOs associated with early-type galaxies – a clear trend: the higher the luminosity the larger is the upper size limit.

The dependency of the structural parameters effective radius, $r_{\rm eff}$, and luminosity, $M_{\rm V}$, of

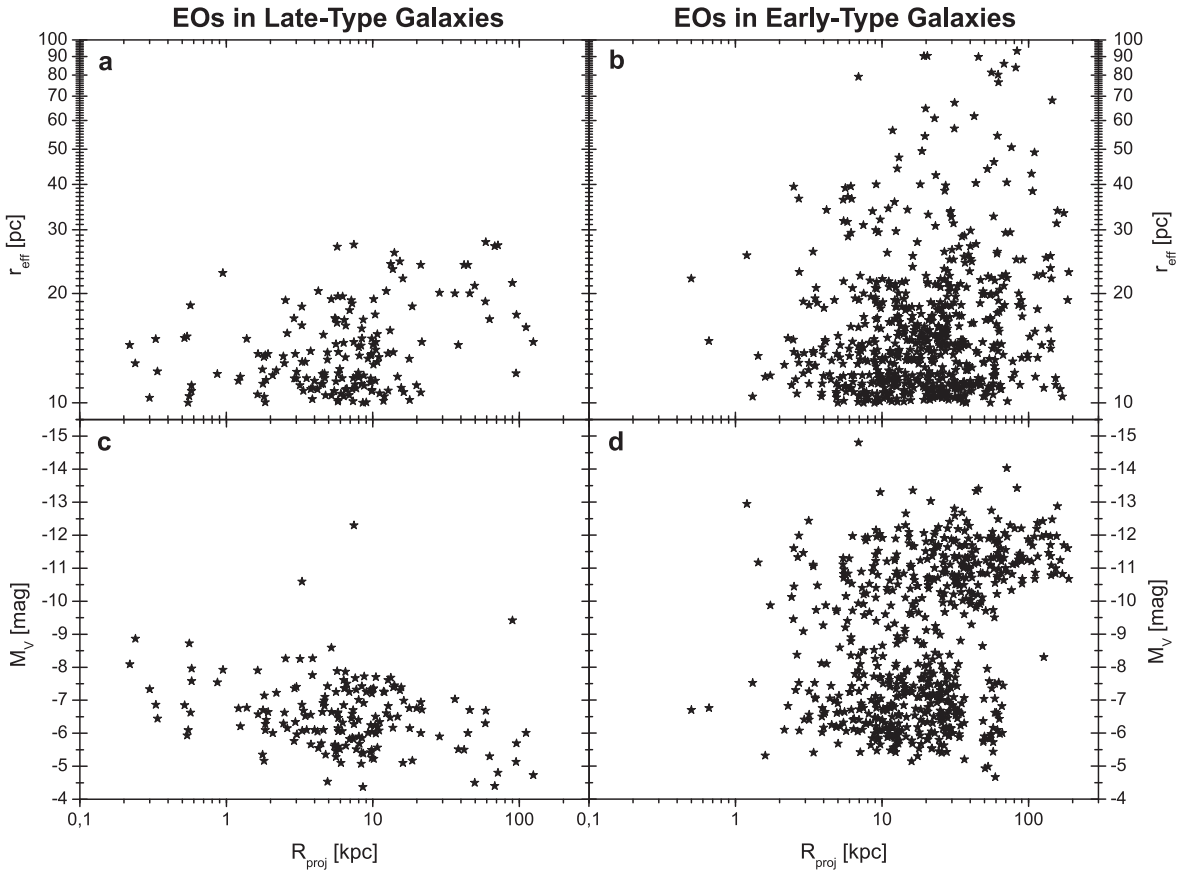

FIGURE 3.2— **a** and **b:** Effective radii, $r_{\rm eff}$, of EOs are plotted against the projected distances, $R_{\rm proj}$, to their host galaxies. **c** and **d:** Absolute V-band luminosities, $M_{\rm V}$, of EOs are plotted against the projected distance, $R_{\rm proj}$.

EOs on the projected distance from their host galaxy, $R_{\rm proj}$, are displayed in Fig. 3.2. For late-type galaxies there is a slight trend of increasing effective radii and decreasing total luminosities with increasing projected distance (Fig. 3.2a and c). On the other hand, very faint and very extended objects are extremely hard to detect at very low projected distances due to the high surface brightness of the underlying host galaxy. Consequently, the slight trends might not be significant. In early-type galaxies the most extended objects are found predominantly at large projected distances (Fig. 3.2b). The most extended EO, VUCD7, with an effective radius of 93.2 pc, was discovered in the central elliptical galaxy M87 of the Virgo Cluster at a projected distance of 83.5 kpc. In early-type galaxies, the low-luminosity objects are comparable to those in late-type galaxies and there are high-luminosity objects that are not present in late-type galaxies. The void at projected distances larger than about 70 kpc and luminosities fainter than -10.5 mag is a result of the limited coverage and sensitivity of most surveys.

Figure 3.3 shows two histograms of the number of EOs with different total V-band luminosities. The EOs in late-type galaxies have a luminosity distribution which peaks at around $M_{\rm V} = -6.5$ mag, while the EOs in early-type galaxies show a bimodal distribution which peaks at $M_{\rm V} = -6.5$ and -11.0 mag and has a clear minimum at about -9 mag. In Sect. 3.4.2.2, it will be shown that the bimodal luminosity distribution is mostly a selection effect due to EO samples covering solely the high luminosity regime.

Figure 3.4 shows two histograms of the number of EOs with different effective radii. For EOs in both early- and late-type galaxies, the majority of objects has small effective radii. The mean size for EOs in early-type galaxies is 18.1 pc and its median value lies at 14.2 pc. For EOs in early-type galaxies that are fainter than $M_{\rm V} = -10$ mag, the mean and the median size are

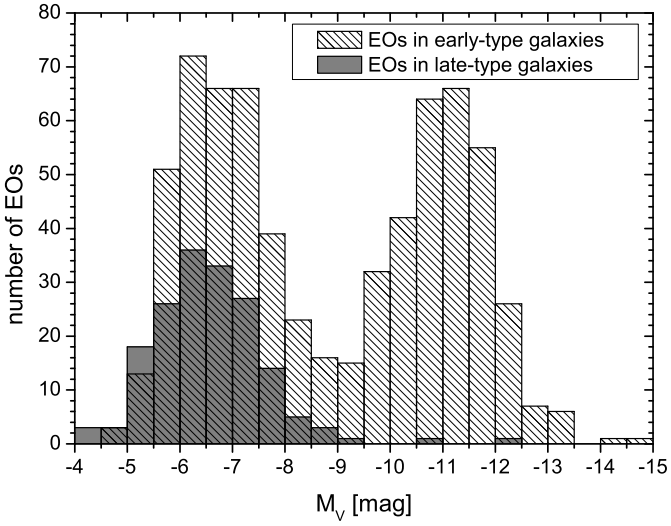

FIGURE 3.3— Histogram of the number of EOs in early- and late-type galaxies at different total V-band luminosities, M_V.

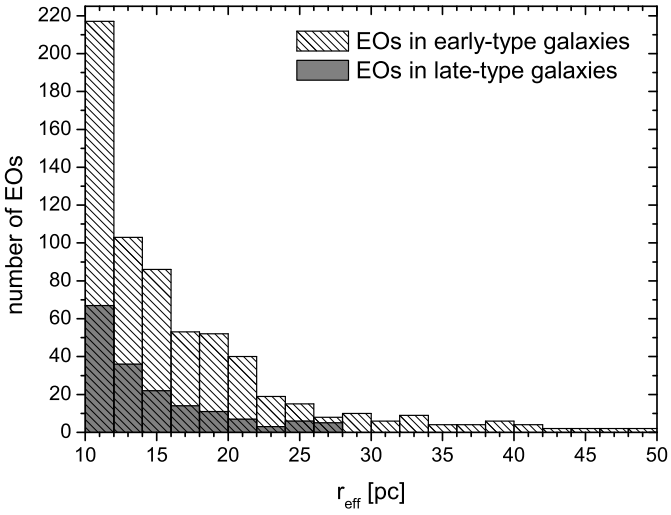

FIGURE 3.4— Histogram of the number of EOs in early- and late-type galaxies at different effective radii, $r_{\rm eff}$.

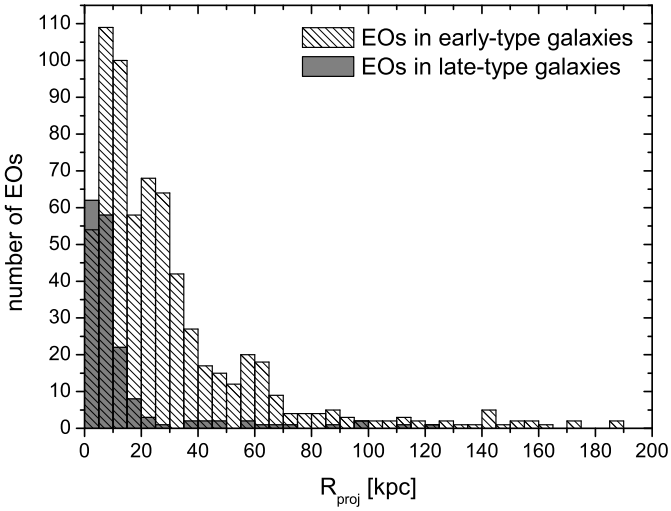

FIGURE 3.5— Histogram of the number of EOs in early- and late-type galaxies at different projected radii, $R_{\rm proj}$.

15.2 and 13.6 pc, respectively. The sizes of EOs in late-type galaxies are slightly smaller: the mean size is 14.4 pc and its median value is 13.2 pc. For EOs in late-type galaxies, 39.2% have effective radii between 10 and 12 pc. For early-type galaxies, 37.6 and 25.4% are in the interval between 10 and 12 pc for EOs fainter and brighter than $M_V = -10$ mag, respectively.

A histogram of the projected distance of EOs to their host galaxies is presented in Fig. 3.5. EOs in late-type galaxies were predominantly found at small projected distances below 20 kpc. It should be noted, however, that the coverage of the halo beyond projected distances of 20 kpc is extremely poor for most late-type galaxies. EOs in early-type galaxies were found also at considerably larger distances. The mean and the median projected distances are 12.7 and 6.5 kpc for EOs in late-type galaxies and 29.5 and 20.6 kpc for EOs in early-type galaxies, respectively. Only few EOs have been discovered beyond 100 kpc. All EOs with projected distances larger than 130 kpc are associated with the giant elliptical galaxies in the center of the Virgo Cluster, the Fornax Cluster, the Perseus Cluster, and the Coma Cluster. This result does not necessarily imply that only the central galaxies of clusters have EOs at very large distances, as rather isolated galaxies scarcely have HST observations at such large projected distances (see Sect. 3.4.3).

3.3.2 Correlation of EO Parameters with those of their Host Galaxies.

Figure 3.6 shows the dependence of the parameters projected distance of EOs to their host galaxies, $R_{\rm proj}$, effective radius, $r_{\rm eff}$, and absolute V-band luminosity of the EOs, $M_{\rm V,EO}$, on the total V-band luminosity of the host galaxies, $M_{\rm V,gal}$.

Figures 3.6a and b illustrate the dependence of the projected distances of the EOs on the total V-band luminosity of the host galaxies. For EOs in late-type galaxies only three galaxies (the Local Group galaxies Milky Way, M31, and M33) host EOs at projected distances beyond 20 kpc. In contrast, for early-type galaxies with luminosities between -21 and -24 mag EOs are found far out from the galactic center even beyond 100 kpc. Only very few objects are found at projected distances less than a few kiloparsecs. This lack of EOs at small projected distances is at least partly due to the fact that EOs have a very low contrast on the bright background light from the host galaxy.

Figures 3.6c and d demonstrate that the upper limit of the effective radii of EOs in late-type and early-type galaxies tends to increase with the total V-band luminosity of the host galaxy. For all galaxies, most EOs have effective radii well below 20 pc.

Figure 3.6e shows that the total luminosity of EOs in late-type galaxies does not depend on the total luminosity of their host galaxy. For EOs in early-type galaxies (Fig. 3.6f) there is a trend: the more massive the parent galaxy the higher is the upper limit of the luminosities of its EOs. This trend is partly a size-of-sample effect, as in large EO samples also extreme luminosities can be realized. In Sect. 3.4.2.2 I will demonstrate, however, that the number of high-luminosity objects is larger than expected from the EO luminosity function.

Figure 3.7a plots the projected distances of the EOs versus the distance of their host galaxies from the Galaxy. Early-type galaxies have been studied nearby as well as at large distances up to 143 Mpc, while late-type galaxies were mainly observed in the local Universe up to distances of 10 Mpc. Only one spiral (NGC 3370) was searched for EOs at a larger distance of about 27 Mpc.

Figure 3.7b displays the absolute V-band luminosity of the EOs versus the distance of the host galaxy from the Galaxy. The maximum absolute V-band luminosity of EOs does not change with the distance of the host galaxy. While EOs brighter than $M_V = -10$ mag were detected at all distances, faint EOs have only been observed in galaxies closer than 30 Mpc.

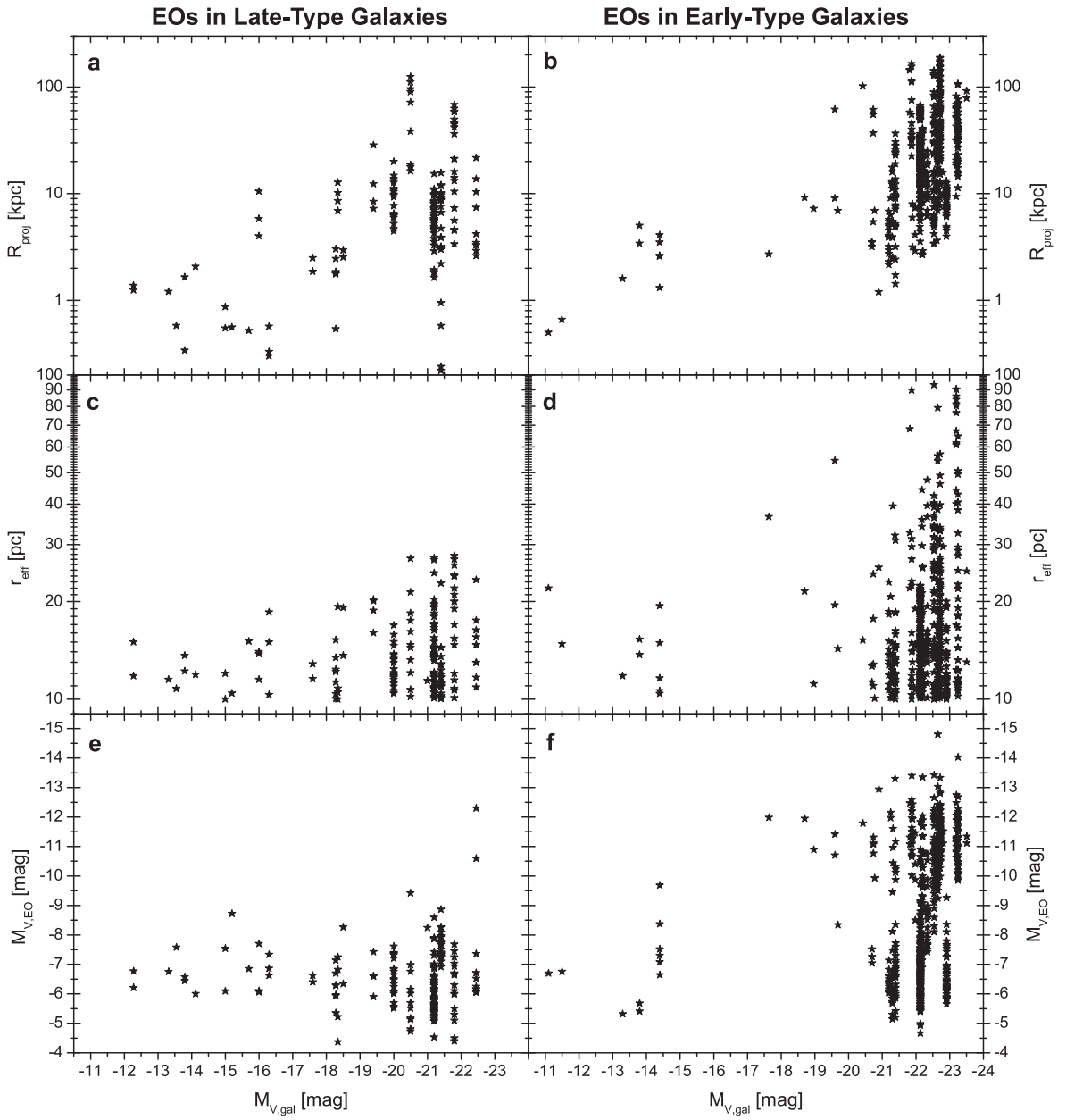

FIGURE 3.6— **a** and **b:** Projected distances, $R_{\rm proj}$, of EOs are plotted against the total V-band luminosity, $M_{\rm V,gal}$, of their host galaxies. **c** and **d:** Effective radii, $r_{\rm eff}$, of EOs are plotted against the total V-band luminosity, $M_{\rm V,gal}$, of the host galaxies. **e** and **f:** Absolute V-band luminosities, $M_{\rm V,EO}$, of EOs are plotted against the total V-band luminosity, $M_{\rm V,gal}$, of the host galaxies.

3.4 Discussion

3.4.1 Distribution in the Effective Radius Versus Total Luminosity Space

Figure 3.1 shows the effective radii, $r_{\rm eff}$, of the 835 EOs as a function of their total V-band luminosities, $M_{\rm V}$. At all luminosities, EOs cover a range between 10 pc and an upper limit, which increases with increasing luminosity from about 25 pc at $M_{\rm V} = -5$ mag to about 100 pc at $M_{\rm V} = -13$ mag.

This trend of the increasing upper limit of effective radii with total luminosities defines the range where EOs have been found so far. It should not, however, be regarded as a firm upper limit, as very extended objects with a low total luminosity are extremely hard to detect.

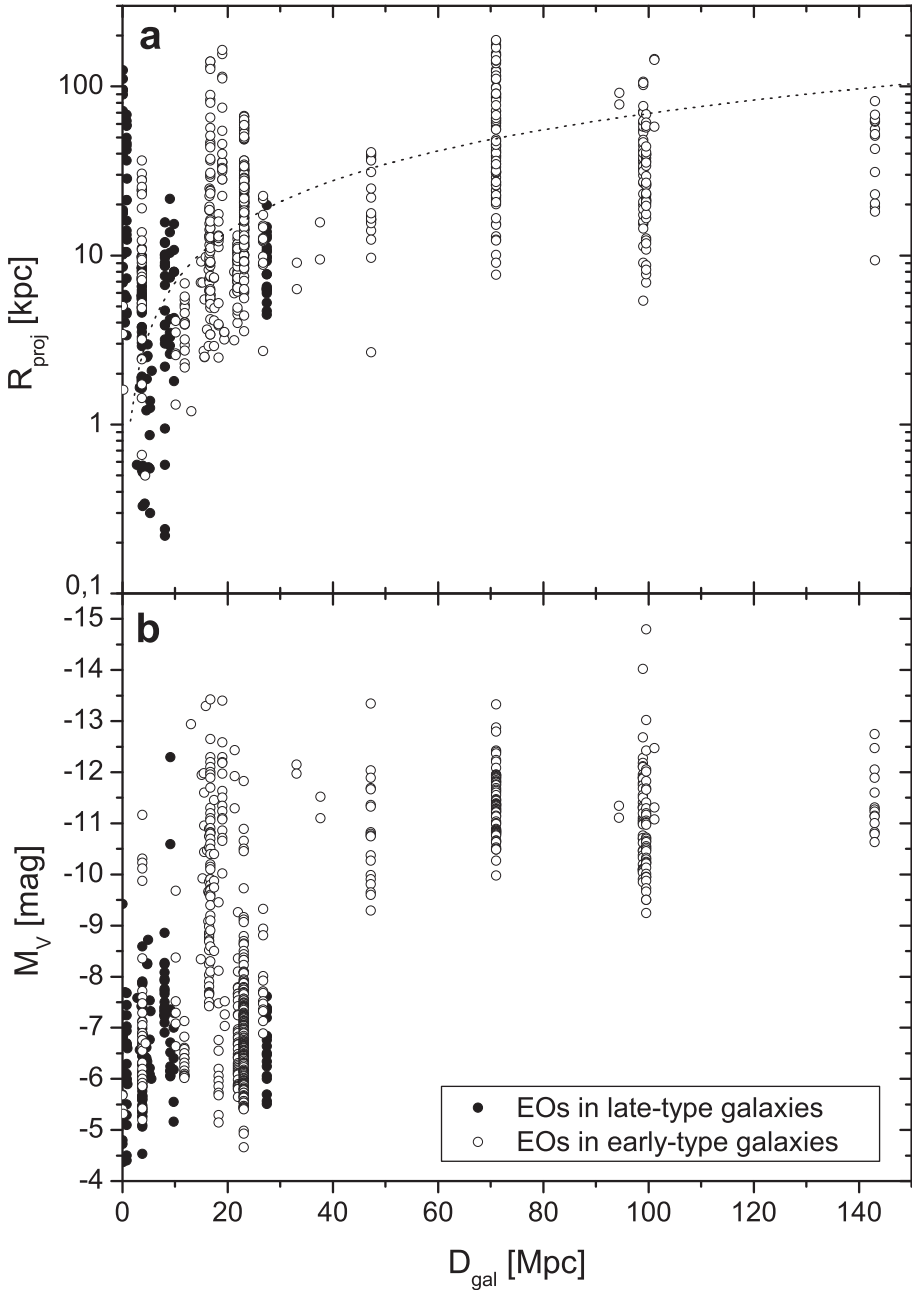

FIGURE 3.7— **a:** Projected distances, $R_{\rm proj}$, of EOs from their host galaxies are plotted against the distance, $D_{\rm gal}$, of the host galaxies. The dotted curve indicates the largest possible projected radius within a single HST ACS image centered on a galaxy at a given distance. **b:** Absolute V-band luminosities, $M_{\rm V}$, of EOs are plotted against the distance, $D_{\rm gal}$, of the host galaxies.

While the detection limit of EOs depends on numerous parameters like the magnitude and the structure of the fore- and background emission, I will focus on the characteristics of the EOs themselves.

The effective radius is defined as the radius where half of the total luminosity of an object is included. A large effective radius means that the luminosity is spread over a large area leading to a low surface brightness. In order to provide a rough estimate of the mean surface brightness, I divide the luminosity within the effective radius, which is by definition half of the total luminosity, by the area of a circle with the size of the effective radius,

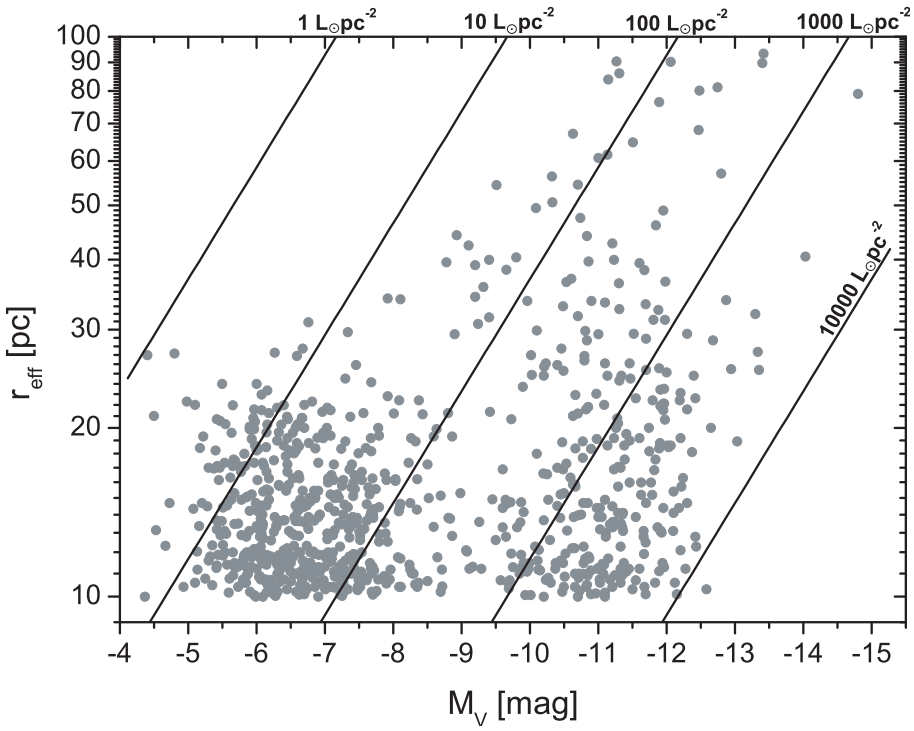

FIGURE 3.8— Effective radii, $r_{\rm eff}$, of EOs are plotted against their absolute V-band luminosities, $M_{\rm V}$ (grey circles). The black lines indicate trends of equal mean surface brightnesses of 1, 10, 100, 1 000, and 10 000 $\mathrm{L_\odot\ pc^{-2}}$.

$$\overline{\Sigma_{\rm V,EO}} = \frac{0.5\ L_{\rm V,EO}}{A(r_{\rm eff})} = \frac{10^{-0.4\ (M_{\rm V}-M_{\rm V,\odot})}}{2\ \pi\ r_{\rm eff}^2}, \tag{3.1}$$

where $\overline{\Sigma_{\rm V,EO}}$ is the mean surface brightness, $L_{\rm V,EO}$ is the total V-band luminosity of an EO, $M_{\rm V,\odot} = 4.83$ mag is the absolute solar V-band luminosity, and $A(r_{\rm eff}) = \pi\ r_{\rm eff}^2$ is the area within $r_{\rm eff}$. Figure 3.8 shows $r_{\rm eff}$ vs. $M_{\rm V}$ of EOs as in Fig. 3.1 and in addition lines with constant mean surface brightness as defined in Eq. 3.1. An EO with $r_{\rm eff} = 10$ pc and $M_{\rm V} = -5.0$ mag has the same mean surface brightness as an EO with $r_{\rm eff} = 50$ pc and $M_{\rm V} = -8.5$ mag. On the other hand, Fig. 3.8 demonstrates that the trend of the increasing upper limits of effective radii with increasing total luminosity is not aligned with the lines of constant mean surface brightness. Consequently, the trend cannot be explained as a simple limit of detectability.

The EO catalog and the results presented in Sect. 3.3 contain both confirmed EOs and EO candidates. EOs are identified initially in HST images on the basis of an almost round shape and a color consistent with being a GC. The criteria exclude a fair fraction of background galaxies. However, the presence of round background galaxies with the same color as GCs cannot be excluded. Only in the very neighborhood of the Local Group, EOs can be resolved into stars discriminating them from background objects. Consequently, all more distant candidates need to be confirmed by follow-on spectroscopy measuring radial velocities of the objects. As such a procedure is extremely time-consuming, only a fraction of the candidate GCs and EOs are observed spectroscopically.

The large extension of EOs leads to significantly lower central surface brightnesses. In terms of central surface brightness, an EO with $r_{\rm eff} = 10$ pc is roughly a factor of 25 or 3.5 magnitudes fainter than a GC with the same total luminosity, but with $r_{\rm eff} = 2$ pc. An EO with $r_{\rm eff} = 30$ pc is already a factor of about 225 or 5.9 magnitudes fainter. Consequently, GCs are typically preferred over EOs during the selection of targets for confirmation, as they are considerably

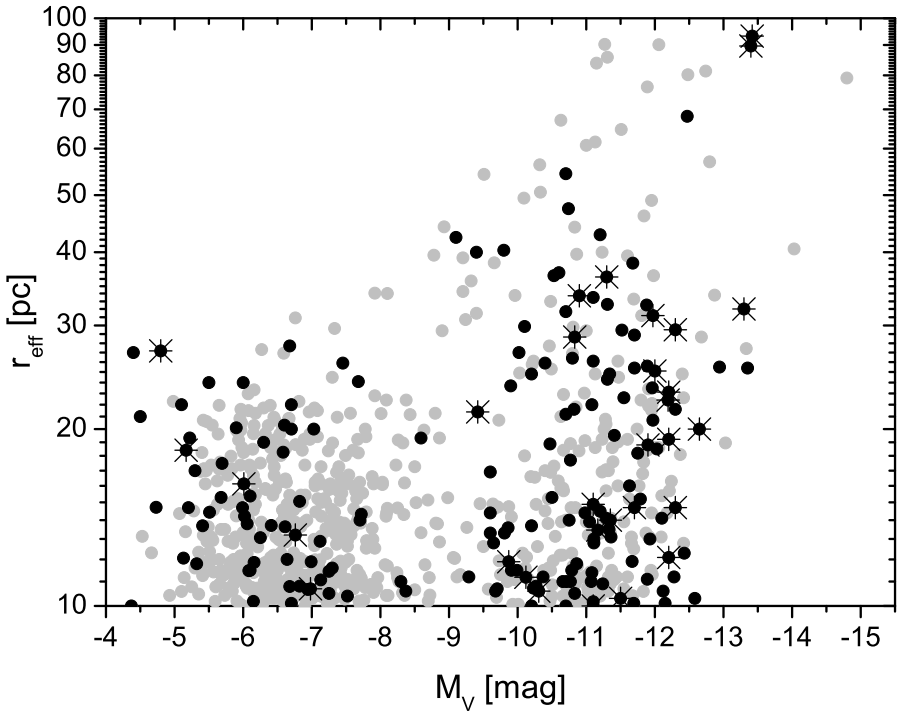

FIGURE 3.9— Effective radii, $r_{\rm eff}$, of EOs are plotted against their absolute V-band luminosities, $M_{\rm V}$. Black circles indicate the 178 confirmed EOs, while grey circles are the 657 EO candidates. The 31 EOs which have a measured dynamical mass are marked by an additional star.

easier to confirm.

From the 835 EOs in the catalog, only 178 EOs were so far spectroscopically confirmed. Figure 3.9 shows effective radii of confirmed (black) and candidate EOs (grey) as a function of their total V-band luminosities. The confirmed EOs cover basically the same $M_{\rm V}$ and $r_{\rm eff}$ parameter space as the entire catalog and show the same trend of increasing upper size limits with increasing luminosity. Consequently, the overall distribution of EOs in the $r_{\rm eff}$ vs. $M_{\rm V}$ space and the trend of increasing upper size-limits with increasing luminosity are not significantly influenced by contaminating background objects.

Figure 3.10 shows next to the effective radii and total luminosities of EOs also the corresponding parameters of GCs with effective radii smaller than 10 pc. The parameters of the GCs were taken from the same papers used for the EOs (see Sect. 3.2). In addition, the ultra-faint Milky Way GCs Segue 3 (Belokurov et al. 2010; Fadely et al. 2011), Muñoz 1 (Muñoz et al. 2012), and Balbinot 1 (Balbinot et al. 2013) were added. The diagram demonstrates that EOs and GCs form a coherent structure in the $M_{\rm V}$ vs. $r_{\rm eff}$ parameter space.

Figure 3.11 is a histogram of the effective radii of all star clusters presented in Fig. 3.10. The largest number of objects is contained in the bin covering effective radii between 2 and 4 pc. For larger effective radii, the number of objects decreases approximately exponentially. Star clusters with effective radii below 6 pc include 82% of all objects, while the EOs represent about 9% of the objects.

In Fig. 3.10, the median effective radii per luminosity bin of the combined GC-EO-sample are given as squares. For luminosities fainter than about $M_{\rm V} = -10.5$ mag, compact clusters with effective radii of a few parsecs dominate. With increasing luminosity, EOs start to dominate over GCs leading to an overall trend of increasing effective radii with increasing total luminosity. The median effective radius increases from 10 pc at $M_{\rm V} = -11.0$ mag to 30 pc at $M_{\rm V} = -13.5$ mag. At the high-luminosity end, the number of objects is quite low. The low

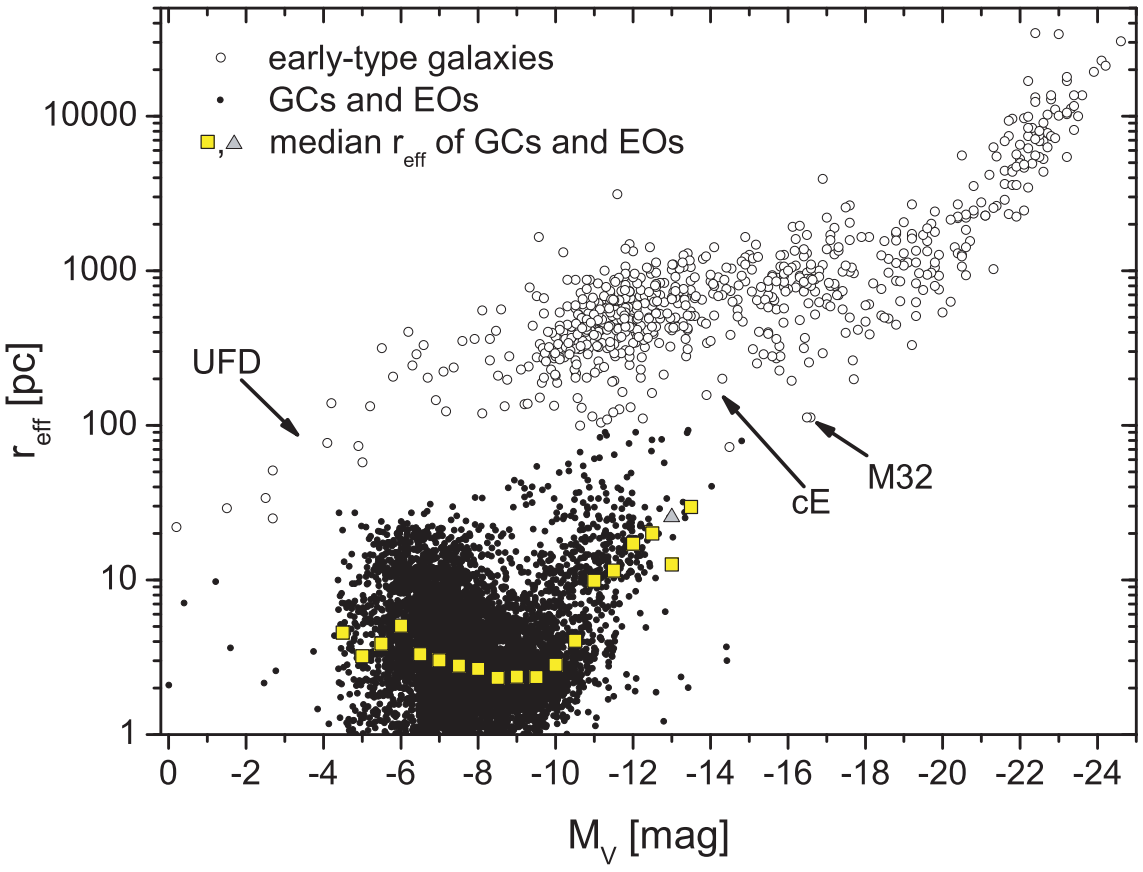

FIGURE 3.10— Effective radii, $r_{\rm eff}$, of GCs and EOs are plotted against their absolute V-band luminosities, $M_{\rm V}$ (black circles). The median effective radius per luminosity bin is given as squares. The six exceptionally bright GCs with luminosities between $M_{\rm V} = -12.5$ and -14.5 mag and effective radii below 4 pc are unconfirmed candidate clusters associated with NGC 4365 (Blom et al. 2012). The grey triangle shows the median effective radius, when these exceptionally bright compact GCs were removed in the bin at $M_{\rm V} = -13.0$ mag. In addition, early-type galaxies are shown as open circles. Highlighted are the two galaxy types compact ellipticals (cE) with their prototype example M32, and the ultra faint dwarf galaxies (UFD) recently found in the Milky Way.

median effective radius at $M_{\rm V} = -13.0$ mag is due to three very compact candidate GCs in this bin. The removal of these unconfirmed GCs results in a median effective radius that fits the overall trend (grey triangle). While the data show a clear trend of increasing effective radii with increasing luminosity, a tight size-luminosity relation as seen in older publications (e.g. Dabringhausen et al. 2008; Evstigneeva et al. 2008) is no longer existing on the basis of the larger dataset presented in this chapter. This result is consistent with the conclusions of Brodie et al. (2011), which were based on a considerably smaller dataset.

Figure 3.10 shows next to the GCs and EOs (black circles) also the effective radii and absolute luminosities of early-type galaxies (open circles). I compiled the parameters of the elliptical, dwarf and compact elliptical, and dwarf spheroidal galaxies from Brasseur et al. (2011), Slater et al. (2011), Bell et al. (2011), McConnachie & Irwin (2006), Cappellari et al. (2006), Sharina et al. (2008), Mieske et al. (2005), Huxor et al. (2011b), Belokurov et al. (2010), Misgeld & Hilker (2011), Da Costa et al. (2009), Martin et al. (2008), Price et al. (2009), Geha et al. (2010), Smith Castelli et al. (2008), Smith Castelli et al. (2012), Blakeslee & Barber DeGraaff (2008), McConnachie (2012), and Lieder et al. (2012). The galaxies span a luminosity range of about 24 magnitudes and a size range of three orders of magnitude.

While the star clusters (GCs and EOs) and the early-type galaxies form both a coherent structure in the $M_{\rm V}$ vs. $r_{\rm eff}$ parameter space, there is a clear gap between star clusters and

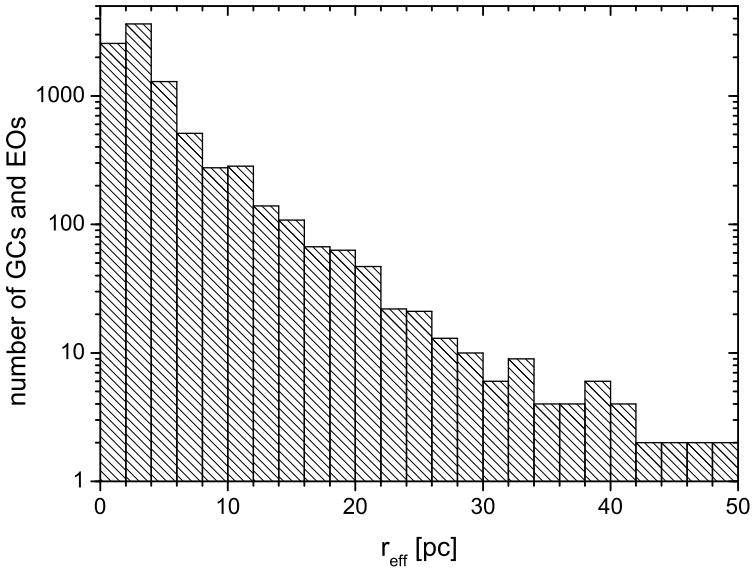

FIGURE 3.11— Histogram of the number of star clusters at different effective radii, $r_{\rm eff}$, for all GCs and EOs shown in Fig. 3.10. The slight increase of numbers at 10 pc is due to the fact that all publications of this chapter were selected to contain EOs, but not all of them also include GCs.

galaxies at least in the luminosity interval between $M_{\rm V} = -6$ and -11 mag. This gap was first discussed by Gilmore et al. (2007). At $M_{\rm V} = -6$ mag, EOs have effective radii up to about 30 pc, while the dwarf spheroidal galaxies at this luminosity have effective radii between about 100 and 400 pc. In the high-luminosity region at about $M_{\rm V} = -12$ mag EOs have effective radii up to about 90 pc, while the dwarf galaxies at this luminosity have effective radii between 100 and 1300 pc. Between $M_{\rm V} = -11$ and -12 mag there are candidate compact ellipticals from Blakeslee & Barber DeGraaff (2008) and Lieder et al. (2012). They have the same parameters as EOs, but they are slightly larger than 100 pc, which lead to the classification as cEs. As there is no clear distinction between EOs and cEs, these cEs might as well be very extended EOs.

The ultra faint dwarf galaxies (UFDs), which were recently found around the Milky Way (e.g. Martin et al. 2008; Belokurov et al. 2010), cover the luminosity range between $M_{\rm V} = 0$ and -5 mag. In the same luminosity interval some ultra faint GCs were detected (e.g. Muñoz et al. 2012; Balbinot et al. 2013), which have effective radii just below 10 pc. The detection of large objects with effective radii greater than 10 pc and luminosities fainter than $M_{\rm V} = -5$ mag is extremely challenging even within the Local Group. While there is no overlap between UFDs and EOs for the Milky Way, a potential overlap of EOs and UFDs for other galaxies cannot be excluded, as neither UFDs nor very faint EOs were within the detection limits of existing surveys.

On the high-luminosity end of the EO distribution, some compact elliptical galaxies have parameters comparable to the most extended EOs. Figure 3.10 shows two EOs brighter than $M_{\rm V} = -14$ mag, with effective radii of about 40 and 80 pc (Madrid et al. 2010; Madrid 2011). The most luminous EO, UCD1 ($M_{\rm V} = -14.8$ mag, $r_{\rm eff} = 77.1$ pc) from NGC 1132, was recently[1] spectroscopically confirmed to be associated with 1132 (Madrid & Donzelli 2013). The next three most luminous, confirmed objects with a total V-band luminosity of $M_{\rm V} \approx -13.4$ mag are VUCD7, UCD3, and HUCD1, which are associated with the central elliptical galaxies of the Virgo Cluster, M87, of the Fornax Cluster, NGC 1399, and the Hydra Cluster, NGC 3311, respectively. In addition, the confirmed object M59cO, which is associated with the giant elliptical galaxy M59, has a luminosity of about $M_{\rm V} \approx -13.3$ mag. VUCD7 and UCD3 have effective

[1]Due to the late publication date of Madrid & Donzelli (2013), this chapter was not updated accordingly.

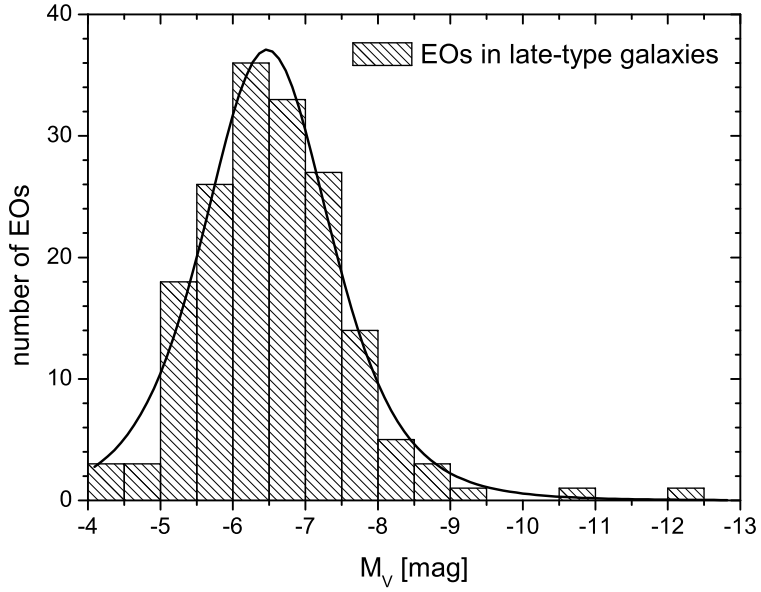

FIGURE 3.12— Histogram of the number of EOs in late-type galaxies at different total V-band luminosities, M_V. The black line represents a fitted t_5 luminosity function.

radii of the order of 90 pc, while HUCD1 and M59cO have effective radii of 25 and 32 pc, respectively.

The Coma Cluster compact elliptical galaxy CcGV19b (Price et al. 2009), which has a luminosity of $M_V \approx -14.5$ mag and an effective radius of $r_{\rm eff} = 72$ pc, is located at a projected distance of 68 kpc to NGC 4874. These parameters could also lead to a classification of CcGV19b as an EO. The observed mass-to-light ratio of about 13 (Price et al. 2009), which is about a factor of three larger than that of VUCD7 and UCD3 (Evstigneeva et al. 2007; Mieske et al. 2008), suggests rather a galactic origin. However, the vast majority of EOs, about 96%, do not have observed velocity dispersions (see Fig. 3.9), which are needed to estimate a dynamical mass. Consequently, some overlap between EOs and compact elliptical galaxies cannot be excluded.

3.4.2 EO Luminosity Functions

A common way of parameterization of samples of astronomical objects are luminosity functions. Secker (1992) analyzed compact GCs in the Milky Way and M31 and concluded that their luminosity functions are well represented by so-called Student t_5 functions

$$LF \propto \left[1 + \frac{(M_V - M_{V,TO})^2}{5\sigma_V^2}\right]^{-3}, \tag{3.2}$$

where M_V are absolute V-band luminosities of star clusters, $M_{V,TO}$ is the turnover of the luminosity function and σ_V is the dispersion of the t_5 function. For compact GCs, the turnover of the luminosity function, $M_{V,TO}$, is very constant for various types of galaxies, making it a reasonable distance estimator (see Rejkuba 2012, and references therein). The mean turnover luminosity for the Milky Way and 18 nearby galaxies is $M_{V,TO} = -7.66 \pm 0.09$ mag.

3.4.2.1 EOs in Late-Type Galaxies

A histogram of the number of EOs at different total luminosities of late-type galaxies is shown in Fig. 3.12. A fit of the luminosity function according to Eq. 3.2 is added. The turnover of the luminosity function is $M_{V,TO} = -6.47 \pm 0.03$ mag and the dispersion of the t_5 function is

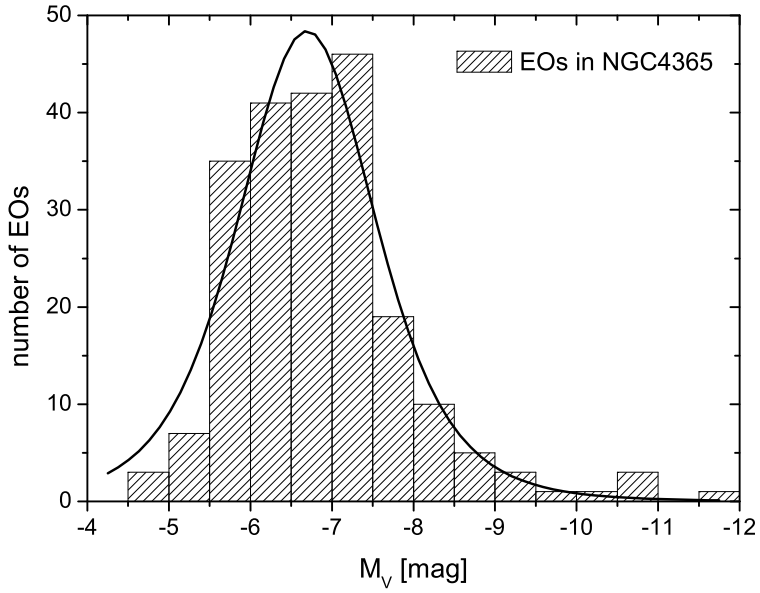

FIGURE 3.13— Histogram of the number of EOs in the elliptical galaxy NGC 4365 at different total V-band luminosities, M_V. The black line represents a fitted t_5 luminosity function.

$\sigma_V = 0.91 \pm 0.03$ mag. The peak of the EO luminosity function is about one magnitude fainter than the typical peak of the GC luminosity function.

For the histogram in Fig. 3.12 all 171 EOs associated with late-type galaxies are used. As discussed in Sect. 3.4.1, only a fraction of EOs were confirmed by follow-on spectroscopy. Consequently, it cannot be excluded that some background galaxies modified the exact result of the luminosity function. The number of confirmed EOs in late-type galaxies is 43. The mean total luminosity of the 43 EOs is $M_V = -6.40$ mag. Considering the low number of objects, this value is quite close to the fitted value for all candidate EOs, indicating that the EOs in late-type galaxies indeed have a fainter peak of the luminosity function than compact GCs.

Considering the very low surface brightness of faint and extended EOs (see Sect. 3.4.1), a fair fraction of very extended and faint EOs is most likely below the detection limit of extragalactic surveys. The true turnover of the EO luminosity function might therefore be at even lower luminosities.

3.4.2.2 EOs in Early-Type Galaxies

Figure 3.3 shows that EOs in early-type galaxies show a bimodal distribution which peaks at about $M_V = -6.5$ and -11.0 mag and has a clear minimum between -8.5 and -9 mag. On the other hand, Fig. 3.7b demonstrates that for a large fraction of early-type galaxies only high-luminosity objects were considered. This is partly due to detection limits especially at large distances, but also due to the fact that since the discovery of UCDs in the Fornax Cluster by Hilker et al. (1999) and Drinkwater et al. (2000), much effort has been made to detect and to analyze EOs brighter than about $M_V = -10$ mag, while fainter EOs were neither in the focus of UCD studies nor in those investigating GCs.

A number of GC surveys applied size limits to reduce the contamination of background galaxies. For instance, the GC surveys covering 100 galaxies of the Virgo Cluster (Jordán et al. 2005) and 43 galaxies of the Fornax Cluster (Masters et al. 2010) applied a size limit of $r_{\rm eff} < 10$ pc to reduce the contamination by background galaxies. As a side effect, they excluded also all EOs from their GC catalogs.

The very different approaches for objects with low and high luminosities have a significant

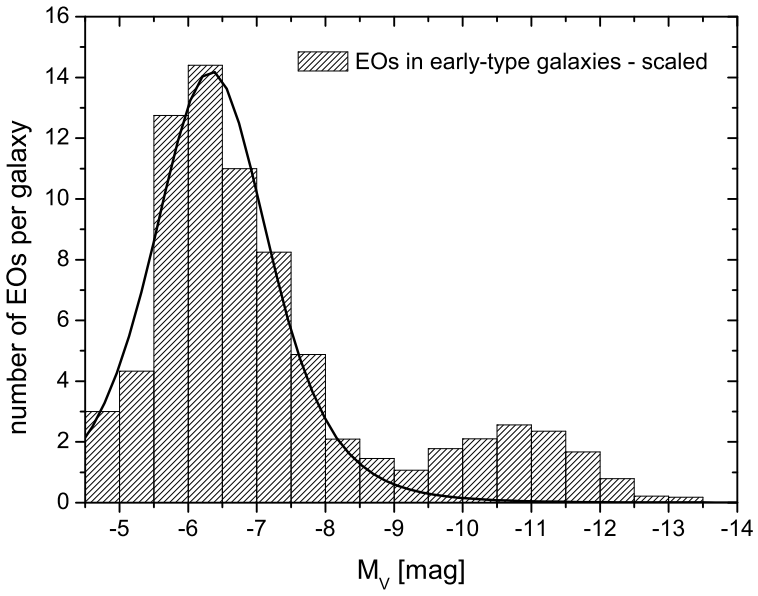

FIGURE 3.14— Histogram of the normalized number of EOs in early-type galaxies at different total V-band luminosities, M_V, scaled by the number of galaxies having observations at the individual bins. The black line represents a fitted t_5 luminosity function.

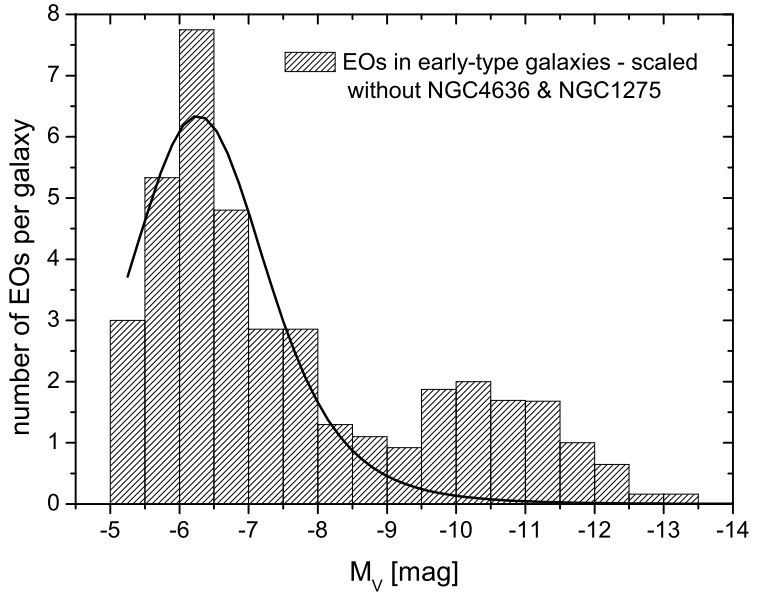

FIGURE 3.15— Histogram of the normalized number of EOs in early-type galaxies except for the large EO samples of NGC 4365 and NGC 1275 at different total V-band luminosities, M_V, scaled by the number of galaxies having observations at the individual bins. The black line represents a fitted t_5 luminosity function.

influence on the luminosity function. One example is the galaxy M85 of the Virgo Cluster. Four EOs are found with luminosities brighter than $M_V = -8.5$ mag (Haşegan et al. 2005; Chies-Santos et al. 2011). Peng et al. (2006) used the same Virgo Cluster survey data as Jordán et al. (2005) to search for diffuse star clusters and concluded that the galaxy M85 has about 30 EOs with luminosities between $M_V = -5.5$ and -8.5 mag. While the low luminosity objects would dominate for this galaxy, my catalog contains only the four bright M85 EOs of Haşegan et al. (2005) and Chies-Santos et al. (2011) as Peng et al. (2006) have not published a catalog of their EOs. In the same field of view Jordán et al. (2005) found 211 compact GCs in M85. For this

specific galaxy, the EOs would add about 15% to the GC sample.

Another example is the giant elliptical galaxy NGC 4365, which was covered by eight HST ACS fields (Blom et al. 2012). Seven HST ACS fields provide a very good coverage of the inner 35 kpc of the galaxy while the last field pointed to the halo delivering clusters with projected distances between about 40 and 60 kpc. Blom et al. (2012) found in total 2038 GC and 217 EO candidates. For this galaxy, EOs add about 10% to the GC sample. Only 5 of the 217 EOs are brighter than $M_{\rm V} = -10$ mag, 19 EOs have a luminosity between $M_{\rm V} = -8$ and -10 mag, and 148 EOs have one between $M_{\rm V} = -6$ and -8 mag. Again, the number of low-luminosity EOs is significantly larger than the number of bright EOs. The EO candidates of NGC 4365 form the largest EO sample of an elliptical galaxy. Figure 3.13 shows the histogram of the number of EO candidates of NGC 4365 as a function of luminosity. The black line shows the corresponding luminosity function having a turnover luminosity of $M_{\rm V,TO} = -6.69 \pm 0.07$ and a dispersion of the t_5 function of $\sigma_{\rm V} = 0.88 \pm 0.07$ mag. The turnover luminosity is at slightly brighter luminosities as for the late-type galaxies.

In their central HST field, Blom et al. (2012) found 681 compact clusters and 30 EOs, i.e. the EOs add about 4.4% to the GC sample in the central region of NGC 4365. For the 100 Virgo galaxies Jordán et al. (2005) found in single HST fields centered on the individual galaxies in total $12\,763$ compact GCs. An EO fraction of 5% would yield for these 100 galaxies an EO population of 638 EOs, which is about ten times the number of high luminosity objects in my catalog associated with these Virgo Cluster galaxies.

Consequently, an interpretation of the bimodal luminosity distribution needs to take into account the varying number of galaxies building the sample at each luminosity bin. Only eight early-type galaxies have observations of EOs fainter than $M_{\rm V} = -8.5$ mag and only five galaxies have observations of EOs fainter than $M_{\rm V} = -6.5$ mag. For EO luminosities from $M_{\rm V} = -8.5$ to -10.5 mag, the number of observed galaxies increases from 11 to 20. EOs brighter than $M_{\rm V} = -11$ mag were observed in 33 galaxies.

Figure 3.14 takes the varying number of galaxies into account, i.e. the number of EOs in each bin is divided by the number of galaxies contributing to this luminosity bin. The second peak at high luminosities has decreased considerably, but it has not entirely vanished, demonstrating that the large number of high-luminosity EOs associated with the most luminous galaxies is not a simple size-of-sample effect. A fit of the luminosity function according to Eq. 3.2 is added to Fig. 3.14. The peak of the luminosity function is at $M_{\rm V,TO} = -6.34 \pm 0.08$ mag and the dispersion of the t_5 function is $\sigma_{\rm V} = 0.90 \pm 0.09$ mag. The values change only slightly to $M_{\rm V,TO} = -6.33 \pm 0.08$ mag and $\sigma_{\rm V} = 0.87 \pm 0.06$ mag when the high-luminosity tail (i.e. objects brighter than $M_{\rm V} = -9$ mag) is excluded from the fit.

The EO sample of early-type galaxies is dominated by the two galaxies NGC 4365 and NGC 1275, which have 217 and 84 EO candidates, respectively. In order to verify that the results for early-type galaxies are not biased towards these two galaxies, I have repeated the exercise of scaling the number of objects per luminosity bin by the number of relevant galaxies excluding NGC 4365 and NGC 1275 from the sample. Figure 3.15 shows the resulting histogram and a fitted luminosity function having $M_{\rm V,TO} = -6.27 \pm 0.15$ mag and $\sigma_{\rm V} = 1.03 \pm 0.18$ mag. The results of the sample without NGC 4365 and NGC 1275 agree well with the results of the entire EO sample of early-type galaxies.

The results for early-type galaxies are very similar to the results for late-type galaxies. The main difference between the luminosity functions is the tail of high-luminosity objects associated with early-type galaxies.

Mieske et al. (2012) studied a sample of confirmed GCs and UCDs to adress the question whether there is an overpopulation of UCDs with respect to compact GCs. They concluded that the number of UCDs is consistent with a continuation of the GC luminosity function towards bright magnitudes. In this chapter, I demonstrate that there is an overpopulation of bright

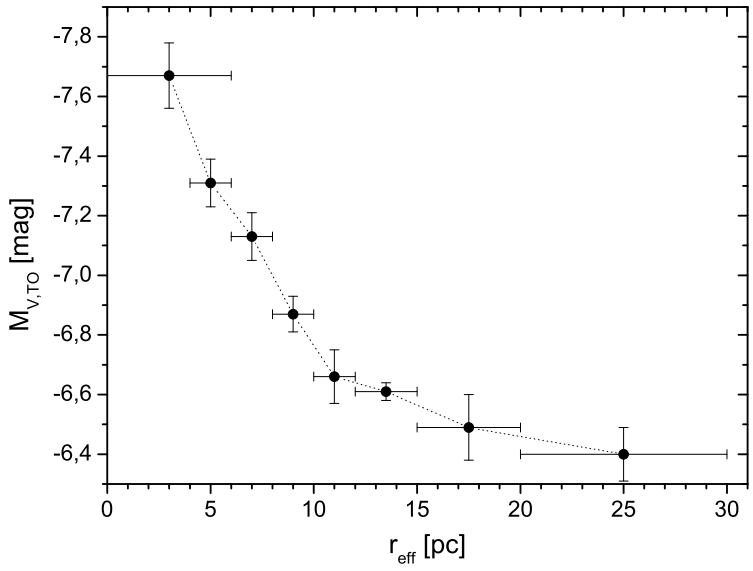

FIGURE 3.16— Turnover of the luminosity function, $M_{\rm V,TO}$, of GC and EOs plotted as a function of the effective radius, $r_{\rm eff}$. The error bars in $r_{\rm eff}$ indicate the individual bin-sizes, the error bars in $M_{\rm V,TO}$ show the statistical error of the fit of the luminosity function to the data.

EOs if compared with the EO luminosity function. While the Mieske et al. (2012) sample is well-defined in the sense that all objects were spectroscopically confirmed, most of them have no measured size. They used all UCDs irrespective of their size and compared the number of UCDs with the GC luminosity function which has a turnover luminosity that is about one magnitude brighter than the EO luminosity function. In addition, the number of GCs is about 10 times larger than the number of EOs. Consequently, the results of Mieske et al. (2012) cannot easily be compared with my results as the samples are largely independent from each other. Larger EO and GC samples of a number of early-type galaxies covering the entire luminosity range from $M_{\rm V} = -4$ to -14 mag are needed to answer the question whether there is a general overpopulation of bright EOs in early-type galaxies or whether it is a specific feature seen only in special environments.

3.4.2.3 Trends of the Turnover Luminosity with Effective Radius

In the previous sections, I concluded that EOs in early- and late-type galaxies have basically the same turnover of the luminosity function, which is about one magnitude fainter than that of compact GCs.

In this section, I explore the trend of the turnover luminosity with increasing effective radii. In order to increase the number of objects per $r_{\rm eff}$-bin, I combine the data for GCs and EOs of early- and late-type galaxies. I exclude the brightest objects in the UCD regime to avoid the second peak as seen in Figs. 3.3 and 3.14 and focus on objects fainter than $M_{\rm V} = -9$ mag.

For the compact GCs with effective radii below 6 pc, I derive a turnover of the luminosity function of $M_{\rm V,TO} = -7.67 \pm 0.11$ mag, which is in very good agreement with the mean turnover luminosity for the Milky Way and 18 nearby galaxies, $M_{\rm V,TO} = -7.66 \pm 0.09$ mag (Rejkuba 2012).

Figure 3.16 shows the trend of the turnover luminosity as a function of the effective radius. The turnover luminosity decreases continuously from $M_{\rm V,TO} = -7.67$ to -6.66 mag at the $r_{\rm eff}$-bin between 10 and 12 pc. For larger effective radii, the turnover luminosity decreases considerably slower to values of $M_{\rm V,TO} = -6.40$ mag at the $r_{\rm eff}$-bin between 20 and 30 pc.

On the basis of the available data, I conclude that the turnover of the luminosity function

depends significantly on the effective radii of star clusters and that the slope of the varying $M_{\mathrm{V,TO}}$ is steeper for GCs than for EOs.

However, the edge in the luminosity function at $M_{\mathrm{V}} = -5.0$ mag (Fig. 3.12) for late-type and at $M_{\mathrm{V}} = -5.5$ mag (Fig. 3.14) for early-type galaxies indicates that the samples are fairly incomplete at very low luminosities. The true turnover of the EO luminosity function is therefore expected to be at even lower luminosities, which might lead to a steeper slope in the EO regime. Considerably larger and more complete datasets especially at low-luminosities, consisting of confirmed star clusters, are necessary to confirm the trend of the luminosity functions from GCs to EOs as shown in Fig. 3.16 and to substantiate the idea that this trend is a general feature of GCs and EOs in early- and late-type galaxies.

3.4.3 Spatial Distribution of EOs

In the Milky Way, the 11 EOs have galactocentric distances between 16 and 125 kpc with a median distance of 72 kpc. In contrast, the GCs of the Milky Way are at considerably lower distances. The median distance of the GCs is 4.8 kpc. For M31 five out of 20 EOs have projected distances smaller than 10 kpc and 11 EOs have projected distances larger than 20 kpc (Peacock et al. 2009; Huxor et al. 2008). The two EOs associated with M33 have projected distances of 12.4 and 28.6 kpc (Stonkutė et al. 2008; Huxor et al. 2009).

The most serious constraint of EO catalogs of galaxies outside the Local Group is the very limited field of view of the HST ACS instrument, as EOs at large distances from the Galaxy can only be spatially resolved by HST. The field of view of the ACS instrument is $202''$ and the pixel size is $0.05''$.

The dotted curve in Fig. 3.7a indicates the largest possible projected distance of a single HST ACS image centered on a galaxy at a given distance. It visualizes the area covered by one Hubble field. At small distances a couple of HST ACS fields are necessary to scan a galaxy for EOs, whereas at large distances the galaxy and part of the halo are completely covered by one HST ACS field.

At the distance of the Whirlpool Galaxy (M51) of about 8 Mpc, the field of view of $202''$ and the pixel size of $0.05''$ correspond to 7.8 kpc and 2 pc, respectively. While the pixel size is well suited to resolve EOs, a number of ACS images are needed to cover the entire galaxy. Figure 3.17 shows an image of the Digitized Sky Survey 2 (DSS2[2]) of M51 and the area covered by the mosaic of six ACS images used by Hwang & Lee (2008) to find EOs in M51, demonstrating that even six HST ACS images do not cover the entire stellar body of the interacting galaxy pair.

The HST mosaic of M51 covers an area of 15.7 kpc $\times$ 23.6 kpc. This coverage is well suited to detect EOs related to the stellar bodies of the two galaxies and EOs in the lower halo. While halo EOs at considerably larger distances from their host galaxies might be found by chance in projection to the main body of the host galaxy, the probability is relatively low. Considering a line-of-sight of ± 100 kpc, the volume covered by the HST mosaic is $15.7 \times 23.6 \times 200$ kpc^3, or $7.4 \cdot 10^4$ kpc^3. In contrast, the volume with a radius of 100 kpc, which would enclose the EOs, is $\frac{4}{3}\pi 100^3$ kpc^3 or $4.2 \cdot 10^6$ kpc^3. The HST mosaic of six ACS images covers less than 2% of the volume expected to contain EOs.

Figure 3.17 shows for comparison also the location of the Milky Way EOs, if the Milky Way would be seen face-on at the distance and the position of M51. The six most distant EOs of the Milky Way have large galactocentric distances between 70 and 125 kpc, or projected distances between 41 and 84 kpc in Fig. 3.17. This figure demonstrates that only 3 of 11 EOs would be located within the HST mosaic. Consequently, also a number of EOs of M51 are expected to

[2]The Digitized Sky Survey data used in this chapter have been taken from the ESO Archive, see http://archive.eso.org/dss/dss

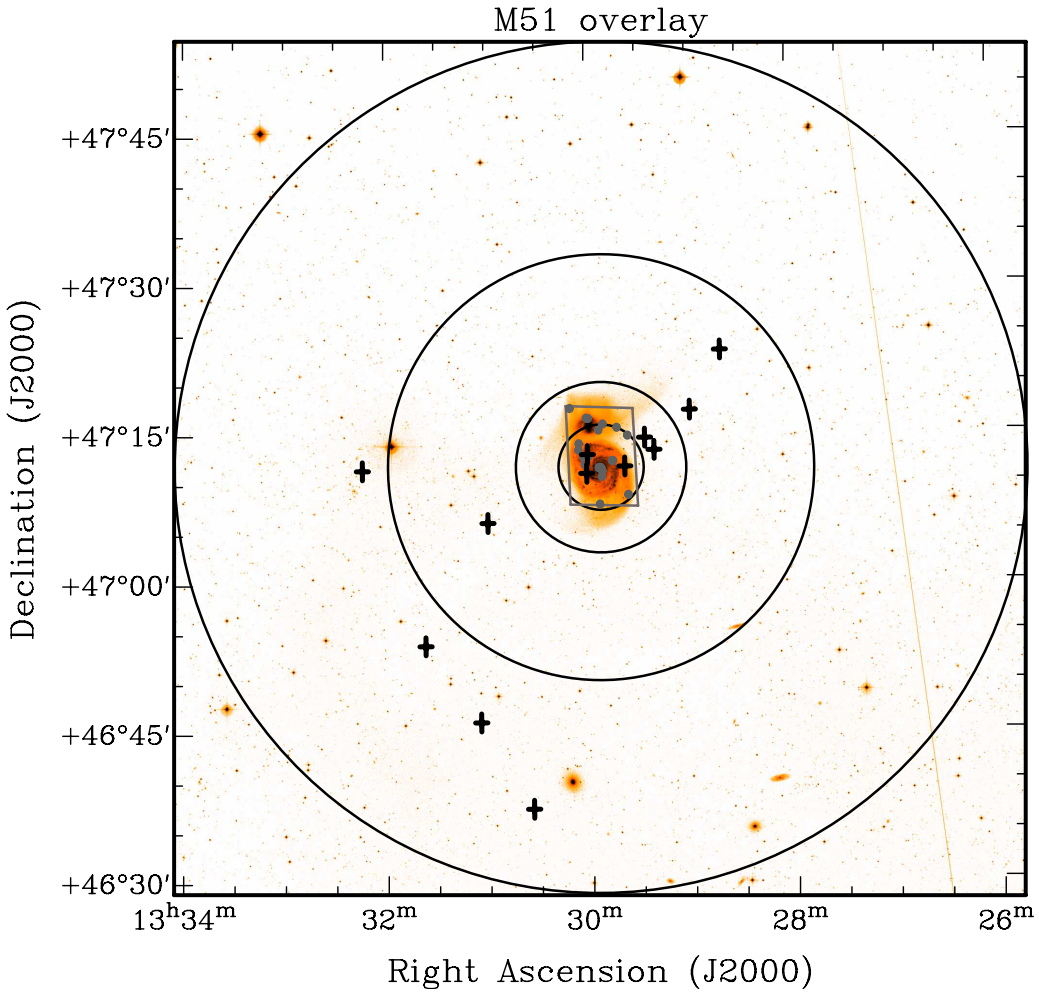

FIGURE 3.17— M51 EOs (grey dots) overlayed on a Digitized Sky Survey 2 (DSS2) image of M51. The grey lines indicate the size of the HST mosaic of six ACS images used by Hwang & Lee (2008) to find EOs in M51. The black circles indicate projected distances from M51 of 10, 20, 50, and 100 kpc. For comparison, the projected position of the Milky Way EOs, if the Milky Way would be seen face-on at the distance and the position of M51, are added as black crosses.

have considerably larger projected distances beyond the currently covered survey area.

In addition to EOs located in galactic halos, Larsen & Brodie (2000) and Brodie & Larsen (2002) have discovered a population of EOs co-rotating with the disk of the lenticular galaxy NGC 1023. These so-called faint fuzzies have similar structural parameters as halo EOs and are therefore not easily distinguishable from halo EOs projected onto the disk on the basis of imaging data alone. A fair fraction of EOs found in extragalactic surveys – especially those covering only the disk regions like the M51 survey (Hwang & Lee 2008) – might therefore be associated with the disks and not the halos of these galaxies.

The Hydra Cluster is located at a distance of about 47.2 Mpc. Misgeld et al. (2011) searched with ground based telescopes for massive star clusters in Hydra and detected and spectroscopically confirmed 118 objects with total V-band luminosities between $M_V = -9.7$ and -13.3 mag and projected distances between 3 and 300 kpc. The median projected distance is 44 kpc. Only 26 of the 118 stellar objects are located within two HST WFPC2 fields (see Fig. 3.18). 19 of the 26 objects are EOs and the remaining seven objects have effective radii between 8 and 10 pc. It is expected that also a large fraction of the remaining 92 objects in the outer halo are EOs. In addition, Fig. 7 of Misgeld et al. (2011) demonstrates that star clusters are not uniformly dis-

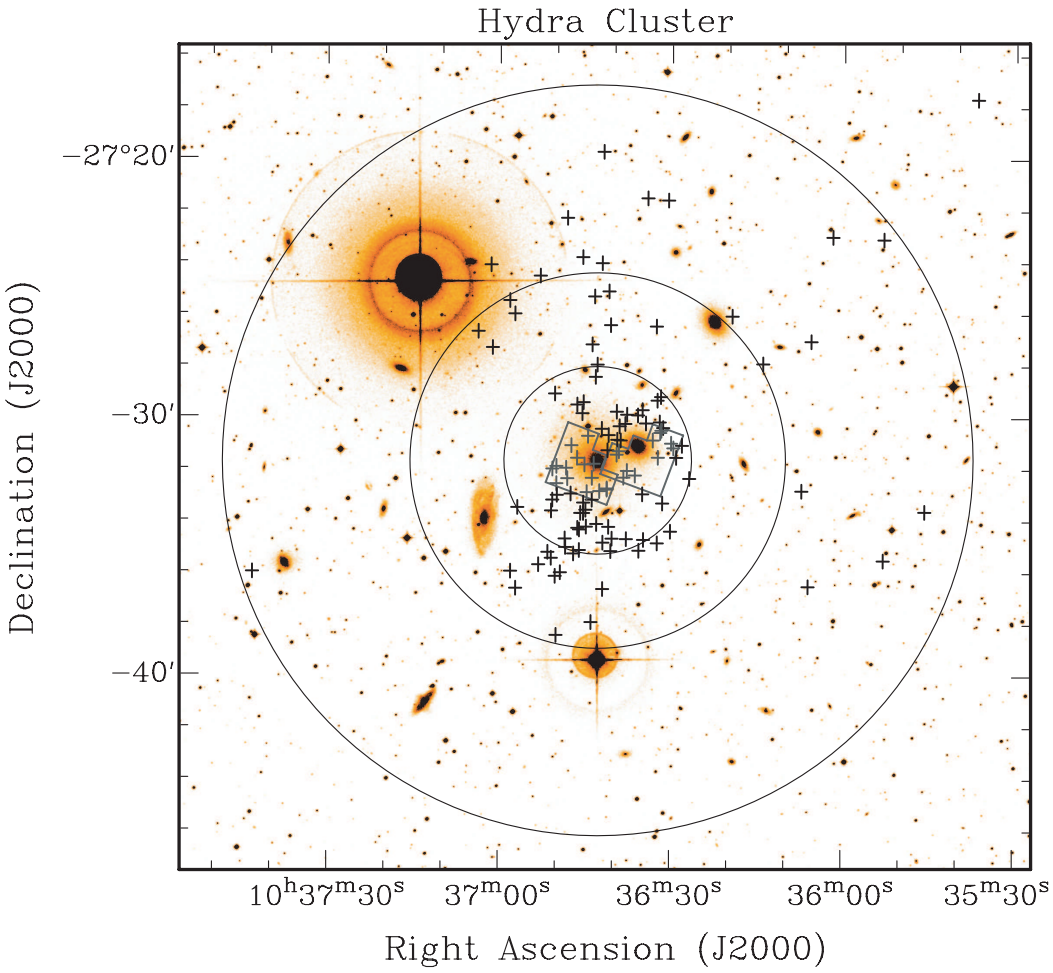

FIGURE 3.18— Spectroscopically confirmed star clusters (crosses) of the Hydra Cluster (Misgeld et al. 2011) overlaid on a DSS2 image of the Hydra Cluster. Only those clusters which are located within the two HST WFPC2 fields (marked by grey lines) have measured sizes. The black circles indicate projected distances from the central galaxy NGC3311 of 50, 100, and 200 kpc.

tributed in the halo. While some halo fields contain several UCDs, other fields have no UCDs at all. Consequently, random samples of small fields in a halo cannot be used to extrapolate to the entire population.

Another example is the giant elliptical galaxy NGC 4365, which was covered by eight HST ACS fields (Blom et al. 2012). Seven HST ACS fields provide a very good coverage of the inner 35 kpc of the galaxy. In their central HST field, Blom et al. (2012) found 681 GC and 30 EO candidates, while the six HST fields surrounding the central field have on average 216 GCs and 26 EOs. The results demonstrate that the number density of compact clusters decreases rapidly towards larger projected distances while the number of EOs per HST field is almost constant. In addition, Blom et al. (2012) searched for star clusters outside the HST fields with ground based telescopes and concluded that the cluster system extends out to projected radii of about 135 kpc and contains about three times the number of clusters as the HST fields. Consequently, there are several hundreds of EOs expected in the halo of NGC 4365 outside the HST fields.

The three examples M51, NGC 4365, and the Hydra Cluster are typical for the entire sample of galaxies with EOs. The vast majority of the studied galaxies have a reasonable coverage of the main stellar body, but a very poor coverage of the halo by HST observations. Only very distant galaxies like the elliptical galaxy ESO325-G004 in the galaxy cluster Abell S0740 at a Galactic distance of 143 Mpc are well covered (including the halo) by one HST ACS field.

However, the pixel size of the HST ACS of $0.05''$ corresponds to a linear scale of about 35 pc at this distance, which is too coarse to resolve rather compact EOs.

A considerably larger fraction of the halos of early- and late-type galaxies needs to be covered by HST observations to allow for a conclusive view on the spatial distribution of EOs and possible differences between early- and late-type galaxies.

3.5 Summary & Conclusions

I searched the available literature to compile the largest possible catalog of star clusters with effective radii larger than 10 pc. As there is no clear distinction between ECs and UCDs, both types of objects are called extended stellar dynamical objects – abbreviated "EOs" – in this thesis.

In total, I compiled a catalog of 835 EOs of which 171 were found associated with late-type galaxies and 664 EOs associated with early-type galaxies. The main results presented in this chapter are

1. EOs cover a luminosity range from about $M_{\rm V} = -4$ to -14 mag. However, almost all EOs brighter than $M_{\rm V} = -10$ mag are associated with giant elliptical galaxies.

2. For all luminosities, extended objects are found with effective radii between 10 pc and an upper size limit, which shows a clear trend: the higher the luminosity the larger is the upper size limit. This upper limit increases from about 25 pc at $M_{\rm V} = -5$ mag to about 100 pc at $M_{\rm V} = -14$ mag.

3. The 178 confirmed EOs cover the same region in the $r_{\rm eff}$ vs. $M_{\rm V}$ space and show the same trends of increasing size with increasing luminosities as the 657 candidate EOs.

4. For all luminosities, the majority of EOs have effective radii which are only slightly larger than 10 pc. The median effective radius of EOs in late-type and early-type galaxies is 13.2 pc and 14.2 pc, respectively.

5. The effective radii are increasing with increasing total luminosity of the host galaxy.

6. For late-type galaxies there is no trend of the EO luminosities with the luminosity of the host galaxies, while for early-type galaxies there is a trend that the most luminous EOs are found associated with the most luminous galaxies.

7. EOs and GCs form a coherent structure in the $r_{\rm eff}$ vs. $M_{\rm V}$ parameter space, which is well separated from the distribution of early-type dwarf galaxies, except for the rare species of compact elliptical galaxies. Especially at the low-luminosity end considerably deeper observations are needed to answer the question, whether the prominent gap between ECs and dSph galaxies is real.

8. For both EOs associated with early- and late-type galaxies, the EO luminosity functions peaks at about -6.5 mag, which is roughly one magnitude fainter than the turnover of the GC luminosity function. The turnover luminosities decrease continuously between compact GCs and EOs for increasing effective radii. Considering the very low surface brightness of faint and extended EOs, a fair fraction of very extended and faint EOs is most likely below the detection limit of extragalactic surveys. The true turnover of the EO luminosity function might therefore be at even lower luminosities.

While this study presents the to day largest catalog of EOs, it suffers from substantial incompleteness, predominantly with respect to the coverage of the galactic halos, but also with

respect to varying detection limits and the fairly low number of confirmed objects. Larger and more complete datasets and additional information on parameters like metallicities, mass-to-light ratios and age-estimates are necessary to draw final conclusions on the origin of EOs, which in turn has the potential to shed light on the cosmologically important phase of galaxy formation.

4

The Application of the Merging Star Cluster Scenario on Faint Fuzzies and NGC 2419

In this chapter, I perform numerical simulations to test the merging star cluster formation scenario on two types of well studied EOs: the faint fuzzy star clusters (FFs) in the disk of the lenticular galaxy NGC 1023 and the Milky Way EO NGC 2419.
For the FFs in NGC 1023 the CC models have an initial configuration based on the observed mass-size relation of CCs observed in the disk of the spiral galaxy M51. They are placed on various orbits in a galactic potential derived for NGC 1023. All computations in the tidal field end up with stable objects containing 10 to 60% of the initial CC mass after an integration time of 5 Gyr. A conversion to V-band luminosities demonstrates that the resulting objects cover the observed range of FFs. Moreover, the simulated objects show effective radii between 3.6 and 13.4 pc, in good agreement with those observed for FFs.
For the Milky Way cluster NGC 2419 I performed numerical simulations of 27 different CC models moving on a highly eccentric orbit in the Galactic halo. I vary the CC mass, the CC size, and the initial distribution of star clusters in the CC to analyze the influence of these parameters on the resulting merger objects. In all cases, the vast majority of star clusters merged into a stable object. The derived parameters mass, absolute V-band luminosity, effective radius, velocity dispersion and the surface brightness profile are, for a number of models, in good agreement with those observed for NGC 2419. Despite the large range of CC sizes, the effective radii of the merger objects are constrained to a relatively small interval. A turnover in the $r_{\rm eff}$ vs. $M_{\rm encl}$ space leads to degenerate states, i.e. relatively compact CCs can produce an object with the same structural parameters as a more massive and larger CC. In consequence, a range of initial conditions can form a merger object comparable to NGC 2419.
In both environments, i.e. the strong gravitational field within a galactic disk and the weak tidal field within the outer Galactic halo, the CC models evolve into stable objects having structural parameters comparable to those of the observed objects. I conclude that the merging star cluster scenario has the potential to explain the existence of EOs in various environments.

4.1 Introduction

In this chapter, I investigate the merging star cluster scenario in two different environments – the strong gravitational field within a galactic disk and the weak tidal field of a galactic halo outside the main stellar body of a host galaxy.

The merging star cluster scenario was first proposed by Kroupa (1998) who studied the dy-

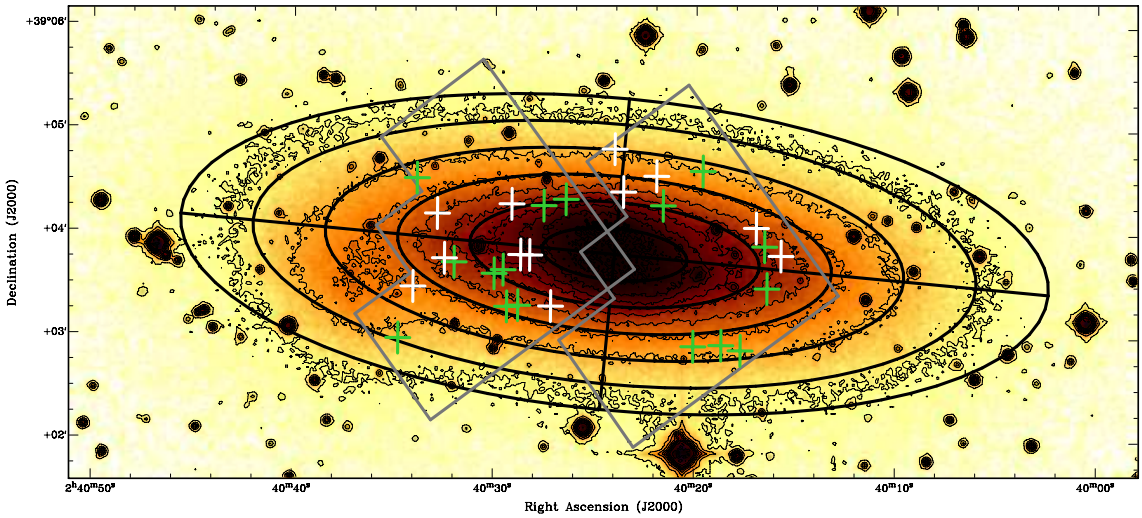

FIGURE 4.1— Digitized Sky Survey (DDS) image of the galaxy NGC 1023. The grey lines mark the WFPC2 HST images used by Larsen & Brodie (2000) to detect FFs. Confirmed FFs with observed radial velocities (Brodie & Larsen 2002; Burkert et al. 2005) are shown as green crosses, the remaining FF candidates from Larsen & Brodie (2000) as white crosses. The orientation of the disk of NGC 1023 is indicated in black. The black ellipses represent galactocentric radii of 2, 4, 6, 8, 10, and 12 kpc.

namical evolution of CCs observed to be forming in the interacting Antennae galaxies. Kroupa (1998) showed that in CCs with a high density of star clusters significant merging of star clusters is likely. The merging process leads to a massive star cluster – the merger object – in the central part of a CC. The star clusters not participating in the merging process are lost due to the tidal field of the host galaxy. The merging star cluster scenario provides a mechanism for the formation of massive and extended star clusters (e.g. Fellhauer & Kroupa 2002a,b).

I focused on two well observed examples of disk and halo EOs and performed two comprehensive computational parameter studies. Both examples offer a good observational database to allow for a detailed comparison of simulations and observations. Section 4.2 studies the dynamical evolution of CCs in the disk of the galaxy NGC 1023 to verify whether the FFs discovered by Larsen & Brodie (2000) can be explained as evolved, merged CCs. In Sect. 4.3 I investigate the merging star cluster scenario as a possible origin of the EO NGC 2419, which is located in the outer halo of the Milky Way.

The proposed formation scenario starts with newly born complexes of star clusters with orbital parameters consistent with the observations. I model the dynamical evolution of various CCs for several gigayears and compare the parameters of the resulting merger objects with the observed parameters of the faint fuzzies in the galaxy NGC 1023 and the Milky Way EO NGC 2419. I do not, however, consider the process which formed the CCs in the first place, i.e. the interaction of two galaxies, as this would increase the complexity of the simulations and add more degrees of freedom making the interpretation of the results difficult.

4.2 Faint Fuzzy Star Clusters in NGC 1023

4.2.1 Introduction

Larsen & Brodie (2000) studied the GC system of the nearby (9.8 Mpc, Ciardullo et al. 2002) lenticular galaxy NGC 1023 and discovered a clear bimodal color distribution. The average effective radius of the blue GCs in NGC 1023 is about 2.0 pc, while the average radius of red compact GCs is slightly smaller ($r_{\rm eff} \sim 1.7$ pc), as observed also for other galaxies (e.g. Larsen et al. 2001a). The sizes for the blue clusters are as large as $r_{\rm eff} = 7$ pc, while the sizes of the

red clusters extend up to $r_{\rm eff} = 18$ pc. The objects larger than 7 pc are generally fainter than the red compact objects. The spatial distribution of these objects appears to be associated with the lenticular disk of NGC 1023 (see Fig. 4.1). Due to their faint and extended appearance this new star cluster population was called "faint fuzzies" (FFs).

Brodie & Larsen (2002) performed spectroscopic observations of the GCs in NGC 1023 and found that the FFs show a clear sign of co-rotation with the galactic disk, while the compact red GCs show no sign of rotation, suggesting that the FFs are indeed a separate population associated with the disk of NGC 1023. They averaged all FF spectra to achieve a high enough signal-to-noise ratio to estimate the age of these objects that appears to be older than 7 – 8 Gyr. Burkert et al. (2005) further analyzed the distribution and radial velocities of the FFs in NGC 1023 and suggested that they are the remnants of a past gravitational interaction forming a ringlike structure. Further observations also discovered FFs in the lenticular galaxy NGC 3384 (Brodie & Larsen 2002), the dwarf irregular galaxy NGC 5195 (Lee et al. 2005), a number of galaxies of the Virgo cluster (Peng et al. 2006), and the lenticular galaxy NGC 1380 (Chies-Santos et al. 2007).

4.2.2 Set-up of the Numericial Simulations and Varied Parameters

This section describes the specific set-up of the numerical simulations and the varied parameters of the FF study. A detailed description of the numerical method is given in Chapter 2.

4.2.2.1 An Estimate of the Gravitational Potential of NGC 1023

NGC 1023 is a disk-dominated SB0-galaxy at a distance of 9.8 Mpc (Ciardullo et al. 2002) in the constellation Perseus. It shows a well behaved rotation in the inner part, while the observed radial velocities in the outer regions appear to be more random (Noordermeer et al. 2008). This behavior is most likely related to a past interaction, which transformed the galaxy into an SB0 lenticular galaxy. Noordermeer et al. (2008) argue that the photometry of the disk is consistent with a passive fading since 1 Gyr after the galaxy lost its gas.

However the exact rotation curve is not required for the simulations because a good guess of the potential is sufficient to study the evolution of CCs. In my simulations NGC 1023 is represented by an analytical potential, which consists of a disk, a bulge, and a halo component. For objects moving on circular orbits within the galactic plane, the results of the simulations depend mainly on the total force at a given distance, but very weakly on the exact choice of bulge, disk, and halo parameters. I use the observed velocities in the center of the galaxy from Simien & Prugniel (1997) to constrain the rotation curve in the region of $R_{\rm gal} < 4$ kpc and assume a flat rotation curve for the outer part (Fig. 4.2).

The disk of NGC 1023 is modeled by a Miyamoto-Nagai potential (Miyamoto & Nagai 1975) with $M_{\rm d} = 5.5 \cdot 10^{10}$ M$_\odot$, $a_{\rm d} = 2.8$ kpc, and $b_{\rm d} = 0.2$ kpc. The bulge is represented by a Hernquist potential (Hernquist 1990) with $M_{\rm b} = 0.7 \cdot 10^{10}$ M$_\odot$ and $a_{\rm b} = 1.1$ kpc. The halo is a logarithmic potential with $v_0 = 170$ km s^{-1} and $r_{\rm halo} = 5.0$ kpc (see Sect. 2.1.4 for details on the gravitational potential).

For this project, I neglected heating sources from non-axisymmetric components like giant molecular clouds (GMC) and spiral arms. This is a good approximation for compact objects with masses of about 10^5 M$_\odot$. Gieles et al. (2006) demonstrated that star clusters with such masses cannot be destroyed by individual encounters with GMCs, if the extended nature of GMCs is taken into account. Close encounters between GMCs and massive star clusters act as tidal heating on the clusters. The corresponding disruption time is much larger than the integration time of the simulations presented in this chapter. Gieles et al. (2007) analyzed the effect of spiral arms passages on the evolution of star clusters and found a disruption time of the order 100 Gyr for massive clusters with masses comparable to FFs.

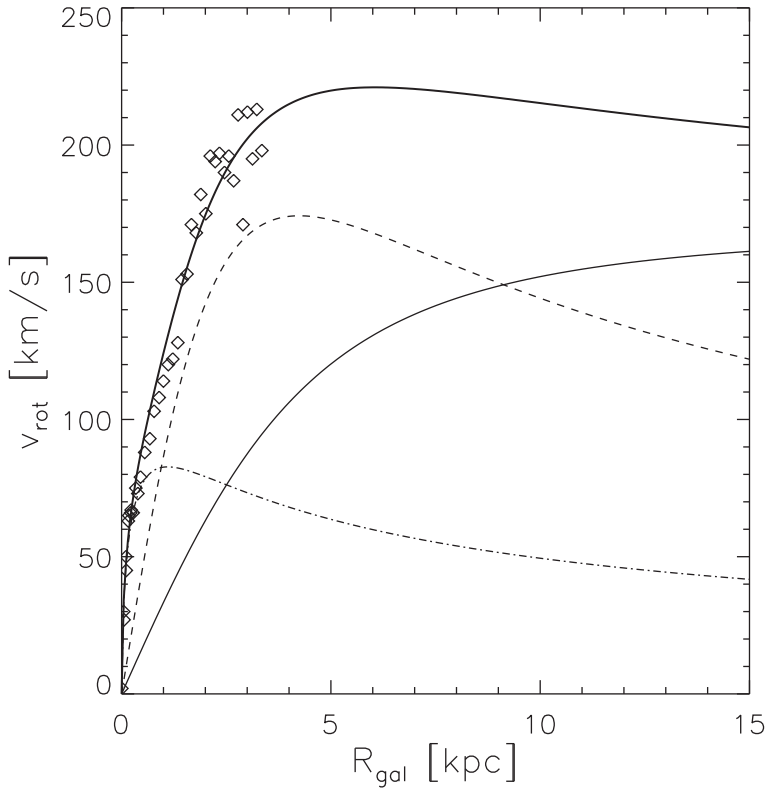

FIGURE 4.2— Rotation curve of a model of the galaxy NGC 1023 used for the numerical simulations: the circular velocity is derived from the chosen analytical potential consisting of a Miyamoto-Nagai disk potential (dashed line), a spherical bulge potential (dashed dotted line) and a logarithmic halo (solid line). Summing up the three components of the potential yields the total circular velocity (bold solid line). The diamond symbols represent the data available for the inner part (Simien & Prugniel 1997).

4.2.2.2 Initial Configuration of the Cluster Complexes

Bastian et al. (2005) derived a mass-radius relation for the CCs in M51 that constrains the parameter space for my CC models. They found eleven CCs with ages younger than 10 Myr in the disk of M51 that have sizes between 85 and 240 pc, and cover a mass range of $0.3 - 3 \cdot 10^5$ $M_\odot$. Most of these CCs show a massive concentration of clusters potentially merging in their centers and a couple of isolated clusters in their vicinity (see Figs. 2 and 3 in Bastian et al. 2005). The size of a CC was defined by Bastian et al. (2005) as the point where the measured color is equal to that of the background stars in the disk. This radius corresponds to the cutoff radius of my models.

The spatial distribution of the CCs is connected to the spiral arms of the disk. Most complexes are found at the outer edges of the spiral arms. The CCs show a mass-radius relation comparable to the one of the progenitor giant molecular clouds. Bastian et al. (2005) estimated a very high star formation efficiency within the CCs, using the CO-to-H_2 conversion factor for M51 from Boselli et al. (2002) and a Salpeter IMF (Salpeter 1955). Due to the high star formation efficiency, gas expulsion has only little influence on the evolution of the merging CCs (Fellhauer & Kroupa 2005b). Consequently, the distorting effect of gas expulsion was not considered in the simulations.

I chose the parameters of CCs in the simulations such that the models cover the two extremes (CC_H and CC_L) of the Bastian relation (Fig. 4.3) and a point in between (CC_M).

The star clusters building up the CCs in my simulations are Plummer spheres (Plummer 1911; Kroupa 2008). The density distribution of the spheres is truncated at $R^{\rm SC}_{\rm cut} = 5\, R^{\rm SC}_{\rm pl}$. Each

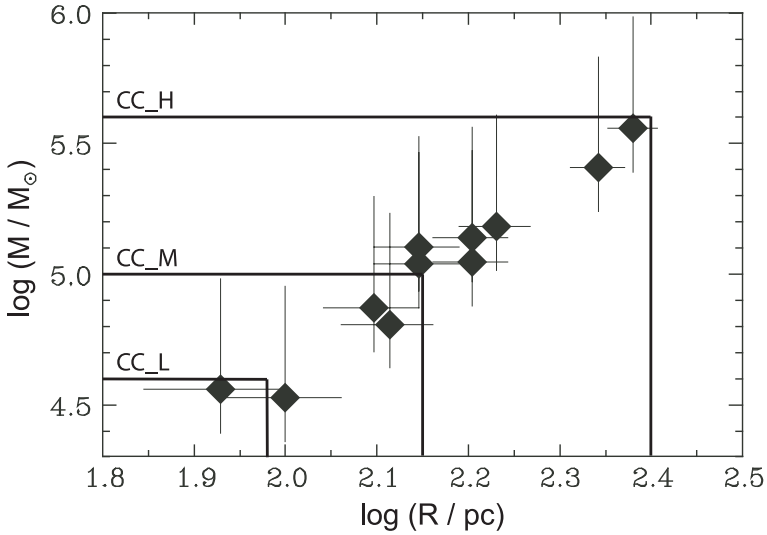

FIGURE 4.3— The mass versus radius relation for CCs in M51 (Bastian et al. 2005). The eleven CCs, indicated by diamonds, have sizes between about 85 and 240 pc and cover a mass range of $0.3 - 3 \cdot 10^5$ $M_\odot$. The size of the complex is defined as the radius where the CC is still clearly distinguishable from the background light of the galaxy. It is the cutoff radius for my models, which cover the high- and low-mass end of the Bastian relation (CC_H and CC_L) and a point in between (CC_M).

star cluster consists of $N_0^{\rm SC} = 100\,000$ particles. The CC models are diced according to a Plummer distribution with masses and radii taken from the Bastian relation (Fig. 4.3). My models resemble the CCs observed by Bastian et al. (2005) with a high density concentration in their centers.

The number of star clusters comprising the CC is fixed to $N_0^{\rm CC} = 20$ for most models (one additional large CC containing 80 star clusters is also considered). In order to get comparable starting conditions for the models CC_H, CC_M, and CC_L, I use the parameter $\alpha = R_{pl}^{SC}/R_{pl}^{CC}$ (see Sect. 2.1.1.3), which is a measure of how densely the CC is filled with star clusters for an equal number $N_0^{\rm CC}$ of star clusters. In general high values of α accelerate the merging process because the star clusters already overlap in the center of the CC, whereas low values hamper the merging process. I choose a medium value of $\alpha = 0.08$, which leads to a reasonable range of the Plummer radii of the individual star clusters. The chosen initial parameters are displayed in Table 4.1.

The individual high resolution grids cover an entire star cluster, whereas the medium resolution grids of every star cluster embed the whole initial CC. The grids were also scaled to get the same relative resolution for all models. All grids contain $64 \times 64 \times 64$ grid cells.

4.2.2.3 Orbital Parameters

I investigated the evolution of a CC configuration in three different mass regimes for circular orbits at galactic distances of $R_{\rm gal} = 2$, 3, 5, 8, and 12 kpc (Sect. 4.2.3.1) and an eccentric orbit with galactic distances between 3 and 8 kpc (Sect. 4.2.3.2). The orbital parameters are given in Table 4.2. The circular velocities, $v_{\rm circ}$, at the different galactic distances, $R_{\rm gal}$, were derived from the rotation curve of NGC 1023 (Fig. 4.2). The orbital periods lie between 70 and 350 Myr. The coordinate system is chosen such that the disk of NGC 1023 lies in the x-y-plane.

4.2.3 Results

I carried out 25 different numerical simulations to study the influence of varying initial CC conditions and orbital parameters. The computations are presented in the following way.

TABLE 4.1— Initial cluster complex and star cluster parameters

Model	Cluster Complex				Star Cluster			
	N_0^{CC} [a]	M^{CC} [b]	R_{cut}^{CC} [c]	R_{pl}^{CC} [d]	N_0^{SC} [e]	M^{SC} [f]	R_{cut}^{SC} [g]	R_{pl}^{SC} [h]
		($M_\odot$)	(pc)	(pc)		($M_\odot$)	(pc)	(pc)
CC_H_20	20	$4 \cdot 10^5$	250	50	100 000	$2 \cdot 10^4$	20.0	4.0
CC_H_80	80	$4 \cdot 10^5$	250	50	100 000	$5 \cdot 10^3$	10.0	2.0
CC_M_20	20	$1 \cdot 10^5$	141.5	28.3	100 000	$5 \cdot 10^3$	11.5	2.3
CC_L_20	20	$4 \cdot 10^4$	95.5	19.1	100 000	$2 \cdot 10^3$	7.5	1.5

[a] Number of star clusters comprising the CC.
[b] Initial CC mass.
[c] Cutoff radius of the CC.
[d] Plummer radius of the CC.
[e] Number of star cluster particles.
[f] Initial mass of a star cluster.
[g] Cutoff radius of a star cluster.
[h] Plummer radius of a star cluster.

TABLE 4.2— Parameters for the five circular orbits

R_{gal} [a]	v_{circ} [b]	T_{orb} [c]	CC_H_20		CC_M_20		CC_L_20	
			r_t^{CC} [d]	β [e]	r_t^{CC}	β	r_t^{CC}	β
(kpc)	(km s^{-1})	(Myr)	(pc)		(pc)		(pc)	
2	174	70.4	42.1	5.9	26.5	5.3	19.6	4.9
3	202	91.1	50.0	5.0	31.5	4.5	23.2	4.1
5	220	139.7	66.5	3.8	41.9	3.4	30.9	3.1
8	219	224.3	91.3	2.7	57.5	2.5	42.4	2.3
12	212	348.5	122.4	2.0	77.1	1.8	56.8	1.7

[a] Distance to the center of NGC 1023.
[b] Circular velocity obtained from the rotation curve (Fig. 4.2).
[c] Orbital period.
[d] Tidal radius of CC at $t = 0$.
[e] β-parameter at $t = 0$.

In Sects. 4.2.3.1 and 4.2.3.2, I investigate the evolution of CCs in three mass regimes (CC_H, CC_M, CC_L) on circular and eccentric orbits. In Sects. 4.2.3.3 and 4.2.3.4, I consider different initial configurations and a maximal model with 80 star clusters. For comparison, computations without an external gravitational field are presented in Sect. 4.2.3.5.

4.2.3.1 Simulations on Circular Orbits

I have performed 15 simulations on circular orbits holding the initial star cluster configuration and the number of star clusters in the complex fixed. The CC masses were restricted to the high- and low-mass end (CC_H_20 and CC_L_20) of the Bastian relation and a value in between (CC_M_20).

The timescale of the merging process is very short. The merger object forms within a few crossing times of the CC. In all cases the merging leads to a stable final object. The properties of the merger objects at $t = 5$ Gyr are displayed in Table C.1 of Appendix C. The number of merged star clusters varies from 10 to 16. The number increases with galactic distance as the

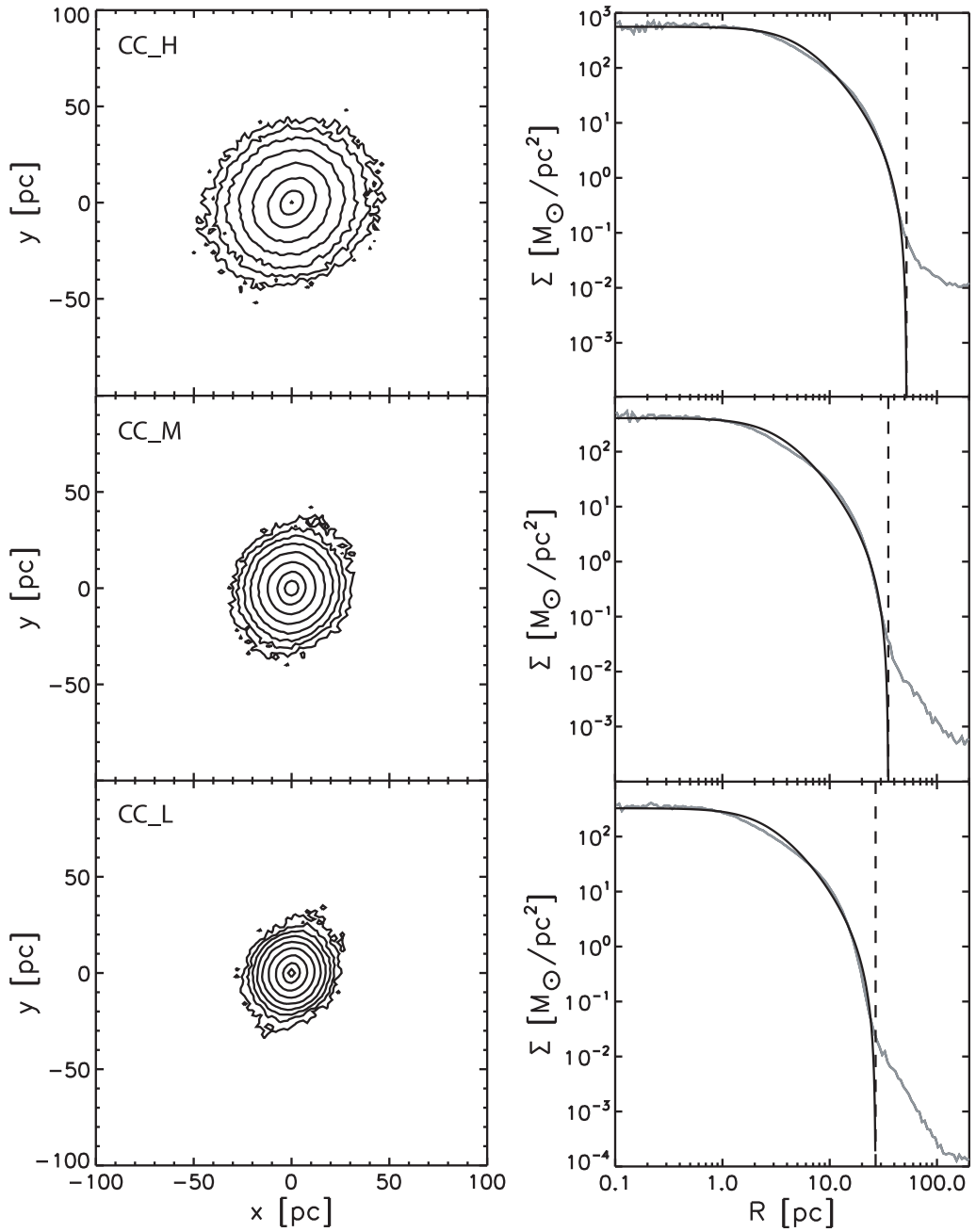

FIGURE 4.4— **Left:** Contour plots at $t = 5$ Gyr on the x-y-plane for the computations CC_H_5_20, CC_M_5_20 and CC_L_5_20 at a galactic distance of $R_{\rm gal} = 5$ kpc. The lowest contour level corresponds to 5 particles per pixel. The pixel size is 2 pc. This yields $0.25\ {\rm M}_\odot\ {\rm pc}^{-2}$ (CC_H), $0.0625\ {\rm M}_\odot\ {\rm pc}^{-2}$ (CC_M) and $0.025\ {\rm M}_\odot\ {\rm pc}^{-2}$ (CC_L). The contour levels increase further by a factor of 3. **Right:** Surface density profile corresponding to the contour plots of CC_H_5_20, CC_M_5_20 and CC_L_5_20. The profiles are fitted by King models. The dashed vertical lines denote the fitted tidal radii.

influence of the tidal field becomes weaker.

In all cases I calculate surface density profiles and fit these by a King profile (King 1966). Three exemplary final merger objects after 5 Gyr are shown in Fig. 4.4 as contour plots on the x-y-plane and as corresponding surface density profiles.

The tidal radii of the merger object obtained from the King fits vary from $r_{\rm t}^{\rm MO} = 18.8$ pc for simulation CC_L_2_20 at $R_{\rm gal} = 2$ kpc to $r_{\rm t}^{\rm MO} = 88.9$ pc for CC_H_12_20 at $R_{\rm gal} = 12$ kpc (Appendix C, Table C.1). The enclosed mass of the merger objects is defined as the mass within

the tidal radius. After 5 Gyr 20 to 60% of the initial CC mass is bound to the merger object. The half-mass radius is the radius of the sphere, wherein half of the mass is enclosed. However, as observers can only derive a projected half-mass radius, I calculate also a projected value defined as the projected radius within which half of the mass is included. The projected half-mass radius is slightly smaller than the three-dimensional half-mass radius (see Table C.1) and corresponds to the observed effective radius, $r_{\rm eff}$.

The enclosed masses and half-mass radii are increasing with galactic distance, $R_{\rm gal}$, leading to small compact merger objects at $R_{\rm gal} = 2$ kpc and more extended massive merger objects at $R_{\rm gal} = 12$ kpc. The comparison of the different models CC_H_20, CC_M_20, and CC_L_20 demonstrates that the tidal field has the largest impact on model CC_H_20 impeding the merging process. An estimate of the influence of the tidal field is given by the parameter β (see Eq. 2.31 of Sect. 2.1.4), which is the fraction of the cutoff radius, $R_{\rm cut}^{\rm CC}$, of the CC and its tidal radius, $r_{\rm t}^{\rm CC}$. The larger the value of β, the larger the impact of the tidal field. The values for the initial tidal radii of the CCs and the corresponding parameter β of the individual models are shown in Table 4.2. The β-values are decreasing from model CC_H_20 to CC_L_20 and from small galactic distances of $R_{\rm gal} = 2$ kpc to large distances of $R_{\rm gal} = 12$ kpc. Therefore model CC_H_20 suffers a higher percental mass loss than simulations CC_M_20 and CC_L_20 and for each simulation the impact of the tidal force on the CC is larger for small galactic distances.

4.2.3.2 Cluster Complexes on an Eccentric Orbit

I performed three simulations on eccentric orbits to test the influence of the orbit on the properties of the final merger object. The orbit was chosen such that the distance of the CC to the center of NGC 1023 varies between 3 and 8 kpc. The orbital period is about 100 Myr. Again the computations were performed for the three different mass regimes (Fig. 4.3). Table C.1 shows the properties of the final merger objects.

For simulation CC_H_ecc_20 the value for the enclosed mass lies between the values obtained for the models on circular orbits at $R_{\rm gal} = 2$ and 3 kpc. The half-mass and tidal radii agree more with those obtained for the circular orbit at 2 kpc. The properties of the final objects of simulations CC_M_ecc_20 and CC_L_ecc_20 are similar to those of the circular orbit at 3 kpc. Thus, for the eccentric orbit the perigalactic distance determines the overall properties of the final merger object.

4.2.3.3 Different Initial Configurations

For comparison, I also performed simulations for two additional initial configurations in the medium mass regime (CC_M_5_c2_20 and CC_M_5_c3_20). Different seeds were used for the random number generator to generate two different initial configurations having the same input parameters as CC_M_20 (Table 4.1). The initial configurations vary considerable due to the low number of star clusters constituting the CC. The models were placed on a circular orbit at a distance of $R_{\rm gal} = 5$ kpc.

The two configurations also lead to a fast merger within the first few CC crossing times. After 5 Gyr the final objects have masses of $2.5 \cdot 10^4$ M$_\odot$ (CC_M_5_c2_20) and $2.9 \cdot 10^4$ M$_\odot$ (CC_M_5_c3_20). The corresponding projected half-mass radii are 5.5 and 5.6 pc (Table C.1). In the case of configuration CC_M_5_c2_20 16 star clusters have merged. Whereas for configuration CC_M_5_c3_20 the number of merged star clusters is only 13 although its final mass is larger. The final mass of a merger object does not necessarily scale with the number of merged star clusters as the newly formed object looses considerable mass on its orbit around the center of NGC 1023. The final parameters of the merger objects are slightly smaller than those of the corresponding model CC_M_5_20 (see Sect. 4.2.3.1). While the enclosed mass and the half-mass radius of a merger object depend considerably on the initial configuration, the general order of magnitude stays the same.

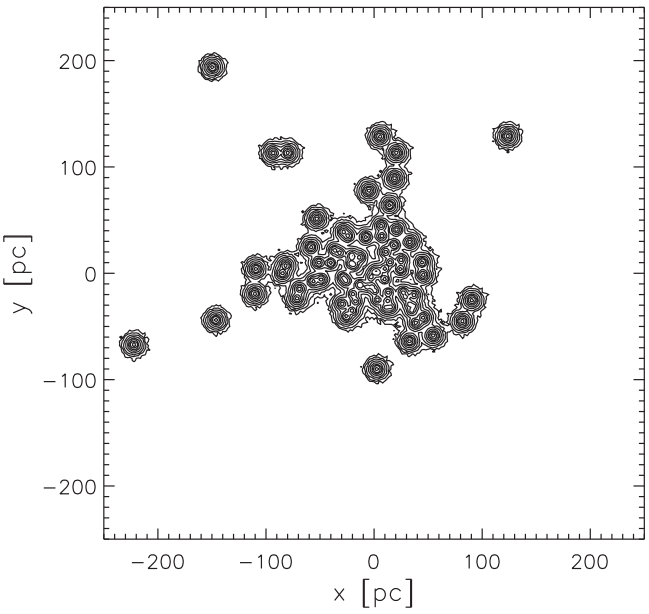

FIGURE 4.5— Contour plot on the x-y-plane of the initial distribution of the big computation CC_H_5_80 with 80 star clusters. The lowest contour level corresponds to 5 particles per pixel. The pixel size is 2 pc. This yields $0.0625\ M_\odot\ pc^{-2}$. The contour levels increase further by a factor of 3.

4.2.3.4 A Model with a Large Number of Star Clusters

In this section I consider a maximal CC with $N_0^{CC} = 80$ star clusters (CC_H_80). The parameters of the initial CC model are presented in Table 4.1. The CC parameters mass, Plummer radius, and cutoff radius are identical with the parameters of model CC_H_20. Due to the larger number of star clusters of model CC_H_80, the individual star clusters have lower masses, which are comparable to the star cluster masses of simulation CC_M_20. The maximal CC is placed only on one circular orbit at a distance of $R_{gal} = 5$ kpc, because the computation is very time-consuming. The initial star cluster distribution is displayed in Fig. 4.5 as a contour plot on the x-y-plane.

Within the first 500 Myr a massive merger object forms and the unmerged star clusters align along the orbit (Fig. 4.6). There is still a close companion star cluster as a satellite of the merger object.

The evolution of the merger object with time is shown in Fig. 4.7 as contour plots. The snapshots were taken at $t = 0.5$, 1, 3, and 5 Gyr. At $t = 500$ Myr (top panel) the merger object has already formed. It is very extended and shows prominent tidal arms. The major mass loss occurs within the first gigayear. Later the merger object becomes more compact and its tidal arms are less pronounced. After 5 Gyr the merger object has reached an almost stable state. The mass loss is small and the fitted tidal radius hardly changes any more.

Table C.1 lists the properties of the final merger object of computation CC_H_5_80 which resulted from the merger of 32 star clusters. The merger object retains only 9% of the initial CC mass and has an effective radius of 8.5 pc. For comparison, the merger object of the corresponding computation CC_H_5_20 with an initial number of SCs of 20 keeps a higher fraction of 29% of the initial CC mass and has a larger effective radius of 10.1 pc.

4.2.3.5 Cluster Complexes without External Gravitational Field

For comparison, I performed simulations without an external tidal field (i.e. $R_t = \infty$) for the three models CC_H_20, CC_M_20, CC_L_20, and the maximal configuration with 80 star clusters, CC_H_80. In case of the three computations with varying CC masses 17 out of 20 star

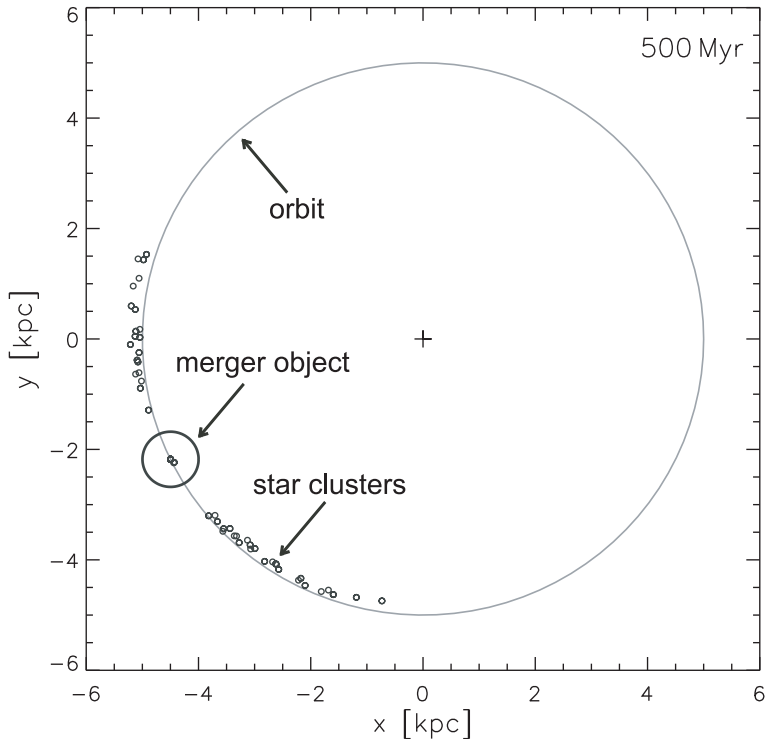

FIGURE 4.6— Illustration of the spatial distribution of the star clusters of computation CC_H_5_80 after 500 Myr. The CC moves on a circular orbit around the center of NGC 1023 (cross). It consists of a large merger object and a leading and trailing arm of about 50 unmerged star clusters. The circles indicate the positions but not the sizes of the star clusters and the merger object.

clusters merge within the first 500 Myr. After 5 Gyr 19 (CC_H_inf_20, CC_M_inf_20) and 20 (CC_M_inf_20) star clusters have merged, respectively, leading to merger objects with effective radii of 22.5 pc (CC_H_inf_20), 12.7 pc (CC_M_inf_20) and 9.0 pc (CC_L_inf_20) which contain more than 90% of the initial CC mass (Table C.1).

For the simulation with 80 star clusters (CC_H_inf_80) the merging process is considerably slower. In the first 500 Myr 46 star clusters merge. The newly formed merger object is surrounded by several unmerged star clusters which are found preferentially in its close vicinity. During the next 500 Myr another 23 star clusters merge into the merger object. After 5 Gyr 79 star clusters have merged resulting in a final object with an effective radius of 45.6 pc and a mass of $3.9 \cdot 10^5$ $M_\odot$ corresponding to 97.5% of the initial CC mass.

The individual star clusters in CC_H_80 have basically the same relative velocities as in CC_H_20, but four times lower masses. This reduces the probability of merging considerably. The resulting longer merging timescale provides the gravitational field more time to tear clusters off the complex. This explains the lower number of merged star clusters and the relatively low mass in the case of the corresponding model within a tidal field.

4.2.4 Discussion and Conclusions

Figure 4.8 summarizes the major properties for all computations. The CC models CC_H_20, CC_M_20, and CC_L_20 were placed on circular orbits at five different distances whereas the big configuration CC_H_5_80 with 80 star clusters and the two additional configurations of CC_M_5_20 were only run on a circular orbit at $R_{\rm gal} = 5$ kpc. The three computations on an eccentric orbit are indicated by dashed lines ranging from 3 to 8 kpc. I plotted the enclosed mass, $M_{\rm encl}$, and the effective radius, $r_{\rm eff}$, against the galactic distance, $R_{\rm gal}$, from the center of NGC 1023.

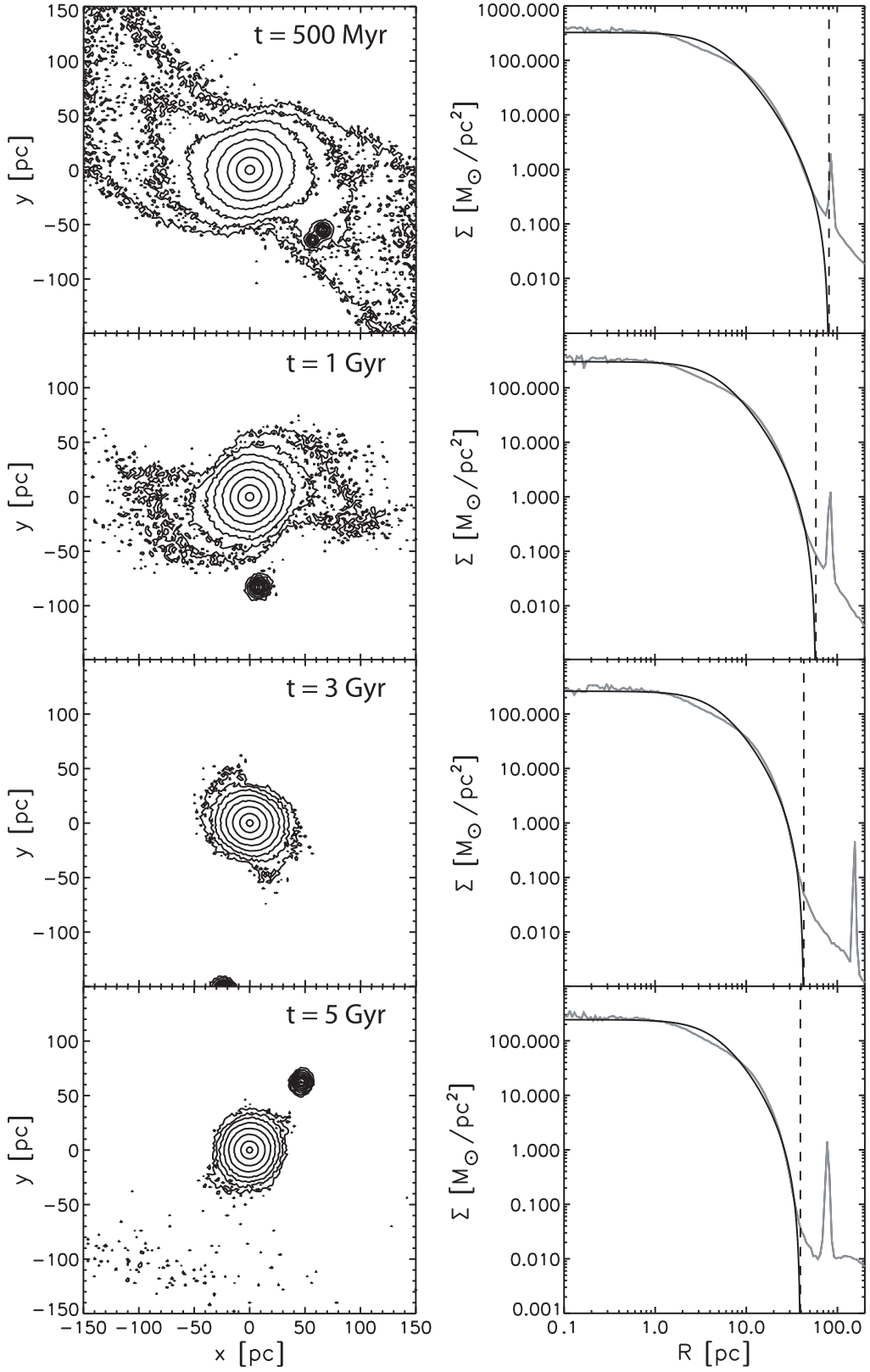

FIGURE 4.7— Time evolution of the merger object in simulation CC_H_5_80 at a galactic distance of $R_{\rm gal} = 5$ kpc. **Left:** Contour plots on the x-y-plane displayed at $t = 0.5$, 1, 3, and 5 Gyr. The lowest contour level corresponds to 5 particles per pixel. The pixel size is 2 pc. This yields 0.0625 $M_\odot$ pc^{-2}. The contour levels increase further by a factor of 3. **Right:** Surface density profiles corresponding to the contour plots. The profiles are fitted by King models. The dashed vertical lines denote the fitted tidal radii.

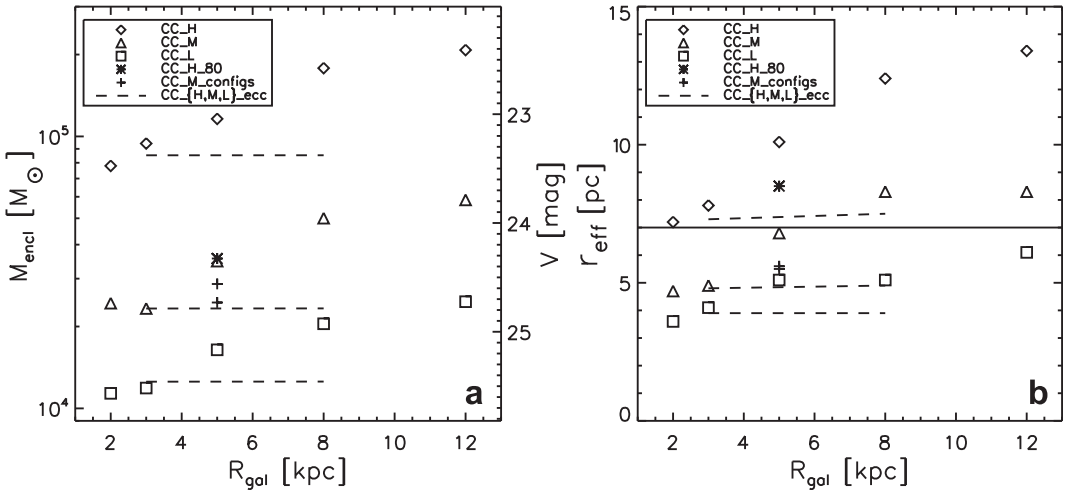

FIGURE 4.8— **a:** Enclosed mass, $M_{\rm encl}$, versus galactic distance, $R_{\rm gal}$, for all computations. Simulation CC_H_20, CC_M_20, and CC_L_20 were performed for different distances of $R_{\rm gal} = 2$, 3, 5, 8, and 12 kpc whereas the big computation CC_H_5_80 with 80 clusters and the two additional configurations of CC_M_5_20 were only run at a distance of $R_{\rm gal} = 5$ kpc. The eccentric orbit models cover a radius range of 3 – 8 kpc and are therefore plotted as dashed lines. **b:** Effective radius, $r_{\rm eff}$, against galactic distance, $R_{\rm gal}$, for all simulations. The horizontal line at 7 pc indicates the lower size limit for FFs defined by Larsen & Brodie (2000).

The enclosed masses were converted into V-band luminosities to allow for direct comparison with the observed data, using the formula

$$V = M_{V,solar} - 2.5 \cdot \log_{10}(M_{\rm encl}/x) + 29.97, \tag{4.1}$$

where $M_{\rm V,solar} = 4.83$ mag is the absolute solar V-band luminosity, $M_{\rm encl}$ the mass of the merger object, x the mass-to-light ratio and the value of 29.97 the distance modulus derived from the planetary nebula luminosity function (Ciardullo et al. 2002). As no observational constraints on the M/L-ratio of FFs are available, I chose a mass-to-light ratio of $x = 2.3$, which was observed by Pryor & Meylan (1993) for 56 GCs in the Milky Way.

Figure 4.8a shows the enclosed mass, $M_{\rm encl}$, as well as the corresponding V-band luminosity versus the galactic distance, $R_{\rm gal}$. The V-band luminosities of the merger objects cover a range from 22.4 mag to 25.6 mag. Larsen & Brodie (2000) detected FFs in the luminosity range 21.4 to 25.0 mag[1], with a median of 23.6 mag, but only one FF is brighter than 22.5 mag. The luminosities of the simulated merger objects are therefore in very good agreement with the observed luminosities of FFs.

Figure 4.8b shows the effective radius, $r_{\rm eff}$, of the merged CCs versus galactic distance, $R_{\rm gal}$. The effective radii for all simulations range between 3.6 and 13.4 pc. The effective radius criterion of $r_{\rm eff} \geq 7$ pc from Larsen & Brodie (2000) is added as a horizontal line. The merger objects of model CC_H_20 (circular and eccentric) and the big simulation CC_H_5_80 with 80 star clusters lie clearly above the radius limit whereas the computations of model CC_M_20 exceed the limit only at galactic distances of $R_{\rm gal} \geq 8$ kpc. The lowest mass merger objects have effective radii below 7 pc. However, the effective radius criterion of $r_{\rm eff} \geq 7$ pc is not to be taken as a definite limit but more as a reference value, because below $r_{\rm eff} = 7$ pc it is not possible to distinguish FFs from compact red GCs. About 80% of the FFs observed by Larsen & Brodie (2000) have effective radii below 14 pc. The median of the observed effective radii is 10.7 pc. The results are therefore in good agreement with observations.

[1]Larsen & Brodie (2000) did not consider objects below 25 mag. Their approximate 50% completeness limit was 24.5 mag.

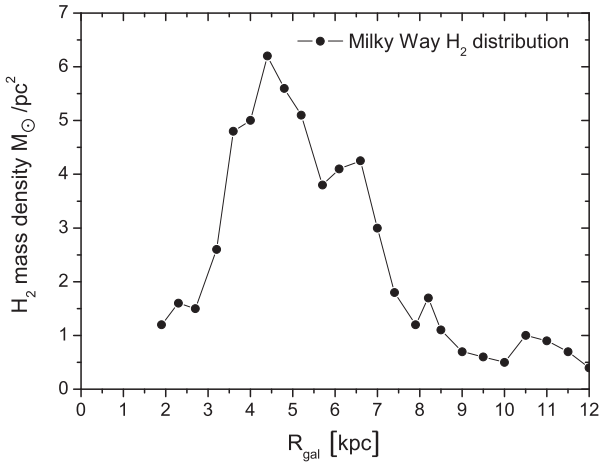

FIGURE 4.9— Radial mass density distribution of molecular clouds in the Milky Way as observed by Dame (1993).

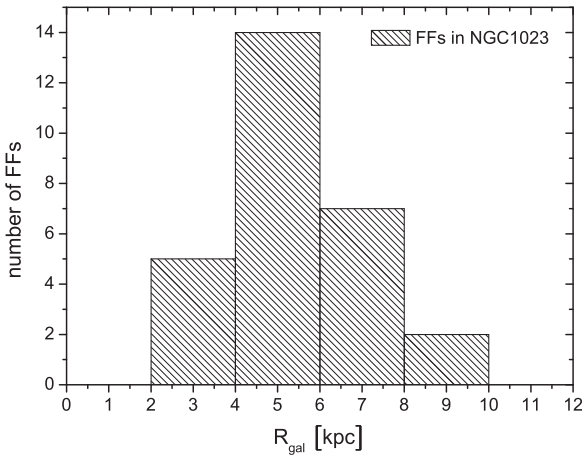

FIGURE 4.10— Radial distribution of the number of FFs per radial bin as observed by Larsen & Brodie (2000).

The simulations presented in this chapter demonstrate that CCs from the high-mass end of the Bastian relation evolve into FF-like objects. The merger objects of the high-mass CC models on orbits larger than 5 kpc would be classified as EOs. My formation scenario suggests that FFs are the remnants of merged CCs formed in spiral arms. NGC 1023 has a prominent bar that extents up to about 3 kpc (Debattista et al. 2002). In barred spiral galaxies, spiral arms usually start where the bar ends (e.g. Elmegreen & Elmegreen 1982). The observed absence of FFs in the inner 3 kpc of NGC 1023 is therefore consistent with the formation scenario presented in this chapter. The Milky Way, which is also a barred galaxy with a size comparable to NGC 1023, has most of its giant molecular clouds in the disk between Galactic radii 3 to 8 kpc, with a peak between 4 and 5 kpc (Dame 1993, see Fig. 4.9). The mass-radius relation found for young massive CCs in M51 is comparable to the corresponding relation for giant molecular clouds in M51 (Bastian et al. 2005). Consequently, the radial distribution of FFs should in general follow the radial distribution of giant molecular clouds. In NGC 1023 FFs were found between projected galactic radii 3 kpc $\leq R_{\rm gal} \leq 10$ kpc, with a clear peak at a projected radius of about 5 kpc (see Fig. 4.10). The observed radial distribution of FFs is therefore in good agreement with the one expected from my formation scenario.

The measured velocities from Brodie & Larsen (2002) confirm the general co-rotation of the FFs with the disk of NGC 1023. Burkert et al. (2005) argued that the annular distribution of FFs on the sky and some deviations from the rotation curve of NGC 1023 indicate that the FFs form a ringlike structure with a mean radius of 5 kpc potentially formed during a past tidal encounter. In their model, FFs are on highly eccentric orbits spanning the entire range between 3 and 8 kpc. In my model, FFs are associated with the former spiral arms of NGC 1023, as the CCs in M51 are associated with the spiral arms of the disk. FFs should therefore follow the rotation of the disk of NGC 1023, which was probably disturbed during a past interaction that transformed NGC 1023 into a lenticular galaxy. However, due to the very low luminosities, the observational uncertainties of the velocities are relatively large. Burkert et al. (2005) re-observed two FFs from Brodie & Larsen (2002). The new measurements of these clusters yield 539 ± 21 and 676 ± 13 km s^{-1}, while the previous measurements found 514 ± 8 and 725 ± 17 km s^{-1}, respectively. These uncertainties are too large for definite statements about deviations from circular orbits.

Brodie & Larsen (2002) averaged all FF spectra shifted to zero velocity to achieve a high enough signal-to-noise ratio to estimate the age of these objects that appears to be older than

TABLE 4.3— Observational parameters of NGC 2419

	BC [a]	B [b]	MvdM [c]	H [d]	H [e]
Absolute V-band luminosity M_V [mag]	-9.28	-9.4	-9.31	-9.58	-9.42
Total mass [f] [10^6 $M_\odot$]	0.90	1.01	0.93	1.19	1.03
Central surface brightness μ_V [mag arcsec^{-2}]	19.61	19.55	19.44	19.83	19.67
Core radius r_c [pc]	7.8	7.8	7.9	8.57	7.7
Effective radius r_{eff} [pc]	19.2	23.5	19.9	17.88	21.38
Tidal radius r_t [pc]	190	174	204	214	180

[a] Baumgardt et al. (2009).
[b] Bellazzini (2007).
[c] McLaughlin & van der Marel (2005).
[d] Harris (1996).
[e] Harris (1996, 2010 edition).
[f] Using the mass-to-light ratio of 2.05 from Baumgardt et al. (2009).

7 – 8 Gyr. Moreover, they used the same integrated spectrum to derive a mean metallicity of [Fe/H] $= -0.58 \pm 0.24$ and a mean alpha-to-iron ratio [α/Fe] between $+0.3$ and $+0.6$ compared to solar values. Enhanced alpha-to-iron ratios are usually associated with rapid, burst-like star formation on short timescales. Indeed, the 5 to 8 Myr old CCs observed by Bastian et al. (2005) show a low age spread, indicating that the stellar mass of the order of 10^5 $M_\odot$ has been formed in a burst-like event.

In summary, the simulated merger objects based on the observed mass-radius relation from Bastian et al. (2005) resemble the observed parameters mass/luminosity, size, and spatial distribution of FFs in NGC 1023 very well. The merging of young massive CCs is therefore a likely formation scenario for FFs.

The FFs need to be further analyzed with respect to additional and more precise kinematical data to allow for a reliable estimate of their orbits. In addition, age estimates, metallicities, and alpha-to-iron ratios are needed for individual FFs. The scatter and the variation of these parameters with galactic distance will shed light on the FF evolution and further test whether the discussed formation scenario is valid.

4.3 The Milky Way EO NGC 2419

4.3.1 Introduction

The Milky Way and its satellite galaxies have a combined GC system of 182 objects. In total, 18 of these objects (or 10%) are EOs (see Sect. 1.1). The vast majority of the EOs are fainter than about $M_V = -7$ mag, only NGC 2419 has a high luminosity of about $M_V = -9.4$ mag. While all GCs with a comparable luminosity are quite compact, NGC 2419 has a projected half-light or effective radius of about 20 pc. The structural properties of NGC 2419 derived by various authors are displayed in Table 4.3. NGC 2419, located at (l,b)=(180.°4, 25.°2), is one of the most metal-poor GCs with a metallicity of [Fe/H] $= -2.12$ (Harris 1996) at a Galactocentric distance of about 91.5 kpc and a heliocentric distance of 82.4 kpc (Harris 1996). NGC 2419 shows a single stellar population with an age of 12 to 13 Gyr (Salaris & Weiss 2002).

Figure 4.11 shows all known EOs associated with late-type galaxies (see Chapter 3 for details on the EO sample). It is evident that NGC 2419 has a rather isolated location in the M_V vs. r_{eff} space. Only two EOs associated with the Sombrero galaxy (M104) are brighter than NGC 2419. However, M104 is a rather unusual late-type galaxy having a huge bulge and a

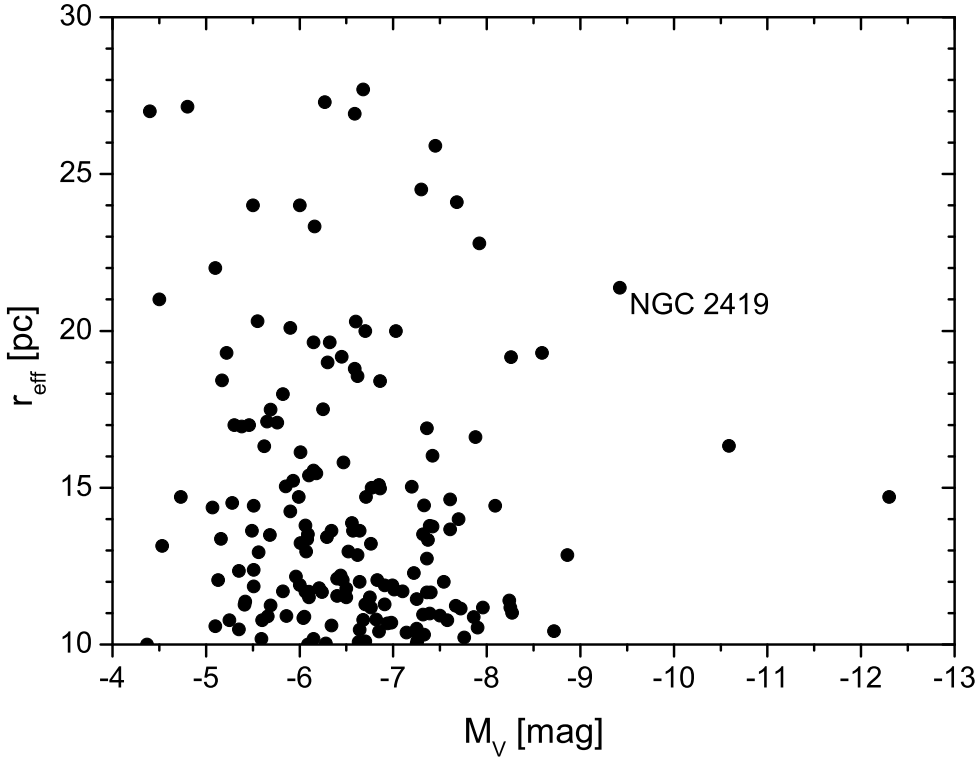

FIGURE 4.11— Overview of EOs in late-type galaxies (see Chapter 3). NGC 2419 is in a rather isolated position.

large globular cluster system, which are similar to those of giant elliptical galaxies (Larsen et al. 2001b).

The unusual size and mass of NGC 2419 led to the speculation that NGC 2419 is not a GC, but the stripped core of a dSph galaxy captured by the Milky Way (e.g. van den Bergh & Mackey 2004). A stripped core, however, is expected to show multiple stellar populations from the progenitor galaxy. In contrast, Ripepi et al. (2007) demonstrated that NGC 2419 shows no sign of multiple stellar populations and concluded that NGC 2419 is not a stripped core of a dwarf galaxy. Ripepi et al. (2007) also found that NGC 2419 is an Oosterhoff II cluster. They concluded that an extragalactic origin of NGC 2419 is unlikely as the GCs of the Galactic dwarf galaxies usually show parameters between Oosterhoff types I and II. On the other hand, differences between NGC 2419 and typical values of GCs associated with Galactic dwarf spheroidal galaxies do not rule out an extragalactic origin of NGC 2419 per se. For instance, five out of twelve GCs from the LMC are Oosterhoff II clusters (Catelan 2009).

4.3.2 Set-Up and Varied Parameters

4.3.2.1 Orbit of NGC 2419

4.3.2.1.1 Gravitational Potential of the Milky Way

In my computations the Milky Way is represented by an analytical potential, which consists of a disk, a bulge, and a halo component (see Sect. 2.1.4). The disk of the Milky Way is modeled by a Miyamoto-Nagai potential (Miyamoto & Nagai 1975), with $M_{\rm d} = 1.0 \cdot 10^{11}$ M$_\odot$, $a_{\rm d} = 6.5$ kpc, and $b_{\rm d} = 0.26$ kpc. The bulge is represented by a Hernquist potential (Hernquist 1990), with $M_{\rm b} = 3.4 \cdot 10^{10}$ M$_\odot$ and $a_{\rm b} = 0.7$ kpc. The halo is a logarithmic potential, with $v_0 = 186.0$ km s^{-1} and $r_{\rm halo} = 12.0$ kpc. This set of parameters gives a realistic rotation curve for the Milky Way.

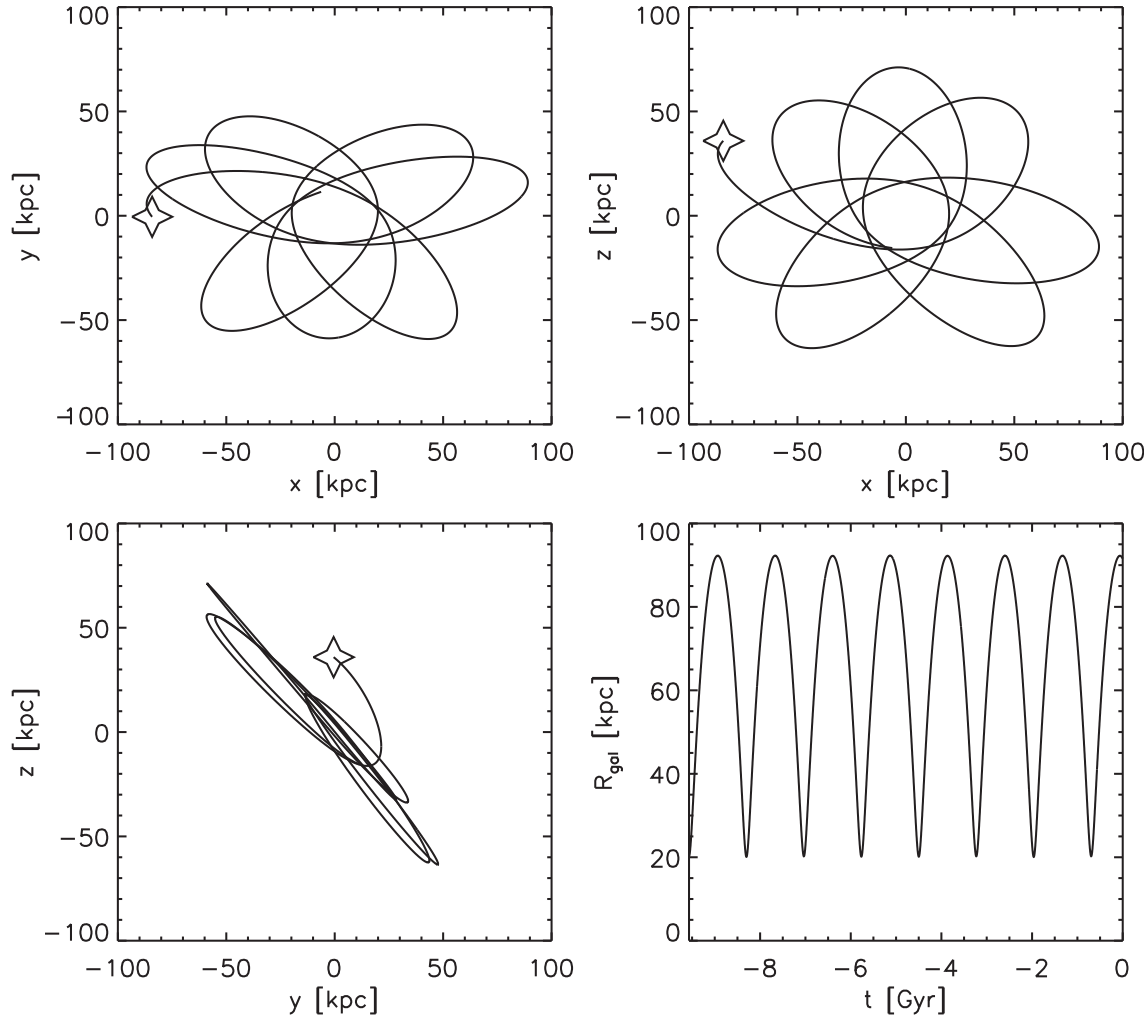

FIGURE 4.12— The orbit of NGC 2419 traced back from its current position and projected to the x-y-, the x-z-, and the y-z-plane The stars indicate the observed current position of NGC 2419. **Bottom right:** The distance of NGC 2419 to the Galactic center. The orbital period is about 1.3 Gyr.

4.3.2.1.2 Orbital Parameters

The calculation of an orbit for NGC 2419 requires, next to the spatial coordinates, a good knowledge of the actual velocity vector of the cluster. As no proper motion measurements for NGC 2419 are available, the orbit cannot be properly fixed without major assumptions.

King (1962) suggested that the tidal radius of a GC is determined by the orbital position with the highest gravitational force, which is the perigalacticon. van den Bergh (1995) used this method to estimate a perigalactic distance of 20 kpc for NGC 2419. While this method provides only a very rough estimate of the perigalactic distance, I use it to narrow down the range of possible orbits.

NGC 2419 is one of the outermost Galactic GCs at a distance of $R_{\rm gal} = 91.5$ kpc (Harris 1996). The very large distance and the observed low (heliocentric) negative radial velocity of $v_{\rm hel} = -20.3$ km s^{-1} (Baumgardt et al. 2009), which corresponds to a Galactic-standard-of-rest velocity of $v_{\rm GSR} = -26.8$ km s^{-1}, suggests that NGC 2419 is close to its apogalacticon.
I choose a velocity vector for NGC 2419 in a way that it

- is consistent with the observed radial velocity,
- produces an orbit between Galactic radii 20 and about 92 kpc,

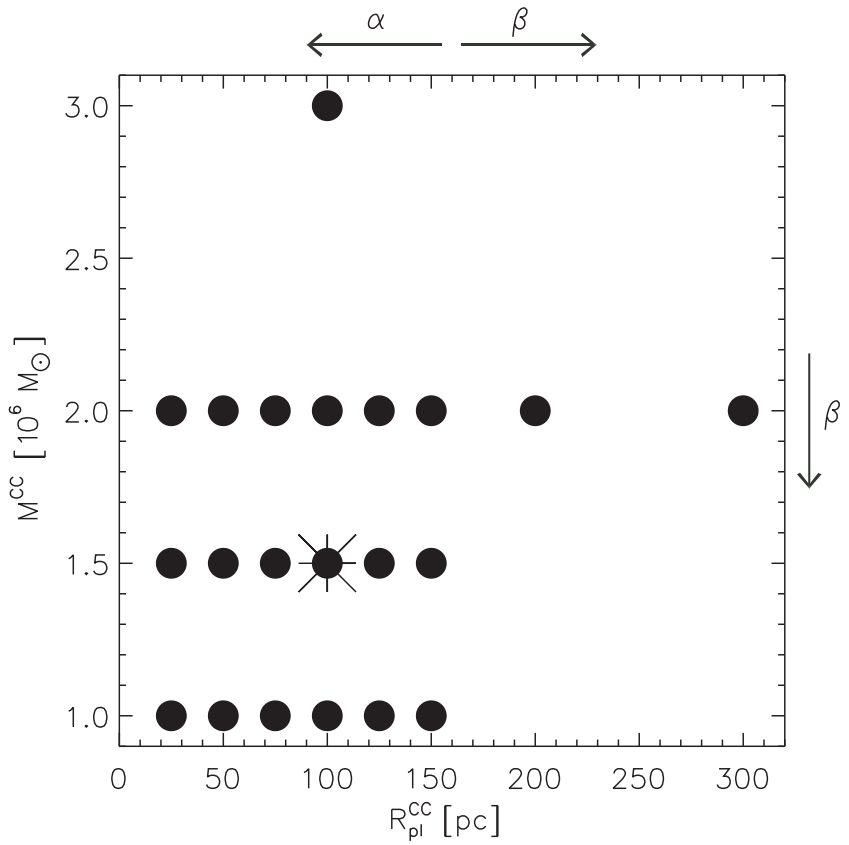

FIGURE 4.13— The parameter range covered in the M^{CC} vs. R_{pl}^{CC} space. The arrows indicate the increase of the parameters α and β (see Sect. 4.3.3.2). The circle with the additional asterisk marks the values of M^{CC} and R_{pl}^{CC} of the model, where the initial distribution of star clusters within the CC was varied (see Sect. 4.3.3.3).

- is neither a polar orbit nor an orbit within the Galactic plane.

The velocity vector (v_x, v_y, v_z) = (45 km s^{-1}, -56 km s^{-1}, 47 km s^{-1}) will be used as the current velocity vector of NGC 2419 for calculating the orbit.[2]

Figure 4.12 shows the orbit of NGC 2419 calculated back in time using the Milky Way potential as given in Sect. 4.3.2.1.1. The orbital period is about 1.3 Gyr. The CC will most likely be formed during the first perigalactic passage of the parent galaxy. However, as the calculated objects will not change significantly after about 7 Gyr of evolution (see Sect. 4.3.3.1), I do not start at $t = -12$ Gyr (the age estimate of NGC 2419) in order to cut down the computing time. For all numerical simulations I choose the perigalactic passage at $t = -9.568$ Gyr as a starting point.

4.3.2.2 *Initial Configuration of the Cluster Complex and Model Parameters*

The CC models consist of $N_0^{CC} = 20$ star clusters and are diced according to a Plummer distribution (Plummer 1911; Kroupa 2008). The cutoff radius, R_{cut}^{CC}, of the CC is four times the Plummer radius, R_{pl}^{CC}. The initial velocity distribution of the CC models is chosen such that the CC is in virial equilibrium. A detailed description of the generation of initial coordinates (space and velocity) for Plummer models is given in Sect. 2.1.1.1.

The individual star clusters building up the CCs in my simulations are Plummer spheres with a Plummer radius of $R_{pl}^{SC} = 4$ pc and a cutoff radius of $R_{cut}^{SC} = 20$ pc. Each star cluster has

[2]The coordinate system is chosen such that the disk of the Milky Way lies in the x-y-plane with origin at the Galactic center.

TABLE 4.4— Initial cluster complex and star cluster parameters

	Parameter range
Star Cluster (SC)	
Number of star cluster particles, N_0^{SC}	100 000
Initial SC mass, M^{SC} [10^5 $M_\odot$]	0.5 – 1.5
Plummer radius of the SC, R_{pl}^{SC} [pc]	4
Cutoff radius of the SC, R_{cut}^{SC} [pc]	20
Cluster Complex (CC)	
Number of star clusters, N_0^{CC}	20
Initial CC mass, M^{CC} [10^6 $M_\odot$]	1.0 – 3.0
Plummer radius of the CC, R_{pl}^{CC} [pc]	25 – 300
Cutoff radius of the CC, R_{cut}^{CC} [pc]	100 – 1200
α-parameter	0.160 – 0.013

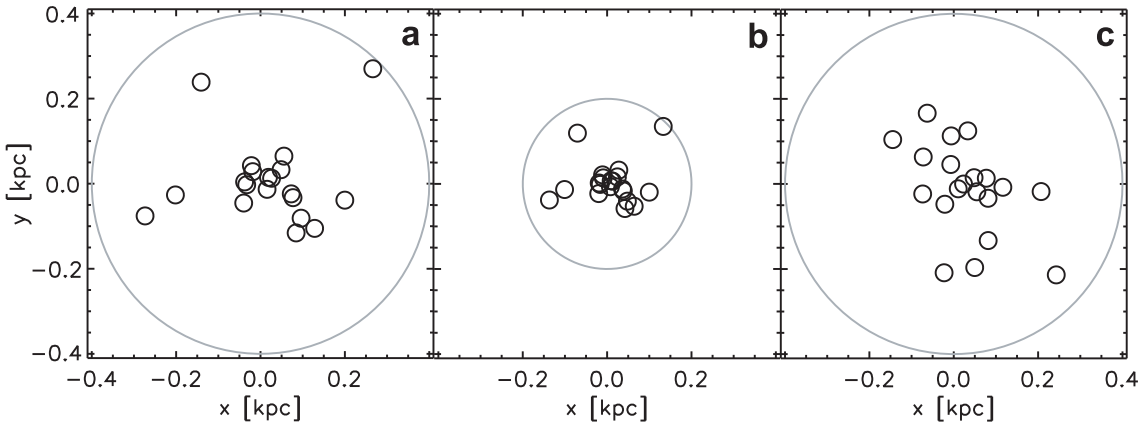

FIGURE 4.14— Three exemplary initial spatial distributions of star clusters (small circles with radius R_{cut}^{SC}) in a CC (surrounding circle with radius R_{cut}^{CC}) projected onto the x-y-plane. Model M_1_1.5_50 (b) is a scaled version of M_1_1.5_100 (a) only differing in Plummer radius, R_{pl}^{CC}. Some star clusters do already overlap in the center at the beginning. Model M_4_1.5_100 (c) has a less concentrated distribution of clusters than M_1_1.5_100.

a mass of $M^{SC} = 0.05\ M^{CC}$ and consists of $N_0^{SC} = 100\,000$ particles. The velocity distribution of the individual star clusters is chosen to be initially in virial equilibrium.

In total, I considered 27 different models (see Tables 4.4 and C.2), which are denoted by M_x_y_z, where x is the number of the initial configuration, i.e. the detailed distribution of the individual star clusters in the CC, y is the CC mass, M^{CC}, in units of 10^6 $M_\odot$, and z is the CC Plummer radius, R_{pl}^{CC}, in pc. Figure 4.13 visualizes the CC parameter range covered in the M^{CC} vs. R_{pl}^{CC} space.

Figure 4.14 illustrates the different initial distributions. Figure 4.14a and b are the same initial distribution of star clusters that were scaled according to their R_{pl}^{CC}, while Fig. 4.14c shows a less concentrated distribution of star clusters.

In order to get a good resolution of the star clusters, the grids were chosen to contain $128 \times 128 \times 128$ grid cells.

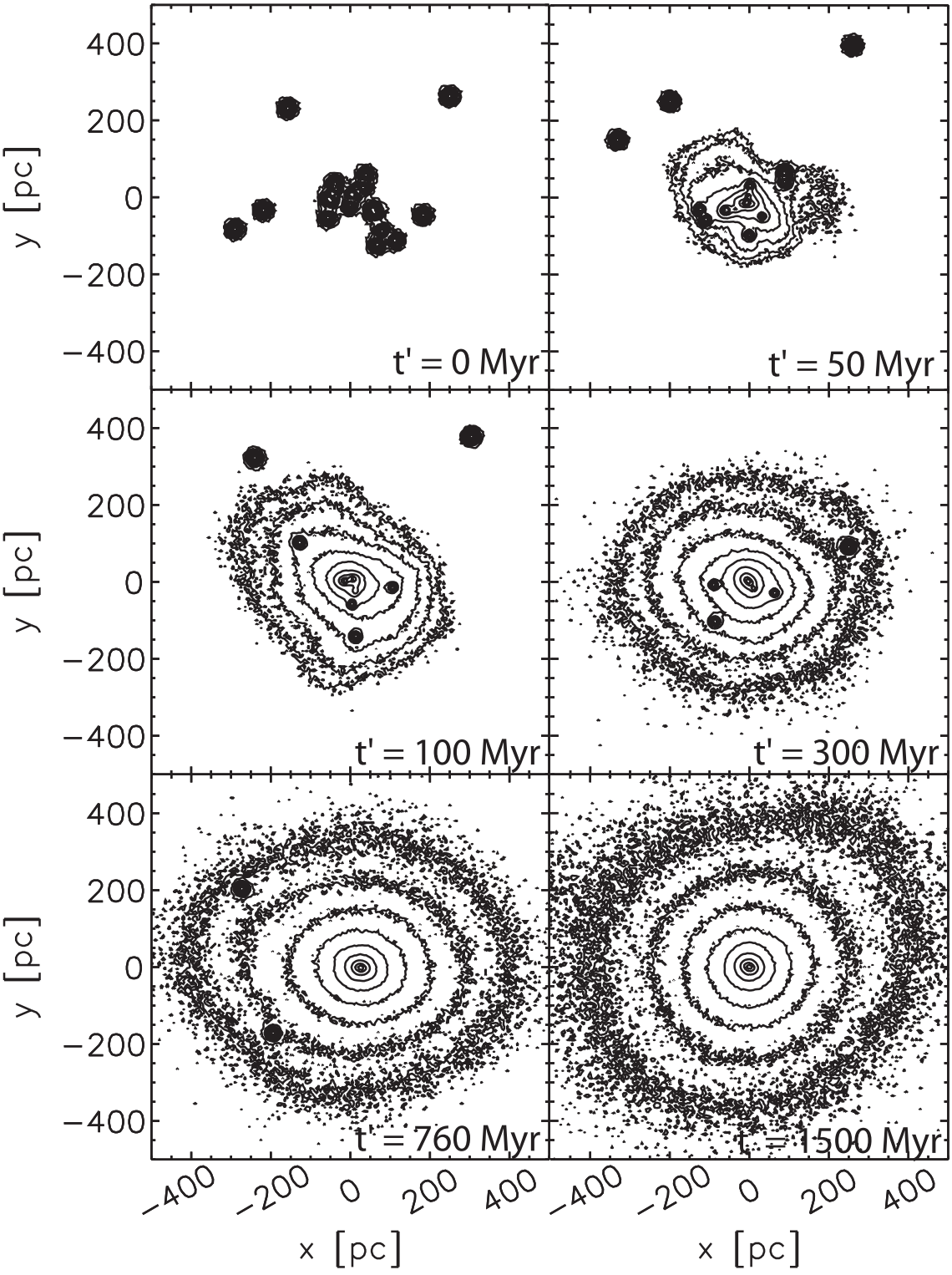

FIGURE 4.15— Time evolution of the merger object in model M_1_1.5_100. Contour plots on the x-y-plane displayed at $t' = 0$, 50, 100, 300, 760, and 1500 Myr. The lowest contour level corresponds to 5 particles per pixel. The pixel size is 5 pc. This yields $0.15\ M_\odot\ pc^{-2}$. The contour levels increase further by a factor of 3.

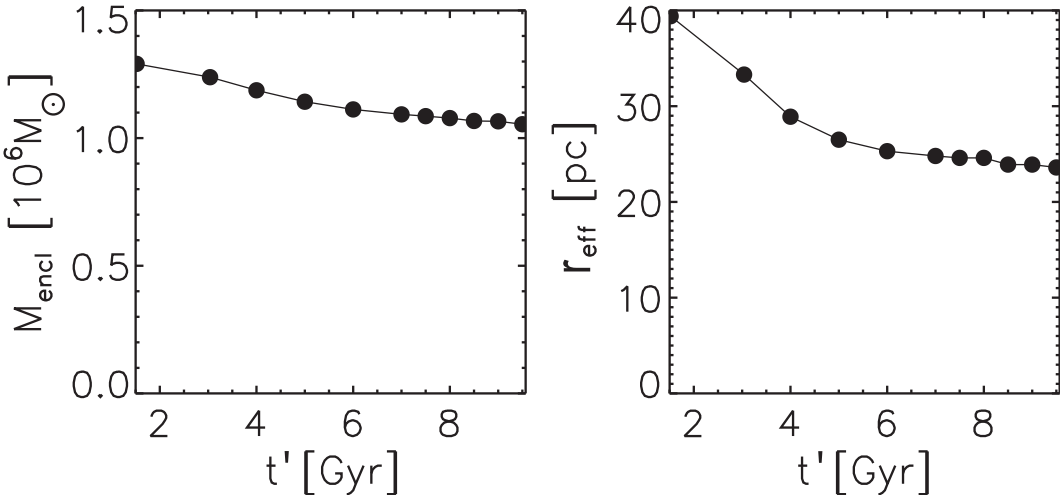

FIGURE 4.16— **Left:** Enclosed mass, $M_{\rm encl}$, versus time, t', for model M_1_1.5_100. The time evolution is plotted after the merging phase, described in detail in Sect. 4.3.3.1, is completed. Thus the plot starts after 1.5 Gyr. The curve becomes fairly flat with increasing time. An almost stable merger object forms suffering only slightly from mass loss. **Right:** Effective radius, $r_{\rm eff}$, against time, t', for model M_1_1.5_100. The effective radius decreases with time up to about 7 Gyr. Thereafter it is almost constant.

4.3.3 Results

I carried out 27 different numerical simulations to get an estimate of the influence of varying initial CC conditions. All calculations start at the perigalactic passage at $t_0 = -9.568$ Gyr and are calculated up to the current position of NGC 2419.

4.3.3.1 Time Evolution of the Merging Process

The merging process of model M_1_1.5_100 is shown in Fig. 4.15 as contour plots on the x-y-plane to illustrate the detailed evolution of the merging process. The snapshots were taken at $t' = t - t_0 = 0$, 50, 100, 300, 760, and 1500 Myr. At $t' = 50$ Myr the merger object is already in the process of formation, but the majority of star clusters are still individual objects. In the course of time an increasing number of star clusters are captured by the merger object. Thus the merger object becomes more extended. After 10 CC crossing times ($t' = 760$ Myr) there are still two unmerged star clusters in the vicinity of the merger object. In the last snapshot at $t' = 1500$ Myr the merging process is completed and 19 out of 20 star cluster have merged forming a smooth extended object. One star cluster escaped the merging process. It follows the merger object on its orbit around the Milky Way at a distance of about 14 kpc (at $t' = 9.568$ Gyr).

The timescale of the merging process depends on the initial CC mass, the CC size, and the distribution of star clusters within the CC. For model M_1_1.5_100 50% of the star clusters have merged after approximately 100 Myr. The time within which half of the clusters merge increases with the CC size (from 15 Myr for model M_1_1.5_25 to 200 Myr for model M_1_1.5_150) and decreases with CC mass (from 150 Myr for model M_1_1.0_100 to 65 Myr for model M_1_3.0_100).

The further time evolution of the merger object of model M_1_1.5_100 is plotted in Fig. 4.16. The enclosed mass of the merger objects is defined as the mass within 800 pc. The projected half-mass radius is slightly smaller than the three-dimensional half-mass radius (Table C.2) and corresponds to the observed effective radius, $r_{\rm eff}$, if mass follows light. The effective radius and mass of the merger object decrease and become fairly constant after about 7 Gyr. The structural parameters change only very slightly in the next few gigayears.

4.3.3.2 Variation of the Initial CC Mass and Size

I consider models with three CC masses, $M^{\rm CC} = 1.0$, 1.5, and $2.0 \cdot 10^6$ $M_\odot$, and six CC Plummer radii between $R_{\rm pl}^{\rm CC} = 25$ and 150 pc in steps of 25 pc to analyze the dependence of the structural parameters of the merger objects on the initial CC mass and size. In addition, two models with $R_{\rm pl}^{\rm CC} = 200$ and 300 pc are calculated for $M^{\rm CC}$ = 2.0 $\cdot 10^6$ $M_\odot$. All models have the same relative initial distribution of star clusters, which is scaled according to the respective Plummer radii (see Figs. 4.14a and b). The velocities of the individual star clusters are also scaled with CC mass and size to keep the CCs initially in virial equilibrium.

For all models the merging process leads to a stable object. The number of merged star clusters is between 10 and 20. The properties of the merger objects at the current position of NGC 2419 are displayed in Table C.2 of Appendix C.

Figure 4.17a shows the enclosed mass, $M_{\rm encl}$, of the merger objects as a function of the initial CC Plummer radius, $R_{\rm pl}^{\rm CC}$. The fraction of the initial CC mass, which is bound to the merger object, decreases almost linearly with increasing CC size for all three masses from about 92% at $R_{\rm pl}^{\rm CC} = 25$ pc to values of 46, 53, and 59% at $R_{\rm pl}^{\rm CC} = 150$ pc for CC masses of $M^{\rm CC} = 1.0$, 1.5, and $2.0 \cdot 10^6$ $M_\odot$, respectively. Mass loss occurs either by the escape of individual stars from the diffuse stellar component, which builds up during the merging process (see Sect. 4.3.3.1), or by entire star clusters escaping the merging process. For all three masses, all 20 star clusters merge for compact models up to $R_{\rm pl}^{\rm CC} = 75$ pc, i.e. mass loss is only from the diffuse component for these models. For the more extended models with $R_{\rm pl}^{\rm CC} \geq 100$ pc star clusters escape from the merging process. For extended models with $R_{\rm pl}^{\rm CC} = 150$ pc six, five, and two star clusters escape for CC masses of $M^{\rm CC} = 1.0$, 1.5, and $2.0 \cdot 10^6$ $M_\odot$, respectively.

Figure 4.17b shows the effective radii, $r_{\rm eff}$, of the merger objects as a function of the initial CC Plummer radius, $R_{\rm pl}^{\rm CC}$. The effective radii of the merger objects increase with increasing CC size up to $R_{\rm pl}^{\rm CC} = 75$ pc for $M^{\rm CC} = 1.0 \cdot 10^6$ $M_\odot$ and up to $R_{\rm pl}^{\rm CC} = 100$ pc for the more massive models. For larger values of $R_{\rm pl}^{\rm CC}$ the effective radii decrease rapidly. Despite the large range of CC sizes ($R_{\rm pl}^{\rm CC} = 25$ to 300 pc), the effective radii of the merger objects are constrained to a relatively small interval, e.g. models with $M^{\rm CC} = 2.0 \cdot 10^6$ $M_\odot$ are constrained to values between 13.2 and 25.6 pc.

Figure 4.18 combines Figs. 4.17a and b showing the effective radius of the merger objects as a function of their enclosed mass. Only the six radii $R_{\rm pl}^{\rm CC} = 25$, 50, 75, 100, 125, and 150 pc, where data for all three masses are available, were used to allow for an overview on the trends (models with the same initial CC Plummer radius are connected by dotted lines, models with the same initial CC mass with solid lines). For all CC Plummer radii the effective radii increase with the initial CC mass. While the effective radii vary only slightly with mass for models with $R_{\rm pl}^{\rm CC} = 25$, 50, and 75 pc, the slope is considerably steepening for larger CC sizes.

The formation process of the merger objects depends on the compactness of the initial CC. A measure of how densely a CC is filled with star clusters for an equal number $N_0^{\rm CC}$ of star clusters is given by the parameter α (see Sect. 2.1.1.3). As the individual star clusters are not scaled with $R_{\rm pl}^{\rm CC}$, the values of α decrease from 0.16 for $R_{\rm pl}^{\rm CC} = 25$ pc to 0.013 for $R_{\rm pl}^{\rm CC} = 300$ pc. In general, large values of α accelerate the merging process because the star clusters already partly overlap in the center of the CC, whereas small values hamper the merging process.

Also the tidal field counteracts the merging process. An estimate of the influence of the tidal field on the CC is given by the parameter β, which is the ratio of the cutoff radius $R_{\rm cut}^{\rm CC}$ of the CC and its tidal radius $r_{\rm t}^{\rm CC}$ (see Sect. 2.1.4). The tidal radii at the perigalactic distance of 20 kpc are $r_{\rm t}^{\rm CC} = 296$, 291, 283, 274, and 262 pc for $M^{\rm CC} = 1.5 \cdot 10^6$ $M_\odot$ and $R_{\rm pl}^{\rm CC} = 50$, 75, 100, 125, and 150 pc, respectively. The corresponding values of β are 0.68, 1.03, 1.41, 1.83, and 2.29.

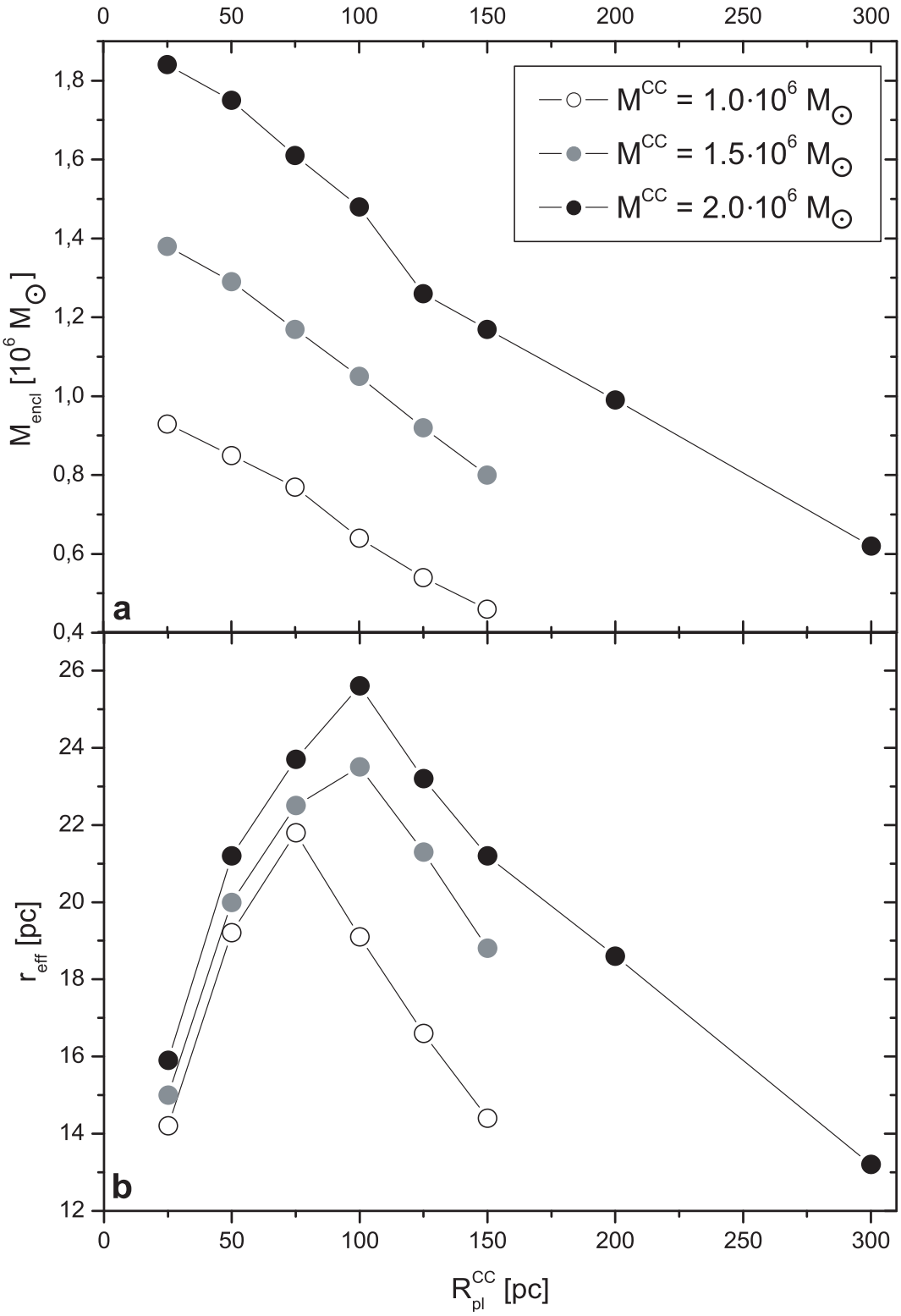

FIGURE 4.17— **a:** Enclosed mass, $M_{\rm encl}$, of the merger objects as a function of the initial CC Plummer radius, $R_{\rm pl}^{\rm CC}$. **b:** Effective radius, $r_{\rm eff}$, of the merger objects as a function of the initial CC Plummer radius, $R_{\rm pl}^{\rm CC}$.

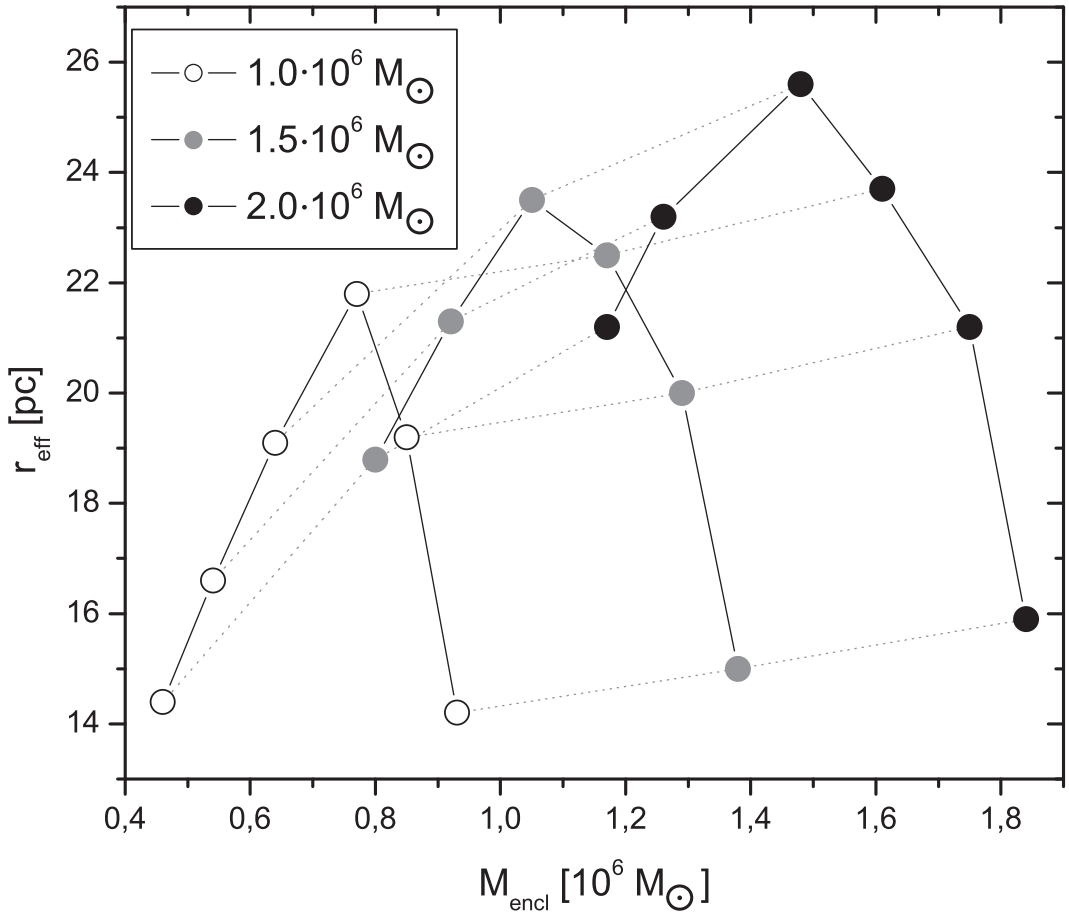

FIGURE 4.18— Effective radius, $r_{\rm eff}$, as a function of the enclosed mass, $M_{\rm encl}$, of the merger objects for the CC models with $R_{\rm pl}^{\rm CC} = 25$, 50, 75, 100, 125, and 150 pc (symbols from right to left) and $M^{\rm CC} = 1.0$, 1.5, and $2.0 \cdot 10^6$ M$_\odot$. Models with the same initial CC mass, $M^{\rm CC}$, are connected by solid lines. Models with the same initial CC Plummer radius, $R_{\rm pl}^{\rm CC}$, are connected by dotted lines to illustrate the dependence on the initial CC mass.

The values of β are slightly higher for the models with $M^{\rm CC} = 1.0 \cdot 10^6$ M$_\odot$ and slightly lower for models with $M^{\rm CC} = 2.0 \cdot 10^6$ M$_\odot$ (Table 4.5).

TABLE 4.5— β-values of the initial CC models of NGC 2419

β	25 pc [a]	50 pc	75 pc	100 pc	125 pc	150 pc	200 pc	300 pc
1.0×10^6 M$_\odot$ [b]	0.38	0.77	1.19	1.63	2.14	2.73		
1.5×10^6 M$_\odot$	0.33	0.68	1.03	1.41	1.83	2.29		
2.0×10^6 M$_\odot$	0.31	0.62	0.94	1.28	1.64	2.04	3.02	7.27
3.0×10^6 M$_\odot$				1.11				

[a] Initial CC Plummer radius, $R_{\rm pl}^{\rm CC}$.
[b] Initial CC mass, $M^{\rm CC}$.

The fraction of the enclosed mass of a merger object and the initial CC mass, $\frac{M_{\rm encl}}{M^{\rm CC}}$, is plotted as a function of β in Fig. 4.19. The merger objects of the models for the three initial CC masses show the same linear correlation with β.

The models with $R_{\rm pl}^{\rm CC} = 75$ pc start already at the perigalactic distance with a β of about one. Consequently, all 20 clusters merge. For the more extended models a number of star cluster are

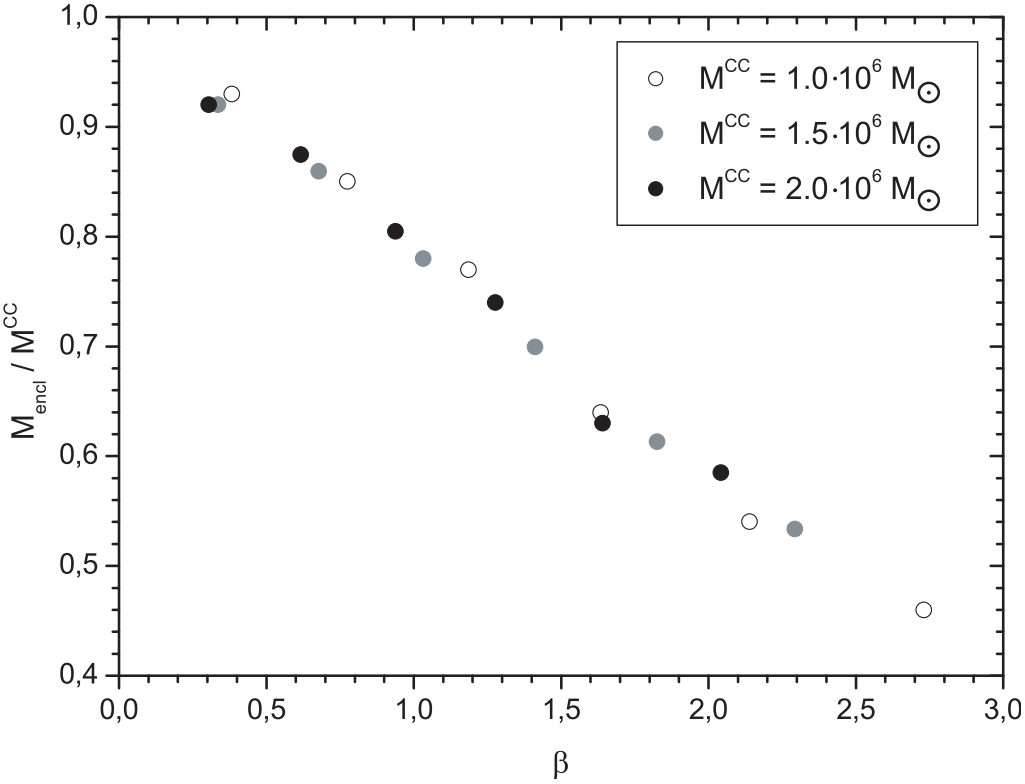

FIGURE 4.19— The ratio of the merged mass and the initial CC mass, $M_{\rm encl}/M^{\rm CC}$, as a function of the parameter β for the models with $M^{\rm CC} = 1.0$, 1.5, and $2.0 \cdot 10^6$ $M_\odot$ and $R_{\rm pl}^{\rm CC} = 25$, 50, 75, 100, 125, and 150 pc.

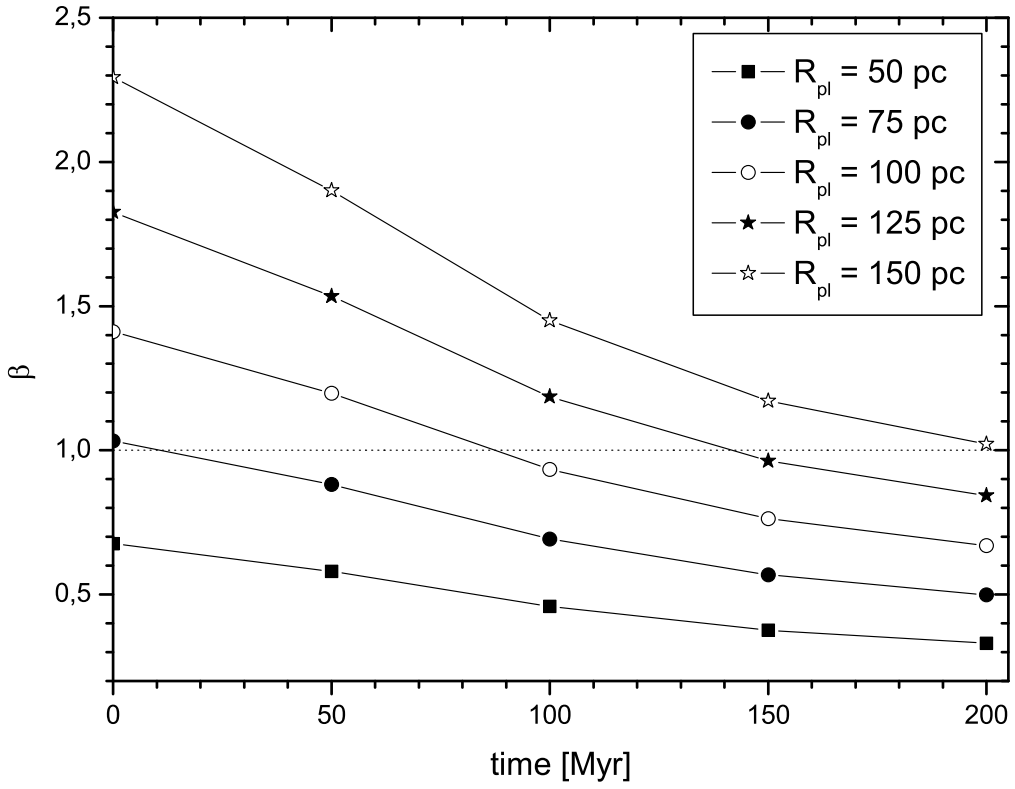

FIGURE 4.20— Parameter β as a function of time for models with $M^{\rm CC} = 1.5 \cdot 10^6$ $M_\odot$ and $R_{\rm pl}^{\rm CC} = 50$, 75, 100, 125, and 150 pc for the first 200 Myr (the orbital period is about 1.3 Gyr).

initially located outside the tidal radius. As I use a highly eccentric orbit, the CCs move rapidly towards larger Galactic distances, e.g. after 100 Myr they are at a distance of about 35 kpc. Due to the lower gravitational field of the Milky Way at larger distances, the tidal radii increase leading to lower values of β. Figure 4.20 shows the variation of β with time for models with $M^{\rm CC} = 1.5 \cdot 10^6$ M$_\odot$. For models M_1_1.5_100, M_1_1.5_125, and M_1_1.5_150 the period with $\beta > 1$ is getting longer, resulting in lower numbers of merged clusters for larger CCs. The turnover in $r_{\rm eff}$, as shown in Figs. 4.17b and 4.18, occurs at those $R_{\rm pl}^{\rm CC}$, where β is sufficiently large to allow entire star clusters to escape the merging process.

4.3.3.3 Variation of the Initial Distribution of Star Clusters

I use the CC parameters of model M_1_1.5_100 as a basis to analyze the influence of the detailed distribution of star clusters in the CC. I calculate the evolution of five additional models, of which two (M_2_1.5_100 and M_3_1.5_100) have a similar concentration of clusters in their center as M_1_1.5_100, whereas the other three models (M_4_1.5_100, M_5_1.5_100, and M_6_1.5_100) show a less concentrated distribution of star clusters (see Fig. 4.14c). All six models result from exactly the same Plummer model parameters, but with different random number seeds.

The average and the standard deviation of the effective radii and enclosed masses of the merger objects of all six models are $r_{\rm eff} = 23.8 \pm 3.2$ pc and $M_{\rm encl} = 0.95 \pm 0.17 \cdot 10^6$ M$_\odot$, respectively. The standard deviations, which correspond to relative deviations of 13% ($r_{\rm eff}$) and 18% ($M_{\rm encl}$), provide an order of magnitude estimate of the influence of the distribution of star clusters on the structural parameters of the merger objects.

The merger objects resulting from the compact initial configurations 1 to 3 have on average a significantly higher mass ($M_{\rm encl} = 1.10 \pm 0.06 \cdot 10^6$ M$_\odot$) than the less concentrated configurations 4 to 6 ($M_{\rm encl} = 0.81 \pm 0.06 \cdot 10^6$ M$_\odot$). In contrast, no clear difference in the effective radii of the merger objects is present between concentrated and extended initial distributions.

For comparison, an additional model M_7_1.5_200 has been calculated. It has a CC Plummer radius of 200 pc and a relatively small cutoff radius of 400 pc. A scaled version of model M_1_1.5_100 with $R_{\rm pl}^{\rm CC} = 200$ pc and a CC cutoff radius of 800 pc, which is four times the CC Plummer radius, would have six star clusters beyond 400 pc. Model M_7_1.5_200 has the same cutoff radius and therefore the same values of β as model M_1_1.5_100. Due to the broader initial distribution of star cluster in M_7_1.5_200 the enclosed mass and the effective radius are slightly lower than in model M_1_1.5_100.

The results demonstrate that next to the CC mass and the CC Plummer radius also the cutoff radius and the exact distribution of star clusters in a CC are key parameters for extended models, influencing the structural parameters of the merger objects.

4.3.3.4 Comparison with Observations

The enclosed masses were converted into absolute V-band luminosities to allow for direct comparison with the observed data, using the formula

$$M_{\rm V} = M_{\rm V,solar} - 2.5 \ \log_{10}(M_{\rm encl} \frac{L_{\rm V}}{M}), \tag{4.2}$$

where, $M_{\rm V,solar} = 4.83$ mag is the absolute solar V-band luminosity, $M_{\rm encl}$ the enclosed mass of the merger object and $\frac{M}{L_V}$ the mass-to-light ratio. I use a mass-to-light ratio of 2.05 ± 0.50, as determined by Baumgardt et al. (2009) for NGC 2419. Apparent V-band luminosities can by calculated by adding the distance modulus of NGC 2419 $(m - M)_0 = 19.60$ (Ripepi et al. 2007) and a V-band extinction of $A_{\rm V} = 0.25$ using a reddening of $E(B-V) = 0.08$ (Ripepi et al. 2007).

Figure 4.21 shows an exemplary contour plot of the merger object of model M_1_1.5_100 projected onto the sky using Galactic coordinates. The lowest contour line corresponds to

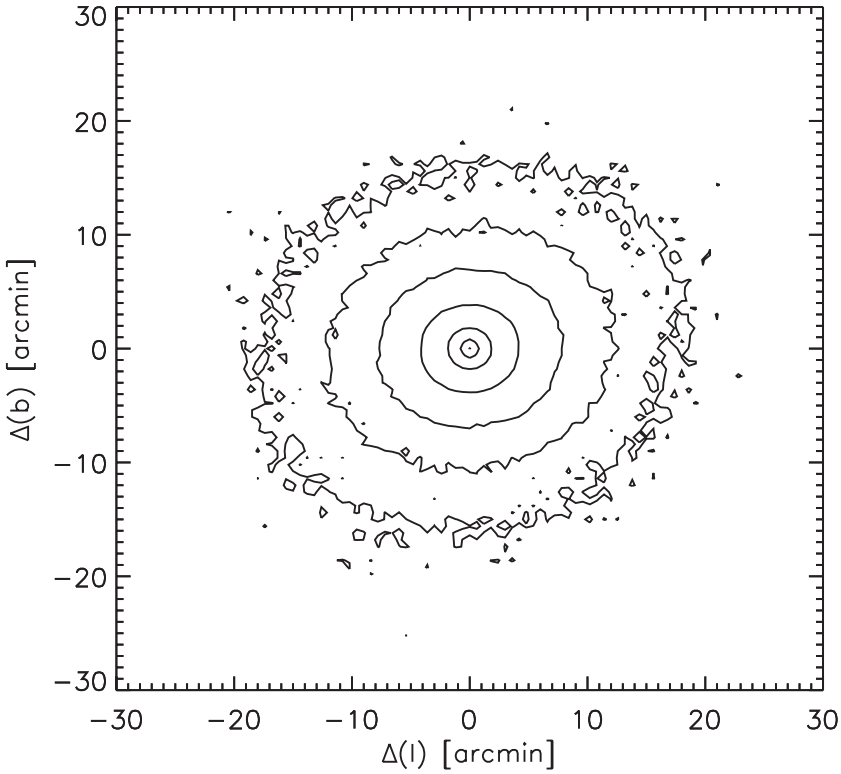

FIGURE 4.21— Contour plot projected onto the sky in Galactic coordinates for model M_1_1.5_100 at the current observed position of NGC 2419. The pixel size is $0.'6$. The contour levels go from 32 to 20 mag arcsec^{-2} in steps of two mag arcsec^{-2}.

32 mag arcsec^{-2}. At this low surface brightness, NGC 2419 is detectable up to radii of about $17'$ corresponding to 415 pc. Observed photometry, however, covers only a region within the inner $60''$ of NGC 2419, while surface densities need to be derived from star counts in the outer parts. Ripepi et al. (2007) found evidence for stars associated with NGC 2419 up to radii of $15'$.

Figure 4.22 shows the effective radius, $r_{\rm eff}$, versus the absolute V-band luminosity, $M_{\rm V}$, of the observations and the models. The observational parameters of NGC 2419 and the parameters of the resulting merger objects are summarized in Tables 4.3 and C.2, respectively. Due to the scatter of the observed parameters of NGC 2419 and the turnover in the effective radii of the models as described in Sect. 4.3.3.2, a large number of models are compatible with the observed parameters of NGC 2419. Only extended models with initial CC masses of $M^{\rm CC} = 1.0 \cdot 10^6$ M$_\odot$ and compact models with $M^{\rm CC} = 2.0 \cdot 10^6$ M$_\odot$ are clearly incompatible with observations.

A more detailed comparison between models and observations can be achieved using surface brightness profiles. Bellazzini (2007) compiled a surface brightness profile out to projected radii of $477.''5$. However, as he used radii between $720''$ and $900''$, which are well inside NGC 2419, as a reference field to estimate the background level, Bellazini's surface brightness estimates are expected to be slightly too faint in the outer parts of NGC 2419.

The radial surface brightness profiles of four exemplary models projected onto the sky and converted to units of mag arcsec^{-2} are shown in Fig. 4.23. The merger objects show a King-like profile out to radii of about $1000''$. The observed profile from Bellazzini (2007) is added to Fig. 4.23 to allow for a direct comparison. The surface brightness profile of model M_1_1.0_50 agrees very well with the observed profile at all radii. The other three models in Fig. 4.23 illustrate how the profiles change when one of the parameters mass, size and initial distribution of star clusters is modified. Model M_1_1.5_50 has a similar shape as M_1_1.0_50, but is too bright at all radii due to the larger mass. Model M_1_1.5_100, which is a more extended

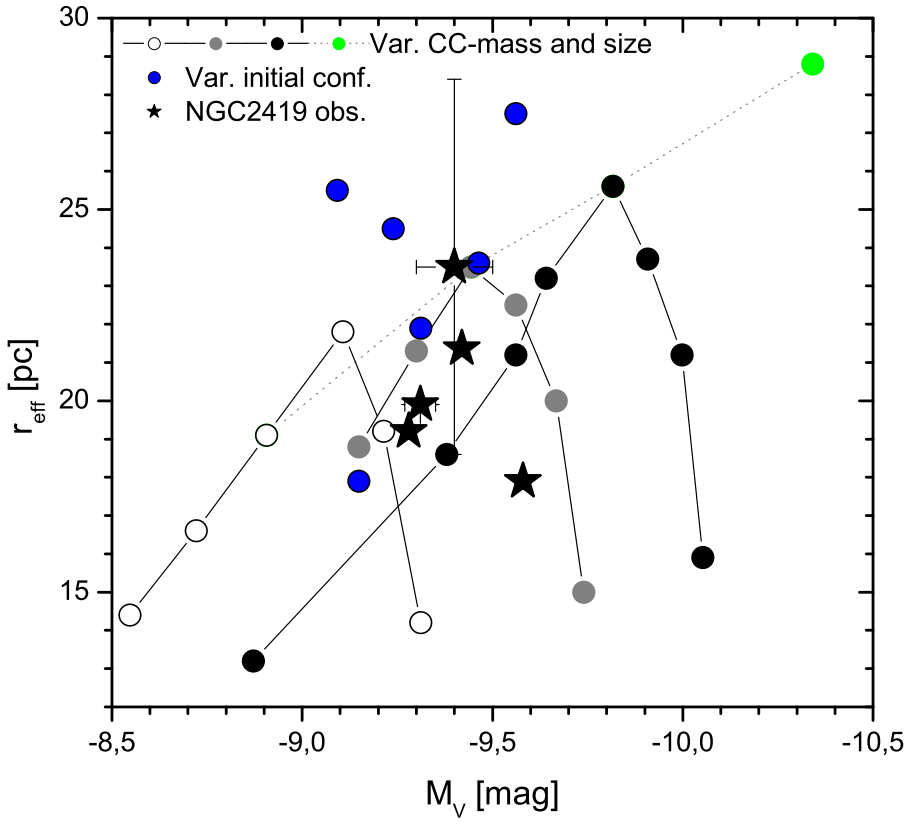

FIGURE 4.22— Effective radius, $r_{\rm eff}$, as a function of absolute V-band luminosity, $M_{\rm V}$, for all computations (see Table C.2). The dotted line connects models with $R_{\rm pl}^{\rm CC} = 100$ pc. The colors white, grey, black and green correspond to CC masses of $M^{\rm CC} = 1.0$, 1.5, 2.0, and $3.0 \cdot 10^6$ $M_\odot$, respectively. The different initial configurations at a CC mass of $M^{\rm CC} = 1.5 \cdot 10^6$ $M_\odot$ are plotted as blue circles. The different observed values of NGC 2419 are shown as black stars. The error bars for the observed values are from the respective papers (see Table 4.3).

version of model M_1_1.5_50, agrees well with the observations between $10''$and $100''$, but it is considerably brighter in the center and the outer parts. Model M_4_1.5_100, which has a broader initial distribution of star clusters than model M_1_1.5_100, shows a smaller deviation from the observed surface brightness profile than model M_1_1.5_100.

Baumgardt et al. (2009) observed the radial velocities of 40 stars within a projected radius of 100 pc of NGC 2419 and derived a velocity dispersion of $\sigma = 4.14 \pm 0.48$ km s^{-1}. The line-of-sight velocity dispersions within a projected radius of 100 pc of the models are listed in Table C.2. A number of models with masses $M^{\rm CC} = 1.0$, 1.5, and $2.0 \cdot 10^6$ $M_\odot$ have velocity dispersions that are within the one sigma error of the observed velocity dispersion. Model M_1_1.0_50, which has an effective radius and enclosed mass very close to the newest observed values from Baumgardt et al. (2009) and a surface brightness profile that is a good approximation of the observed profile from Bellazzini (2007), has a velocity dispersion of $\sigma = 4.13$ km s^{-1}, i.e. almost exactly the observed one.

Ibata et al. (2011) increased the sample from Baumgardt et al. (2009) by a factor of about four, allowing to compute not only an overall velocity dispersion, but a velocity dispersion profile. For all stars, where more than one observation is available, the mean of these values is used. Within a radial distance of 180 pc, in total 169 stars build up the sample. Individual stars deviating significantly from the system velocity of NGC 2419 ($v_{\rm hel} = -20.3$ km s^{-1}, Baumgardt et al. 2009) are discarded, leading to 156 stars used to compile the velocity dispersions. The individual radial bins comprise between 10 and 37 stars. The uncertainty of the standard deviation is estimated by means of the standard error of the standard deviation, SE(σ_i) $= \sigma_i / \sqrt{2N_i - 2}$,

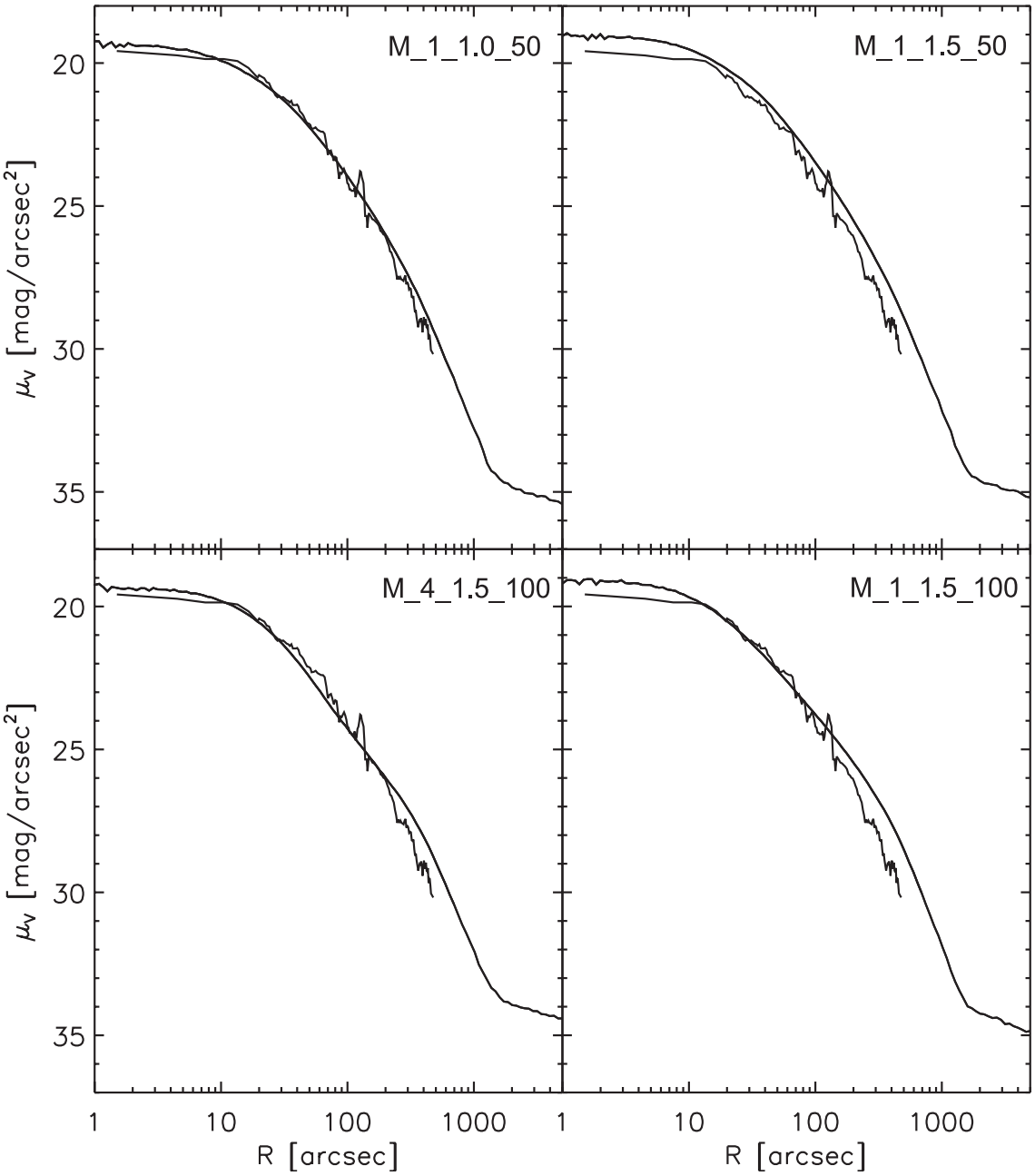

FIGURE 4.23— Surface brightness profiles of four exemplary models at the current position of NGC 2419 using a mass-to-light ratio of 2.05. A V-band extinction of $A_V = 0.25$ was applied to the models to allow for a direct comparison with the observed surface brightness profile of Bellazzini (2007).

where N_i is the number of stars in bin i. Figure 4.24 shows the observed velocity dispersion profile and the profile of the model M_1_1.0_50. The observed profile agrees very well with model M_1_1.0_50 except for the inner two bins, where the observed values are larger than the model. The deviation of these two values is, however, due to the low number of stars and the correspondingly large error bars statistically not significant.

Considering masses, effective radii, surface brightness profiles, and velocity dispersions, model M_1_1.0_50 provides the best representation of NGC 2419. However, a number of models reproduce the observed structural parameters of NGC 2419 quite well within the observational uncertainties, demonstrating that an object like NGC 2419 can be formed from merged

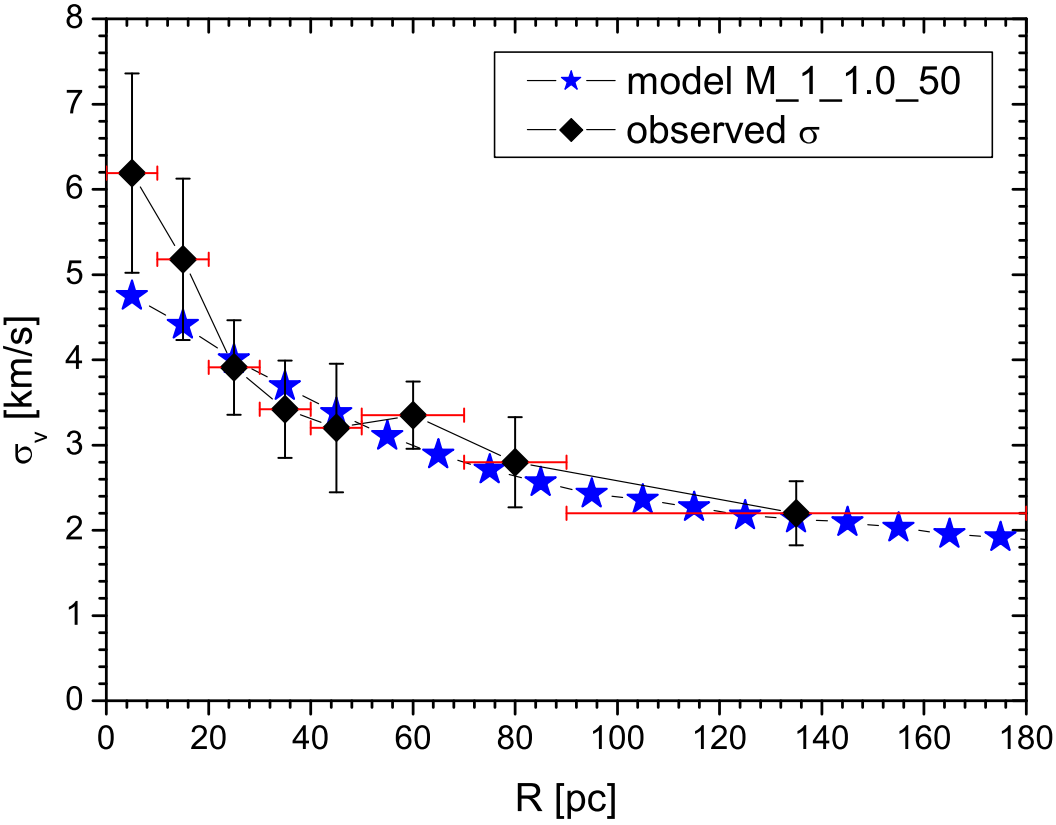

FIGURE 4.24— Comparison of the observed velocity dispersion profile (black), derived from the combined data of Baumgardt et al. (2009) and Ibata et al. (2011), and the velocity dispersion profile of model M_1_1.0_50 (blue). The horizontal error bars (red) indicate the bin-size used for the observed velocity dispersion profile, the vertical error bars indicate the standard error of the observed velocity dispersion.

CCs without the need of fine-tuning of the input parameters.

4.3.4 Discussion

4.3.4.1 The Merging Star Cluster Scenario

The proposed formation scenario for NGC 2419 starts with newly born complexes of star clusters in the Galactic halo with orbital parameters allowing for an highly eccentric orbit. For all 27 models the majority of star clusters merge into a stable object. The turnover in the $r_{\rm eff}$ vs. $M_{\rm encl}$ space (Figs. 4.17, 4.18, and 4.22) leads to degenerate states, because a relatively compact CC can produce a comparable merger object as a more massive CC having a significantly larger CC size. In consequence, a range of initial conditions can form a merger object comparable to NGC 2419, which prevents to pinpoint the exact parameters of the original CC, which formed NGC 2419. On the other hand, the larger the range of initial conditions that end up in a NGC 2419-like object, the larger is the probability of creating a massive EO like NGC 2419.

As the individual star clusters of the CC formed at approximately the same time from molecular clouds of a galaxy, the observed absence of multiple stellar populations (Ripepi et al. 2007) is fully consistent with my model. A small scatter in metallicity would also be explained, as the individual pre-cluster cloud cores of the complex could have had slightly different metallicities. In addition, some stars from the parent galaxy might have been captured by NGC 2419 during its formation as demonstrated for massive star clusters like ω Cen by Fellhauer et al. (2006).

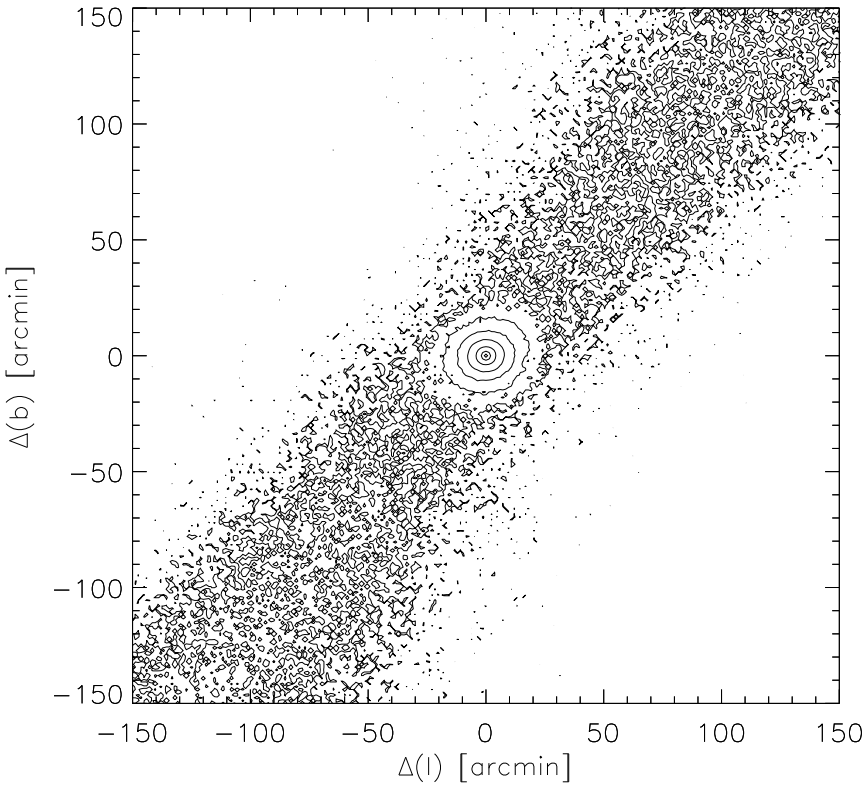

FIGURE 4.25— Contour plot projected onto the sky in Galactic coordinates for model M_1_1.5_100 at the current observed position of NGC 2419. The pixel size is $1\farcm2$. The contour levels go from 34 to 20 mag arcsec^{-2} in steps of two mag arcsec^{-2}.

4.3.4.2 *Potential Association with Stellar Streams in the Milky Way Halo*

As stellar structures in the outer halo are long lived features, remnants of a parent galaxy or stellar tidal streams associated with NGC 2419 may still be observable in the Milky Way halo.

Figure 4.25 is a contour plot comparable to Fig. 4.21, but showing a larger field of view and going to fainter magnitudes. At the very low surface brightness of 34 mag arcsec^{-2} a stellar stream associated with model M_1_1.5_100 is visible. Küpper et al. (2010) have studied star clusters of the Milky Way using N-body computations and demonstrated that near apogalacticon a compression of tidal debris occurs. As NGC 2419 is close to its apogalactic distance, the faint stellar stream seen in my simulations is consistent with the results of Küpper et al. (2010).

Newberg et al. (2003) found an over-density of A-type stars at a distance of 83 to 85 kpc, which has a width of at least 10° and which was traced for more than 20° on the sky. NGC 2419 is located within this debris (on the sky and at the same distance). This observed stellar over-density is consistent with my simulations and can therefore be explained as debris originating from NGC 2419 itself. Newberg et al. (2003), however, argued that NGC 2419 and the stellar over-density might be associated with the Sagittarius dwarf galaxy, as NGC 2419 lies only 13 kpc from its orbital plane. As the stellar streams from Sgr dwarf have mean metallicities between [Fe/H] $= -0.4$ near the core and -1.1 within the arms (Chou et al. 2007), while NGC 2419 has a very low metallicity of [Fe/H] $= -2.12$ (Harris 1996), an association with the Sagittarius dwarf galaxy is rather unlikely.

The Virgo Stellar Stream (VSS) has a metallicity of [Fe/H] $= -1.86$ with a large scatter of 0.40 dex (Duffau et al. 2006), which makes it comparable to the metallicity of NGC 2419. Casetti-Dinescu et al. (2009) determined the proper motion of the VSS and calculated an orbit

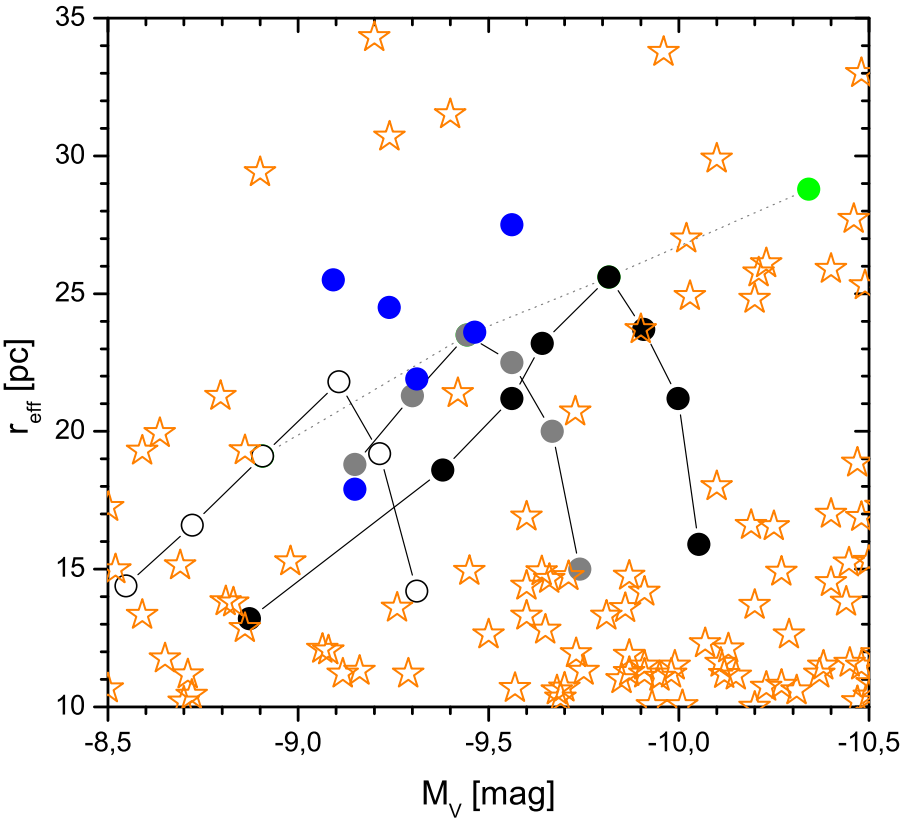

FIGURE 4.26— Effective radius, $r_{\rm eff}$, as a function of absolute V-band luminosity, M_V, for all computations. Colors and lines are the same as in Fig. 4.22. In addition, the EOs from the EO catalog (Chapter 3) are added as orange stars.

with a pericentric distance of 11 kpc and an apocentric distance of 89 kpc. They concluded that the current position of NGC 2419 is compatible with this orbit.

Newberg et al. (2009) found a new stellar stream at a distance of 35 kpc in the constellation Cetus having a nearly polar orbit. The so-called Cetus Polar Stream (CPS) has a very low metallicity of [Fe/H] $= -2.1$. While the metallicity of CPS is in excellent agreement with NGC 2419, the polar orbit along Galactic longitude $l = 143°$ appears to be in conflict with the current location of NGC 2419, which is at $l = 180°$.

The Orphan Stream, independently discovered by Grillmair (2006) and Belokurov et al. (2006), has been analyzed in detail by Newberg et al. (2010). They found a very low metallicity of [Fe/H] $= -2.1$ and a likely orbit between a pericentric distance of 16.4 kpc and an apocentric distance of about 90 kpc. These parameters are very similar to those of NGC 2419.

Any potential association with the Sgr stream, VSS, CPS, or Orphan stream can only be verified after the proper motion of NGC 2419 has been measured.

4.3.4.3 NGC 2419-like Objects in other Galaxies

NGC 2419 has a rather isolated location in the M_V vs. $r_{\rm eff}$ space, if compared with EOs from other late-type galaxies (see Fig. 4.11). In Chapter 3, it was demonstrated that HST surveys of late-type galaxies outside the Local Group have an extremely poor coverage of their outer halo. Consequently, the non-detection of NGC 2419-like objects might be related to this poor sampling.

On the other hand, a large number of extended, high-luminosity EOs were detected in early-type galaxies. Figure 4.26 combines Fig. 4.22, which shows the models, with all known

EOs in this luminosity interval, which are associated with late-type and early-type galaxies (see Chapter 3). Figure 4.26 demonstrates that a number of massive objects with effective radii of $r_{\rm eff} \approx 20$ pc have been found.

Richtler et al. (2005) presented a NGC 2419-like object in the halo of the elliptical galaxy NGC 1399 which is the central galaxy of the Fornax Cluster. This object, labeled 90:12 in Richtler et al. (2005), is located at a projected distance of about 40 kpc and has a very blue color indicating a very low metallicity. It has an absolute V-band luminosity of $M_{\rm V} = -10.04$ mag, which corresponds to a mass of $M_{90:12} = 1.8 \cdot 10^6$ M$_\odot$, assuming the same mass-to-light ratio as NGC 2419. The effective radius of $r_{\rm eff} = 27$ pc is larger than that of NGC 2419. In Fig. 4.22, this EC is located between the values of models M_1_2.0_100 and M_1_3.0_100. Therefore, the parameters of EC 90:12 are consistent with being a more massive version of NGC 2419. In addition, the M87 EOs M87EO-35 and M87EO-37 have structural parameters very close to models M_1_2.0_75 and M_1_1.5_25, respectively.

Figure 4.26 demonstrates that the merging star cluster scenario has the potential to reproduce the observed parameters of a number of EOs. A parametric study covering the entire EO mass range from $M^{\rm CC} = 10^{5.5}$ to 10^8 M$_\odot$ will be presented in the next chapter to explore the merging star cluster scenario on a larger scale.

4.3.5 Summary

The Galactic star cluster NGC 2419 has unique parameters. It is one of the most luminous, one of the most distant, and as well one of the most extended GCs of the Milky Way. Apart from these unusual parameters, NGC 2419 appears to be a normal Galactic GC having a low metallicity and a single stellar population.

I propose a new formation scenario for NGC 2419, being a remnant of a merged star cluster complex, which was formed during an interaction between a gas-rich galaxy and the Milky Way. To test this hypothesis, I performed particle-mesh code computations of 27 different CC models. I vary the CC mass, the CC size, and the initial distribution of star clusters in the CC to analyze the influence of these parameters on the resulting objects. These CCs are comparable to those observed in the tidal stream of the Tadpole galaxy UGC 10214 (Tran et al. 2003), in the Antennae galaxies (Bastian et al. 2006a), and in NGC 922 (Pellerin et al. 2010).

For all 27 models, the vast majority of star clusters merged into a stable object. The derived parameters mass, absolute V-band luminosity, effective radius, velocity dispersion and the surface brightness profile are, for a number of models, in good agreement with those observed for NGC 2419.

The effective radii of the merger objects increase with increasing CC size up to $R_{\rm pl}^{\rm CC} = 75$ pc for $M^{\rm CC} = 1.0 \cdot 10^6$ M$_\odot$ and up to 100 pc for the more massive models. For larger values of $R_{\rm pl}^{\rm CC}$ the effective radii decrease rapidly (Fig. 4.17). The turnover in the $r_{\rm eff}$ vs. $M_{\rm encl}$ space (Figs. 4.18 and 4.22) leads to degenerate states, as relatively compact CCs can produce a comparable merger object as a more massive CC having a significantly larger size. Despite the large range of CC sizes ($R_{\rm pl}^{\rm CC} = 25$ to 300 pc) of the models with initial CC masses of $M^{\rm CC} = 2.0 \cdot 10^6$ M$_\odot$, the effective radii of the merger objects are constrained to values between 13.2 and 25.6 pc.

In consequence, a range of initial conditions can form a merger object comparable to the Milky Way cluster NGC 2419 preventing me to pinpoint the exact parameters of the original CC, which formed NGC 2419. On the other hand, the larger the range of initial conditions that end up in a NGC 2419-like object, the larger is the probability of creating a massive EO like NGC 2419.

I conclude that NGC 2419 can be well explained by the merging star cluster scenario. Measurements of the proper motion of NGC 2419 are indispensable to further study the proposed scenario and to potentially associate NGC 2419 with one of the stellar streams in the outer

Galactic halo.

4.4 Conclusions

I performed numerical simulations to test the merged CC formation scenario on two types of well studied EOs: the faint fuzzie star clusters in the disk of the galaxy NGC 1023 and the Milky Way EO NGC 2419. In both environments, i.e. the strong gravitational field within a galactic disk and the weak tidal field within an outer galactic halo, the CC models evolve into stable objects having structural parameters comparable to those of the observed objects.

I conclude that the merging star cluster scenario has the potential to explain the existence of EOs in various environments. Comprehensive parameter studies covering the entire EO mass range from $M^{\rm CC} = 10^5$ to 10^8 $\rm M_\odot$ will be presented in the next chapter to explore the merging star cluster scenario on a larger scale.

5

A General Study on the Formation of ECs and UCDs

This chapter aims to analyze how the structural parameters of the final merger objects correlate with the underlying CC parameter space. I systematically scan a suitable parameter space for CCs and perform numerical simulations to investigate their further fate. The varied sizes and masses of the CCs cover CC Plummer radii between 10 and 160 pc and CC masses between 10^5 and 10^8 $M_\odot$, which are consistent with the range of observed CC parameters. The CCs of the parameter studies presented in this chapter are on eccentric and circular orbits with galactocentric distances between 20 and 120 kpc. All 102 simulations end up with stable merger objects, wherein 20 to 98% of the initial CC mass is bound. The objects show a general trend of increasing effective radii with increasing CC mass and with decreasing external tidal field. The structural parameters of the modeled merger objects are comparable to those of the observed EOs as presented in Chapter 3. The merger objects show a similar trend of increasing maximal effective radii with increasing luminosity as the observed EOs. The vast majority of the observed ECs and UCDs, i.e. about 95%, are located within the parameter space covered by the modeled merger objects on an eccentric orbit between 20 and 60 kpc. The results of CC models on circular orbits demonstrate that even very extended objects like the M31 ECs found by Huxor et al. (2005) and the very extended ($r_{\rm eff} > 80$ pc), high-mass UCDs can be explained by merged cluster complexes in regions with low gravitational fields, i.e. at large galactocentric radii. In conclusion, the merger objects of my parameter study represent the overall observed parameters of EOs and the observed trends very well. Even detailed structural features like the core-halo profiles of some massive and extremely extended UCDs are well reproduced by my simulations.

5.1 Introduction and General Set-Up

In the previous chapter, I demonstrated that the merging star cluster scenario is able to explain the structural parameters of EOs in the disk of the galaxy NGC 1023 and of the Milky Way EO NGC 2419. In this chapter, I will broaden the scope of the merging star cluster scenario by analyzing the entire parameter space of observed CCs, which have masses in the range from a few 10^4 to 10^8 $M_\odot$ and effective radii between a few parsecs and a few hundred parsecs.

All CC models in this chapter consist of $N_0^{\rm CC} = 32$ star clusters. The individual star clusters are represented by Plummer models (Plummer 1911; Kroupa 2008) with $N_0^{\rm SC} = 100\,000$ particles. The Plummer radius, which corresponds to the effective radius, is chosen for all models to be 4 pc, which is the median effective radius of the combined data sets of observed YMCs of Bastian et al. (2006b), Mengel et al. (2008), and Bastian et al. (2009). I select a cutoff radius of $R_{\rm cut}^{\rm SC} = 5\ R_{\rm pl}^{\rm SC} = 20$ pc. For each CC, the 32 star clusters have the same mass, which is $1/32^{th}$ of the corresponding CC mass. The initial velocity distribution of the star clusters is chosen such

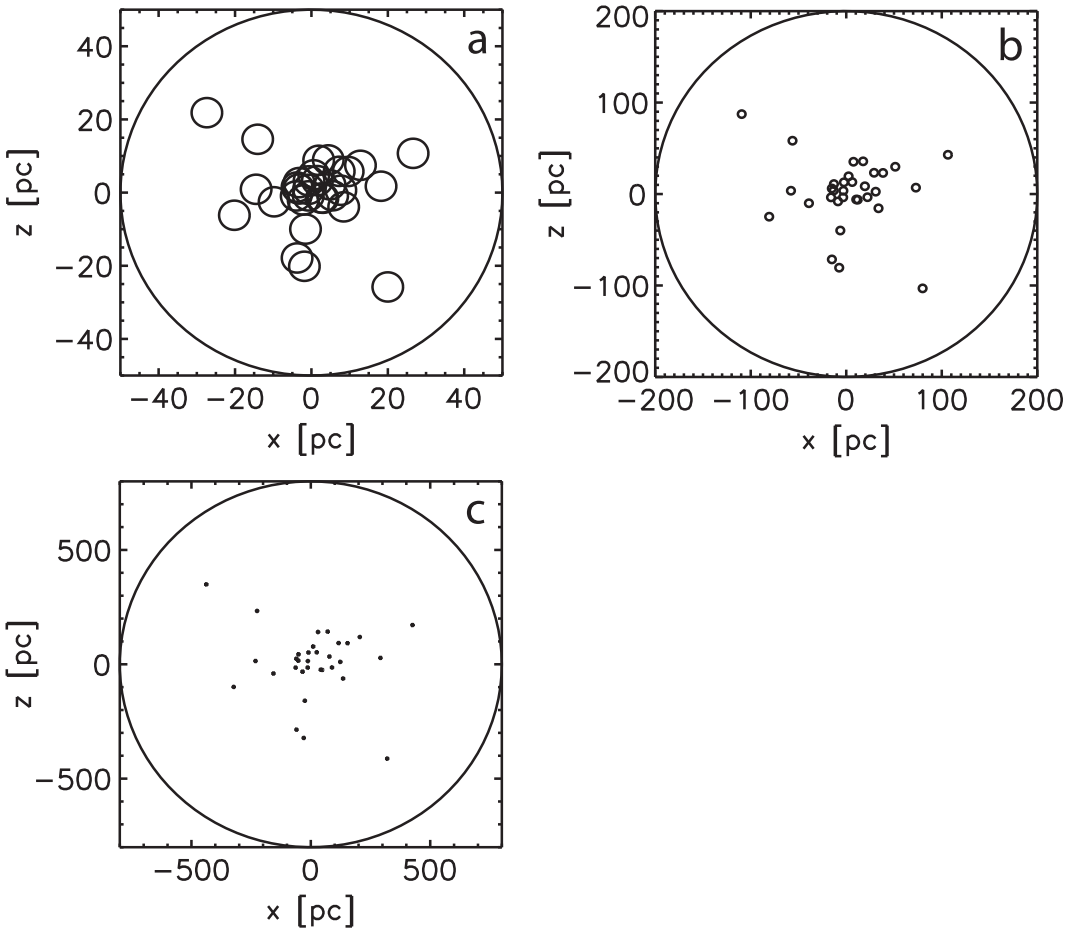

FIGURE 5.1— Three exemplary initial spatial distributions of star clusters (small circles with radius $R_{\rm pl}^{\rm SC}$) in a CC (surrounding circle with radius $R_{\rm cut}^{\rm CC}$) projected onto the x-z-plane. **a:** $R_{\rm pl}^{\rm CC} = 10$ pc, **b:** $R_{\rm pl}^{\rm CC} = 40$ pc, and **c:** $R_{\rm pl}^{\rm CC} = 160$ pc. They have α-values of 0.4, 0.1, and 0.025, respectively.

that they are in virial equilibrium.

The observed CCs show a clear concentration of star clusters towards their centers (Tran et al. 2003; Bastian et al. 2006a; Pellerin et al. 2010). Unfortunately, no detailed observational constraints on the distribution of star clusters in the complex and their dynamical state are available. In the absence of observed density profiles of CCs, I choose a simple model and distribute the star clusters in the CC models according to a Plummer distribution, which is truncated at the cutoff radius $R_{\rm cut}^{\rm CC} = 5\, R_{\rm pl}^{\rm CC}$. This cutoff radius is large enough to prevent a clear break or edge in the spatial distribution and small enough to avoid single star clusters at very large distances that would be stripped away immediately. If I would increase the cutoff radius $R_{\rm cut}^{\rm CC}$ from 5 times the Plummer radius, $R_{\rm pl}^{\rm CC}$, to infinity, there would be only one or two star clusters beyond the actual cutoff radius. Hence, the exact value of the cutoff radius will have a negligible impact on the results.

The formation process of the merger object depends on the compactness of the initial CC. A measure of how densely a CC is filled with star clusters for an equal number $N_0^{\rm CC}$ of star clusters is given by the parameter α (see Sect. 2.1.1.3). The models presented in this chapter cover α-values of 0.4, 0.2, 0.1, 0.05, and 0.025 for CC Plummer radii of $R_{\rm pl}^{\rm CC} = 10$, 20, 40, 80, and 160 pc, respectively. High values of α (≥ 0.1) correspond to compact CCs with overlapping star clusters in the center, where the majority of star clusters merge within a few megayears. Low values of α (≤ 0.05) correspond to extended CCs where the merging process can take up

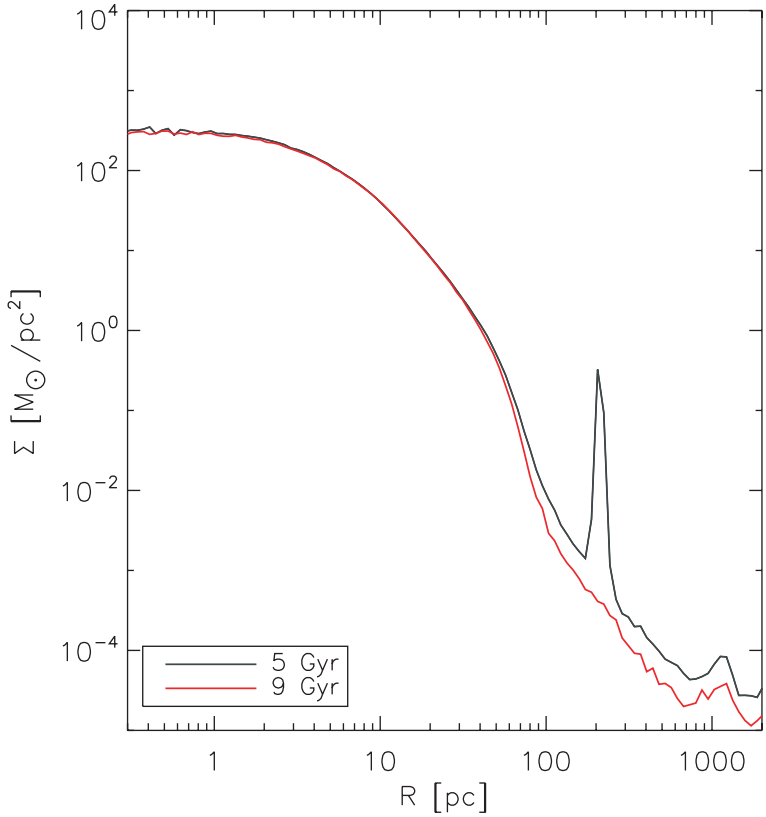

FIGURE 5.2— Surface density profiles of the merger object resulting from a CC with $M^{\rm CC} = 10^{5.5}$ M$_\odot$ and $R_{\rm pl}^{\rm CC} = 160$ pc on a circular orbit at $R_{\rm gal} = 20$ kpc (CC_51-CIRC_20) after 5 and 9 Gyr. The peak at 200 pc constitutes an unmerged star cluster.

to several hundred megayears.

In Sect. 4.3 on the extended Milky Way cluster NGC 2419, I have demonstrated that the exact initial distribution of star clusters in an extended CC leads to variations in the structural parameters mass and size of the order 10 to 20%. This uncertainty will, however, have no impact on the overall trends that will be discussed in this chapter. Therefore, I use the same seeds for the random number generator to generate the same distribution of star clusters scaled to the corresponding Plummer radii of individual CC models for all models presented in the following sections. Figure 5.1 shows three exemplary initial distributions of star clusters in a CC.

The initial velocity distribution of the CC models is chosen such that each CC is initially in virial equilibrium, which is consistent with the results of Whitmore et al. (2005), who found that the cluster to cluster velocity dispersion of five CCs in the Antennae is small enough to keep them just gravitationally bound. A detailed description of the generation of initial coordinates (space and velocity) for Plummer models is given in Sect. 2.1.1.1.

ECs are found near late-type disk galaxies, early-type lenticular and elliptical galaxies, and dwarf galaxies, while UCDs are predominantly found associated with giant elliptical galaxies (see Chapter 3). As the gravitational potential has a larger impact on the low-mass objects and as I would like to use the same potential for all computations to allow for a direct comparison of all results, I chose an analytical Milky-Way-like potential consisting of a disk-, a bulge-, and a halo component (see Sect. 2.1.4 for details). The coordinate system is chosen such that the disk of the host galaxy lies in the x-y-plane. The disk is modeled by a Miyamoto-Nagai potential (Miyamoto & Nagai 1975), with $M_{\rm d} = 1.0 \cdot 10^{11}$ M$_\odot$, $a_{\rm d} = 6.5$ kpc, and $b_{\rm d} = 0.26$ kpc. The bulge is represented by a Hernquist potential (Hernquist 1990), with $M_{\rm b} = 3.4 \cdot 10^{10}$ M$_\odot$

and $a_{\rm b} = 0.7$ kpc. The dark matter halo is a logarithmic potential, with $v_0 = 186.0$ km s^{-1} and $r_{\rm halo} = 12.0$ kpc. This set of parameters gives a reasonable Milky-Way-like rotation curve.

In order to get a good resolution of the star clusters two grids with high and medium resolution are focused on each star cluster following their trajectories. The individual high resolution grids have a size of ± 80 pc and cover an entire star cluster, whereas the medium resolution grid of every star cluster has a size between ± 800 pc and ± 1200 pc embedding the whole initial CC. The local universe is covered by a fixed coarse grid, which contains the orbit of the CC around the center of the galaxy. All grids contain $128 \times 128 \times 128$ grid cells.

EOs are in general rather old objects with ages between 5 and 13 Gyr. In Sect. 4.3.3.1, it was shown that the structural parameters change mainly in the first few Gyr and stay almost constant afterwards. As the influence of the tidal field is the largest for a very extended, low-mass CC in high gravitational field environments, I use a CC model with a low CC mass of $M^{\rm CC} = 10^{5.5}$ M$_\odot$, a large CC Plummer radius of $R_{\rm pl}^{\rm CC} = 160$ pc, and a low galactic distance of $R_{\rm gal} = 20$ kpc to analyze the time dependence. Figure 5.2 shows the surface density profile of the merger object of the extended CC model after 5 and 9 Gyr of evolution. The shape of the surface density profiles are almost identical in the inner part and only differ in the outer parts ($R > 50$ pc) of the profile. The structural parameters hardly change. The enclosed mass decreases slightly from $M_{\rm encl} = 0.64 \cdot 10^5$ M$_\odot$ at 5 Gyr to $M_{\rm encl} = 0.60 \cdot 10^5$ M$_\odot$ at 9 Gyr and the effective radius, $r_{\rm eff}$, decreases from 10.5 to 10.4 pc. Therefore, I decided to integrate all models only up to 5 Gyr to save computing time.

The above mentioned parameters are used for all models in the following sections. In the individual sections, different sub-sets of initial CC Plummer radii, $R_{\rm pl}^{\rm SC}$, initial CC masses, $M^{\rm CC}$, and orbital parameters of the CCs are used.

In Sect. 5.2, I study how the parameter space of the final merger objects correlate with the underlying CC parameter space ($R_{\rm pl}^{\rm SC}$ and $M^{\rm CC}$) for a fixed eccentric orbit. In Sect. 5.3, I investigate the influence of various orbits on the evolution of CCs of a fixed mass but for a range of initial CC Plummer radii. Section 5.4 explores the framework for the formation of extremely extended EOs. Section 5.5 provides a discussion of the results and the overall agreement between the modeled merger objects and the observed EOs.

5.2 The Effect of the Initial CC Parameters Mass and Size

5.2.1 Numerical Set-Up and Varied Parameters

In this section, I study how the parameter space of the final merger objects correlate with the underlying CC parameter space ($R_{\rm pl}^{\rm SC}$ and $M^{\rm CC}$) for one eccentric orbit.

The parameters of the CC models constitute a matrix of 5×6 values (Fig. 5.3 and Appendix C.3) with CC Plummer radii of $R_{\rm pl}^{\rm CC} = 10$, 20, 40, 80, and 160 pc and initial CC masses of $M^{\rm CC} = 10^{5.5}$, 10^6, $10^{6.5}$, 10^7, $10^{7.5}$, and 10^8 M$_\odot$. The range of sizes and masses are motivated by the observed parameters of ECs and UCDs (see Chapter 3) consistent with observations of CCs (see Sect. 1.4). For the CC masses $M^{\rm CC} = 10^{6.5}$ and $10^{7.5}$ M$_\odot$ two additional models with $R_{\rm pl}^{\rm CC} = 240$ and 360 pc were considered.

In this section, I focus on ECs and UCDs located far from the galactic disk in the halo of the respective galaxies. As orbital parameters for such objects are unknown, I chose a polar orbit (orbit 1) between galactic radii of 20 and 60 kpc for my simulations. These values are motivated by the projected distances of the M31 ECs of 13 to 60 kpc (Mackey et al. 2006) and the projected distances of Fornax UCDs between 8 and 74 kpc (Mieske et al. 2008). Figure 5.4 illustrates the chosen orbit, which has an orbital period of about 860 Myr.

In my formation scenario, the CCs are most likely formed at the perigalactic passage of the parent galaxy where the impact of the interaction is strongest. Therefore, I start the calculations

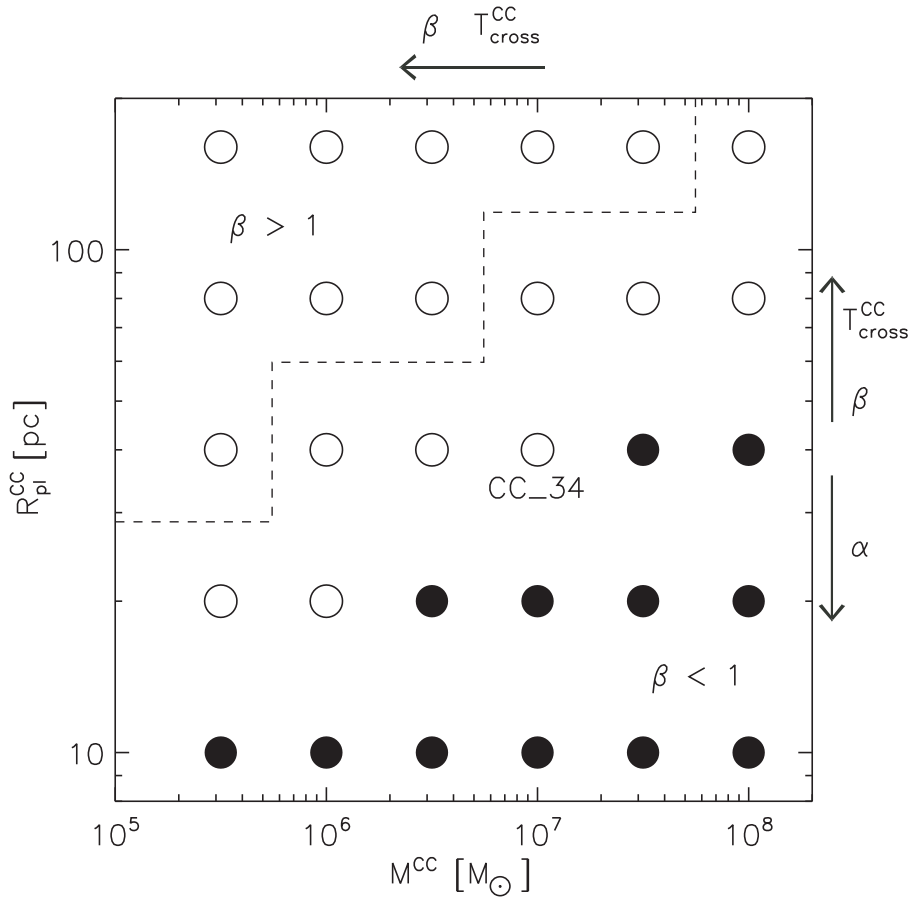

FIGURE 5.3— Parameter space for the CC models. The parameters CC Plummer radius, $R_{\rm pl}^{\rm CC}$, and CC mass, $M^{\rm CC}$, constitute a matrix of 5×6 values. All circles mark the 30 simulations on orbit 1. The open circles indicate the 18 additional simulations on orbit 2. The arrows indicate the increase of CC crossing time, $T_{\rm cross}^{\rm CC}$, and α- and β-values (see Chapter 2). The dashed line separates the CC models with $\beta < 1$ from the CC models with $\beta > 1$. CC_34-ECC_20_60 is an example of the nomenclature of the models (see Appendix C.3 for details). The first index is the row number which corresponds to the CC Plummer radius, $R_{\rm pl}^{\rm CC}$. The second index indicates the column synonymous to the CC mass, $M^{\rm CC}$.

at the perigalactic distance.

To analyze the impact of a polar orbit relative to an inclined orbit, I recalculated a subset of the models also on an inclined orbit (see Fig. 5.4, orbit 2). The orbit is expected to have its largest impact on the most extended and lowest mass CC models. The additional computations are indicated by open circles in Fig. 5.3.

5.2.2 Results

In total, I carried out 52 different numerical simulations to study the influence of varying initial CC parameters.

5.2.2.1 Time Evolution of the Merging Process

To illustrate the merging process, the evolution of model CC_34-ECC_20_60 ($R_{\rm pl}^{\rm CC} = 40$ pc, $M^{\rm CC} = 10^7$ M$_\odot$) is shown in Fig. 5.5 as contour plots on the x-z-plane. The snapshots were taken at $t = 0$, 10, 70, 280, 1300, and 5000 Myr. At $t = 10$ Myr (top panel) the merger object is already in the process of formation. In the course of time an increasing number of star clusters merge and the merger object becomes more extended. At $t = 70$ Myr which is about

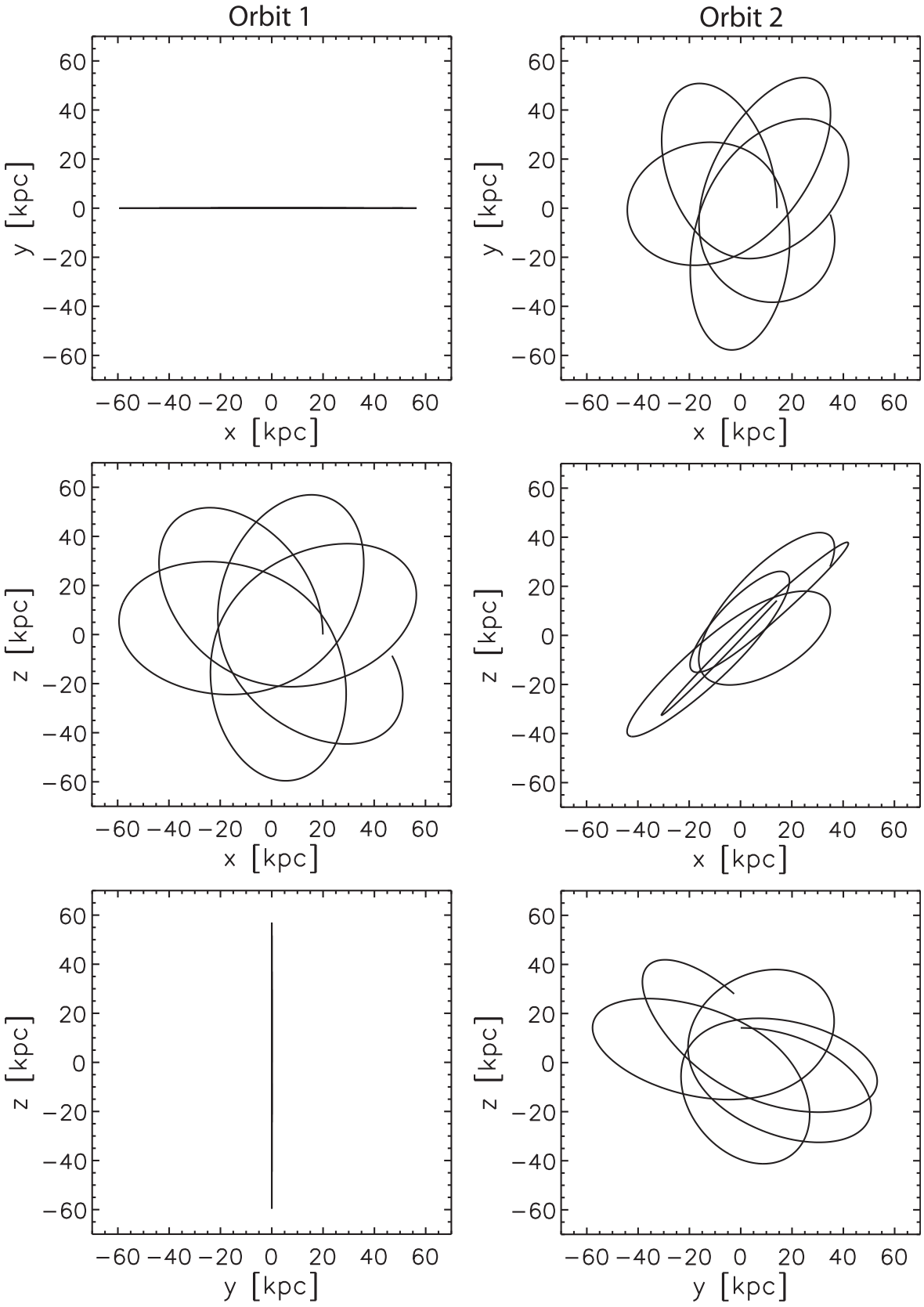

FIGURE 5.4— The orbits projected to the x-y-, the x-z-, and the y-z-plane. Orbit 1 is a polar orbit and orbit 2 is an inclined orbit between galactic radii of 20 and 60 kpc.

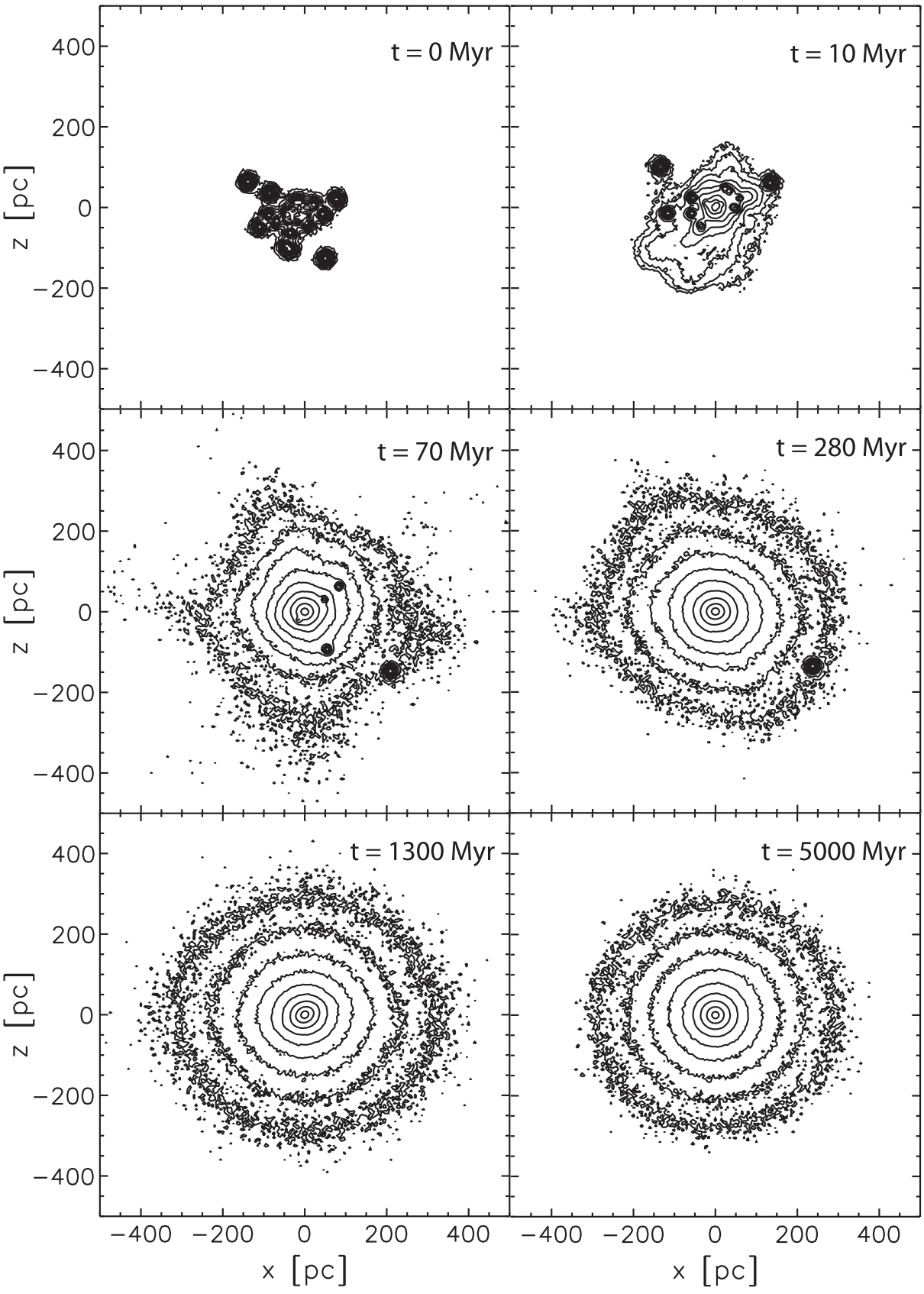

FIGURE 5.5— Time evolution of the merger object of model CC_34-ECC_20_60 ($M^{\rm CC} = 10^7$ M$_\odot$, $R_{\rm pl}^{\rm CC} = 40$ pc). Contour plots on the x-z-plane displayed at $t = 0$, 10, 70, 280, 1300, and 5000 Myr. The lowest contour level corresponds to 5 particles per pixel. The pixel size is 5 pc. This yields 0.625 M$_\odot$ pc^{-2}. The contour levels increase further by a factor of 3.

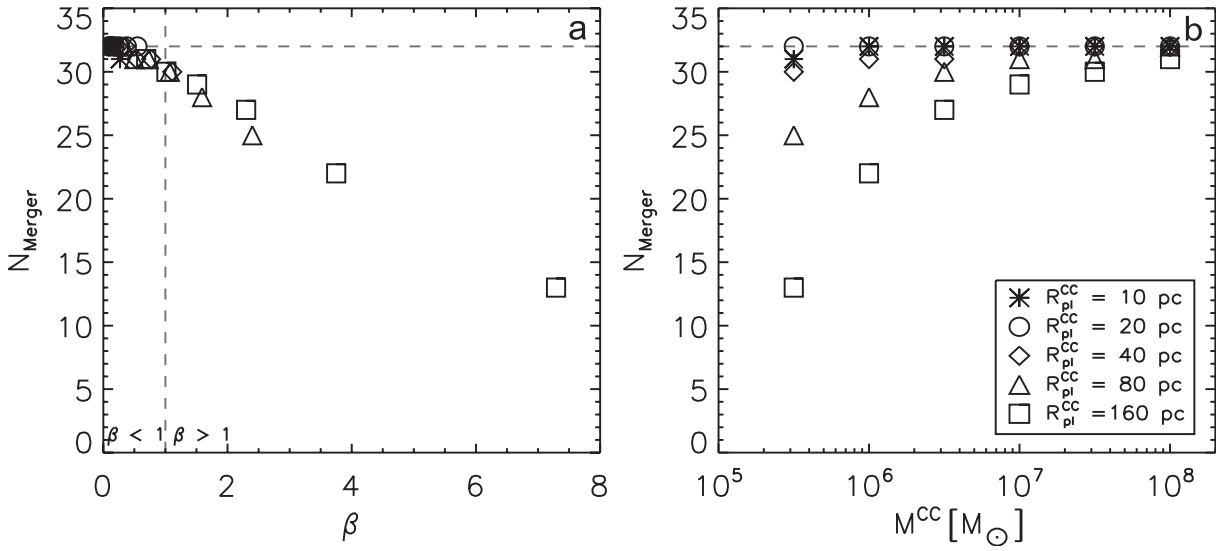

FIGURE 5.6— **a:** Number of merged star clusters, $N_{\rm Merger}$, versus parameter β for different initial CC Plummer radii, $R_{\rm pl}^{\rm CC}$, for orbit 1 after 5 Gyr. The horizontal dashed line marks the number of star clusters, $N_0^{\rm CC} = 32$, in the initial CC. The vertical dashed line separates the CC models with $\beta < 1$ from the CC models with $\beta > 1$. **b:** Number of merged star clusters, $N_{\rm Merger}$, against the initial CC mass, $M^{\rm CC}$, for different initial CC Plummer radii, $R_{\rm pl}^{\rm CC}$. The horizontal dashed line denotes the number of star clusters in the initial CC as in Fig. 5.6a.

10 CC crossing times, the vast majority of star clusters has merged into the merger object. Another 20 CC crossing times later the merging process is almost completely terminated and 31 out of 32 star clusters have merged. There is still a close companion star cluster as a satellite of the merger object which is eventually (after $t = 1300$ Myr) also captured by the merger object. After the merging process has been completely terminated the merger object becomes slightly smaller and reaches a stable state within a few gigayears. As the structural parameters vary only marginally after a couple of gigayears the simulations are all terminated at $t = 5$ Gyr.

The general merging process is very similar for all models, but the corresponding timescale varies considerably. A typical timescale for a CC is the crossing time of a star cluster through the CC,

$$T_{\rm cross}^{\rm CC} = \left(\frac{3\pi}{32}\right)^{-1.5} \sqrt{\frac{(R_{\rm pl}^{\rm CC})^3}{GM^{\rm CC}}}, \tag{5.1}$$

where G is the Gravitational constant. The values of the crossing times of the CC models cover a range between 0.3 Myr (CC_16-ECC_20_60) and 340 Myr (CC_51-ECC_20_60). The general trend of the crossing time is indicated by arrows in Fig. 5.3. The results of my calculations show that on average half of the individual star clusters have merged after approximately two-and-a-half $T_{\rm cross}^{\rm CC}$.

5.2.2.2 Number of Merged Star Clusters

The larger the impact of the tidal field, i.e. the larger the value of β, which is the ratio of the cutoff radius $R_{\rm cut}^{\rm CC}$ of the CC and its tidal radius $r_{\rm t}^{\rm CC}$ (see Sect. 2.1.4), the smaller is the number of merger events. Fig. 5.6a shows the number of merged star clusters, $N_{\rm Merger}$, as a function of the parameter β. For models with $\beta < 1$, practically all star clusters merge, while for larger values of β an increasing number of star clusters is able to escape and align along the orbit.

Figure 5.6b demonstrates how the number of merged star clusters depends on the mass and size of the initial CC. The number of merged star clusters increases for larger intial CC masses and decreases for larger intial CC Plummer radii. The number of merged clusters becomes as

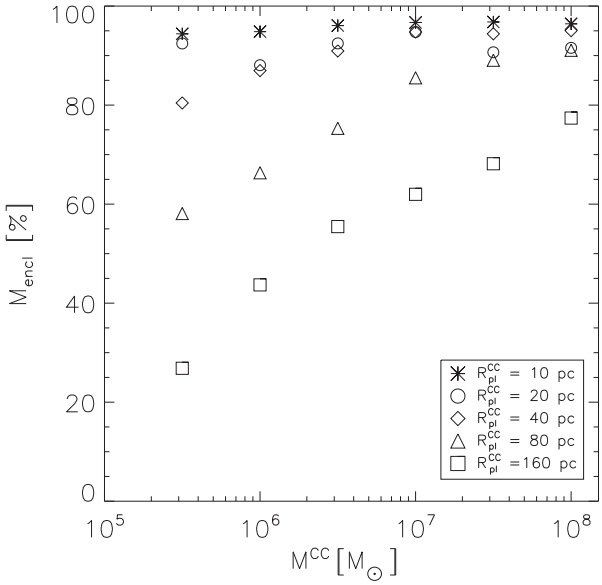

FIGURE 5.7— Remaining fraction of mass of the initial CC which ended up in the merger object vs. the initial CC mass, $M^{\rm CC}$, for orbit 1 after 5 Gyr.

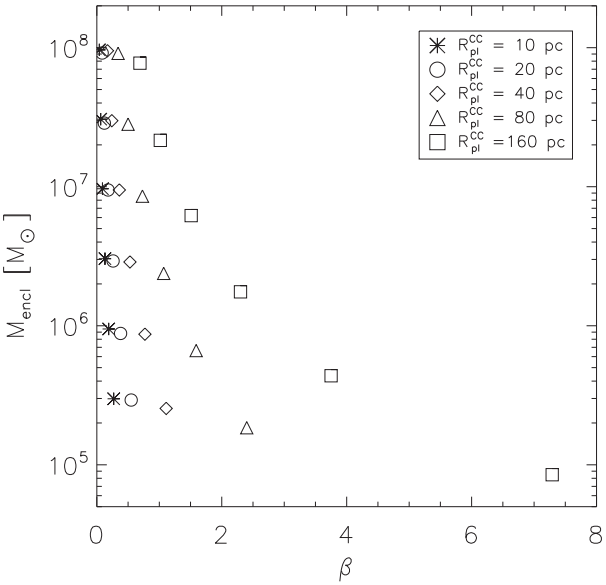

FIGURE 5.8— Enclosed mass of merger objects, $M_{\rm encl}$, as a function of parameter β for orbit 1 after 5 Gyr.

low as 13 for the least massive and most extended model CC_51-ECC_20_60 ($M^{\rm CC} = 10^{5.5}$ M$_\odot$ and $R_{\rm pl}^{\rm CC} = 160$ pc). As the unmerged clusters remain compact GCs, the merging of 13 clusters to one merger objects leads to 19 compact GCs originating from the same initial CC.

5.2.2.3 Correlation of Structural Parameters of Merger Objects with CC Parameter Space

The number of merged star clusters has a substantial influence on the structural parameters of the merger object. The fraction of the merged mass is compared to the initial CC mass in Fig. 5.7 for varying CC Plummer radii. For compact models ($\alpha \geq 0.1$), where almost every star cluster merges and mass loss is small (less than 20%), the final mass of the merger object is comparable to the initial CC mass. In contrast, the enclosed mass of extended CCs strongly depends on the initial CC mass and size. For the most extended CC models the merger object masses are between 25 and 80% of the initial CC mass. The smaller the CC mass and the more extended the CC the larger is the influence of the tidal field, i.e. the larger is the parameter β (Fig. 5.8). For larger values of β, the CC experiences a larger mass loss and the merging process gets suppressed.

Figure 5.9 shows the effective radius, $r_{\rm eff}$, of the merger object vs. the Plummer radius of the CC, $R_{\rm pl}^{\rm CC}$, for different CC masses, $M^{\rm CC}$. Compact CCs result in merger objects with effective radii comparable to the Plummer radius of the CC, while extended CCs result in merger objects with effective radii that are significantly smaller than the corresponding CC Plummer radii. A CC with a Plummer radius of $R_{\rm pl}^{\rm CC} = 10$ pc leads to merger objects with sizes between 10 and 15 pc while a CC with a Plummer radius of $R_{\rm pl}^{\rm CC} = 160$ pc yields an effective radius range of about 15 to 55 pc. The more extended the CC becomes the larger is the spread in the effective radii of the merger objects.

For high CC masses of $M^{\rm CC} \geq 10^{6.5}$ M$_\odot$ the effective radii increase with increasing Plummer radii. In contrast for lower mass CCs, the effective radii decrease again for large Plummer radii of $R_{\rm pl}^{\rm CC} = 160$ pc.

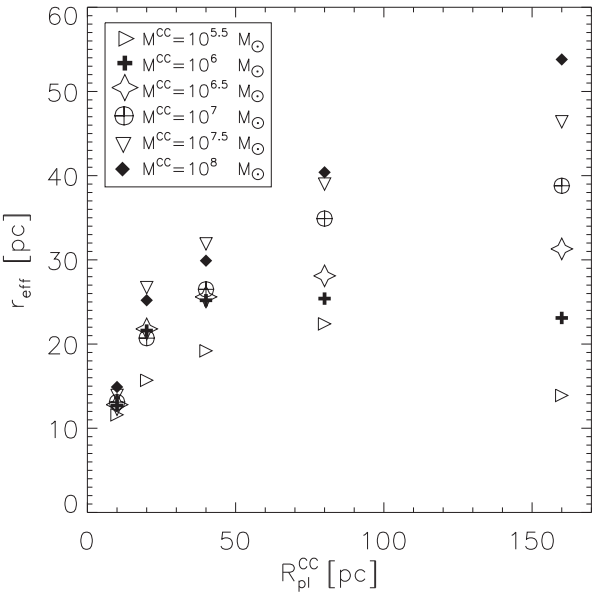

FIGURE 5.9— Effective radius, $r_{\rm eff}$, of the merger object vs. Plummer radius, $R_{\rm pl}^{\rm CC}$, of the initial CC for different initial CC masses, $M^{\rm CC}$, for orbit 1 after 5 Gyr of evolution.

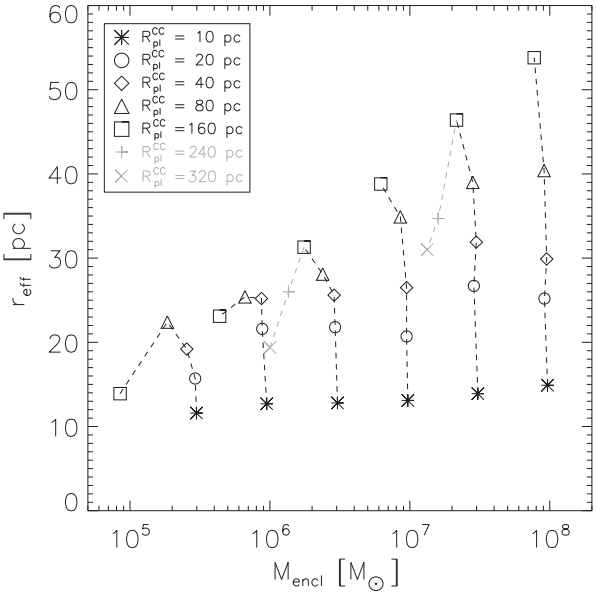

FIGURE 5.10— Effective radii, $r_{\rm eff}$, of the merger objects against the merger object masses, $M_{\rm encl}$, for different initial CC Plummer radii, $R_{\rm pl}^{\rm CC}$, for orbit 1 after 5 Gyr of evolution. The dashed lines connect models with the same initial CC mass. Grey symbols represent additional models.

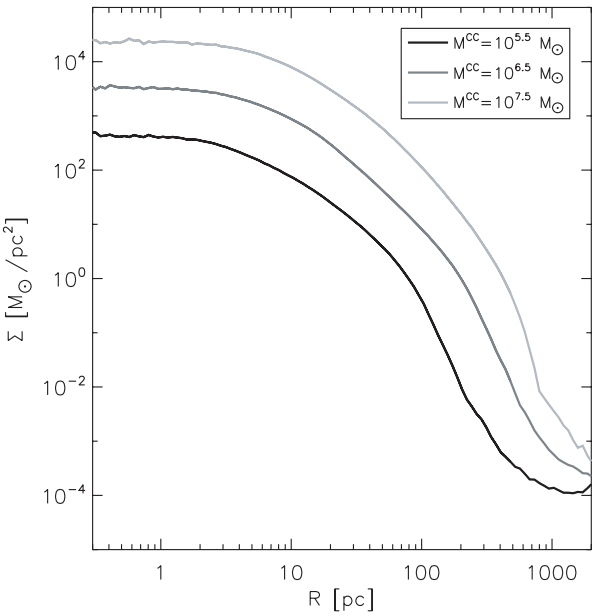

FIGURE 5.11— Surface density profiles of merger objects resulting from extended CC models with a Plummer radius of $R_{\rm pl}^{\rm CC} = 80$ pc and masses of $M^{\rm CC} = 10^{5.5}$, $10^{6.5}$, and $10^{7.5}$ $M_\odot$ for orbit 1 after 5 Gyr.

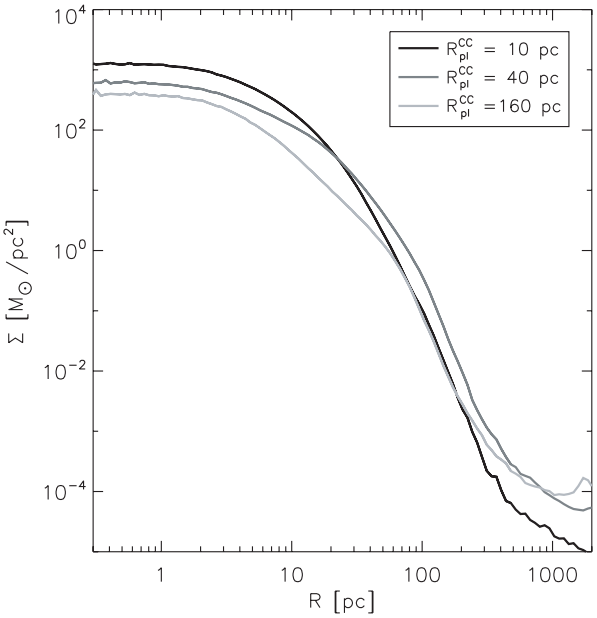

FIGURE 5.12— Surface density profiles of merger objects resulting from low-mass CC models with a mass of $M^{\rm CC} = 10^{5.5}$ $M_\odot$ and Plummer radii of $R_{\rm pl}^{\rm CC} = 10, 40,$ and 160 pc for orbit 1 after 5 Gyr.

5.2.2.4 *Trends in the $r_{\rm eff}$ vs. $M_{\rm encl}$ Space*

The parameter space of the CC models covers the $R_{\rm pl}^{\rm CC}$ vs. $M^{\rm CC}$ space uniformly (Fig. 5.3). The corresponding $r_{\rm eff}$ vs. $M_{\rm encl}$ space of the merger objects is shown in Fig. 5.10. For the most compact CC models with Plummer radii of $R_{\rm pl}^{\rm CC} = 10$ pc the effective radii and masses of the

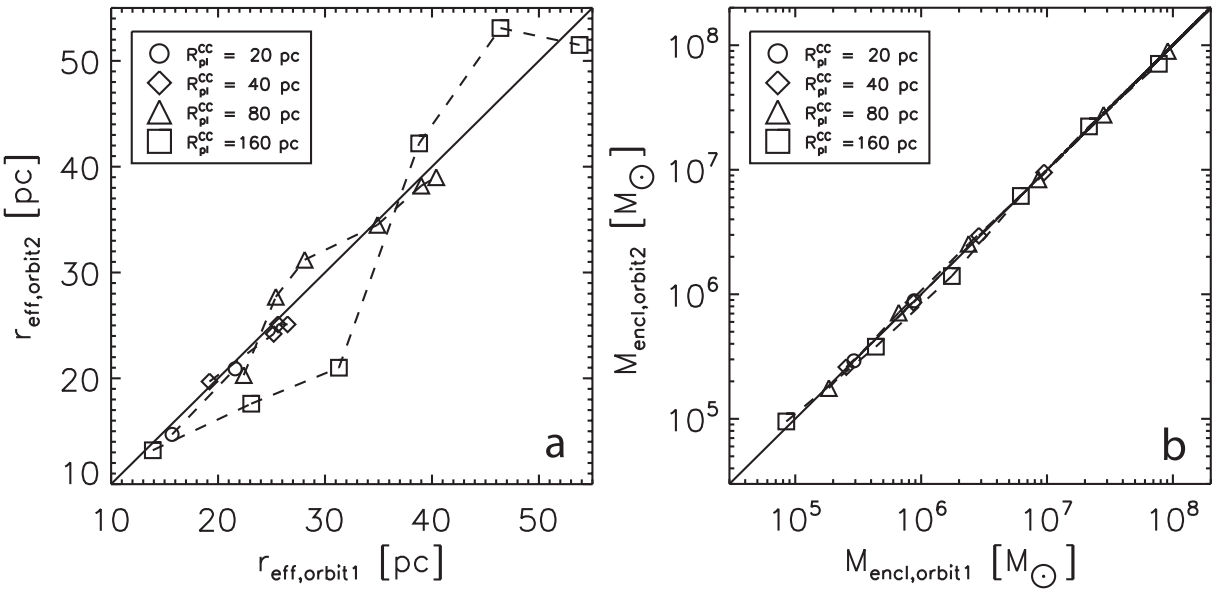

FIGURE 5.13— **a:** Effective radius, $r_{\rm eff,orbit2}$, of the inclined orbit vs. effective radius, $r_{\rm eff,orbit1}$, of the polar orbit for four CC sizes. **b:** Enclosed mass, $M_{\rm encl,orbit2}$, of the inclined orbit vs. enclosed mass, $M_{\rm encl,orbit1}$, of the polar orbit for different CC Plummer radii. For the solid line the values of orbit 1 are equal to those of orbit 2.

merger objects are very similar to the Plummer radii and masses of the CCs, while for the most extended models the effective radius, $r_{\rm eff}$, strongly increases with increasing merger object mass, $M_{\rm encl}$. Figure 5.11 shows surface density profiles of models with $R_{\rm pl}^{\rm CC} = 80$ pc and masses of $M^{\rm CC} = 10^{5.5}$, $10^{6.5}$, and $10^{7.5}$ $M_\odot$. The surface density profiles are well represented by King profiles. The structural parameters central surface density, core radius, effective radius, and tidal radius increase significantly with mass.

For a given CC mass, increasing the size of the CC results in a larger mass loss and larger effective radii of the resulting merger objects. For the lowest-mass models the effective radii decrease again for the largest $R_{\rm pl}^{\rm CC}$. Figure 5.12 illustrates how the surface density profiles of the merger objects change with the CC Plummer radius ($R_{\rm pl}^{\rm CC} = 10$, 40, and 160 pc) for a CC mass of $M^{\rm CC} = 10^{5.5}$ $M_\odot$. The merger objects show King-like profiles. Increasing $R_{\rm pl}^{\rm CC}$ from 10 pc to 40 pc leads to a lower central surface density and larger values in the outer parts resulting in a larger effective radius. The merger object with $R_{\rm pl}^{\rm CC} = 160$ pc suffered a major mass loss, which leads to considerably lower surface densities especially at intermediate radii (5 to 50 pc) resulting in a lower effective radius.

For the very extended, low-mass models, the parameter β is much larger than one, i.e. a considerable number of star clusters of the initial CC is located outside the tidal radius, leading to a rapidly decreasing number of merged star clusters. In Sect. 4.3, I studied such a turnover in detail for the Milky Way EC NGC 2419 and found that the turnover occurs at those $R_{\rm pl}^{\rm CC}$, where the parameter β is sufficiently large to allow entire star clusters to escape the merging process.

As high-mass models have larger tidal radii, their size continuously increases with CC size up to $R_{\rm pl}^{\rm CC} = 160$ pc. However, increasing the CC size further will eventually result in decreasing $r_{\rm eff}$ also for high-mass models. This is demonstrated for two additional models with CC masses of $M^{\rm CC} = 10^{6.5}$ $M_\odot$ and $M^{\rm CC} = 10^{7.5}$ $M_\odot$. The CC sizes were extended to $R_{\rm pl}^{\rm CC} = 240$ pc and $R_{\rm pl}^{\rm CC} = 320$ pc (grey symbols in Fig. 5.10). For both CC masses the results show a clear turnover in the effective radii of the merger objects for these large CC Plummer radii.

The turnover leads to degenerate states in the merger object parameter space, as a relatively compact CC can produce the same merger object as a more massive CC having a significantly

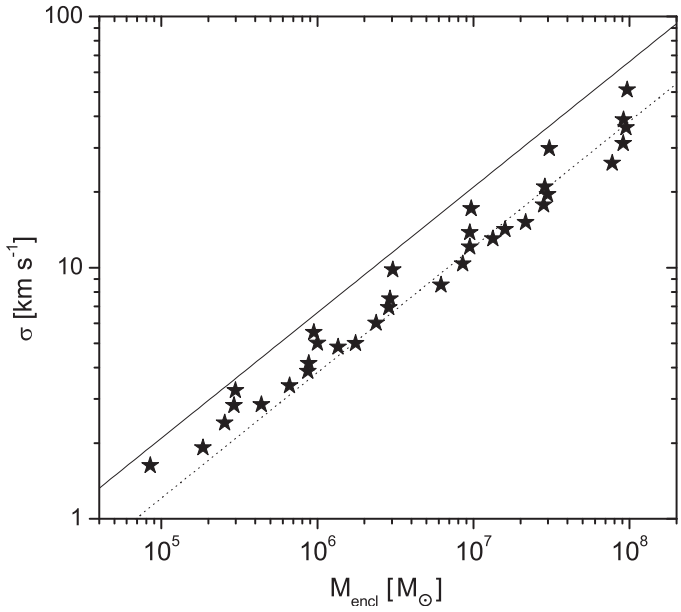

FIGURE 5.14— Global line-of-sight velocity dispersion, σ, of the merger objects as a function of the enclosed mass, $M_{\rm encl}$, for orbit 1 after 5 Gyr. The solid and the dotted line show the scaling relation (Eq. 5.2) for objects with an effective radius of 10 and 30 pc, respectively.

larger CC size. The turnover is a general feature of the merging scenario which occurs when a significant fraction of star clusters is located beyond the tidal radius of the initial CC. Therefore the merging star cluster scenario predicts for each CC mass for a given orbit an upper size limit of the merger objects. The exact CC sizes, where the turnover occurs, will also depend considerably on the initial configuration, i.e. the exact distribution of star clusters in the complex, the number of star clusters constituting the CC, and the orbit (see Sect. 5.3).

5.2.2.5 Impact of Polar Orbit

I recalculated 18 CC models on an inclined orbit (see Fig. 5.4, orbit 2) to estimate its impact on the structural parameters of the merger objects. In order to save computing time I only recalculated CC models where the inclination of the orbit is expected to have a measurable effect. These are the extended CC models with large CC crossing times, large values of β, and low values of α. The CC models on orbit 2 are indicated by open circles in Fig. 5.3.

Figure 5.13a compares the effective radii of the merger objects on the inclined orbit with those on the polar orbit evaluated after 5 Gyr. Both orbits produce merger objects with comparable sizes. Only the most extended models ($R_{\rm pl}^{\rm CC} = 160$ pc), which are most sensitive to the tidal field, show significant deviations between both orbits.

Figure 5.13b compares the enclosed mass of the merger objects on the inclined orbit with those on the polar orbit. While there are some deviations of $M_{\rm encl}$ between the two orbits for the most extended models, the values for both orbits correlate very well.

The results of the inclined orbit as presented in Fig. 5.13 demonstrate that the inclination of the orbit has no significant influence on the overall results and trends of this parametric study.

5.2.2.6 Velocity Dispersion and Dynamical Mass

The global line-of-sight velocity dispersion, σ, is an important observable parameter as it can be used in combination with $r_{\rm eff}$ to estimate the dynamical mass, $M_{\rm dyn}$, of a star cluster. According

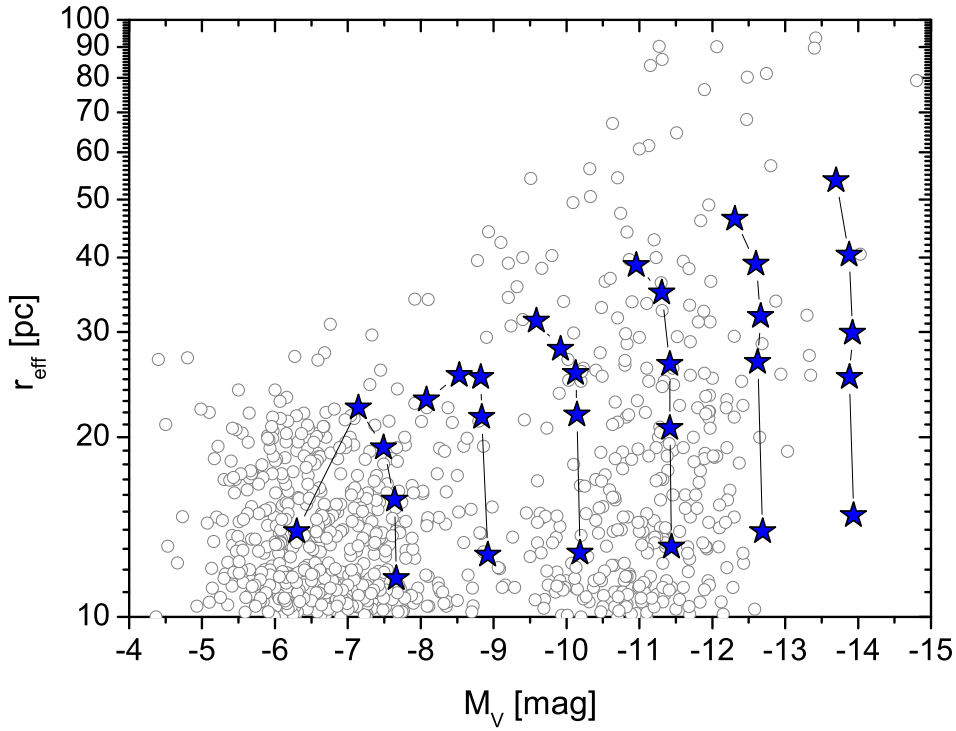

FIGURE 5.15— Diagram of the effective radius, $r_{\rm eff}$, as a function of the total luminosity, $M_{\rm V}$, of the observed EOs as presented in Chapter 3 (grey circles) and the modeled merger objects (blue stars). Objects with the same initial CC mass but different Plummer radii between $R_{\rm pl}^{\rm CC} = 10$ and 160 pc are connected by black lines.

to Spitzer (1987), $M_{\rm dyn}$ can be estimated by

$$M_{\rm dyn} \approx 9.75 \, \frac{r_{\rm eff} \, \sigma^2}{G}, \tag{5.2}$$

where G is the Gravitational constant. Figure 5.14 shows the global line-of-sight velocity dispersion, σ, as a function of the enclosed mass of the merger objects on the eccentric polar orbit. The turnover, which was discussed in Sect. 5.2.2.4, is clearly seen also in the velocity dispersion, as $r_{\rm eff}$ and σ are not independent from each other. For a given mass, an increasing $r_{\rm eff}$ results in a decreasing σ. The solid and the dotted line in Fig. 5.14 show the scaling relation of σ versus mass for objects with an effective radius of 10 and 30 pc, respectively.

The dynamical masses calculated according to Eq. 5.2 are for all models in very good agreement with the enclosed masses with a scatter of about five percent. The small deviations are due to slight deviations from virial equilibrium and due to the fact that Eq. 5.2 is only a rough estimate of the dynamical mass.

5.2.3 Comparison with Observations

I convert the enclosed masses of the merger objects into absolute V-band luminosities to allow for direct comparison with the 835 observed EOs presented in Chapter 3, using the formula

$$M_{\rm V} = M_{\rm V,solar} - 2.5 \times \log_{10}(M_{\rm encl} \frac{L_{\rm V}}{M}), \tag{5.3}$$

where $M_{\rm V,solar} = 4.83$ mag is the absolute solar V-band luminosity, $M_{\rm encl}$ the enclosed mass of the merger object and $\frac{M}{L_V}$ the mass-to-light ratio in units of $M_{\odot}/L_{V,\odot}$. I use a mass-to-light ratio of 3, as an intermediate value between the typical mass-to-light ratios of about 2 and 4 of GCs and UCDs, respectively.

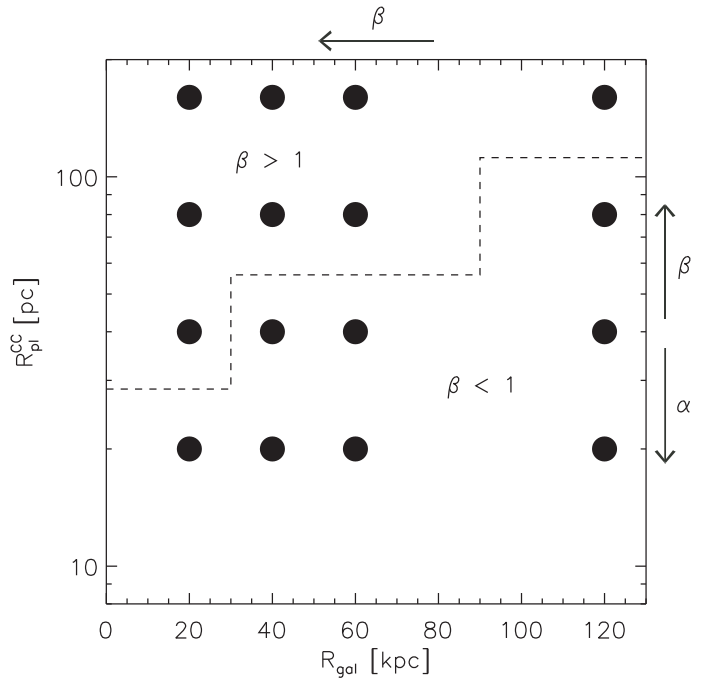

FIGURE 5.16— Parameter space for the CC models of the circular orbit simulations. The parameters CC Plummer radius, $R_{\rm pl}^{\rm CC}$, and galactic distance, $R_{\rm gal}$, constitute a matrix of 4×4 values. The circles mark the 16 simulations for the low-mass CC models of $M^{\rm CC} = 10^{5.5}$ M$_\odot$. The arrows indicate the increase of α- and β-values (see Chapter 2). The dashed line separates the CC models with $\beta < 1$ from the CC models with $\beta > 1$.

Figure 5.15 shows $r_{\rm eff}$ as a function of the total luminosity of the observed ECs and UCDs (grey circles) and the models (blue stars). The merger objects show a similar trend of increasing maximal effective radii with increasing luminosity as the observed EOs. The vast majority of the observed ECs and UCDs, i.e. about 95%, are located within the parameter space covered by the modeled merger objects. Only the extremely extended EOs, which represent about five percent of the EO-sample, are outside the parameter space covered by the objects on the eccentric orbit chosen for this section.

It is quite remarkable that the modeled merger objects, which were calculated on one single orbit, agree that well with the overall distribution of observed EOs. This finding demonstrates that the initial CC mass and size are the basic and most important parameters of a CC that define the evolution of a CC.

5.3 The Influence of the Orbit on the Evolution of Merger Objects

Next to the initial CC mass and size the external tidal field is the third important factor which determines the fate of a CC. In this section, I systematically study the influence of the tidal field on the evolution of a CC.

5.3.1 Numerical Set-Up and Varied Parameters

The parameters of the CCs and the individual star clusters are the same as those of the previous section, except that the very compact CCs with $R_{\rm pl}^{\rm CC} = 10$ pc are not considered for this study and that the CC mass is fixed to $M^{\rm CC} = 10^{5.5}$ M$_\odot$.

I first investigate circular orbits which are the simplest orbits with only one parameter which is the galactic distance, $R_{\rm gal}$. The circular orbit is a special case of the eccentric orbit where the perigalactic distance, $R_{\rm p}$, equals its apogalactic distance, $R_{\rm a}$, i.e. $R_{\rm p} = R_{\rm a} = R_{\rm gal}$.

TABLE 5.1— Orbital parameters of the circular orbit simulations

Orbit [a]	$R_{\rm gal}$ [b] (kpc)	$v_{\rm circ}$ [c] (km s^{-1})	$T_{\rm orb}$ [d] (Myr)	$t_{\rm int}$ [e] (Myr)	$\frac{t_{\rm int}}{T_{\rm orb}}$ [f]
CIRC_20	20	230	534	5000	9.4
CIRC_40	40	214	1151	5000	4.3
CIRC_60	60	207	1784	5000	2.8
CIRC_120	120	198	3730	5000	1.3

[a] Circular orbit: CIRC_$R_{\rm gal}$.
[b] Galactic distance.
[c] Circular velocity obtained from the rotation curve of the Milky Way.
[d] Orbital period $T_{\rm orb} = \frac{2\pi R_{\rm gal}}{v_{\rm circ}}$.
[e] Integration time.
[f] Number of revolutions.

The model parameters of the circular orbit simulations are visualized in Fig. 5.16. The nomenclature of the models is explained in Appendix C.3. I performed 16 simulations for the low-mass CC models of $M^{\rm CC} = 10^{5.5}$ M$_\odot$ with Plummer radii of $R_{\rm pl}^{\rm CC} = 20$, 40, 80, and 160 pc at four different galactic distances of $R_{\rm gal} = 20$, 40, 60, and 120 kpc and additional four simulations without an external tidal field. The orbital parameters of the circular orbit simulations are displayed in Table 5.1.

In addition, I performed simulations on eccentric orbits (Table 5.2) to determine the influence of the peri- and apogalactic distance of an orbit. The eccentric orbit between 20 and 60 kpc has already been discussed in detail in Sect. 5.2. I considered three additional eccentric orbits between 20 and 120 kpc, 40 and 60 kpc, and 40 and 120 kpc (Fig. 5.17) for CC models with Plummer radii of $R_{\rm pl}^{\rm CC} = 40$ and 160 pc. The orbital periods lie between 872 and 1814 Myr. In the merging star cluster scenario, the CCs are most likely formed at the perigalactic passage of the parent galaxy where the impact of the interaction is strongest. Therefore, the calculations start at the perigalactic distance. At an integration time of 5 Gyr the merger objects are all in different orbital phases. To get comparable values for the structural parameters of the extended objects the simulations are all analyzed at the perigalactic distance closest to 5 Gyr. To get a feeling how an apogalactic starting point would affect the outcome of the simulations I also considered two eccentric simulations for CC models with $R_{\rm pl}^{\rm CC} = 160$ pc and a perigalactic distance of $R_{\rm p} = 20$ kpc, which start at the apogalactic distances of $R_{\rm a} = 60$ and 120 kpc (Table 5.2), respectively.

5.3.2 Results from the Circular Orbits

5.3.2.1 *Correlation of the Structural Parameters of the Merger Objects with the $R_{\rm pl}^{\rm CC}$ vs. $R_{\rm gal}$ Parameter Space*

Figure 5.18 shows the fraction of mass of the initial CC which ended up in the merger object versus the galactic distance of the circular orbits, $R_{\rm gal} = 20$, 40, 60, and 120 kpc, after 5 Gyr of evolution. For compact CC models almost every SC merges (see Table C.6) and mass loss is small. For extended CC models the tidal field has a larger influence. The mass loss for the extended CC models is larger than for compact CC models. For CC models with $R_{\rm pl}^{\rm CC} = 160$ pc the mass loss lies between 80 and 30%. The stronger the tidal field, i.e. the smaller the galactic distance of the circular orbit, the larger is the mass loss.

Figure 5.19 shows the effective radius, $r_{\rm eff}$, of the merger object against the Plummer radius

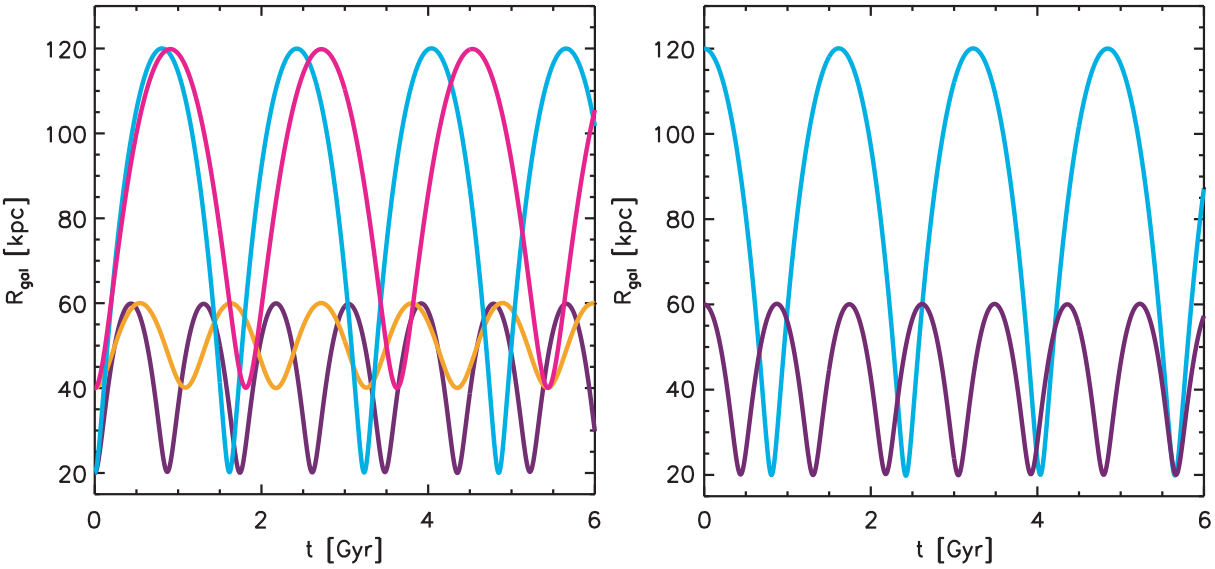

FIGURE 5.17— Galactic distance, R_{gal}, of the merger object vs. time, t. The simulations were terminated at the perigalactic distance closest to 5 Gyr (Table 5.2). **Left:** Eccentric orbits between 20 – 60 kpc, 20 – 120 kpc, 40 – 60 kpc, and 40 – 120 kpc starting at the perigalactic distance. **Right:** Eccentric orbits between 20 – 60 kpc and 20 – 120 kpc starting at the apogalactic distance.

TABLE 5.2— Orbital parameters of the eccentric orbit simulations

Orbit [a]	R_p [b] (kpc)	R_a [c] (kpc)	e [d]	T_{orb} [e] (Myr)	t_{int} [f] (Myr)	$\frac{t_{int}}{T_{orb}}$ [g]	R_{start} [h] (kpc)
ECC_20_60	20	60	0.5	872	5220	6	20
ECC_20_120	20	120	0.7	1616	4846	3	20
ECC_40_60	40	60	0.2	1090	5432	5	40
ECC_40_120	40	120	0.5	1814	5438	3	40
ECC_60_20	20	60	0.5	872	4795	5.5	60
ECC_120_20	20	120	0.7	1616	5652	3.5	120

[a] Eccentric orbit: ECC_R_p_R_a and ECC_R_a_R_p, respectively.
[b] Perigalactic distance.
[c] Apogalactic distance.
[d] Eccentricity of the orbit.
[e] Orbital period.
[f] Integration time.
[g] Number of revolutions.
[h] Starting point.

of the initial CC, R_{pl}^{CC}, for different galactic distances of $R_{gal} = 20$, 40, 60, and 120 kpc of the circular orbits and without an external tidal field after 5 Gyr of evolution. Compact CC models with $R_{pl}^{CC} = 20$ pc result in merger objects with slightly smaller sizes than the initial R_{pl}^{CC}. The effective radii for these merger objects are between 15 and 17 pc. In contrast, extended CC models lead to merger objects with effective radii that are significantly smaller than the corresponding CC Plummer radii. A CC with an initial Plummer radius of $R_{pl}^{CC} = 160$ pc covers an effective radius range from 11 to 93 pc. The more extended the initial CC the larger the spread in the effective radii of the merger objects. The weaker the tidal field, i.e. the larger the galactic distance of the orbit, the more extended the merger objects become. At small galactic distances

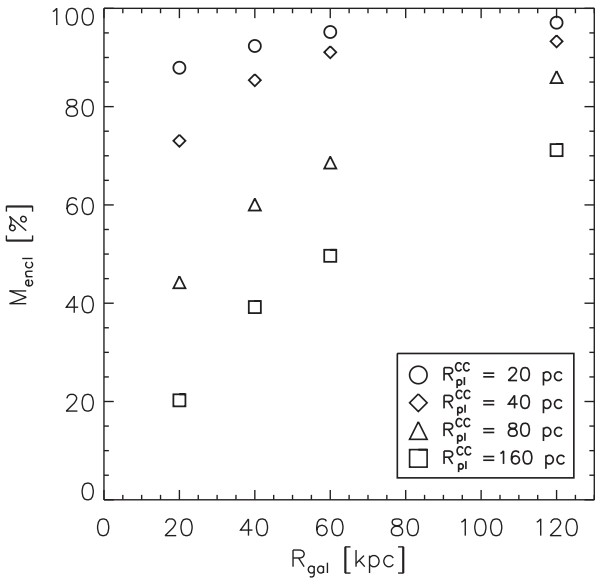

FIGURE 5.18— Fraction of mass of the initial CC which ended up in the merger object vs. the galactic distance of the circular orbit, $R_{\rm gal} = 20$, 40, 60, and 120 kpc, after 5 Gyr.

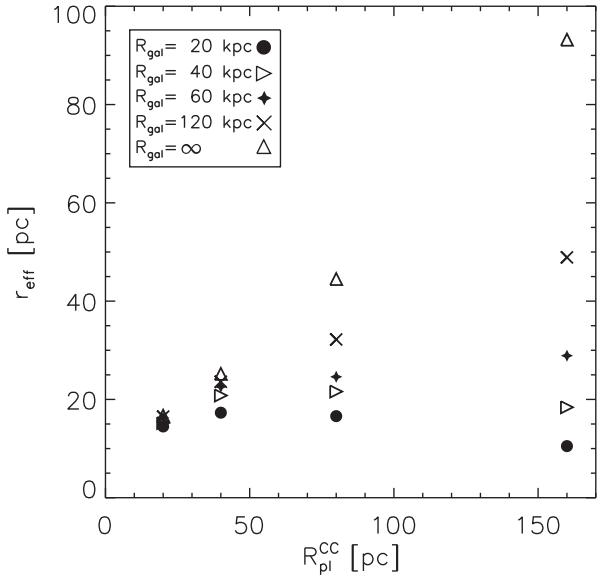

FIGURE 5.19— Effective radius, $r_{\rm eff}$, of the merger object vs. Plummer radius of the initial CC, $R_{\rm pl}^{\rm CC}$, for different galactic distances of $R_{\rm gal} = 20$, 40, 60, and 120 kpc of the circular orbits and without an external tidal field after 5 Gyr of evolution.

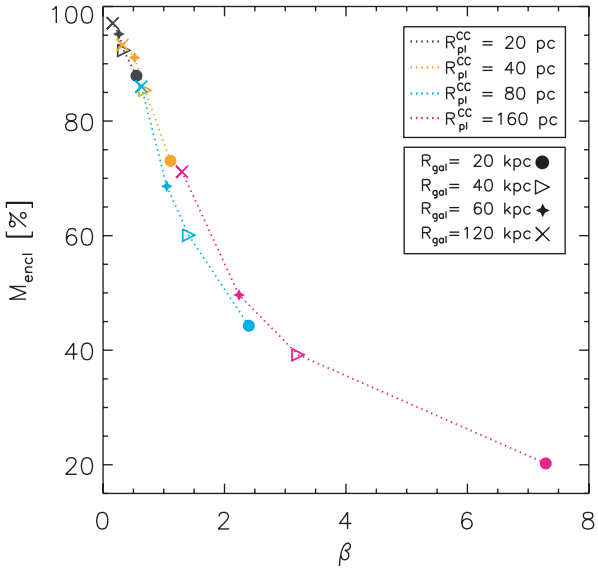

FIGURE 5.20— Fraction of mass of the initial CC which ended up in the merger object versus the parameter β for different galactic distances of $R_{\rm gal} = 20$, 40, 60, and 120 kpc of the circular orbit after 5 Gyr. Models with the same initial CC Plummer radius, $R_{\rm pl}^{\rm CC}$, are connected by dotted lines.

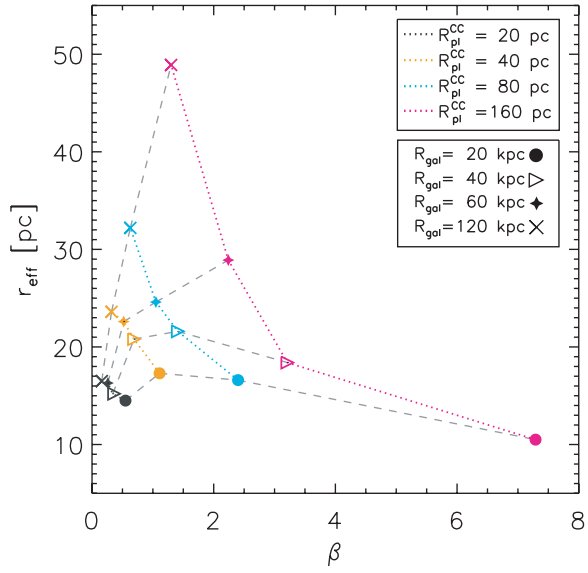

FIGURE 5.21— Effective radii, $r_{\rm eff}$, of the merger objects vs. the parameter β for different galactic distances of the circular orbits, $R_{\rm gal} = 20$, 40, 60, and 120 kpc, after 5 Gyr. Models with the same initial CC Plummer radius, $R_{\rm pl}^{\rm CC}$, are connected by dotted lines. The dashed gray lines connect models at the same galactic distance.

of 20 and 40 kpc there is a turnover in the effective radii of the merger objects and the effective radii decrease again for larger CC Plummer radii.

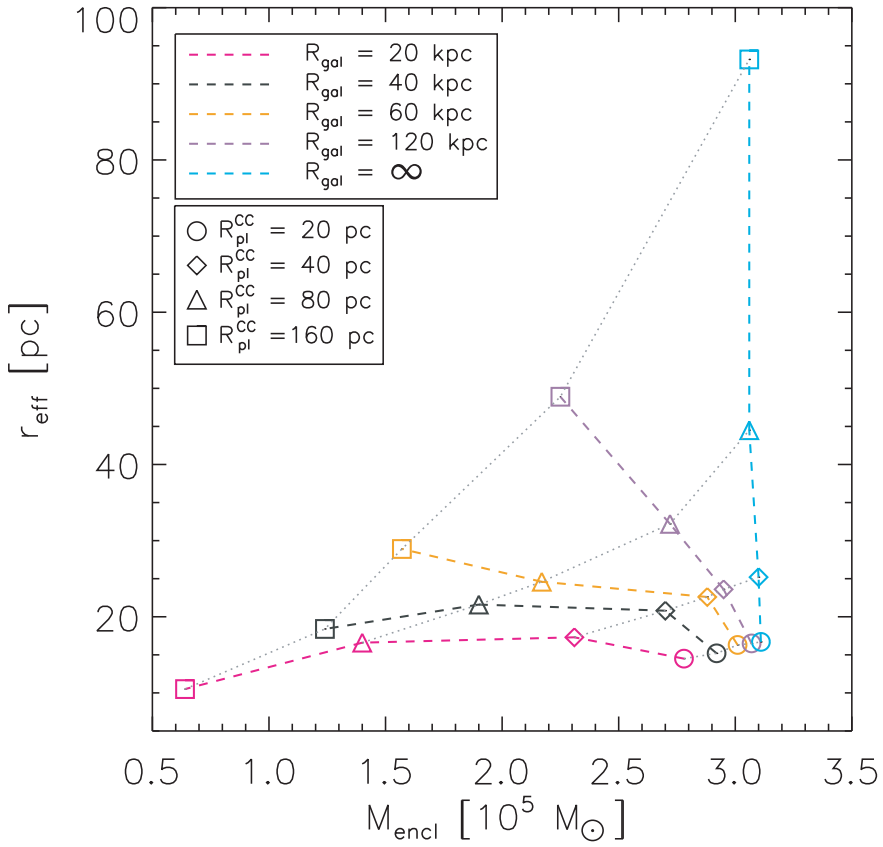

FIGURE 5.22— Effective radii, $r_{\rm eff}$, of the merger objects against the merger object masses, $M_{\rm encl}$, for different galactic distances of the circular orbits, $R_{\rm gal} = 20$, 40, 60, and 120 kpc, and without a tidal field after 5 Gyr. The dotted lines connect models with the same initial CC Plummer radius, $R_{\rm pl}^{\rm CC}$.

5.3.2.2 *Correlation of Structural Parameters of Merger Object with β*

The impact of the tidal field on the evolution of the CC can be estimated by the parameter β (see Sect. 2.1.4). The beta-values of the models are presented in Table C.6. The larger the value of the parameter β the larger the influence of the tidal field. Figures 5.20 and 5.21 show the enclosed mass, $M_{\rm encl}$, and the effective radius, $r_{\rm eff}$, of the merger object as a function of the parameter β for four different galactic distances, $R_{\rm gal}$, of the orbit. Compact CC models with a Plummer radius of $R_{\rm pl}^{\rm CC} = 20$ pc all have β-values less than one and are therefore only slightly affected by the tidal field. Extended models, however, cover a larger range of β-values. For the models with $R_{\rm pl}^{\rm CC} = 160$ pc the parameter β varies between 1.3 and 7.3. The smaller the galactic distance, $R_{\rm gal}$, of the circular orbit the larger is the corresponding β-value for a given CC size and thus the larger is the impact of the tidal field on the CC evolution. The stronger the tidal field the smaller the effective radii and masses of the resulting merger objects.

5.3.2.3 *Trends in the $r_{\rm eff}$ vs. $M_{\rm encl}$ Space*

The $r_{\rm eff}$ vs. $M_{\rm encl}$ space for merger objects on circular orbits and without an external tidal field is presented in Fig. 5.22.

For simulations without a tidal field almost all of the initial CC mass is kept and the sizes of the merger objects are only determined by its initial CC Plummer radius as the configuration is the same for all models. The larger the CC Plummer radius the larger the size of the corresponding merger object. But even in the absence of a tidal field the effective radii of the merger

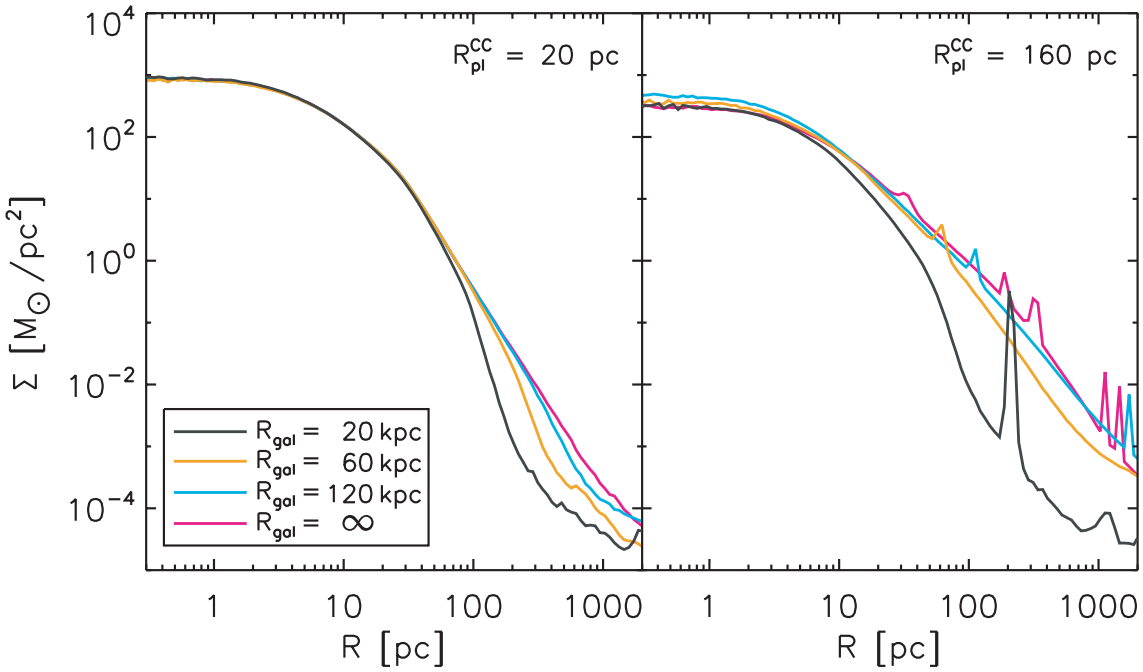

FIGURE 5.23— Surface density profiles of the merger objects resulting from a CC with $M^{CC} = 10^{5.5}$ $M_\odot$ and $R_{pl}^{CC} = 20$ and 160 pc for circular orbits at $R_{gal} = 20$, 60, and 120 kpc and without tidal field after 5 Gyr. The spikes (e.g. near 200 pc) are unmerged star clusters.

objects are smaller than the initial CC Plummer radii.

In simulations with an external tidal field the effective radii and masses of the merger objects are smaller than the corresponding values of the merger objects in simulations without a tidal field. For each CC Plummer radius the mass and effective radius of the merger objects become smaller with decreasing galactic distance and accordingly increasing tidal field.

For the most compact CC models with Plummer radii of $R_{pl}^{CC} = 20$ pc the effective radii of the merger objects are quite similar to the results of the simulations without a tidal field. Mass loss for these models is of the order of a few percent in weak tidal fields and increases further to about 10% for stronger tidal fields. Thus compact CCs are hardly affected by their environment.

For the most extended CC models considered in this study with CC Plummer radii of $R_{pl}^{CC} = 160$ pc the effective radii, r_{eff}, of the merger objects cover a larger range from 11 pc ($R_{gal} = 20$ kpc) to 93 pc (without tidal field). Also the masses of the merger objects increase from about $M_{encl} = 0.64 \cdot 10^5$ $M_\odot$ ($R_{gal} = 20$ kpc) to $M_{encl} = 3.1 \cdot 10^5$ $M_\odot$ (without tidal field). The tidal field has a strong influence on the evolution of extended CC models.

The orbits at small galactic distances of $R_{gal} = 20$ and 40 kpc show a turnover in the r_{eff} vs. M_{encl} space, i.e. at a certain CC size the effective radii of the merger objects do not increase further for larger CC sizes but become smaller again. Therefore a compact CC model (e.g. $R_{pl}^{CC} = 20$ pc) on a circular orbit at 20 kpc results in a larger merger object with $r_{eff} = 14.5$ pc than an extended CC model (e.g. $R_{pl}^{CC} = 160$ pc) which evolves into a merger object with an effective radius of only $r_{eff} = 10.5$ pc. For simulations at larger galactic distances ($R_{gal} = 60$ and 120 kpc) the turnover disappears and the effective radii of the merger objects increase with increasing initial CC sizes.

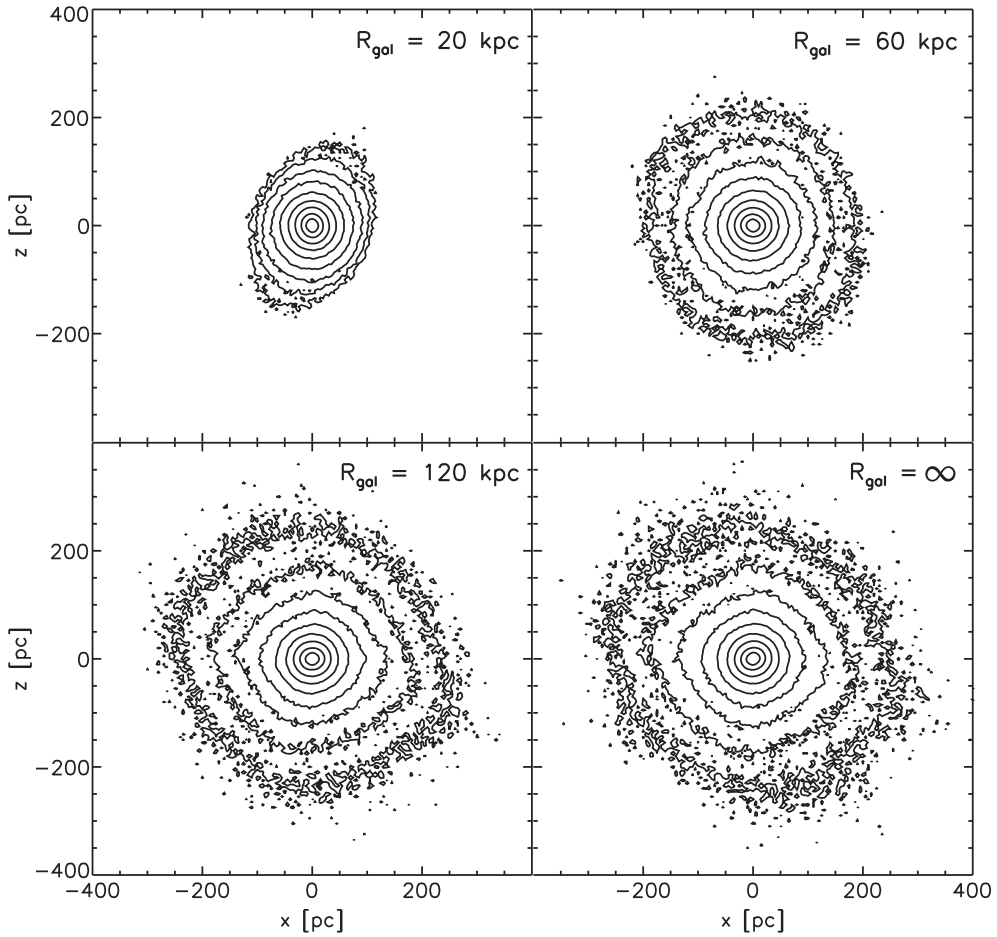

FIGURE 5.24— Contour plots on the x-z-plane of the merger objects for the CC models with $R_{\rm pl}^{\rm CC} = 20$ pc and $M^{\rm CC} = 10^{5.5}$ $M_\odot$ for circular orbits at $R_{\rm gal} = 20$, 60, and 120 kpc and without tidal field displayed at $t = 5$ Gyr. The lowest contour level corresponds to 5 particles per pixel. The pixel size is 5 pc. This yields 0.02 $M_\odot$ pc^{-2}. The contour levels increase further by a factor of 3.

5.3.2.4 *Surface Density Profiles of the Merger Objects*

Figure 5.23 illustrates how the surface density profiles of the merger objects differ for compact ($R_{\rm pl}^{\rm CC} = 20$ pc) and extended ($R_{\rm pl}^{\rm CC} = 160$ pc) initial CC models at galactic distances of $R_{\rm gal} = 20$, 60, and 120 kpc and without a tidal field. The merger objects resulting from compact and extended CC models show different characteristics.

For compact CC models the shape of the surface density profiles of the merger objects are very similar in the inner part and only differ significantly in the outer parts ($R > 50$ pc) of the profile. The corresponding contourplots for CC models with $R_{\rm pl}^{\rm CC} = 20$ pc are displayed in Fig. 5.24.

Merger objects resulting from extended CC models, however, are very orbit dependent. The structural parameters central surface density, core radius, effective radius, and tidal radius increase significantly with galactic distance. The merger object at $R_{\rm gal} = 20$ kpc has suffered a major mass loss, which leads to considerably lower surface densities especially at intermediate radii (5 to 50 pc) resulting in a lower effective radius. The spike in the profile is a close star cluster around the merger object. For the simulations at large galactic distances ($R_{\rm gal} = 60$ and 120 kpc) and without a tidal field mass loss is small and the surface density profiles look more alike. The larger the galactic distance the larger the values of the surface densities in the outer parts and the profiles are less tidally truncated. Extended models in weak tidal fields frequently

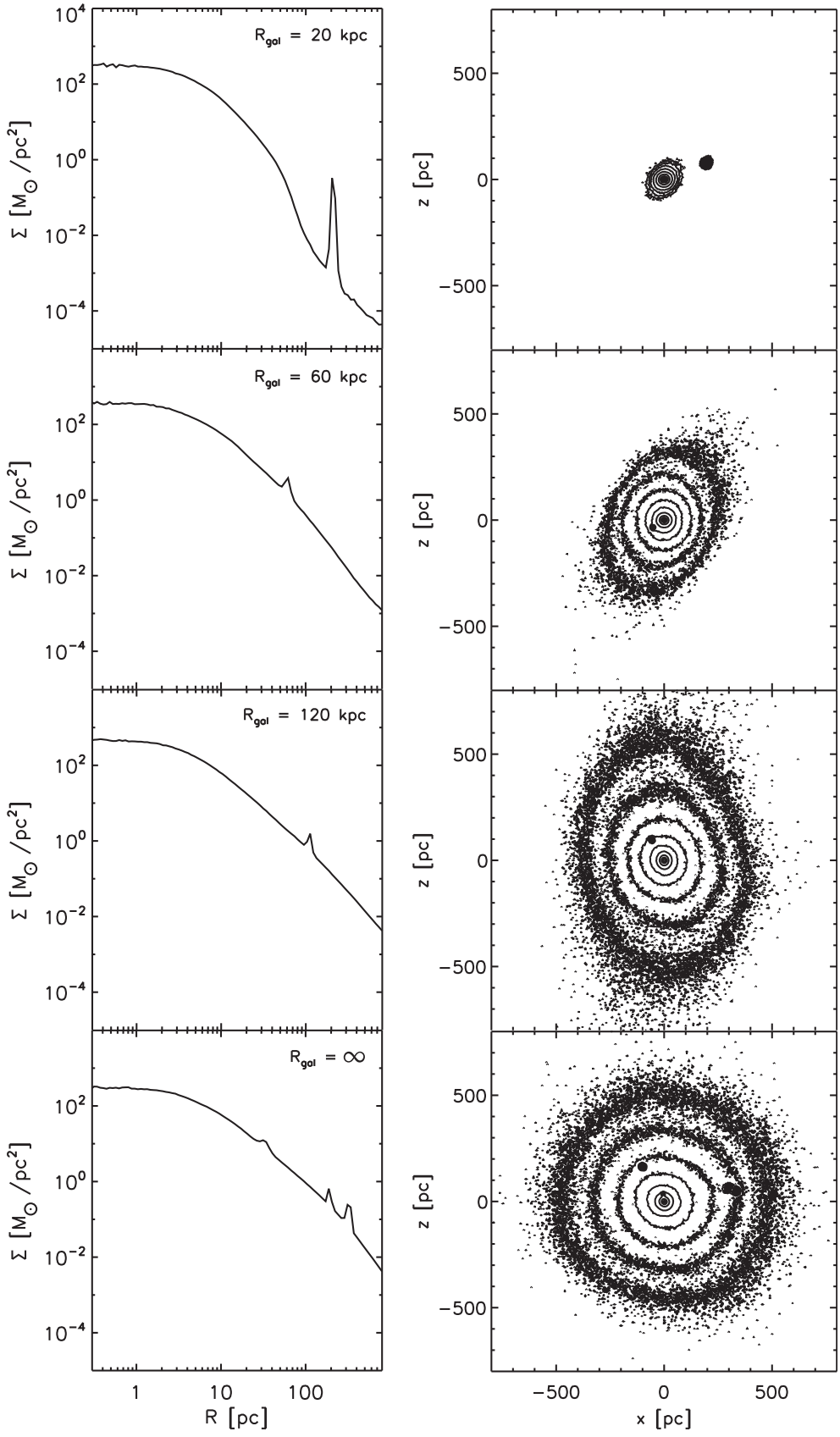

FIGURE 5.25— **Left:** Surface density profiles of the merger objects with $M^{\rm CC} = 10^{5.5}$ $M_\odot$ and $R_{\rm pl}^{\rm CC} = 160$ pc for circular orbits at $R_{\rm gal} = 20, 60$, and 120 kpc and without a tidal field after 5 Gyr. **Right:** Corresponding contour plots on the x-z-plane of the merger objects. The lowest contour level corresponds to 5 particles per pixel. The pixel size is 5 pc. This yields 0.02 $M_\odot$ pc^{-2}. The contour levels increase further by a factor of 3.

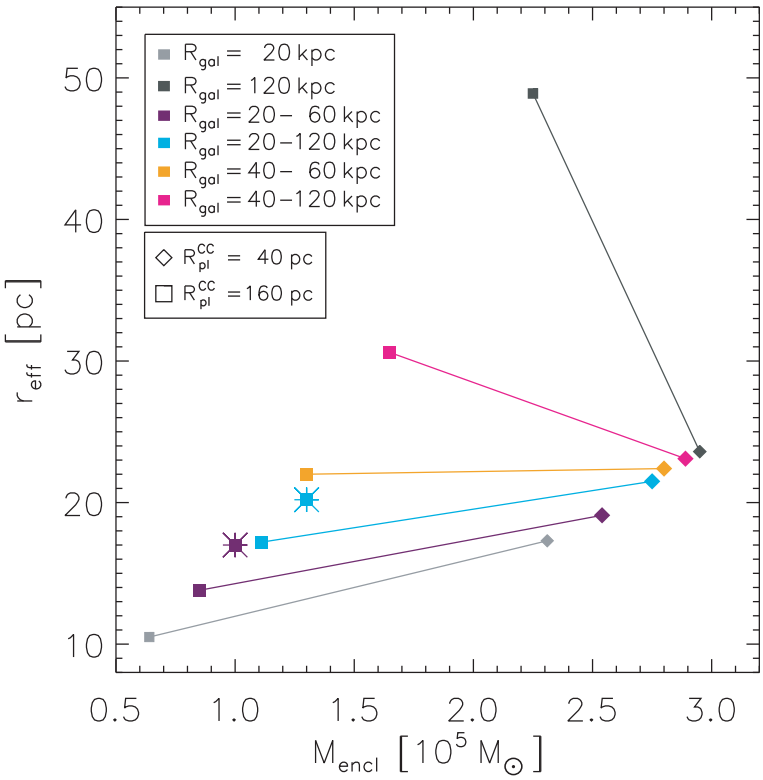

FIGURE 5.26— Effective radii, $r_{\rm eff}$, of the merger objects against the merger object masses, $M_{\rm encl}$, for different eccentric orbits (20 – 60 kpc, 20 – 120 kpc, 40 – 60 kpc, 40 – 120 kpc). The circular orbits at $R_{\rm gal} = 20$ and 120 kpc of Fig. 5.22 are also plotted for comparison. The two eccentric simulations marked by an additional asterisk were started at the apocenter instead of the pericenter

show several unmerged SCs which are recognizable as multiple spikes in the surface density profiles. The corresponding contourplots for CC models with $R_{\rm pl}^{\rm CC} = 160$ pc are displayed in Fig. 5.25. At small galactic distances the CCs end up in rather compact objects which is due to the turnover. In weak tidal fields, however, their size increases with galactic distance. The number of unmerged star clusters in the vicinity of the merger objects is larger the weaker the tidal field.

5.3.3 Results from the Eccentric Orbits

5.3.3.1 Trends in the $r_{\rm eff}$ vs. $M_{\rm encl}$ Space

Figure 5.26 shows the effective radii, $r_{\rm eff}$, of the merger objects against the merger object masses, $M_{\rm encl}$, for the different eccentric orbits listed in Table 5.2. All simulations without an additional asterisk start at a perigalactic distance of 20 or 40 kpc. I considered one compact CC model ($R_{\rm pl}^{\rm CC} = 40$ pc) and one extended CC model ($R_{\rm pl}^{\rm CC} = 160$ pc). For comparison, I added the results of the circular orbit simulations of Sect. 5.3.2 at distances of 20 and 120 kpc as they coincide with the peri- and apogalactic distances of the eccentric orbits.

The final structural parameters for the merger objects of the computations of compact CCs with $R_{\rm pl}^{\rm CC} = 40$ pc lie between the values obtained from the circular orbit simulations at their peri- and apogalactic distances, $R_{\rm p}$ and $R_{\rm a}$. Both, the peri- and apogalactic distance of an eccentric orbit, have an influence on the structural parameters of the resulting merger objects.

For a fixed perigalactic distance increasing the apogalactic distance of an eccentric orbit from $R_{\rm a} = 60$ to 120 kpc leads to larger effective radii and masses of the merger objects. For example a compact CC model on a circular orbit at 20 kpc ($R_{\rm p}$ = $R_{\rm a} = 20$ kpc) leads to a merger

object with an effective radius of $r_{\rm eff} = 17.3$ pc containing 73% of the initial CC mass (Table C.6). Increasing the apogalactic distance to $R_{\rm a} = 60$ kpc results in a merger object which already keeps 80% of the initial CC mass and its effective radius increases to $r_{\rm eff} = 19.1$ pc (Table C.7). For an apogalactic distance of $R_{\rm a} = 120$ kpc the resulting merger object retains 87% of the initial CC mass and its effective radius increases further to $r_{\rm eff} = 21.5$ pc (Table C.7).

Keeping the apogalactic distance fixed and increasing the perigalactic distance from 20 to 40 kpc results in merger objects with larger effective radii and masses as well. For example a CC on an eccentric orbit between $R_{\rm p} = 20$ kpc and $R_{\rm a} = 120$ kpc leads to a merger object with an effective radius of $r_{\rm eff} = 21.5$ pc containing 87% of the initial CC mass (Table C.7). Increasing the perigalactic distance to $R_{\rm p} = 40$ kpc results in a merger object which already keeps 91% of the initial CC mass and its effective radius increases to $r_{\rm eff} = 23.1$ pc (Table C.7). For a perigalactic distance of $R_{\rm p} = R_{\rm a} = 120$ kpc (circular orbit at 120 kpc) the resulting merger object retains 98% of the initial CC mass and its effective radius increases further to $r_{\rm eff} = 25.2$ pc (Table C.6). Thus the larger the peri- and apogalactic distances of the orbit become, the more massive and extended are the resulting merger objects.

The merger objects resulting from extended CC models with $R_{\rm pl}^{\rm CC} = 160$ pc show the same sequence as the compact CC models. This is visualized in Fig. 5.26 by the lines connecting the compact and extended models which do not cross each other. The structural parameter values for the extended models also lie in between the values of the circular orbit simulations at their peri- and apogalactic distances. In contrast to the compact CC models the influence of the apogalactic distance is much smaller. For all extended CC models the values of the structural parameters of the merger objects are closer to the results of the circular orbit simulations at the pericentric distance than to the values obtained at apocenter. But it still holds that the larger the apogalactic distance of the orbit the more massive and extended the merger objects become.

I performed two simulations of extended CCs ($R_{\rm pl}^{\rm CC} = 160$ pc) that start at the apogalactic distance instead of the perigalactic distance (they are indicated by an additional asterisk in Fig. 5.26). The orbital parameters are displayed Table 5.2. Both orbits have the same perigalactic distance of $R_{\rm p} = 20$ kpc, but a different apogalactic distance of $R_{\rm a} = 60$ and 120 kpc, respectively. The simulations starting at the apogalactic distance have a larger number of merged SCs (Table C.7). For the eccentric orbit between 20 and 60 kpc for example only 13 SCs merged in the simulations with the starting point at the pericenter (CC_51-ECC_20_60) while 17 SCs merged when starting at the apocenter (CC_51-ECC_60_20). The larger number of merged SCs in the simulations with an apogalactic starting point leads to larger masses and effective radii of the resulting merger objects. The enclosed mass and the effective radii of the merger object increased from $M_{\rm encl} = 0.85 \cdot 10^5$ M$_\odot$ and $r_{\rm eff} = 13.8$ pc (CC_51-ECC_20_60) to $M_{\rm encl} = 1.00 \cdot 10^5$ M$_\odot$ and $r_{\rm eff} = 17.0$ pc (CC_51-ECC_60_20).

5.3.3.2 Influence of the Orbital Phase and the Line-of-Sight on the Surface Density Profile

Figure 5.27 is an illustration of the influence of the orbital phase on the merger object. The figure shows the merger object and the leading and trailing arm of unmerged star clusters of model CC_51-ECC_20_120 ($M^{\rm CC} = 10^{5.5}$ M$_\odot$, $R_{\rm pl}^{\rm CC} = 160$ pc, $R_{\rm p} = 20$ kpc, $R_{\rm a} = 120$ kpc) at the last apo- and perigalacticon of the calculations. The unmerged star clusters align along the orbit. The line-of-sight is perpendicular to the orbital plane. At perigalacticon the unmerged star clusters have their largest distance to the merger object. Close to apogalacticon the merger object and its tails of unbound material and unmerged star clusters get decelerated and thus compressed. The outer part of the surface density profile is therefore enhanced with unbound stars and shows spikes of unmerged star clusters. Figure 5.28 shows the corresponding contourplots at peri- and apogalacticon. When the merger object approaches its perigalacticon it becomes more elongated and no unmerged star clusters or diffuse unbound material are found

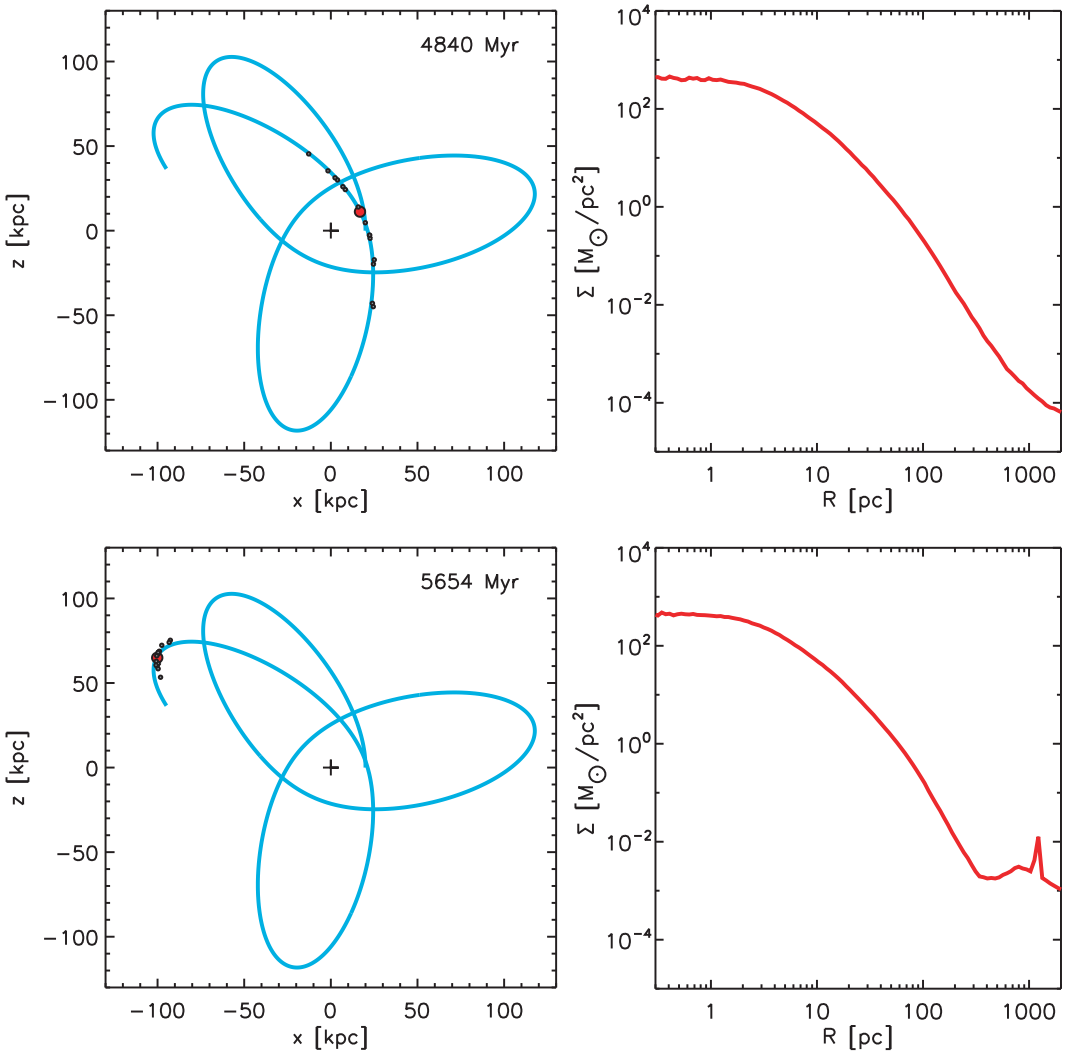

FIGURE 5.27— **Left:** Illustration of the spatial distribution of the star clusters of computation CC_51-ECC_20_120 at the peri- and apogalactic distance. It consists of a large merger object and a leading and trailing arm of unmerged star clusters. The circles indicate the positions but not the sizes of the star clusters. **Right:** Corresponding surface density profiles of the merger objects at the peri- and apogalactic distance.

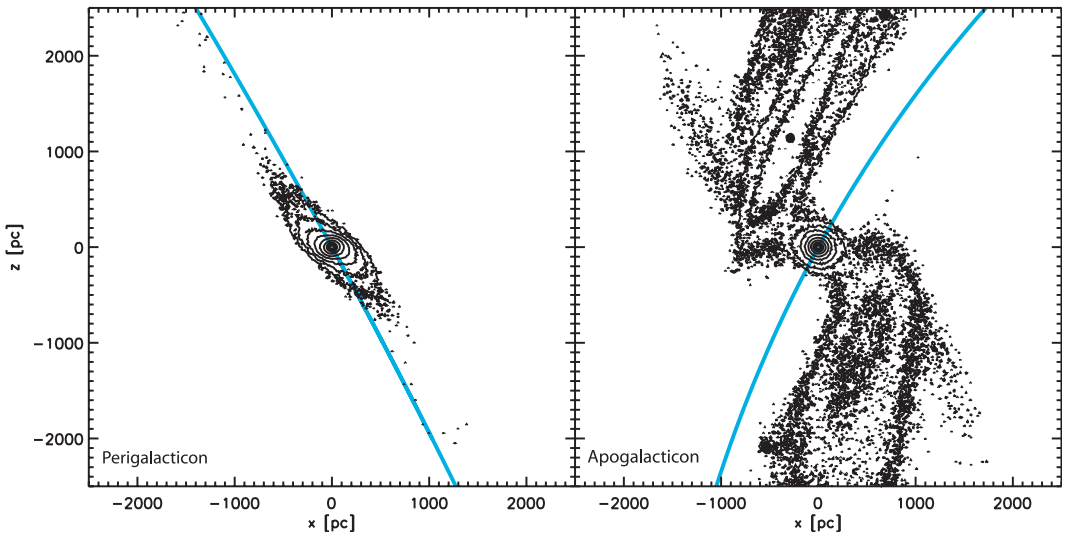

FIGURE 5.28— Contour plots on the x-z-plane of the merger object of the CC model CC_51-ECC_20_120 at the peri- and apogalactic distance. The lowest contour level corresponds to 5 particles per pixel. The pixel size is 15 pc. This yields $2.2 \cdot 10^{-3}$ $M_\odot$ pc^{-2}. The contour levels increase further by a factor of 3.

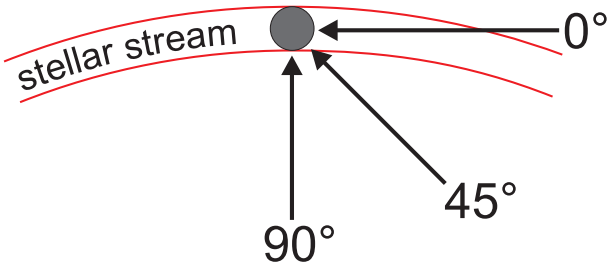

FIGURE 5.29— Scetch of the different sight angles relative to the orbital plane of the merger object. An angle of $0°$ corresponds to a line-of-sight parallel to the stream of unmerged star clusters and unbound material. Consequently an angle of $90°$ constitutes a line-of-sight perpendicular to the orbital plane.

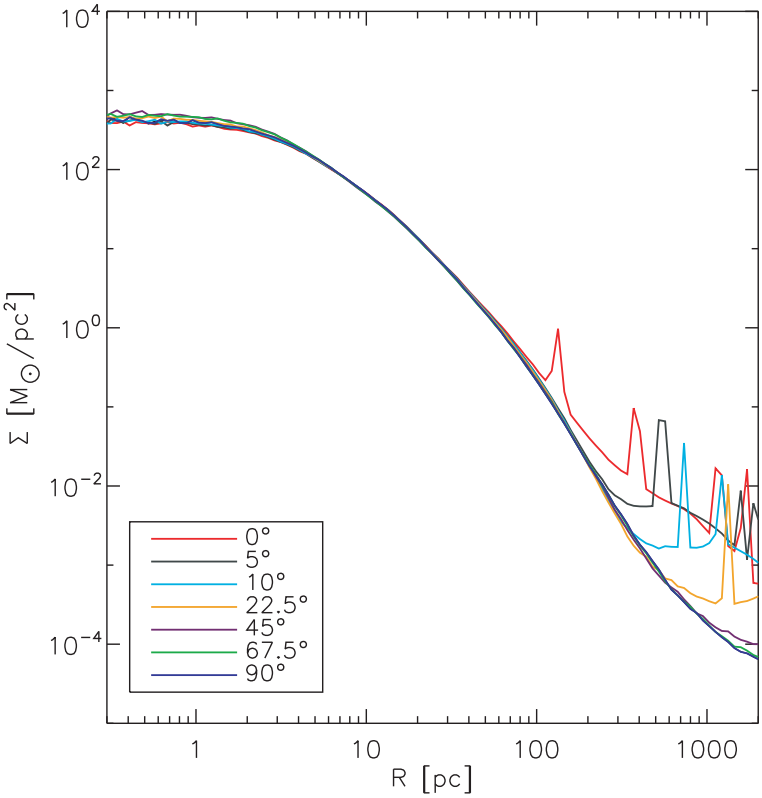

FIGURE 5.30— Surface density profiles of the merger object of computation CC_51-ECC_20_120 at the perigalactic distance for different sight angles.

in its vicinity. At apogalacticon the shape of the merger object becomes round again and the unbound material and unmerged star clusters form pronounced nearby tidal debris. This orbital compression of tidal debris near apogalacticon has also been shown by Küpper et al. (2010) by N-body computations of star clusters of the Milky Way.

To illustrate the influence of the sight angle on the appearance of the merger object I computed the surface density profiles of computation CC_51-ECC_20_120 at the perigalactic passage for seven sight angles. Figure 5.29 illustrates the different sight angles with respect to the orbital plane. An angle of $0°$ corresponds to a line-of-sight parallel to the stream of unmerged star clusters and unbound material, while an angle of $90°$ constitutes a line-of-sight perpendicular to the orbital plane. Figure 5.30 demonstrates that a merger object observed at small sight angles during its perigalactic passage shows a comparable enhancement in the outer part of the surface density profile as at the apogalactic distance. Sight angles larger than $22.5°$ already show only small deviations from the profile obtained from a line-of-sight perpendicular

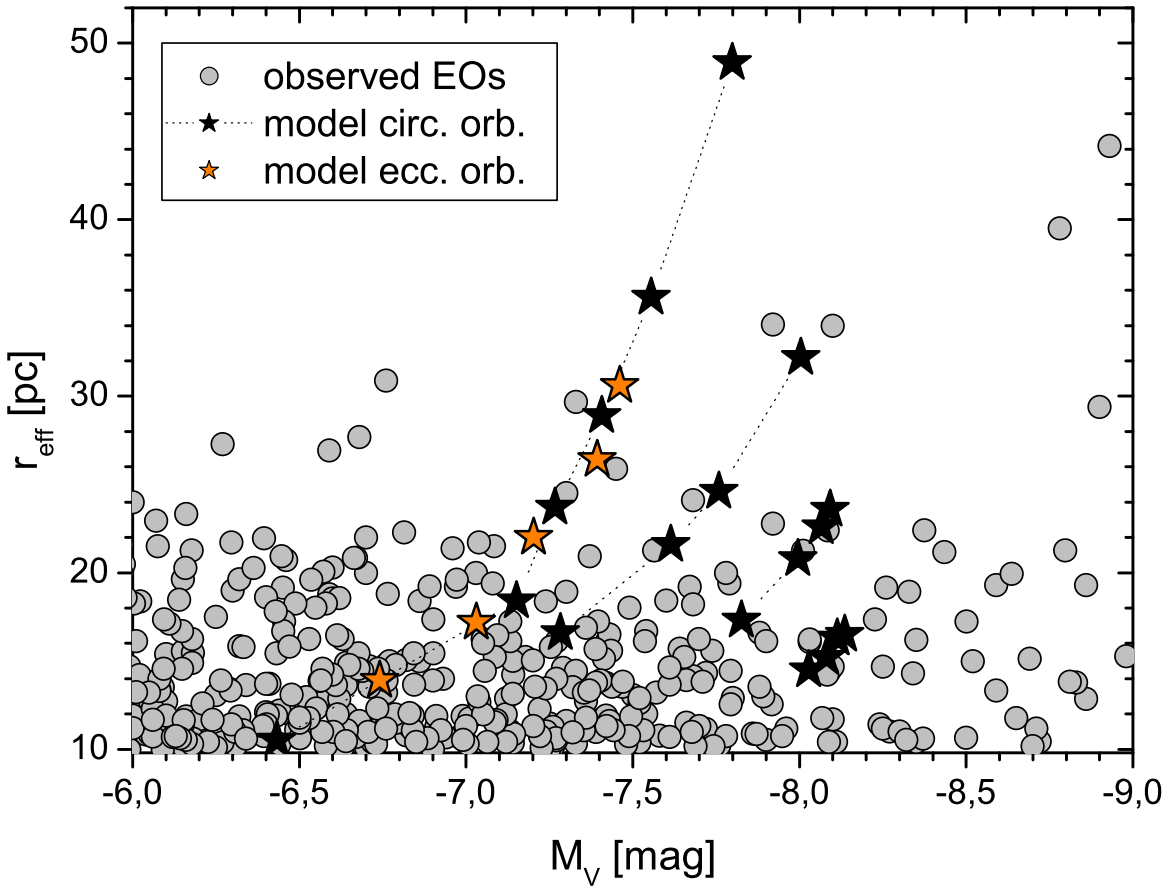

FIGURE 5.31— The diagram shows the effective radius, $r_{\rm eff}$, as a function of the total luminosity, $M_{\rm V}$, of the observed EOs (grey circles) from Chapter 3 and the modeled merger objects (stars) on different circular and eccentric orbits. The initial CC models have a mass of $M^{\rm CC} = 10^{5.5}$ M$_\odot$ and Plummer radii of $R_{\rm pl}^{\rm CC} = 20$, 40, 80, and 160 pc. The circular orbits cover galactic distances of $R_{\rm gal} = 20$, 40, 60, and 120 kpc (black stars). For the CC models with $R_{\rm pl}^{\rm CC} = 160$ pc additional circular orbits at $R_{\rm gal} = 50$ and 70 kpc and the eccentric orbits with a perigalactic distance of $R_{\rm p} = 20$ kpc with $R_{\rm a} = 60$ and 120 kpc and $R_{\rm p} = 40$ kpc with $R_{\rm a} = 60$, 90, and 120 kpc are plotted (orange stars).

to the orbital plane. Figure 5.30 demonstrates that an enhancement in the outer part of a surface brightness profile does not necessarily imply that the object is close to its apogalacticon - in contrast to the conclusions of Küpper et al. (2010). However taking into account that only a small range of viewing angles produce such an enhancement at perigalacticon and that a stellar dynamical object on an eccentric orbit spends considerably more time close to the apogalacticon than close to perigalacticon, there is a large probability that an enhancement in the outer parts of a surface density profile is related to an apogalactic position.

5.3.4 Comparison with Observations

The results from the simulations presented in this section demonstrate that the parameters enclosed mass and effective radius of merger objects from extended CC models depend significantly on the orbit (see Fig. 5.22). To allow for a direct comparison with the observed EOs as presented in Chapter 3 I use Eq. 5.3 and a mass-to-light ratio of 2, which is a typical value for GCs, to convert the enclosed masses of the merger objects into total V-band luminosities.

Figure 5.31 shows $r_{\rm eff}$ as a function of total luminosity of the observed EOs (grey circles) from Chapter 3 and the modeled merger objects (stars) on different circular and eccentric orbits. I considered the circular orbits between 20 and 120 kpc (see Fig. 5.22) and the eccentric orbits

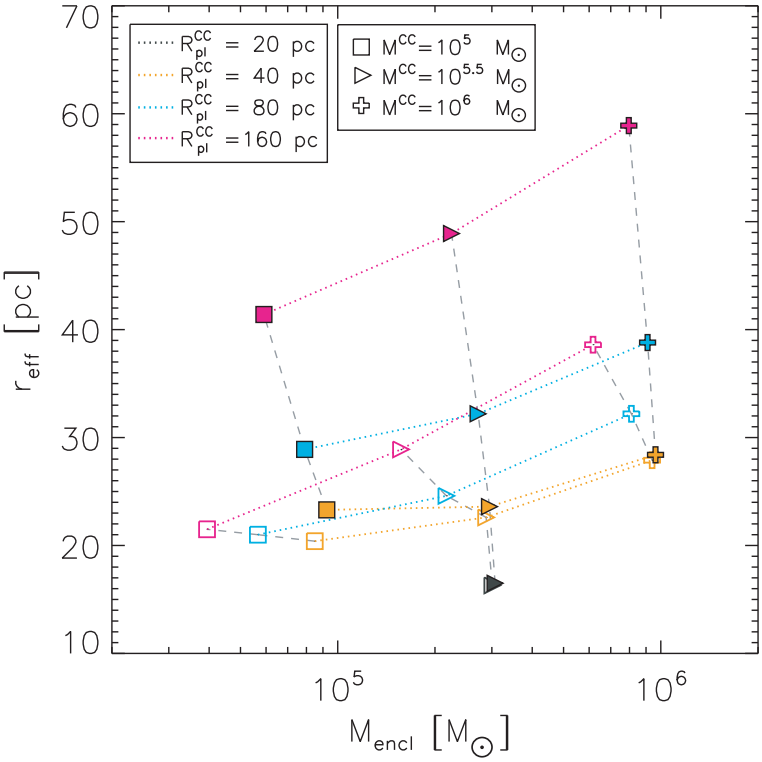

FIGURE 5.32— Effective radii, $r_{\rm eff}$, of the merger objects against the merger object masses, $M_{\rm encl}$, for three different initial CC masses, $M^{\rm CC} = 10^5$, $10^{5.5}$, and 10^6 $M_\odot$, at galactic distances of $R_{\rm gal} = 60$ kpc (open symbols) and $R_{\rm gal} = 120$ kpc (filled symbols). Models with the same initial CC Plummer radius, $R_{\rm pl}^{\rm CC}$, are connected by dotted lines. The dashed gray lines connect models with the same initial CC mass, $M^{\rm CC}$.

for the extended CC models with an initial CC Plummer radius of 160 pc. To scan the region of extremely extended EOs more closely, I performed additional simulations on two circular orbits at galactic distances of $R_{\rm gal} = 50$ and 70 kpc and on an eccentric orbit between 40 and 90 kpc which are presented in Tables C.6 and C.7.

The compact CC models ($R_{\rm pl}^{\rm CC} = 20$ pc) and all merger objects on circular orbits at galactic distances of $R_{\rm gal} = 20$ kpc and on eccentric orbits with a perigalactic distance of $R_{\rm p} = 20$ kpc result in merger objects with effective radii below $r_{\rm eff} = 20$ pc. Some combinations of orbits and CC sizes produce merger objects with effective radii between 20 and 25 pc. The most extended EOs with $r_{\rm eff} > 25$ pc can only be reproduced by the most extended CC models in environments with a very low tidal field. For the CC models with $R_{\rm pl}^{\rm CC} = 160$ pc, the circular orbit at 60 kpc and the eccentric orbits with a perigalacticon of 40 kpc and apogalactica at 90 and 120 kpc result in merger objects comparable to the most extended EOs, while the circular orbits at 70 and 120 kpc end up in a region called the Gilmore gap, where neither EOs nor dwarf galaxies have been found so far (see Sect. 5.5 for a discussion). Figure 5.31 demonstrates that the merging star cluster scenario is able to explain also the most extended EOs, if very low gravitational fields are considered.

5.4 The Formation of Extremely Extended Clusters

In this section, I will focus on the extremely extended EOs that were not covered by the merger objects on the eccentric orbit between 20 and 60 kpc as presented in Fig. 5.15 in Sect. 5.2.

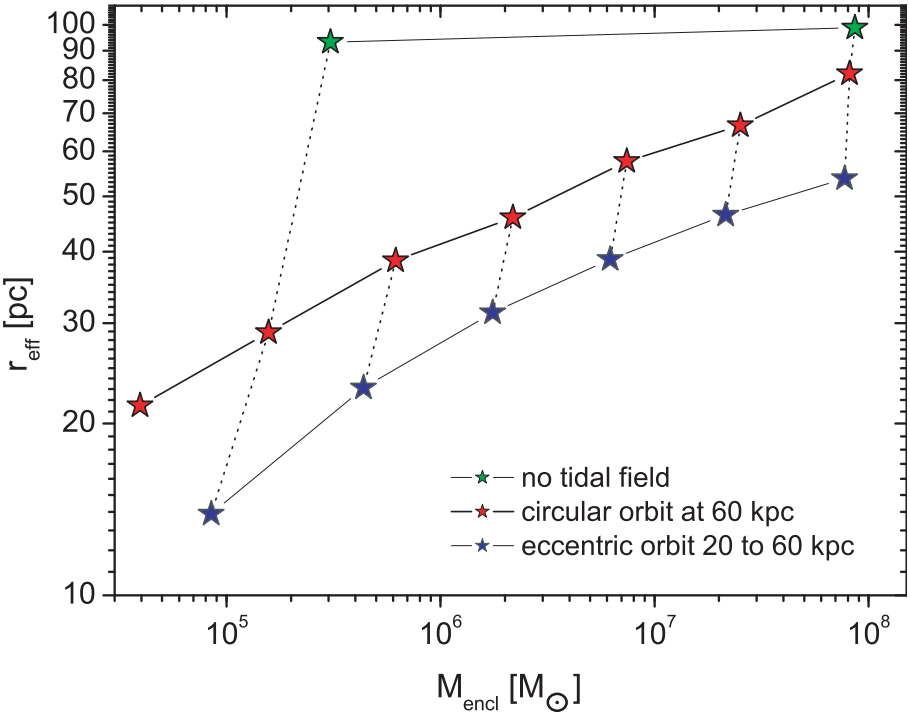

FIGURE 5.33— Effective radii, $r_{\rm eff}$, of the merger objects against the merger object masses, $M_{\rm encl}$, for extended CC models with $R_{\rm pl}^{\rm CC} = 160$ pc on a circular orbit at 60 kpc (red stars), an eccentric orbit between 20 and 60 kpc (blue stars, see Sect. 5.2) and two models ($M^{\rm CC} = 10^{5.5}$ and 10^8 M$_\odot$) without an external tidal field (green stars). Models with the same initial initial CC mass, $M^{\rm CC}$, are connected by dashed lines.

5.4.1 Numerical Set-Up and Varied Parameters

The previous section demonstrated that rather weak tidal fields are necessary to produce the extremely extended EOs. Therefore, I consider two circular orbits at galactic distances of $R_{\rm gal} = 60$ and 120 kpc in this section. In addition to the simulations for the CC models of $M^{\rm CC} = 10^{5.5}$ M$_\odot$ from the previous section, I performed 12 additional simulations for the two orbits for the CC models of $M^{\rm CC} = 10^5$ M$_\odot$ and 10^6 M$_\odot$ for CC models with Plummer radii of $R_{\rm pl}^{\rm CC} = 40$, 80, and 160 pc.

To cover the entire mass range studied in Sect. 5.2, I also performed simulations of extended CC models ($R_{\rm pl}^{\rm CC} = 160$ pc) on the circular orbit at 60 kpc for the CC masses $M^{\rm CC} = 10^{6.5}$, 10^7, $10^{7.5}$, and 10^8 M$_\odot$. For comparison, I calculated also extended CC models ($R_{\rm pl}^{\rm CC} = 160$ pc) with $M^{\rm CC} = 10^{6.5}$ and 10^7 M$_\odot$ on a circular orbit at a galactic distance of 120 kpc and with $M^{\rm CC} = 10^8$ M$_\odot$ without a tidal field.

5.4.2 Results

5.4.2.1 *Trends in the $r_{\rm eff}$ vs. $M_{\rm encl}$ Space*

Figure 5.32 shows the effective radius of the merger objects as a function of their enclosed mass. The open symbols represent the merger objects on a circular orbit at a galactic distance of $R_{\rm gal} = 60$ kpc and the filled symbols on a circular orbit at $R_{\rm gal} = 120$ kpc. Models with the same initial CC Plummer radius are connected by dotted lines and models with the same initial CC mass by dashed lines. For all CC Plummer radii the effective radii increase with the initial CC mass. For small CC Plummer radii of $R_{\rm pl}^{\rm CC} = 40$ pc the orbit only has a small impact on the results. The values for the merger object masses and the effective radii deviate slightly at the low-mass end of $M^{\rm CC} = 10^5$ M$_\odot$ and match almost for $M^{\rm CC} = 10^6$ M$_\odot$. The

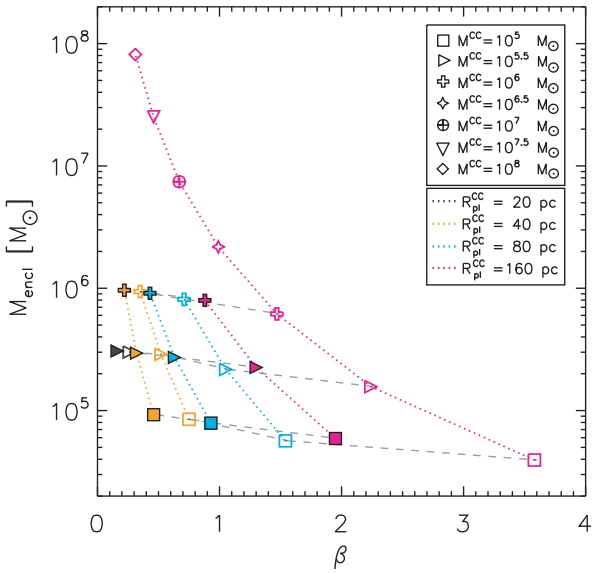

FIGURE 5.34— Merger object masses, $M_{\rm encl}$, versus the parameter β for different initial CC masses, $M^{\rm CC}$, and Plummer radii, $R_{\rm pl}^{\rm CC}$, at galactic distances of $R_{\rm gal} = 60$ kpc (open symbols) and $R_{\rm gal} = 120$ kpc (filled symbols) after 5 Gyr. Models with the same initial CC Plummer radius, $R_{\rm pl}^{\rm CC}$, are connected by dotted lines. The dashed gray lines connect models with the same initial CC mass, $M^{\rm CC}$. The masses of the merger objects resulting from high-mass CC models with CC masses ranging from $M^{\rm CC} = 10^{6.5}$ to 10^8 $M_\odot$ for the circular orbit at $R_{\rm gal} = 60$ kpc are added.

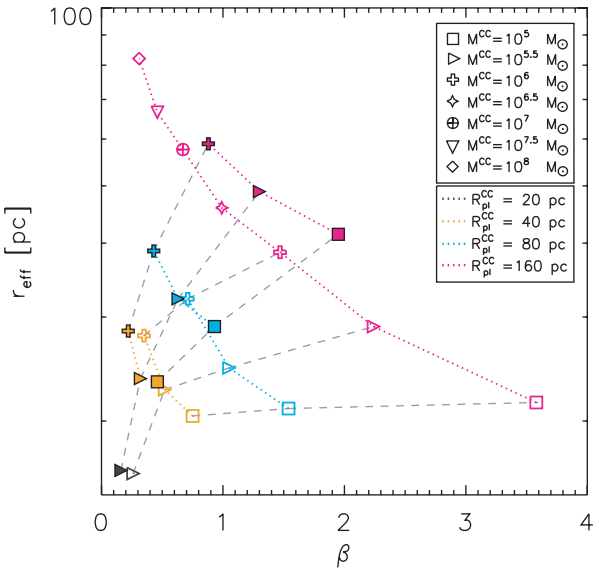

FIGURE 5.35— Effective radii, $r_{\rm eff}$, of the merger objects against the parameter β for different initial CC masses, $M^{\rm CC}$, and Plummer radii, $R_{\rm pl}^{\rm CC}$, at galactic distances of $R_{\rm gal} = 60$ kpc (open symbols) and $R_{\rm gal} = 120$ kpc (filled symbols) after 5 Gyr. Models with the same initial CC Plummer radius, $R_{\rm pl}^{\rm CC}$, are connected by dotted lines. The dashed gray lines connect models with the same initial CC mass, $M^{\rm CC}$. The effective radii of the merger objects resulting from high-mass CC models with CC masses ranging from $M^{\rm CC} = 10^{6.5}$ to 10^8 $M_\odot$ for the circular orbit at $R_{\rm gal} = 60$ kpc are added.

larger the initial CC mass the better the concordance. For even more compact CC models with $R_{\rm pl}^{\rm CC} = 20$ pc the values already match at smaller CC masses as demonstrated for the CC model with $M^{\rm CC} = 10^{5.5}$ $M_\odot$. For the extended CC models with $R_{\rm pl}^{\rm CC} = 80$ and 160 pc the structural parameters of the merger objects depend considerably on the orbit. The larger the initial CC Plummer radius becomes the larger are the deviations between the orbits. For a CC with $R_{\rm pl}^{\rm CC} = 80$ pc the difference between the values on the two orbits becomes smaller for larger CC masses. Whereas for CC with $R_{\rm pl}^{\rm CC} = 160$ pc it stays fairly constant. For both orbits there is a trend of increasing effective radii with increasing enclosed mass and accordingly with the initial CC mass. The more massive the initial CC and the more distant the orbit the larger the sizes of the merger objects.

Figure 5.33 shows effective radii, $r_{\rm eff}$, of the merger objects against the merger object masses, $M_{\rm encl}$, for CC models with $R_{\rm pl}^{\rm CC} = 160$ pc on a circular orbit of 60 kpc and initial CC masses between $M^{\rm CC} = 10^5$ and 10^8 $M_\odot$ (red stars), the eccentric orbit between 20 and 60 kpc for initial CC masses between $M^{\rm CC} = 10^{5.5}$ and 10^8 $M_\odot$ (blue stars, see Sect. 5.2) and two models at $M^{\rm CC} = 10^{5.5}$ and 10^8 $M_\odot$ that were calculated without an external tidal field (green stars). Figure 5.33 demonstrates that for simulations without an external tidal field the effective radii of the resulting merger objects depend only slightly on the initial CC mass. Whereas in simulations with tidal fields the effective radii depend considerably on the CC masses. In the mass range between $M^{\rm CC} = 10^{5.5}$ and 10^8 $M_\odot$ the effective radii increase from 14 to 54 pc for the eccentric orbit, from 29 to 82 pc for the circular orbit and from 93 to 99 pc without a tidal field.

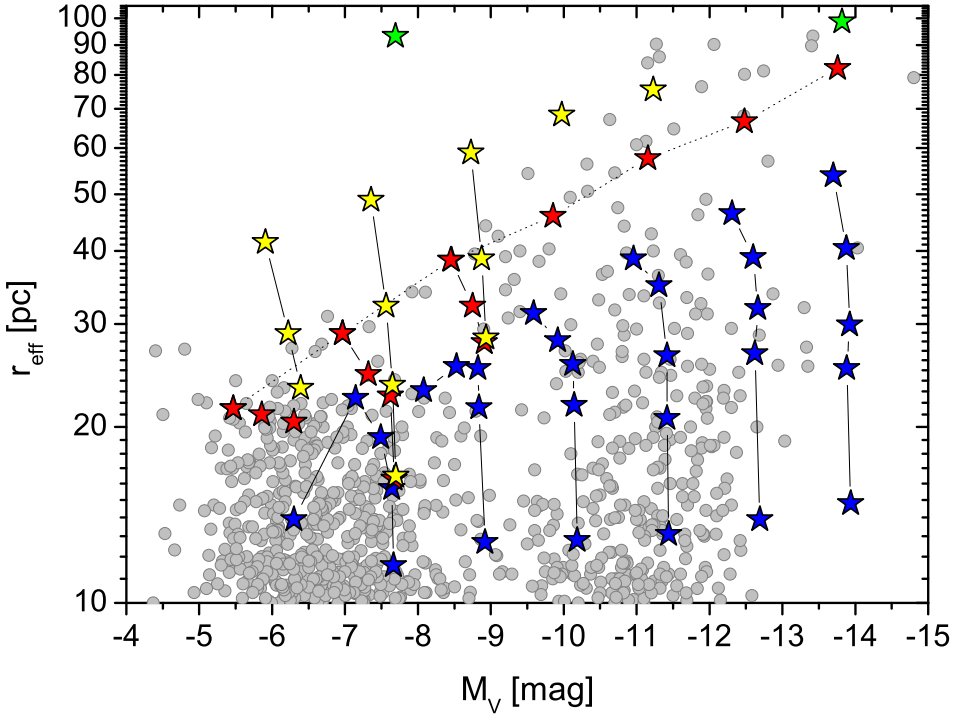

FIGURE 5.36— Diagram of the effective radius, $r_{\rm eff}$, as a function of the total luminosity, $M_{\rm V}$, of the observed EOs as presented in Chapter 3 (grey circles) and the modeled merger objects on circular orbits at 60 kpc (red stars) and 120 kpc (yellow stars), the two models with $R_{\rm pl}^{\rm CC} = 160$ pc without a tidal field (green stars), and the eccentric orbit between 20 and 60 kpc as shown in Fig. 5.15 of Sect. 5.2 (blue stars). Objects with the same initial CC mass but different initial CC Plummer radii are connected by black lines. The merger objects with $R_{\rm pl}^{\rm CC} = 160$ pc on the circular orbit at 60 kpc are connected by dotted lines.

5.4.2.2 *Correlation of Structural Parameters of Merger Object with β*

Figures 5.34 and 5.35 show the dependence of the two structural parameters $M_{\rm encl}$ and $r_{\rm eff}$ of the merger object on the parameter β for different CC masses, $M^{\rm CC}$, at galactic distances of $R_{\rm gal} = 60$ and 120 kpc. The β-values of the models are presented in Table C.8. In these plots I also included the values for the CC masses above 10^6 $M_\odot$ for the most extended CC model with $R_{\rm pl}^{\rm CC} = 160$ pc of the circular orbit simulations at a galactic distance of 60 kpc. The larger the initial CC mass the smaller the value of β and the smaller the influence of the tidal field on the merging process. Extended CC models at the high-mass end have β-values, which are all below one for a circular orbit at $R_{\rm gal} = 60$ kpc, whereas the corresponding β-values at the low-mass end are larger than one. They cover a β-range from 1.5 ($M^{\rm CC} = 10^6$ $M_\odot$) to 3.6 ($M^{\rm CC} = 10^5$ $M_\odot$). For larger galactic distances the influence of the tidal field on the low-mass models decreases. The corresponding β-values for the circular orbit at $R_{\rm gal} = 120$ kpc are 0.9 ($M^{\rm CC} = 10^6$ $M_\odot$) and 2.0 ($M^{\rm CC} = 10^5$ $M_\odot$) leading to higher masses and effective radii of the merger objects. More compact CCs have smaller β-values and are therefore less vulnerable to a tidal field. The smaller the initial CC Plummer radius and the larger the initial CC mass and/or the galactic distance of the circular orbit become the smaller is the β-value of the CC.

5.4.3 Comparison with Observations

Figure 5.36 combines Fig. 5.15 of Sect. 5.2, which shows $r_{\rm eff}$ as a function of the total luminosity of the observed EOs and the merger objects on an eccentric orbit between 20 and 60 kpc, with the merger objects on circular orbits at 60 and 120 kpc as well as those without a tidal field. As for Fig. 5.15, a mass-to-light ratio of 3 was used to transfer masses into total luminosities.

For luminosities fainter than -10 mag, the CC models on circular orbits fill the area between those on the eccentric orbits and the most extended EOs observed so far. The merger objects of the CC models with $R_{\rm pl}^{\rm CC} = 160$ pc on the circular orbit at 120 kpc have even larger sizes than the observed EOs. For luminosities brighter than $M_{\rm V} = -10$ mag, a circular orbit at 120 kpc is needed to cover also the most extreme EOs, as demonstrated by the additional simulations with $R_{\rm pl}^{\rm CC} = 160$ pc at $M^{\rm CC} = 10^{6.5}$ and 10^7 $M_\odot$ in Fig. 5.36. The two merger object that were calculated without an external tidal field demonstrate that even the largest observed EOs can be reproduced, if the external tidal field is extremely low. Note that these two objects calculated without an external tidal field do not represent an upper limit for merger objects but only the largest objects obtained for this specific CC model.

5.5 Discussion

5.5.1 The Merging Star Cluster vs. the Galaxy Threshing Scenario

In this chapter, I have systematically scanned a suitable parameter space for CCs and investigated their future evolution on different orbits. The varied parameters of the CCs covered CC Plummer radii between 10 and 160 pc, CC masses between 10^5 and 10^8 $M_\odot$, and orbits between 20 and 120 kpc in a Milky-Way-like gravitational potential. The results presented in the previous sections demonstrate that all simulations end up with stable merger objects, although the mass enclosed in the merger objects is considerably lower than the initial mass of the CC. For the most extended and lowest mass CCs experiencing the strongest impact of the external tidal forces (i.e. $M^{\rm CC} = 10^{5.5}$, $R_{\rm pl}^{\rm CC} = 160$ pc, and $R_{\rm gal} = 20$ kpc) the merger object contains only about 20% of the initial CC mass. Thus, even such a CC that would be regarded as gravitationally unstable - if viewed in its entirety - can produce stable EOs.

Figure 5.36 demonstrates that the observed and modeled EOs cover the same parameter space and show the same trend of increasing effective radii with increasing luminosity.

In Chapter 3, I demonstrated that all types of galaxies have low-mass EOs, while the vast majority of high-mass EOs are associated with elliptical galaxies. This finding is consistent with the merging star cluster scenario: YMCs and CCs with masses below $M = 10^6$ $M_\odot$ have been observed in all types of galaxies containing sufficient amounts of gas to form star clusters, while high-mass YMCs and CCs ($M \gtrsim$ few$\times 10^6$ $M_\odot$) were so far only observed in major encounters like the Antennae (Whitmore et al. 2005), Arp 220 (Wilson et al. 2006), or NGC 7252 (Maraston et al. 2004), which may be in the process of becoming elliptical galaxies. Consequently, only the major interactions that create the early-type galaxies in the first place build CCs massive enough to form the EOs considerably brighter than about $M_{\rm V} = -10$ mag.

The evolution of low-mass EOs in a weak gravitational environment has also been studied by Hurley & Mackey (2010), who performed direct N-body models of extended low-mass star clusters incorporating a stellar mass function and stellar evolution. Internal evolution processes of the star clusters lead to considerably larger effective radii compared to the initial values. They concluded that extended star clusters with an initial mass of $5.8 \cdot 10^4$ $M_\odot$ are sufficiently stable to survive a Hubble time in a weak gravitational field environment.

Murray (2009) addressed the question why compact star clusters are absent in the high-mass regime, i.e. at masses larger than few 10^6 $M_\odot$. Murray (2009) modelled proto-clusters and found that high-mass clusters become optically thick to infrared radiation leading to a modified initial mass function of the cluster stars, to a larger mass-to-light ratio, and to considerably larger sizes of the proto-clusters. While the idea of optically thick proto-clusters explains the absence of compact clusters in the high-mass regime, it cannot explain the existence of EOs over the large observed mass range.

An alternative formation scenario for high-mass EOs, that is not based on a star cluster origin, is the galaxy threshing scenario, where nucleated dwarf galaxies loose, during a heavy

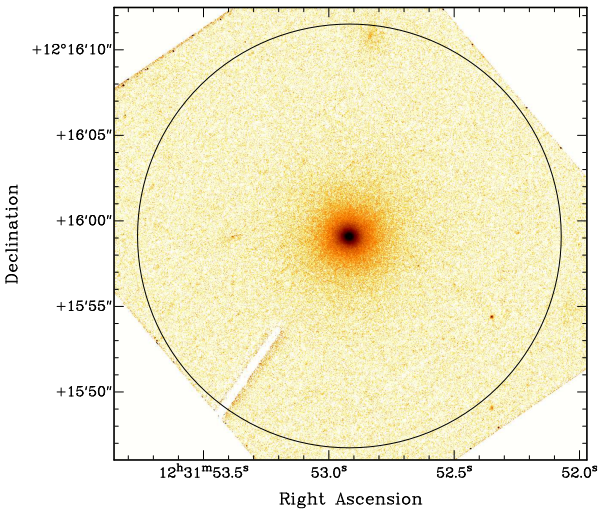

FIGURE 5.37— High resolution HST ACS image of VUCD7 in the F606W filter. The black circle has a projected radius of 1 kpc indicating the extent of the surface brightness profile shown in Fig. 5.38 (The HST ACS image of VUCD7 was taken from the Hubble Legacy Archive, see http://hla.stsci.edu/hlaview.html).

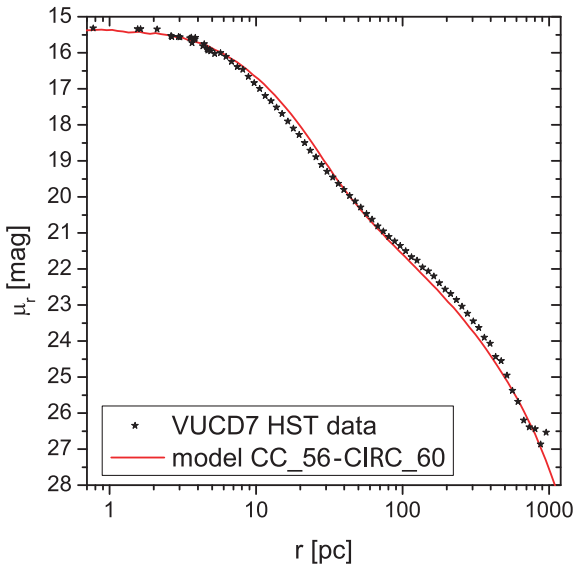

FIGURE 5.38— Surface brightness profile compiled from archival HST ACS data (black stars) of the EO VUCD7 and the surface brightness profile of model CC_56-CIRC_60 using a mass-to-light ratio of 2.8. The model and the observed EO show the same "core-halo" structure.

interaction with a larger galaxy, almost all stars of the main body except for the nucleus (Bekki et al. 2001; Pfeffer & Baumgardt 2013, and references therein). This formation scenario connects EOs with compact elliptical galaxies like M32, as this rare species of compact galaxies is also expected to be the end-product of an interaction that stripped the bigger part of a formerly larger galaxy. Bekki et al. (2003) performed numerical simulations to demonstrate that nucleated dwarf galaxies can indeed evolve into EOs if they are on a highly eccentric orbit. Very recently, Pfeffer & Baumgardt (2013) performed a first parametric study where three models of nucleated dwarf ellipticals (dE,N) were placed on different elliptical and "box orbits". Box orbits were mimiced by placing the dE,N galaxies first on elliptical orbits and after a few passages resetting them on a circular orbit at the apocentric distance. Pfeffer & Baumgardt (2013) conclude that all observed sizes of UCDs can be reproduced by these "box orbits". However, these studies on the threshing scenario focussed on the UCD regime. So far, it was not demonstrated that the threshing scenario is able to reproduce also low-mass EOs.

According to Bekki et al. (2003), a two-component "core-halo" surface brightness profile is a major prediction of the galaxy threshing scenario, where the core is the former nucleus and the halo is the remnant of the main body of the former galaxy. Three of the most luminous confirmed EOs, i.e. VUCD7, UCD3, and M59cO, show a clear two-component or core-halo surface brightness profile. Following the results of Bekki et al. (2003), this kind of structure was used as evidence for a galactic origin of UCDs (e.g. Haşegan et al. 2005; Chilingarian & Mamon 2008; Norris & Kannappan 2011).

The most extended and most luminous of the three objects, VUCD7, is located about 83 kpc from M87 and has neither disturbing foreground nor background objects in its vicinity, while UCD3 is largely overlapping with a background spiral galaxy and M59cO has a projected distance to M59 of only 9.7 kpc. Figure 5.37 shows an HST ACS high-resolution image of VUCD7 in the F605W band[1]. The HST data allow to compile a surface brightness profile out to large

[1]The HST ACS image of VUCD7 was taken from the Hubble Legacy Archive, see

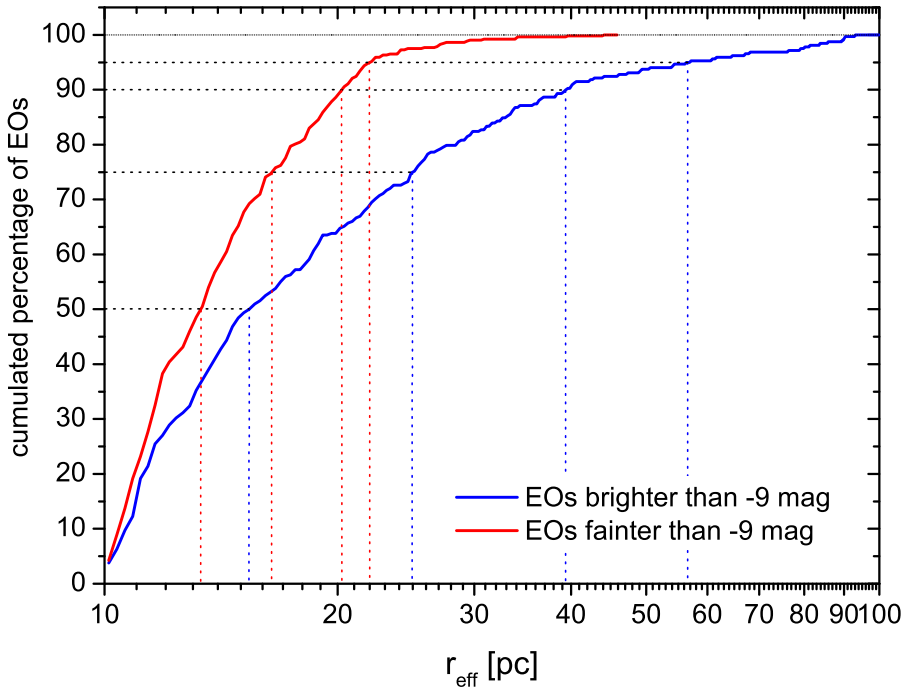

FIGURE 5.39— The diagram shows the cumulated percentage of observed EOs having radii up to a given $r_{\rm eff}$ as a function of this $r_{\rm eff}$. EOs brighter and fainter than $M_{\rm V} = -9$ mag are plotted in blue and red, respectively. Black dotted lines mark 50, 75, 90, and 95%. The effective radii at these cumulated percentages are plotted as blue and red dotted lines for EOs brighter and fainter than $M_{\rm V} = -9$ mag, respectively.

projected radii of about 1 kpc. Figure 5.38 shows the surface brightness profile of VUCD7 compiled from the archival HST ACS data presented in Fig. 5.37 using a median filter for the radial bins to exclude faint emission from possible foreground or background objects. The observed profile of VUCD7 shows a clear two-component structure. Whereas most of the models presented in this chapter show a single component profile (e.g. Figs. 5.11, 5.12, and 5.23), the surface brightness profiles of the most massive and most extended models on a circular orbit at 60 kpc, which have a comparable mass and effective radius as VUCD7, show a two-component profile. Figure 5.38 demonstrates that the surface brightness profile of model CC_56-CIRC_60 shows a very similar two-component structure as the observed VUCD7. Consequently, a two-component core-halo surface brightness profile cannot be used as evidence for the galaxy threshing scenario as also the merging star cluster scenario is able to explain this specific structure of the most massive and most extended UCDs.

While the observed EOs cover a large range of effective radii, the majority of EOs has rather low values of $r_{\rm eff}$. Figure 5.39 shows the cumulated percentage of EOs as a function of $r_{\rm eff}$ for EO brighter and fainter than $M_{\rm V} = -9$ mag. Half the EOs fainter and brighter than $M_{\rm V} = -9$ mag have effective radii below 13.2 and 15.4 pc, respectively. Ninety percent of the EOs fainter and brighter than $M_{\rm V} = -9$ mag have effective radii below 20.2 and 39.4 pc.

The merging star cluster scenario is able to explain the cause for the observed decrease of the number of EOs with size. In Fig. 5.9 of Sect. 5.2.2.3 and Fig. 5.19 of Sect. 5.3.2 I have shown that compact CC models always result in compact merger objects irrespective of the CC mass and of the strength of the external tidal field. In contrast, extended CC models with a low mass lead to merger objects with a large spread of effective radii. In a strong tidal field an extended, low-mass CC evolves into a compact merger object while in a weak tidal field an extended CC

http://hla.stsci.edu/hlaview.html

results in an extended merger object. Thus extended merger objects with low masses can only evolve from extended CCs in weak tidal fields whereas compact merger objects result from all compact CC models as well as from extended CC models in strong tidal fields. The situation changes at the high-mass end, were extended CCs evolve into larger merger objects compared to merger objects at the low-mass end (see Fig. 5.33). Therefore, the shallower distribution for EOs brighter than $M_{\rm V} = -9$ mag is consistent with the merging star cluster scenario.

The galaxy threshing scenario starts with dwarf galaxies having effective radii of a few hundred parsecs. Most orbits strip only a fraction of the initial dwarf galaxy leading to peculiar galaxies, while extreme orbits are needed to transform nucleated dwarf elliptical galaxies into UCDs (Pfeffer & Baumgardt 2013). Unfortunately, no systematic parametric studies are available that allow for a detailed comparison with the observed EO distribution in the $r_{\rm eff}$ vs. $M_{\rm V}$ parameter space.

In contrast to the galaxy threshing scenario, the merging star cluster scenario for EOs explains the existence of EOs over the entire observed range of luminosities of ECs and UCDs, the trends in and the distribution of the structural parameters, and the differences between early- and late-type galaxies at the high-luminosity end of EOs.

5.5.2 The Gilmore Gap

Figure 5.40 shows the distribution of the observed EOs and early-type dwarf galaxies in the $r_{\rm eff}$ vs. $M_{\rm V}$ parameter space (see also Chapter 3). While EOs and early-type dwarf galaxies have a contiguous distribution for objects brighter than $M_{\rm V} \approx -11$ mag, there is a clear gap between both types of objects at lower luminosities. This gap is most pronounced between $M_{\rm V} = -5$ and -8 mag, where EOs have effective radii up to about 30 pc, while the dwarf spheroidal galaxies at this luminosity have effective radii between about 100 and 400 pc. This gap, which is also known as the Gilmore gap, was first discussed by Gilmore et al. (2007). At that time in 2007, the gap was covering the entire luminosity range of all EOs. In recent years, a huge number of extremely extended EOs and compact elliptical galaxies were discovered (see Chapter 3), which led to the considerably smaller gap solely at luminosities fainter than $M_{\rm V} \approx -11$ mag.

Figure 5.41 combines Fig. 5.40, which shows the observed EOs and dwarf galaxies, with Figs. 5.31 and 5.36 that contain the results of the simulations. To obtain merger objects with effective radii above 30 pc very extended CCs *and* extremely weak tidal fields are needed. In a Milky Way potential extended CCs with $R_{\rm pl}^{\rm CC} = 160$ pc moving on a circular orbit at 40 kpc lead to merger objects with effective radii just below 20 pc. Circular orbit simulations at distances of 50 and 60 kpc result in the extended EOs like the Huxor EOs (Huxor et al. 2011a), which have effective radii between 25 and 30 pc. CCs at even larger galactic distances evolve into objects of the Gilmore gap. A merger object on a circular orbit at 70 kpc already has an effective radius of about 35 pc. One on a circular orbit at 120 kpc has an effective radius of 49 pc. Of the CCs on eccentric orbits with a perigalacticon of 40 kpc even the merger object on the orbit with the largest apogalacticon of 120 kpc does not reach the Gilmore gap, demonstrating that very extended merger objects can only form on orbits at large galactic distances with a low eccentricity. Considering the need of extreme parameters to create an object in the Gilmore gap, a low number of objects in this region is expected from the merging star cluster scenario. I will refer to objects in the Gilmore gap as ultra fluffy objects (UFOs), because they are extremely extended with a very low central surface brightness.

From the observational side, a fundamental constraint is the decreasing completeness level for extended objects. A larger effective radius means that half of the light is spread over a significantly larger area. For example, Fig. 5.42 shows four projected surface density profiles of Plummer spheres having all the same total luminosity, but different effective radii of $r_{\rm eff} = 2$, 10, 30, and 100 pc. The central surface brightness of a Plummer profile with $r_{\rm eff} = 10$ pc is 25 times lower than a profile with $r_{\rm eff} = 2$ pc. For a Plummer profile with $r_{\rm eff} = 30$ pc it is already 225

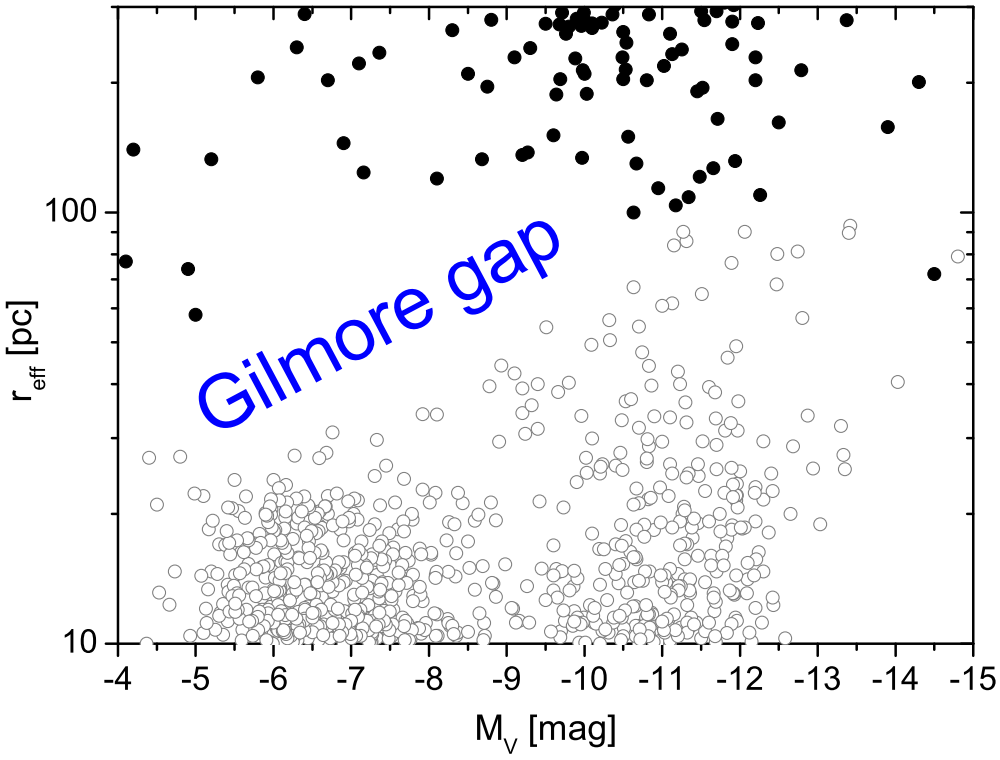

FIGURE 5.40— Diagram of the effective radius, $r_{\rm eff}$, as a function of the total luminosity, $M_{\rm V}$, of the observed EOs (grey circles) and the observed early-type dwarf galaxies (black circles) as presented in Chapter 3. The region between EOs and dwarf galaxies that contains no observed objects, is called Gilmore gap (Gilmore et al. 2007).

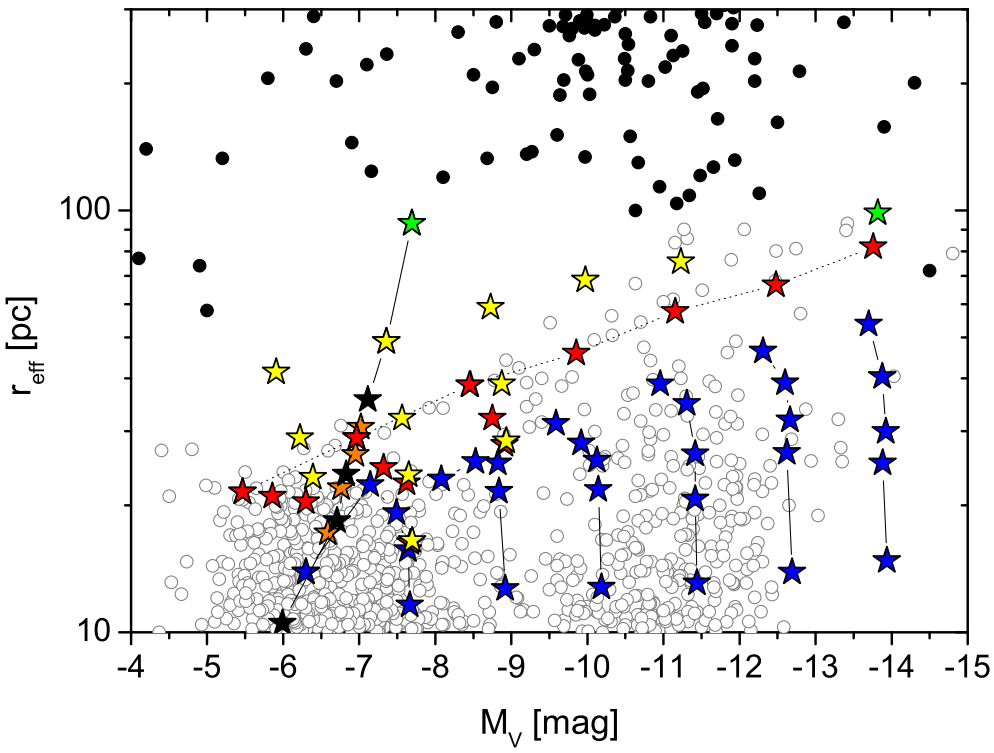

FIGURE 5.41— Diagram of the effective radius, $r_{\rm eff}$, as a function of the total luminosity, $M_{\rm V}$, of the observed EOs (grey circles) and the observed early-type dwarf galaxies (black circles) as presented in Chapter 3. The models as presented in this chapter are shown as stars. The colours are the same as in Figs. 5.31 and 5.36.

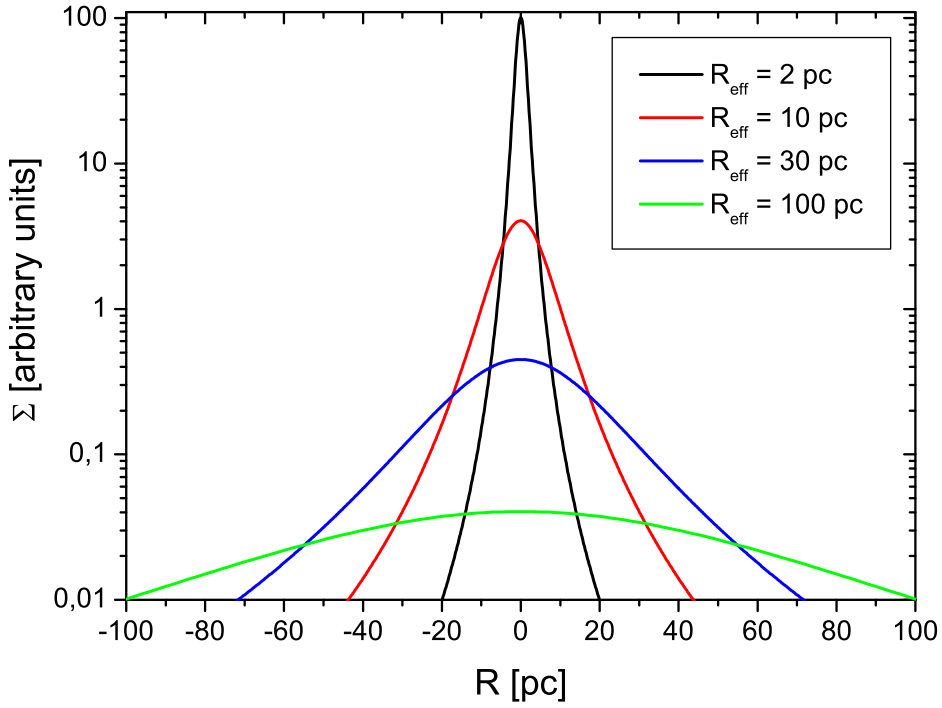

FIGURE 5.42— The diagram shows the surface density of Plummer profiles having the same total luminosity, but different effective radii of $r_{\rm eff} = 2$, 10, 30, and 100 pc.

times lower. In terms of central surface brightness in magnitudes, the Plummer spheres with $r_{\rm eff} = 10$, 30, and 100 pc are 3.5, 5.9, and 8.5 mag arcsec^{-2} fainter than a Plummer sphere with $r_{\rm eff} = 2$ pc. Consequently, the faintest Milky Way GC Segue 3, which has an effective radius of $r_{\rm eff} = 2$ pc and a total luminosity of $M_{\rm V} = 0$ mag (Fadely et al. 2011), has about the same central surface brightness as an EO with $r_{\rm eff} = 30$ pc and $M_{\rm V} = -5.9$ mag or an EO with $r_{\rm eff} = 100$ pc and $M_{\rm V} = -8.5$ mag.

Such faint objects are hard to detect even in the Local Group. The PAndAs Survey, which performed deep integrations of the Andromeda galaxy out to distances of about 150 kpc, has a detection limit for UFOs of approximately $M_{\rm V} = -6$ mag (Brasseur et al. 2011). Consequently, the larger part of the Gilmore gap is within the detection limits of the PAndAs survey, but no UFOs have been detected in this region so far. Brodie et al. (2011) searched the galaxy M87 for EOs with effective radii between 10 and 100 pc down to a detection limit of $M_{\rm V} = -8.5$ mag, but found no objects larger than $r_{\rm eff} = 40$ pc at such low luminosities.

Another important observational aspect is the coverage of the outer halos of galaxies with HST images. According to the merging star cluster scenario, objects with parameters in the Gilmore gap region are expected to be located at very large distances to their host galaxies. However, as shown in Chapter 3, the outer halo of most galaxies is extremely poorly covered by HST observations. Consequently, the chance that one of the few faint and extremely extended EOs is covered by one of the few HST fields at large projected distances of a galaxy is rather low.

The merging star cluster scenario predicts that CCs forming UFOs need quite extreme orbital parameters and large initial sizes. Consequently, the actual non-detection of such objects is fully consistent with my scenario. However, it should be noted that the existence of UFOs is *not* ruled out by the merging star cluster scenario, as even extreme parameters can sometimes materialize in the Universe.

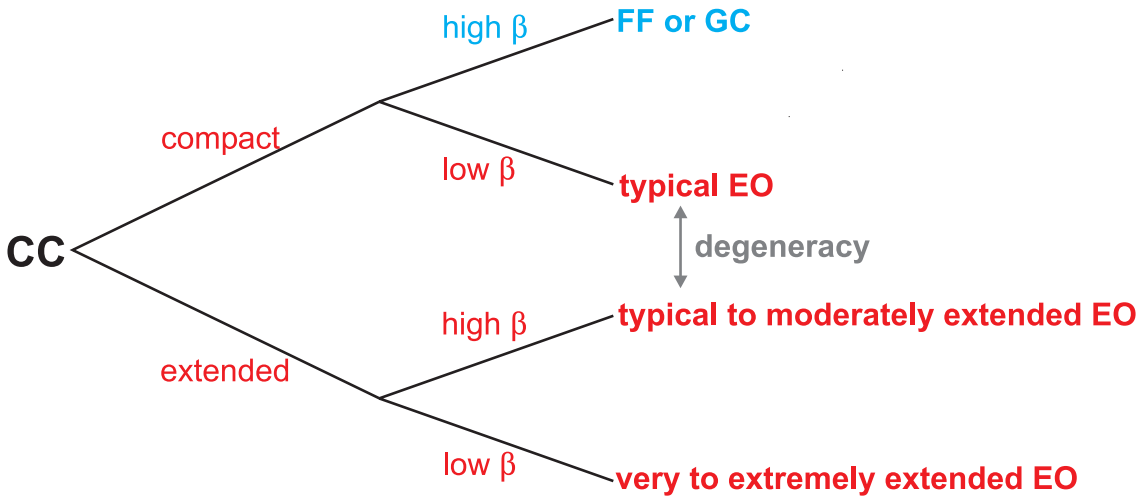

FIGURE 5.43— The diagram illustrates the fate of compact and extended CCs. The evolution of CCs in the outer galactic halos of galaxies covered in this chapter is highlighted in red and the evolution of CCs in the lower halo or in the disk of galaxies studied in Chapter 4 is highlighted in blue. Compact CCs in a galactic halo evolve into EOs with typical sizes of about 13 to 15 pc. The evolution of extended CCs in a galactic halo is more complex and depends crucially on the value of the parameter β. Simulations with large β-values develop into typical EOs and moderately extended EOs, whereas simulations with small β-values evolve into very to extremely extended EOs.

5.6 Conclusion

In conclusion, the merger objects of my parameter studies represent the overall observed parameters of EOs, as presented in Chapter 3, very well. Even detailed structural features like the core-halo profiles of some massive and extremely extended UCDs are well reproduced by my simulations.

The parametric studies demonstrate that the final fate of a CC depends crucially on its initial size and mass, and on the external tidal field. These three parameters are combined in the parameter β. The parameter β is the ratio of the cutoff radius and the tidal radius of the CC (see Sect. 2.1.4). The tidal radius in turn depends on the CC mass and the strength of the tidal field. In Sect. 5.2 I studied the parameter space of CC mass, $M^{\rm CC}$, and CC Plummer radius, $R_{\rm pl}^{\rm CC}$, for a fixed orbit (Fig. 5.3) and in Sect. 5.3 the parameter space of galactic distance, $R_{\rm gal}$, of circular orbits and CC Plummer radius, $R_{\rm pl}^{\rm CC}$, for a fixed CC mass (Fig. 5.16). Figures 5.7 and 5.9 of Sect. 5.2.2.3 for different initial CC masses $M^{\rm CC}$ are comparable to the outcome displayed in the Figs. 5.18 and 5.19 of Sect. 5.3.2.1 with the galactic distance, $R_{\rm gal}$, of the orbit as a free parameter. A weak gravitational field, i.e. a large galactic distance of the orbit, has the same effect on the evolution of a CC as a large initial CC mass. Both, larger CC masses and weaker gravitational fields lead to larger tidal radii which result in larger effective radii of the final merger objects.

Figure 5.43 schematically illustrates the evolution of compact and extended CCs. The two types of CCs show different evolution channels depending on the value of the parameter β. Compact CCs in a galactic halo have small β-values and are therefore hardly affected by the tidal field of the parent galaxy. For low-mass CCs of $M^{\rm CC} = 10^{5.5}$ M$_\odot$ with Plummer radii of $R_{\rm pl}^{\rm CC} = 20$ pc, the value of β becomes larger than one only at distances below 10 kpc in a Milky-Way-like potential. For CCs moving in the lower halo or in the disk of a galaxy like the FFs studied in Chapter 4, the values of β can be larger than one also for compact CC models leading to merger objects even smaller than 10 pc. For high-mass CCs of $M^{\rm CC} = 10^7$ M$_\odot$ the distances with $\beta > 1$ are even less than 2 kpc. Thus in this study of halo objects compact CCs have always β-values below one and evolve into typical EOs with sizes comparable to the initial CC sizes.

The mean sizes for typical observed EOs are between 13 and 15 pc (Sect. 5.5.1 and Fig. 5.39) for EOs fainter and brighter than -9 mag, respectively.

The evolution of extended CCs, however, is far more complex. CCs having initially a large β-value loose a significant fraction of the initial mass and evolve into typical (Sect. 5.5.1 and Fig. 5.39) and moderately extended EOs, whereas simulations with small β-values evolve into very to extremely extended EOs like for example VUCD7 in M87 or the Huxor EOs in M31.

For a well-defined CC in a well-known tidal field it is possible to determine the end-product of the merging event. For an observed EO, however, it is *not* possible to determine the initial CC from which it evolved. Even for a fixed orbit a range of initial conditions can lead to the same merger object due to the turnover in the $r_{\rm eff}$ vs. $M_{\rm encl}$ space. The turnover leads to degenerate states, i.e. relatively compact CCs in the galactic halo can produce an object with the same structural parameters as a more massive and extended CC with a high β-value. It is thus not possible to pinpoint the exact parameters of the parent CC. The parameter space of the progenitor CCs can be narrowed only for the extremely extended EOs. The more extended an EO the more specialized the initial conditions to obtain it. An extremely extended EO requires a large initial parent CC as well as a weak tidal field.

6

Summary

In the last decade, unusually extended old stellar clusters have been observed, which cover a huge mass range. Extended objects at the low-mass end with masses comparable to normal globular clusters (GCs) are called extended clusters (ECs), whereas objects at the high-mass end are called ultra-compact dwarf galaxies (UCDs). As there is no clear physical distinction between ECs and UCDs, both types of objects are called extended stellar dynamical objects (EOs) in this thesis. The rapidly increasing number of detected EOs, which are associated with various types of galaxies in different environments, allows for the first time an in-depth investigation of their nature. I compiled the first large catalog of observed EOs with effective radii larger than 10 pc from the literature (Chapter 3). The EO catalog constitutes the foundation of all subsequent simulations.

In addition, young massive star clusters (YMCs) with GC-like properties were found in all types of gas-rich galaxies. YMCs are particularly abundant in starburst and interacting galaxies, but are also present in apparently unperturbed disk galaxies. Observations have shown that YMCs are often not isolated, but are part of larger structures called cluster complexes (CCs). The CCs contain few to several dozens or possibly even hundreds of YMCs spanning up to several hundred parsecs in diameter. Observations show that most CCs have a massive concentration of star clusters in their centers and isolated star clusters in their vicinity and that there is evidence for merging in the central region. Since galaxy-galaxy encounters are anticipated to have been more common during early cosmological structure formation it is expected that star formation in CCs has been a significant star formation mode during early cosmological epochs. Indeed, the preponderance of clumpy galaxies (Elmegreen 2007, and references therein) indicates that early gas-rich galaxies went through an epoch of profuse CC formation.

In this thesis, I performed extensive numerical simulations to investigate whether CCs are the progenitors of EOs associated with galactic disks, also known as faint fuzzies (FFs), and of EOs located in galactic halos (halo ECs and UCDs). In this formation scenario all kinds of EOs evolve from CCs by merging of their constituent star clusters. The type of the resulting EO depends mainly on the initial CC mass, the initial CC size, and the external tidal field. I carried out different parameter studies on the evolution of CCs to investigate how the resulting merger objects correlate with the underlying CC parameter space and studied the influence of the tidal field by taking different orbits into account (Chapters 4 and 5). The first two parameter studies of Chapter 4 focused on well observed examples for EOs in the disk and the outer halo, whereas the parameter studies of Chapter 5 covered the topic of EOs located in galactic halos more generally. The major results of this thesis are summarized below.

6.1 A Comprehensive Catalog of Observed EOs

I compiled a catalog comprising 835 EOs with effective radii larger than 10 pc to be compared with the results of the simulations. The most important parameters required for the comparison are the effective radii and the total luminosities of the EOs. I distinguish between EOs found in late-type and early-type galaxies. The vast majority of EOs, i.e. 664, are associated with early-type galaxies, while only 171 EOs are associated with late-type galaxies. A table of the data is available in Appendix A. The results of the catalog are presented in Chapter 3 and were published in the Journal *Astronomy & Astrophysics* (Brüns & Kroupa 2012).

EOs and GCs form a coherent structure in the $r_{\rm eff}$ vs. $M_{\rm V}$ parameter space, while there is a clear gap between EOs and early-type dwarf galaxies. At each V-band luminosity, extended objects are found with effective radii between 10 pc and an upper limit, which shows a clear trend: the higher the luminosity the larger is the upper size limit. For all luminosities, the majority of EOs have effective radii which are only slightly larger than 10 pc. The median effective radius of EOs in late-type and early-type galaxies is 13.2 and 14.2 pc, respectively.

For EOs associated with early- and late-type galaxies, the peak of the EO luminosity function is about one magnitude fainter than the peak of the GC luminosity function. Plotting the turnover luminosity as a function of the effective radius shows that the turnover luminosity decreases continuously from $M_{\rm V,TO} = -7.67$ mag for compact GCs to $M_{\rm V,TO} = -6.66$ mag at the $r_{\rm eff}$-bin between 10 and 12 pc. For larger effective radii, the turnover luminosity decreases considerably slower to values of $M_{\rm V,TO} = -6.40$ mag at the $r_{\rm eff}$-bin between 20 and 30 pc. On the basis of the available data, I conclude that the turnover of the luminosity function depends significantly on the effective radii of star clusters and that the slope, $\Delta M_{\rm V,TO}/\Delta r_{\rm eff}$, is steeper for GCs than for EOs.

The EO populations in early- and late-type galaxies are very similar in the low-luminosity part ($M_{\rm V}$ fainter than about -10 mag). The main difference between the luminosity functions for late-type and early-type galaxies is the tail of high-luminosity objects associated with elliptical galaxies.

6.2 The Application of the Formation Scenario to Specific EOs

Observations have demonstrated that there are two types of EOs: EOs associated with galactic disks and EOs located in galactic halos outside the main stellar body of their host galaxy. I focused on a well observed example for both cases and performed two comprehensive computational parameter studies (Chapter 4). The results of the two parameter studies are summarized in the Appendices C.1 and C.2.

6.2.1 Faint Fuzzy Star Clusters in NGC 1023

The lenticular galaxy NGC 1023 hosts a population of EOs that are co-rotating with the stellar disk of this galaxy (Larsen & Brodie 2000; Brodie & Larsen 2002). These EOs were called faint fuzzies (FFs) by Larsen & Brodie (2000). As the FFs in NGC 1023 represent the sample with the best observational database, I use them as a test case for my first computational parameter study. The results are presented in Sect. 4.2 and were published in the *Astrophysical Journal* (Brüns et al. 2009).

Bastian et al. (2005) observed CCs in the disk of the spiral galaxy M51 and found evidence for merging in their centers. They discovered a mass-radius relation for the CCs that follows the mass-radius relation observed for the giant molecular clouds. These findings support the merging star cluster scenario and place a constraint on the initial conditions for CCs in simulations for the very first time.

The galaxies NGC 1023 and M51 are quite similar concerning their physical dimensions and both have a close companion galaxy. NGC 1023 is a lenticular galaxy now, but it might have

had star formation comparable to M51 in the past. I used the Bastian mass-radius relation of M51 as a constraint on the initial conditions of the CCs.

In my simulations, the CCs evolved in the gravitational field of NGC 1023 for five gigayears. Although the number of merged star clusters and the fraction of mass associated with the final objects varies considerably, all models resulted in a stable object. The apparent V-band luminosities of the modeled merger objects cover a range from 22.4 to 25.6 mag, while Larsen & Brodie (2000) detected FFs in the luminosity range 21.4 to 25.0 mag with a median value of 23.6 mag. The luminosities of the simulated merger objects are therefore in very good agreement with the observed luminosities of FFs. The effective radii for all simulations ranged between 3.6 and 13.4 pc. About 80% of the FFs observed by Larsen & Brodie (2000) have effective radii below 14 pc. The median of the observed effective radii is 10.7 pc. My results are therefore in good agreement with observations also with respect to effective radii.

The results of the simulations demonstrate that CCs from the high-mass end of the Bastian relation evolve into FF-like objects. The modeled merger objects resemble the observed parameters luminosity, mass, size and spatial distribution of FFs in NGC 1023 very well. The merging of star clusters in CCs is therefore a possible formation scenario for FFs.

6.2.2 The Milky Way Cluster NGC 2419

I chose the Milky Way cluster NGC 2419 to study the future fate of CCs in low gravitational field environments like galactic halos. NGC 2419 is one of the most luminous, one of the most distant, and as well one of the most extended star clusters of the Milky Way. For NGC 2419 comprehensive observational data are available to allow for a detailed comparison of simulations and observations.

The proposed formation scenario for NGC 2419 starts with newly born complexes of star clusters in the Galactic halo which were possibly formed during a past interaction between a gas-rich galaxy and the Milky Way. I varied the initial CC masses, initial CC Plummer radii, and initial distributions of star clusters in the CCs to analyze which initial conditions evolve into a NGC 2419-like object. The results are presented in Sect. 4.3 and were published in the *Astrophysical Journal* (Brüns & Kroupa 2011).

The data on NGC 2419 available at the time of the publication at the beginning of 2011 – mass, absolute V-band luminosity, effective radius, overall velocity dispersion and the surface brightness profile – are in good agreement with a number of merger objects with different model parameters. The velocity dispersion profile published later by Ibata et al. (2011) is also well reproduced by the models except for the innermost two bins, where the observed values are larger than the values of the merger object models. The deviation of these two values is, however, most likely due to the low number of observed stars in these bins.

The merger objects cover a significantly smaller parameter space than the input CC models. For each CC mass there is an upper limit of the effective radius which increases with the initial CC mass. For compact CCs the merger object radii increase with increasing initial CC Plummer radii. The larger the CCs become the easier it is for star clusters to escape the merging process which eventually leads to decreasing effective radii of the merger objects. For each CC mass there is a turnover in the effective radii of the merger objects at a certain CC Plummer radius. The effective radii of the merger objects are therefore constrained to a relatively small interval. The turnover of the simulations in the $r_{\rm eff}$ vs. $M_{\rm encl}$ space leads to degenerate states, i.e. relatively compact CCs can produce an object with the same structural parameters as a more massive and larger CC which looses a fair fraction of its initial star clusters during the merging process. In consequence, a range of initial conditions can form a merger object comparable to NGC 2419 which prevents us from pinpointing the exact parameters of the original CC, that could have formed NGC 2419.

An object like NGC 2419 can therefore be formed from merged CCs without the need of fine-tuning of the input parameters demonstrating that such halo clusters can be well explained by the merging star cluster scenario.

6.3 A General Study on the Formation of EOs

In the last years the number of observed ECs and UCDs has steadily increased. EOs have now been observed in all types of galaxies ranging from dwarf galaxies to giant elliptical galaxies. To cover the topic of EOs more generally, I performed three comprehensive parameter studies to allow to link the individual types of observed EOs with the initial parameters of the CC models and their environment. The basic and most important parameters of a CC are its mass and size. These two parameters were studied in detail in the parameter study of Sect. 5.2 for a fixed eccentric orbit between 20 and 60 kpc in a Milky-Way-like gravitational potential. The third important factor is the external tidal field which also has a large impact on the evolution of a CC. The tidal field was therefore covered by a subsequent parameter study varying the orbital parameters for a fixed CC mass (Sect. 5.3). The third parameter study focused on the extremely extended EOs and discussed the special conditions of their formation (Sect. 5.4). The results of the three parameter studies are summarized in the Appendices C.4 – C.6.

6.3.1 A Parameter Study of the Initial CC Parameters Mass and Size

I have performed an extended parameter study on the whole mass range of the observed EOs of the catalog. The varied sizes and masses of the CCs are covered by a matrix of 5×6 values with CC Plummer radii between 10 and 160 pc and CC masses between $10^{5.5}$ and 10^{8} $M_{\odot}$, which are consistent with the range of observed CC parameters. As observations demonstrate, massive CCs predominantly form during severe gravitational encounters between late-type galaxies like for example the Antennae galaxies. Therefore, the CC models were placed on eccentric orbits between 20 and 60 kpc and were integrated up to 5 Gyr. The aim was to analyze how the final merger objects correlate with the underlying CC parameter space. The results are presented in Sect. 5.2 and were published in the Journal *Astronomy & Astrophysics* (Brüns et al. 2011).

The merger objects cover basically the same parameter space as the observed EOs from the catalog and show the same trend of increasing effective radii with increasing mass. Solely the extremely extended EOs, which represent only about 5% of all EOs, were not covered by these simulations. The turnover in the $r_{\rm eff}$ vs. $M_{\rm encl}$ space, which was also discovered in the NGC 2419-project (Sect. 4.3), depends on the mass of the initial CC and occurs at larger CC Plummer radii for higher CC masses. In addition, the turnover leads to a higher probability for merger objects to have rather low effective radii which is consistent with the findings of the EO catalog.

6.3.2 A Parameter Study of the Dependence on the Orbit

I carried out simulations on different circular and eccentric orbits to study the influence of the tidal field on the merging process. I restricted the simulations to the low-mass end of the models ($M^{\rm CC} = 10^{5.5}$ $M_{\odot}$), because extended low-mass CC models are most affected by a tidal field. The simulations cover initial CC Plummer radii of 20, 40, 80, and 160 pc and circular orbits at 20, 40, 60, and 120 kpc. In addition, different eccentric orbits as well as simulations without an external tidal field were performed. The results of this study are presented in Sect. 5.3.

The merger objects show a turnover in the $r_{\rm eff}$ vs. $M_{\rm encl}$ space, which depends on the orbit of the CC and occurs at larger CC sizes for weaker tidal fields. The results of the models at large galactic distances resemble the findings of the simulations for higher CC masses, which were studied in the parameter study of Sect. 5.2. A weak gravitational field, i.e. a large galactic

distance, has the same effect on the evolution of a CC as a high initial CC mass. Both, higher CC masses and weaker gravitational fields lead to larger tidal radii which result in larger enclosed masses and larger effective radii of the final merger objects.

Simulations with an initial CC Plummer radius of 160 pc, which is in the dwarf galaxy regime, result after 5 Gyr of evolution in EOs having effective radii between 10 and 50 pc for circular orbits between 20 and 120 kpc. The most extended low-mass CC models loose up to 80% of their initial CC mass, which would classify these initial CCs as unstable objects if viewed in their entirety. Nevertheless, even these CCs evolve into stable low-mass EOs. My simulations demonstrate that CCs with initial parameters similar to dwarf galaxies do not necessarily end up as dwarf galaxies as anticipated in some publications (e.g. Dabringhausen & Kroupa 2013), if the disturbing effect of an external tidal field is considered.

6.3.3 A Parameter Study on the Formation of Extremely Extended EOs

To explain the formation of extremely extended EOs, which were not covered by the merger objects on the eccentric orbit as presented in Sect. 5.2, I performed a parameter study for different CC masses in weak tidal fields and without a tidal field. I investigated the evolution of CC models on circular orbits at 60 and 120 kpc for different initial CC Plummer radii in the mass interval between $M^{\rm CC} = 10^5$ and 10^6 $\mathrm{M}_\odot$. Moreover, I extended the simulations of my most extended CC models ($R_{\rm pl}^{\rm CC} = 160$ pc) to CC masses up to $M^{\rm CC} = 10^8$ $\mathrm{M}_\odot$ for the circular orbit at 60 kpc and $M^{\rm CC} = 10^7$ $\mathrm{M}_\odot$ for the circular orbit at 120 kpc. The results are presented in Sect. 5.4. Some elements were published in the Journal *Astronomy & Astrophysics* (Brüns & Kroupa 2012).

For luminosities fainter than $M_{\rm V} = -10$ mag, the CC models on circular orbits fill the area between those on the eccentric orbits as presented in Sect. 5.2 and the most extended EOs observed so far. The merger objects of the CC models with $R_{\rm pl}^{\rm CC} = 160$ pc on the circular orbit at 120 kpc have even larger sizes than the observed EOs. For luminosities brighter than $M_{\rm V} = -10$ mag, a circular orbit at 120 kpc is needed to cover also the most extreme EOs. Consequently, the merging star cluster scenario predicts that the extremely extended EOs, which represent about 5% of the total EO population, are located in environments with weak tidal fields, which are the outer halos of galaxies. This is consistent with the observational trend of observing the majority of extremely extended EOs only at large projected distances.

6.4 Conclusion

In my thesis I addressed the questions whether EOs could have evolved from CCs by merging of their constituent star clusters and whether the overall distribution and the trends of observed EOs can be reproduced by this formation scenario.

I have shown that all types of EOs, i.e. FFs, halo ECs, and UCDs, can be explained as the final objects of a merging process of star clusters in CCs. The distinction made between FFs, ECs, and UCDs is no longer existent in my formation scenario. They all stem from the same formation process and are therefore united under the name "extended stellar dynamical object".

The merging star cluster scenario reproduces the structural parameters, the distribution and the overall trends of all the observed EOs very well, whereas alternative formation scenarios such as the galaxy threshing scenario can only explain a part of the EO sample. Detailed structural features of specific objects like two-component or core-halo surface brightness profiles, which were taken as evidence for the galaxy threshing scenario in some publications, are also well reproduced in my formation scenario.

The results of this thesis demonstrate that the final fate of a CC depends crucially on its initial size and mass, and on the external tidal field. For a well-defined CC in a well-known

tidal field it is possible to determine the end-product of the merging event. For an observed EO, however, it is *not* possible to determine the initial CC from which it evolved. Even for a fixed orbit, a range of initial conditions can lead to the same merger object due to the turnover in the $r_{\rm eff}$ vs. $M_{\rm encl}$ space, as relatively compact CCs can produce an object with the same structural parameters as a more massive and extended CC having a high β-value, i.e. a size larger than the tidal radius. The situation is somewhat different for very extended EOs as they need very special initial conditions. The formation of an extremely extended EO requires a large initial parent CC as well as a weak tidal field (i.e. a low β-value).

Considering the need of extreme parameters, i.e. weak tidal fields and very extended CCs, to create extremely extended objects, a low number of these objects is expected from the merging star cluster scenario, which is consistent with the observed EO distribution as shown in Sect. 5.5.

There is a gap region in the $r_{\rm eff}$ vs. $M_{\rm V}$ parameter space between ECs and dwarf spheroidal galaxies known as the Gilmore gap where so far no objects have been detected. According to the merging star cluster scenario EOs in the Gilmore gap are not prohibited, but require extreme conditions and are therefore expected to be very rare. These objects, which I referred to as ultra fluffy objects (UFOs), will be a real challenge for observers as they are extremely extended with a very low central surface brightness, and they are expected only in very low numbers far out in galactic halos.

In conclusion, the results of my thesis demonstrate that the merging star cluster scenario is a very promising formation scenario that explains for the very first time the formation of FFs, halo ECs, and UCDs in a coherent picture.

7

Outlook

This thesis presents the first systematic study on the evolution of cluster complexes (CCs). The basic and most important parameters of a CC are its mass and size. These two parameters were varied in all parameter studies to investigate how the structural parameters of the final merger objects correlate with the underlying CC parameter space. The third important factor which has a large impact on the evolution of a CC is the external tidal field. The influence of the external tidal field was studied by varying the orbital parameters of the CCs. These three parameters were varied systematically and the results were compared with observed EOs. In addition, I also varied the number of SCs building up the CCs and the distribution of the SCs of the CCs.

Next to the basic parameters, there are other secondary parameters like for example the detailed spatial distribution of the star clusters, their mass distribution, the internal kinematics of CCs etc. which could be varied to further refine the merging star cluster scenario. In order to constrain the number of simulations, it is of paramount importance to narrow down the parameter space of the initial CCs and of their orbits. The corresponding observational needs are presented in Sect. 7.1. Section 7.2 discusses the computational refinements for the merging star cluster scenario, which would be based on new observational results (see Sect. 7.1).

The most promising alternative model, expecially for UCDs, is the galaxy threshing scenario (Bekki et al. 2001; Drinkwater et al. 2003). Bekki et al. (2003) showed that in principle UCDs can be explained as cores of stripped dwarf galaxies. Systematic parameter studies similar to those of the merging star cluster scenario presented in this thesis are needed for this scenario as well. Possible projects are suggested in Sect. 7.3.

In order to allow for a final conclusion whether the merging star cluster or the galaxy threshing scenario is the dominant process, further observational details of the EO sample are necessary. The observational requirements on EOs are discussed in Sect. 7.4.

7.1 Observational Constraints on the Initial CCs

The observational foundation of CCs is basically limited to four general facts: Firstly, they exist in different environments from galactic disks like M51 to major galaxy-galaxy interaction events like the Antennae. Secondly, they cover a mass range from a few $10^4\,M_\odot$ to about $10^8\,M_\odot$. Thirdly, CCs contain few to several dozens or possibly even hundreds of YMCs. Fourthly, CCs tend to have a centrally peaked luminosity distribution and total dimensions of up to several hundred parsecs in diameter.

Little is known about the internal parameters of CCs. In the simulations presented in this thesis, the star clusters of the CC models are distributed according to a Plummer distribution, as this is a reasonable first order approximation of the observed CCs. However, the surface

brightness profiles of CCs need to be analyzed in greater detail using high-resolution observations to scrutinize the distribution of star clusters within CCs as well as their individual masses and sizes. A deeper knowledge of the mass distribution within a CC is necessary to refine the set-up of the CC models.

In addition, the internal kinematics of CCs are largely unknown. Whitmore et al. (2005) found that the cluster-to-cluster velocity dispersion of five CCs in the Antennae galaxies is small enough to keep them just gravitationally bound. This result was the observational basis for the decision to use CC models that are initially in virial equilibrium. A considerably larger sample of CCs is necessary to clarify the typical dynamical state of CCs, which might as well be slightly expanding or collapsing.

While I used CCs that are composed of star clusters having all the same initial mass, observations demonstrate that the individual YMCs in a CC cover a considerable range of masses. The CCs observed in the Antennae galaxies by Whitmore et al. (2005, 2010) typically consist of a few YMCs with masses well above 10^5 $M_\odot$, about 25 YMCs with masses greater than 10^4 $M_\odot$ and about 60 lower-mass clusters. Apart from this study no detailed mass functions for the YMCs in CCs were published.

Bastian et al. (2005) derived a mass-size relation for eleven CCs in the disk of the spiral galaxy M51 (see Fig. 4.3 in Sect. 4.2). Even eight years after the discovery of Bastian et al. (2005), no comparable follow-on studies of CCs in other galaxies were performed. Therefore, it is not clear whether CCs in other galaxies also show a tight mass-size relation or whether the CC mass spectrum and the CC size spectrum are independent from each other, i.e. they would cover a large parameter space. If tight mass-size relations were the norm, it would be of high importance to answer the question whether there is a general mass-size relation for all CCs in different kind of galaxies. A general mass-size relation would help to constrain the parameter space of CC models of future computational studies.

While YMCs and CCs with masses below $M = 10^6$ $M_\odot$ were found in all types of galaxies containing sufficient amounts of gas to form star clusters, the currently available data indicate that high-mass YMCs and CCs ($M \gtrsim$ few$\times 10^6$ $M_\odot$) are associated solely with major encounters like the Antennae (Whitmore et al. 2005), Arp 220 (Wilson et al. 2006), or NGC 7252 (Bastian et al. 2013), which may be in the process of becoming elliptical galaxies. Further studies of CCs in different environments are necessary to shed light on the detailed boundary conditions for the creation of CCs with different masses and sizes.

So far, CCs were detected within the disk of spiral galaxies like M51 (Bastian et al. 2005), in the outer parts of the disks of heavily interacting galaxies like the Antennae (Whitmore et al. 2005), and in tidal tails at large galactic distances like the CCs in the tidal tail of the Tadpole galaxy (Tran et al. 2003). A comprehensive study on the spatial distribution of CCs as well as their kinematical state is necessary to shed light on the range of gravitational environments during the first few CC crossing times, which are decisive for the merging process. Such results would help to narrow down the parameter space of realistic initial locations and orbits of CC models in future parameter studies.

7.2 Computational Refinements of the Merging Star Cluster Scenario

In the current simulations the star clusters of the CC models are distributed according to a Plummer distribution, the CCs are initially in virial equilibrium ($Q \approx 0.5$)[1] and do not rotate. On the basis of new observational results (see Sect. 7.1), additional computational studies could be performed to explore the influence of different star cluster distributions and CC kinematics.

[1]The virial ratio $Q = \frac{T}{|V|}$ of a CC is defined as the ratio between the total kinetic energy, T, of its constituting star clusters and the total potential energy, V, treating each star cluster as a point mass. For $Q = 0.5$ the CC is in virial equilibrium. For $Q < 0.5$ the CC tends to collapse and for $Q > 0.5$ the CC tends to expand.

The CCs in my simulations do not contain any residual gas, i.e. all the gas of the initial giant molecular cloud complex, which formed the CC, was completely converted into stars which corresponds to a star formation efficiency[2] of $\epsilon = 1$. A low to medium star formation efficiency implies considerable amounts of residual gas associated with the individual star clusters and also the overall CC. Depending on the mass of the individual star clusters and the CC, supernova explosions will blow out a part or all of the residual gas leading to a significant mass loss and potentially to a major expansion of the CC. On the other hand, Mengel et al. (2008) observed individual young (≈ 10 Myr) clusters associated with CCs in the Antennae and NGC 1487. They compared dynamical mass estimates with derived photometric masses and found them in excellent agreement, implying that most of the YMCs survived the gas removal phase and are bound stellar objects. Besides the star formation efficiency there are more free parameters like the exact instant of time when the star clusters expel their gas (before or after the merging of the star clusters), a possible time delay between the gas expulsion of the individual star clusters and the gas expulsion timescale (instantaneous gas removal or slow gas expulsion). Accounting for all these free parameters will result in a computationally very demanding and extensive project. Fellhauer & Kroupa (2005b) investigated the influence of the star formation efficiency on one rather compact CC model on a fixed circular orbit at a distance of 10 kpc. For this CC model they varied the star formation efficiency between 0.1 and 1.0 and studied the effect of coeval and time delayed mass loss. While they demonstrated that even a star formation efficiency as low as 0.2 leads to a stable merger object, it was not yet shown how this result depends on the CC parameters mass and Plummer radius and on the orbit.

In my simulations I used CCs with YMCs of equal mass. Observations demonstrate that YMCs in a CC are distributed with a spectrum of masses. However, the mass range covered by the YMCs and also the relative frequency of different YMC masses in a CC are not well constrained by observations. Simply assuming a power law mass function for YMCs in CCs would result in computationally very expensive calculations, because in order to sample the power law correctly a very large number of low-mass objects for each high-mass object are needed. Therefore simulations with a mass spectrum have to deal with significantly more star clusters than simulations with equal mass star clusters. Such projects are not possible in a reasonable period of time – at least not with the current computational infrastructure available at the AIfA.

The external gravitational potentials in my simulations are time-independent and mimic the Milky Way and NGC 1023 today. However, structure formation in a standard cosmological model suggests that in the early Universe galaxies were considerably smaller and grew by mergers between galaxies and/or accretion of lower mass galaxies. In the merging star cluster scenario, the galaxy-galaxy interactions are responsible for the creation of the CCs in the first place. To account for the successive growing of the galactic potential simulations could implement a time variable potential for the parent galaxy. An accreting potential will cause the orbit to shrink over time leading to progressively more destructive tidal heating of the merger object. However, the influence of a slowly growing potential should have only a minor impact on the merger object as the merging timescale is short compared to the timescale of galaxy growth.

In the simulations I modeled the dynamical evolution of various CCs leading to merger objects. I did not, however, consider the process which formed the CCs in the first place as this would have increased the complexity of the simulations and added more degrees of freedom making the interpretation of the results difficult. In subsequent simulations the encounter between two live disk galaxies, which leads to the formation of tidal arms, could be calculated. Along these emanating arms CCs could be placed and their evolution could be traced for sev-

[2]The star formation efficiency, ϵ, is the fraction of the initial pre-CC molecular cloud mass, $M_{\rm MC}$, converted into stars: $\epsilon = \frac{M_{\rm stars}}{M_{\rm MC}} = \frac{M_{\rm stars}}{M_{\rm stars}+M_{\rm gas}}$ where $M_{\rm stars}$ is the embedded stellar mass and $M_{\rm gas}$ is the gas left over from the star formation process.

eral gigayears. The live disk and tidal arm computations, however, will be computationally very expensive. Due to the additional free parameters in such simulations, a large parameter study would be necessary to understand the impact of these parameters on the structural parameters of the merger objects. This type of project is not possible in a reasonable period of time – at least not with the current computational infrastructure available at the AIfA.

7.3 Computational Projects for the Galaxy Threshing Scenario

Another popular formation scenario – at least for high-mass EOs – is the galaxy threshing scenario, where UCDs represent former nucleated dwarf galaxies which lost all stars except for their nucleus (Bekki et al. 2001; Drinkwater et al. 2003). Bekki et al. (2003) and Goerdt et al. (2008) performed numerical simulations which demonstrated that in principle UCD-like objects can be formed from stripped galaxies. While Bekki et al. (2003) conclude that highly eccentric orbits are necessary to transform a nucleated dwarf elliptical into a UCD, they neither presented nor discussed the effective radii of their final objects to demonstrate that these objects indeed reproduce the observed structural parameters of UCDs. Similarly, Goerdt et al. (2008) conclude that the threshing scenario explains the observed parameters of UCDs, but they also state that "*the resolution of our hydrodynamic simulation is not sufficient to allow a meaningful comparison with the observations*".

Very recently, Pfeffer & Baumgardt (2013) performed a first parameter study where three models of nucleated dwarf ellipticals (dE,N) were placed on different elliptical and "box orbits". Box orbits were emulated by placing the dE,N galaxies first on elliptical orbits and after a few passages resetting them on a circular orbit at the apocentric distance. Pfeffer & Baumgardt (2013) conclude that all observed sizes of UCDs can be reproduced by these "box orbits". However, their model galaxies are pure stellar objects without any dark matter. A dark matter potential would hamper the stripping of the stellar body of the dwarf galaxy. A systematic extensive parameter study covering a large range of initial dwarf galaxy masses, dark matter contents, and different ratios of the sizes for the nucleus and the envelope for different orbits is needed to quantify how frequently UCDs actually occur in this scenario. Depending on the initial dwarf galaxy parameters and its orbit, all kinds of objects between the extreme cases of the entire dwarf galaxy dissolving and the dwarf galaxy surviving completely are possible. Thus the probability to obtain a UCD via the galaxy threshing scenario is expected to be much more restricted than in the merging star cluster scenario.

So far the threshing scenario focussed only on the UCD regime. It was never demonstrated that the threshing scenario is able to reproduce also low- or medium-mass EOs. Parameter studies covering the entire mass range of observed EOs are needed for direct comparison with the merging star cluster scenario.

Furthermore, the galaxy threshing scenario needs to be applied to specific, well-defined objects to investigate how well threshing can reproduce the observed structural parameters and special features. The Milky Way EO NGC 2419 is frequently assumed to be the nucleus of a stripped dwarf galaxy (e.g. van den Bergh & Mackey 2004), but this assumption was never substantiated by simulations. I have demonstrated in Sect. 4.3 that NGC 2419 can be well explained as the remnant of a merged CC. The merging star cluster scenario is able to reproduce parameters like mass, absolute V-band luminosity, effective radius, velocity dispersion and the surface brightness profile. It would be very interesting to see how well the threshing scenario can reproduce all these features.

7.4 Observational Requirements on EOs

The EO catalog presented in Chapter 3 is the largest possible compilation of EOs based on the currently available literature. Many GC surveys applied size limits to reduce the contam-

ination by background galaxies, thereby excluding potential EOs from the GC catalogs. The existing HST data of these GC catalogs need to be re-examined with a focus on the EOs. Most observational GC and UCD surveys focussed on the main body of galaxies covering only a tiny fraction of their halos. For example in the Hydra Cluster Misgeld et al. (2011) searched for massive star clusters with ground based telescopes and detected and spectroscopically confirmed 118 objects with total V-band luminosities between $M_{\rm V} = -9.7$ and -13.3 mag and projected distances between 3 and 300 kpc. But only 26 of the 118 stellar objects were located within the central two HST fields and thus have size information. It is expected that also a large fraction of the remaining 92 objects in the outer halo are EOs. The EO catalog presented in Chapter 3 needs to be continuously updated with newly discovered EOs and complemented with additional data like mass-to-light ratios, ages, and metallicities.

The turnover of the EO luminosity function seems to be at least one magnitude fainter than the turnover of the GC luminosity function. However, the majority of the observed EOs of my EO catalog, i.e. 657 out of 835 EOs, have not been spectroscopically confirmed yet. Therefore, the current luminosity function might be considerably contaminated by background objects. As the confirmation of faint objects is an extremely time-consuming task, a focus needs to be taken on EO samples that would make maximum use of modern telescopes allowing for multiple spectra taken simultaneously in the same field of view. The 217 EO candidates in the elliptical galaxy NGC 4365 (Blom et al. 2012) represent the largest known sample of low-mass EOs associated with one galaxy. Consequently, the EOs in this galaxy would be a good starting point to confirm the EO luminosity function.

In the $r_{\rm eff}$ vs. $M_{\rm encl}$ parameter space there seems to be a gap at about $M_{\rm V} = -8.5$ mag. In Chapter 3, I demonstrated that this gap is most likely a selection effect and that the luminosity functions for early- and late-type galaxies are almost identical except for a tail of high-luminosity objects associated with early-type galaxies. Further observations of EO samples in early-type galaxies covering the entire luminosity range from $M_{\rm V} = -4$ to -14 mag are necessary to answer the question, whether there is indeed a tail of high-luminosity objects exceeding the normal luminosity function, or whether those galaxies, which have a large number of high-luminosity EOs, have an even larger amount of low-luminosity EOs leading to a normal luminosity function, if viewed in its entirety.

For confirmed EOs additional information like mass-to-light ratios, metallicities and ages should be derived. In my catalog only 31 EOs of 835 EOs have a measured mass-to-light ratio. Based on the currently available data, UCDs appear to have a systematically higher mass-to-light ratio than ECs (Dabringhausen et al. 2008). As the number of EOs with a measured mass-to-light ratio is so small we do not know which mass-to-light ratios are typical for EOs and whether the mass-to-light ratios depend on the masses and sizes of the EOs and/or their projected distances. Other objects of particular interest are the extremely extended UCDs and cE-galaxies. In the $r_{\rm eff}$ vs. $M_{\rm encl}$ parameter space there seems to be an overlap between these two types of objects. The cEs appear to have higher mass-to-light ratios than UCDs. Large samples of confirmed objects with observed mass-to-light ratios are necessary to answer the question whether extremely extended UCDs and cEs are completely different types of objects, as expected from the merging star cluster scenario, or whether there is a continuous transition between UCDs and cEs, representing different evolutionary states, as one would expect in the context of the galaxy threshing scenario.

In this context, it is of interest to answer the question whether there are objects in the Gilmore gap between ECs and dwarf spheroidal galaxies. As the difference in mass-to-light ratios between ECs and dwarf spheroidal galaxies is extremely large in this mass range, objects in the Gilmore gap could prove whether there is a continuous trend of mass-to-light ratios, or whether potential objects in this area are clearly either ECs or dwarf spheroidal galaxies.

Objects in the Gilmore gap are extremely hard to find observationally as they have a very

low surface brightness. Moreover, the merging star cluster scenario predicts that such objects can only be found in weak tidal fields, i.e. in the very outer halo of their host galaxies, and that they are extremely rare. Therefore, detecting EOs in the Gilmore gap requires deep integrations of the outer halos of galaxies, which need to be covered by a huge amount of HST fields. The success of such a proposal for the Hubble Space Telescope is quite unlikely.

The distribution of EOs in different galaxies should be investigated in more detail and compared to the distribution of the GCs. There is some evidence that EOs might not be uniformly distributed (see Chapter 3) which would be an indicator of a tidal origin. In case EOs are not distributed isotropically it would be interesting to know whether EOs are confined to a disk-like structure as the satellites galaxies of the Milky Way. In addition, kinematical data would be needed to investigate whether EOs are kinematically coupled, e.g. in form of a general, ordered rotation of the EO sample. Moreover, ages of individual EOs are required to identify groups of EOs having approximately the same age. Different discrete phases of EO formation would be in favor of a tidal origin whereas a continuous age distribution of EOs would argue against it.

A

Catalog of Extended Stellar Dynamical Objects

In Chapter 3, a catalog of extended stellar dynamical objects was presented. In this appendix, the EO catalog is presented in full, see Table A.1. Table A.2 provides an overview on the galaxies, where EOs were found so far.

In Table A.1, the columns are the running number, the designation of the EO in this thesis, an alternative name or designation in original paper, the coordinates right ascension and declination (J2000), effective radius of the EO, r_{eff}, absolute V-band luminosity of the EO, M_V, projected distance to the host galaxy (for the Milky Way the galactocentric distance is used), R_{proj}, and references for the data: 1 Harris (1996), 2 Salinas et al. (2012), 3 van den Bergh & Mackey (2004),4 Hwang et al. (2011), 5 Huxor et al. (2008), 6 Huxor et al. (2011a), 7 Peacock et al. (2009), 8 Stonkutė et al. (2008), 9 Cockcroft et al. (2011), 10 Georgiev et al. (2009), 11 Taylor et al. (2010), 12 Gómez et al. (2006), 13 McLaughlin et al. (2008), 14 Mouhcine et al. (2010), 15 Chattopadhyay et al. (2009), 16 Nantais et al. (2011), 17 Strader et al. (2012b), 18 Sharina et al. (2005), 19 van den Bergh (2006), 20 Da Costa et al. (2009), 21 Chandar et al. (2004), 22 Hwang & Lee (2008), 23 Hau et al. (2009), 24 Larsen et al. (2001b), 25 Harris et al. (2009), 26 Larsen & Brodie (2000), 27 Norris & Kannappan (2011), 28 Chies-Santos et al. (2011), 29 Haşegan et al. (2005), 30 Chilingarian & Mamon (2008), 31 Evstigneeva et al. (2008), 32 Brodie et al. (2011), 33 Evstigneeva et al. (2007), 34 Chies-Santos et al. (2007), 35 Mieske et al. (2008), 36 Hilker et al. (2007), 37 Richtler et al. (2005), 38 Chilingarian et al. (2011), 39 DeGraaff et al. (2007), 40 Goudfrooij (2012), 41 Blom et al. (2012), 42 Chies-Santos et al. (2006), 43 Cantiello et al. (2009), 44 Da Rocha et al. (2011), 45 Mieske et al. (2007), 46 Misgeld et al. (2011), 47 Penny et al. (2012), 48 Chiboucas et al. (2011), 49 Madrid et al. (2010), 50 Madrid (2011), 51 Blakeslee & Barber DeGraaff (2008), 52 Strader et al. (2012a). The EOs are sorted according to the distance to the host galaxy and for each galaxy from the brightest to the faintest EO.

In Table A.2 the columns denote name of the galaxy, type of host galaxy (LT: late-type, ET: early-type), absolute V-band luminosity of the galaxy, $M_{V.gal}$, distance of the galaxy,D_{gal} size of a HST ACS pixel at the distance of the galaxy, number of EOs, minimum absolute V-band luminosity of the EO, maximum absolute V-band luminosity of the EO, number of GCs in the same publications, references as in Table A.1. The parameters of the host galaxies were taken from the NASA Extragalactic Database (NED) (http://ned.ipac.caltech.edu).

TABLE A.1— A catalog of EOs compiled from the literature

Nr.	Name	alt. Name	RA (deg)	Dec (deg)	r_{eff} (pc)	M_V (mag)	R_{proj} (kpc)	Ref.
1	MWEO-01	NGC2419	114.53529	38.88244	21.4	-9.42	89.9	1
2	MWEO-02	NGC5466	211.36371	28.53444	10.7	-6.98	16.3	1
3	MWEO-03	NGC5053	199.11288	17.70025	13.2	-6.76	17.8	1
4	MWEO-04	IC1257	261.78542	-7.09306	10.2	-6.15	17.9	1
5	MWEO-05	Pal4	172.32000	28.97358	16.1	-6.01	111.2	1
6	MWEO-06	Pal3	151.38292	0.07167	17.5	-5.69	95.7	1
7	MWEO-07	Pal15	254.96250	-0.53889	14.4	-5.51	38.4	1
8	MWEO-08	Pal5	229.02188	-0.11161	18.4	-5.17	18.6	1
9	MWEO-09	Eridanus	66.18542	-21.18694	12.1	-5.13	95.0	1
10	MWEO-10	Pal14	242.75250	14.95778	27.1	-4.80	71.6	1
11	MWEO-11	AM1	58.75958	-49.61528	14.7	-4.73	124.6	1
12	SGRdSphEO-1	Terzan8	295.43504	-33.99947	15.3	-5.68	5.0	2
13	SGRdSphEO-2	Arp2	292.18379	-30.35564	13.7	-5.41	3.4	2
14	LMCEO-1	NGC2257	97.55775	-64.32561	10.5	-7.25	6.9	3
15	LMCEO-2	NGC1841	71.34729	-83.99906	10.8	-6.82	12.8	3
16	LMCEO-3	Reticulum	69.03750	-58.85833	19.3	-5.22	10.2	3
17	LMCEO-4	ESO121-SC03	90.51040	-60.52375	10.0	-4.37	8.6	3
18	FornaxEO-1	Fornax1	39.25792	-34.18361	11.8	-5.32	1.6	3
19	N6822EO-1	N6822C1	295.04904	-15.36314	14.0	-7.70	10.5	4
20	N6822EO-2	N6822C2	295.76829	-14.97264	11.5	-6.10	4.0	4
21	N6822EO-3	N6822C4	296.87725	-14.44703	13.8	-6.06	5.8	4
22	M31EO-01	M31HEC5	9.58125	41.77917	24.1	-7.68	13.3	5;6
23	M31EO-02	M31HEC4	9.51917	40.72250	25.9	-7.45	14.1	5;6
24	M31EO-03	B247	10.25912	41.00878	11.4	-7.25	5.6	7
25	M31EO-04	M31HEC7	10.72917	43.94222	20.0	-7.03	36.4	5;6
26	M31EO-05	H16	10.15750	39.75831	10.7	-6.94	21.3	7
27	M31EO-06	M31HEC11	13.82217	38.84931	20.0	-6.70	46.0	5;6
28	M31EO-07	B066	10.51267	40.74597	10.1	-6.70	7.3	7
29	M31EO-08	M31HEC12	14.56425	38.04944	27.7	-6.68	59.1	5;6
30	M31EO-09	B210	11.01217	41.24026	10.8	-6.68	3.4	7
31	M31EO-10	B025D	10.39300	41.01830	12.0	-6.64	4.5	7
32	M31EO-11	M31HEC10	13.65167	44.95439	19.0	-6.30	58.6	5;6
33	M31EO-12	V031	10.30062	41.09226	15.4	-6.10	4.6	7
34	M31EO-13	M31HEC1	6.39150	40.70572	24.0	-6.00	44.6	5;6
35	M31EO-14	M31HEC9	12.69117	41.67372	24.0	-6.00	21.3	5;6
36	M31EO-15	B257D	11.24758	41.91307	14.7	-5.99	10.5	7
37	M31EO-16	M31HEC6	9.64833	44.25306	24.0	-5.50	42.0	5;6
38	M31EO-17	M31HEC2	7.13188	37.50989	17.0	-5.30	62.8	5;6
39	M31EO-18	M31HEC8	11.36208	40.20361	22.0	-5.10	16.1	5;6
40	M31EO-19	M31HEC3	9.13217	44.72869	21.0	-4.50	49.7	5;6
41	M31EO-20	M31HEC13	14.57054	37.20253	27.0	-4.40	68.2	5;6
42	M33EO-1	M33-EC1	23.24374	29.86750	20.3	-6.60	12.4	8
43	M33EO-2	HM33-A	23.92388	28.82086	20.1	-5.90	28.6	9
44	UGCA86EO-1	UGCA86-20	59.92667	67.14829	10.8	-7.58	0.6	10
45	UGC8638EO-1	UGC8638-01	204.86167	24.76402	13.6	-6.57	1.6	10
46	NGC247EO-1	NGC247-01	11.79050	-20.62785	16.0	-7.42	8.4	10
47	NGC247EO-2	NGC247-02	11.79829	-20.64683	18.8	-6.59	7.3	10

TABLE A.1— A catalog of EOs – continued

Nr.	Name	alt. Name	RA (deg)	Dec (deg)	r_{eff} (pc)	M_V (mag)	R_{proj} (kpc)	Ref.
48	NGC5128EO-01	GC0225	201.38167	-43.00050	13.5	-11.17	1.4	11
49	NGC5128EO-02	GC0123	201.27417	-43.17511	10.6	-10.31	10.9	11
50	NGC5128EO-03	C003	201.24254	-42.93611	10.7	-10.23	7.8	15
51	NGC5128EO-04	GC0171	201.31833	-43.03519	11.2	-10.12	2.4	11
52	NGC5128EO-05	GC0217	201.37542	-42.99317	11.9	-9.87	1.7	11
53	NGC5128EO-06	80	201.43504	-42.64040	10.4	-8.35	24.5	12
54	NGC5128EO-07	129	201.94974	-42.91334	14.3	-7.72	28.3	12
55	NGC5128EO-08	141	201.15768	-43.16919	18.4	-7.60	13.7	12
56	NGC5128EO-09	N21	201.43794	-42.64941	10.4	-7.48	24.0	12
57	NGC5128EO-10	N32	201.69151	-43.19492	14.6	-7.29	19.0	12
58	NGC5128EO-11	F2GC70	201.28717	-43.14814	12.9	-7.12	9.1	15
59	NGC5128EO-12	N34	201.76674	-43.25949	16.2	-7.05	24.4	12
60	NGC5128EO-13	C148	201.38229	-43.09611	10.0	-6.90	5.0	15
61	NGC5128EO-14	210	201.20136	-43.47885	11.9	-6.84	30.5	12
62	NGC5128EO-15	C169	201.46254	-42.92675	30.9	-6.76	7.5	15
63	NGC5128EO-16	C102	201.46696	-42.98733	14.4	-6.64	5.2	13
64	NGC5128EO-17	225	201.37589	-43.45494	18.6	-6.60	28.0	12
65	NGC5128EO-18	C134	201.30500	-43.04203	12.9	-6.56	3.2	15
66	NGC5128EO-19	N35	201.78705	-43.27181	15.8	-6.32	25.6	12
67	NGC5128EO-20	C162	201.42029	-43.08344	10.7	-6.20	4.9	15
68	NGC5128EO-21	F1GC20	201.52271	-42.92289	11.5	-6.08	9.6	15
69	NGC5128EO-22	N37	201.85425	-43.00227	13.4	-6.00	23.0	12
70	NGC5128EO-23	C114	201.16867	-42.89314	12.0	-5.92	12.3	15
71	NGC5128EO-24	C105	201.52133	-42.92694	11.3	-5.85	9.4	13
72	NGC5128EO-25	C175	201.50387	-42.97469	13.2	-5.42	7.1	15
73	NGC5128EO-26	GC0606	201.30167	-43.58762	14.7	-5.20	36.6	14
74	M81EO-01	31	148.66192	69.06959	19.3	-8.59	5.2	16
75	M81EO-02	195	148.87566	69.04019	10.5	-7.90	1.6	16
76	M81EO-03	140	148.82146	69.15063	16.6	-7.88	5.7	16
77	M81EO-04	391	149.09188	68.99518	10.9	-7.86	6.5	16
78	M81EO-05	390	149.09084	69.04158	13.8	-7.42	4.9	16
79	M81EO-06	109	148.78050	69.12628	11.9	-6.99	4.7	16
80	M81EO-07	68	148.73212	69.10929	11.3	-6.91	4.6	16
81	M81EO-08	347	149.03100	69.06371	18.4	-6.86	3.3	16
82	M81EO-09	286	148.95904	69.08145	13.6	-6.64	1.9	16
83	M81EO-10	144	148.82942	69.15271	10.1	-6.63	5.8	16
84	M81EO-11	296	148.96858	68.98121	26.9	-6.59	5.7	16
85	M81EO-12	156	148.83842	69.12107	13.9	-6.56	3.8	16
86	M81EO-13	335	149.02096	68.98834	12.1	-6.46	5.8	16
87	M81EO-14	389	149.08896	68.98058	19.2	-6.45	7.2	16
88	M81EO-15	268	148.94150	68.97047	19.6	-6.32	6.2	16
89	M81EO-16	334	149.02042	68.96019	27.3	-6.27	7.4	16
90	M81EO-17	181	148.86108	68.97620	19.6	-6.15	5.8	16
91	M81EO-18	180	148.86030	69.11928	11.7	-6.10	3.5	16
92	M81EO-19	233	148.90834	69.03748	13.5	-6.09	1.9	16
93	M81EO-20	8	148.56476	69.19183	13.4	-6.08	11.0	16
94	M81EO-21	14	148.60450	69.18077	10.8	-6.04	9.9	16
95	M81EO-22	370	149.06658	69.17279	14.2	-5.90	8.1	16

TABLE A.1— A catalog of EOs – continued

Nr.	Name	alt. Name	RA (deg)	Dec (deg)	r_{eff} (pc)	M_V (mag)	R_{proj} (kpc)	Ref.
96	M81EO-23	72	148.73442	69.16325	10.9	-5.86	7.2	16
97	M81EO-24	25	148.64446	69.16333	15.0	-5.85	8.4	16
98	M81EO-25	138	148.81966	69.17033	18.0	-5.82	7.0	16
99	M81EO-26	383	149.07858	68.97341	11.7	-5.82	7.4	16
100	M81EO-27	326	149.00684	69.08056	17.1	-5.76	2.9	16
101	M81EO-28	12	148.59916	69.13733	13.5	-5.68	8.1	16
102	M81EO-29	320	148.99792	69.02161	10.9	-5.66	3.8	16
103	M81EO-30	41	148.68834	69.01787	17.1	-5.65	5.5	16
104	M81EO-31	382	149.07834	68.98941	16.3	-5.62	6.6	16
105	M81EO-32	357	149.04430	69.00158	10.8	-5.60	5.5	16
106	M81EO-33	139	148.82142	68.97830	10.2	-5.59	5.8	16
107	M81EO-34	411	149.16646	68.94936	13.6	-5.49	9.8	16
108	M81EO-35	27	148.64834	69.07913	17.0	-5.46	5.6	16
109	M81EO-36	414	149.21338	68.97053	11.4	-5.42	9.7	16
110	M81EO-37	103	148.76974	69.18868	11.3	-5.41	8.4	16
111	M81EO-38	241	148.91558	69.19852	16.9	-5.38	8.6	16
112	M81EO-39	149	148.83170	69.13648	10.5	-5.35	4.8	16
113	M81EO-40	127	148.80750	68.98306	14.5	-5.28	5.6	16
114	M81EO-41	361	149.04962	68.92374	10.8	-5.25	9.8	16
115	M81EO-42	409	149.14480	69.04462	10.6	-5.10	6.1	16
116	M81EO-43	134	148.81446	68.93843	14.4	-5.07	8.3	16
117	M81EO-44	42	148.69080	69.09448	13.1	-4.53	4.9	16
118	NGC4449EO-01	B2	187.03550	44.06643	10.4	-7.14	1.8	17
119	NGC4449EO-02	B46	187.00794	44.09277	11.3	-6.70	1.8	17
120	NGC4449EO-03	A29	187.09437	44.10999	13.4	-6.29	2.5	17
121	NGC4449EO-04	B27	187.03375	44.06630	10.0	-6.28	1.9	17
122	NGC4449EO-05	B60	186.98141	44.08702	12.2	-5.96	3.0	17
123	NGC4449EO-06	A44	187.03639	44.09789	15.2	-5.93	0.5	17
124	NGC4449EO-07	B43	187.01067	44.08374	12.4	-5.35	1.8	17
125	IKNEO-1	IKN-03	152.02192	68.40938	14.8	-6.76	0.7	10
126	NGC5237EO-1	NGC5237-02	204.40812	-42.83981	15.1	-6.85	0.5	10
127	ESO269-58EO-1	ESO269-58-03	197.63000	-46.98975	15.0	-6.86	0.3	10
128	ESO269-58EO-2	ESO269-58-06	197.64950	-46.99236	18.6	-6.62	0.6	10
129	UGC7605EO-1	U7605-3-1503	187.16620	35.71690	12.2	-6.44	0.3	18;19
130	ScpEO-1	Scl-dE1 GC1	5.96954	-24.69944	22.0	-6.70	0.5	20
131	KK065EO-1	KK065-3-1095	115.62250	16.57470	11.5	-6.75	1.2	18;19
132	NGC784EO-1	NGC784-09	30.32725	28.86809	12.9	-6.62	2.5	10
133	NGC784EO-2	NGC784-04	30.31904	28.86067	11.6	-6.40	1.9	10
134	M83EO-1	13			11.4	-8.24		21
135	NGC4605EO-1	NGC4605-10	190.05096	61.59190	19.2	-8.26	2.5	10
136	NGC4605EO-2	NGC4605-08	190.05658	61.58687	13.6	-6.34	3.0	10
137	UGC3974EO-1	UGC3974-05	115.47737	16.80936	10.4	-8.72	0.6	10
138	UGC3755EO-1	U3755-3-2401	108.46500	10.51140	12.0	-7.54	0.9	18;19
139	UGC3755EO-2	U3755-3-1732	108.45920	10.51970	10.0	-6.09	0.6	18;19
140	KK112EO-1	KK112-4-792	178.69420	-33.54940	15.0	-6.77	1.4	18;19
141	KK112EO-2	KK112-4-742	178.69710	-33.55640	11.8	-6.21	1.3	18;19
142	NGC1311EO-1	NGC1311-06	50.02788	-52.18227	10.3	-7.33	0.3	10
143	UGC4115EO-1	U4115-2-1042	119.27040	14.37360	11.9	-6.00	2.1	18;19

TABLE A.1— A catalog of EOs – continued

Nr.	Name	alt. Name	RA (deg)	Dec (deg)	r_{eff} (pc)	M_V (mag)	R_{proj} (kpc)	Ref.
144	M51EO-01	61816	202.47208	47.19510	12.9	-8.86	0.2	22
145	M51EO-02	83686	202.50073	47.21319	11.0	-8.27	3.9	22
146	M51EO-03	74939	202.43997	47.20588	11.2	-8.25	3.2	22
147	M51EO-04	60114	202.46873	47.19380	14.4	-8.09	0.2	22
148	M51EO-05	60897	202.47556	47.19435	11.2	-7.96	0.6	22
149	M51EO-06	54755	202.46637	47.18880	22.8	-7.92	0.9	22
150	M51EO-07	67473	202.50967	47.19979	10.2	-7.76	3.9	22
151	M51EO-08	112569	202.47543	47.25743	11.2	-7.72	8.7	22
152	M51EO-09	108285	202.52412	47.23482	11.2	-7.67	7.6	22
153	M51EO-10	96532	202.52521	47.22412	10.9	-7.50	6.7	22
154	M51EO-11	75817	202.44243	47.20624	11.7	-7.40	3.0	22
155	M51EO-12	116983	202.54561	47.29417	11.0	-7.39	15.6	22
156	M51EO-13	114708	202.46480	47.26749	12.7	-7.36	10.1	22
157	M51EO-14	113415	202.43022	47.26162	14.4	-7.33	10.0	22
158	M51EO-15	111483	202.40401	47.24820	13.5	-7.32	9.7	22
159	M51EO-16	116303	202.50087	47.27698	10.1	-7.26	11.8	22
160	M51EO-17	8228	202.40341	47.14904	10.0	-7.25	9.0	22
161	M51EO-18	116382	202.50545	47.27747	10.4	-7.24	12.0	22
162	M51EO-19	43352	202.46779	47.17963	12.3	-7.22	2.2	22
163	M51EO-20	82040	202.51271	47.21186	11.7	-7.10	4.7	22
164	M51EO-21	543	202.47343	47.13341	11.9	-6.91	8.7	22
165	M104EO-01	Sombrero-UCD1	190.01304	-11.66786	14.7	-12.30	7.4	23
166	M104EO-02	C-151	189.98913	-11.64225	16.3	-10.59	3.3	24
167	M104EO-03	C-048	190.00700	-11.60692	11.7	-7.36	2.9	24
168	M104EO-04	H1-07	190.10513	-11.53425	14.7	-6.71	21.6	24
169	M104EO-05	C-115	190.00692	-11.64322	13.0	-6.52	3.5	24
170	M104EO-06	H2-21	190.01829	-11.56003	17.5	-6.25	10.4	24
171	M104EO-07	H2-03	190.01213	-11.53689	23.3	-6.16	13.7	24
172	M104EO-08	C-138	189.99429	-11.63936	15.6	-6.15	2.6	24
173	M104EO-09	C-126	190.00138	-11.64375	13.0	-6.07	3.3	24
174	M104EO-10	C-071	190.01400	-11.60164	10.9	-6.05	4.2	24
175	NGC891EO-1	G40	35.71925	42.41541	24.5	-7.30	15.3	25
176	NGC891EO-2	G19	35.66823	42.38971	11.8	-7.01	8.0	25
177	NGC891EO-3	G20	35.66898	42.38913	12.1	-6.40	8.0	25
178	NGC891EO-4	G27	35.68442	42.40145	15.5	-6.18	10.8	25
179	NGC891EO-5	G22	35.67065	42.34381	20.3	-5.55	4.3	25
180	NGC891EO-6	G05	35.62729	42.34048	13.4	-5.16	1.8	25
181	KK84EO-1	KK84-3-830	151.39620	-7.75000	10.6	-9.68	0.0	18;19
182	KK84EO-2	KK84-4-666	151.38120	-7.75110	10.6	-8.37	2.6	18;19
183	KK84EO-3	KK84-3-917	151.40210	-7.75470	10.4	-7.52	1.3	18;19
184	KK84EO-4	KK84-2-785	151.39920	-7.73560	11.6	-7.30	2.6	18;19
185	KK84EO-5	KK84-4-789	151.37710	-7.74390	19.4	-7.08	3.5	18;19
186	KK84EO-6	KK84-2-974	151.40620	-7.72890	14.9	-6.64	4.1	18;19
187	NGC1023EO-01	84	40.06836	39.05786	11.1	-7.13	5.1	26
188	NGC1023EO-02	56	40.09000	39.07114	15.1	-6.82	2.3	26
189	NGC1023EO-03	126	40.06890	39.06461	13.6	-6.61	4.9	26
190	NGC1023EO-04	62	40.08180	39.07672	18.3	-6.58	4.0	26
191	NGC1023EO-05	160	40.12139	39.07127	10.7	-6.50	3.9	26

TABLE A.1— A catalog of EOs – continued

Nr.	Name	alt. Name	RA (deg)	Dec (deg)	r_{eff} (pc)	M_V (mag)	R_{proj} (kpc)	Ref.
192	NGC1023EO-06	193	40.11474	39.07103	13.7	-6.41	3.0	26
193	NGC1023EO-07	114	40.11950	39.06310	18.6	-6.40	3.2	26
194	NGC1023EO-08	140	40.06550	39.06313	11.9	-6.32	5.5	26
195	NGC1023EO-09	8	40.07783	39.04868	13.1	-6.25	4.5	26
196	NGC1023EO-10	19	40.12233	39.05473	11.9	-6.16	4.0	26
197	NGC1023EO-11	103	40.09826	39.07331	12.7	-6.10	2.2	26
198	NGC1023EO-12	101	40.11321	39.05484	22.9	-6.07	2.7	26
199	NGC1023EO-13	35	40.13530	39.06248	10.7	-6.06	5.7	26
200	NGC1023EO-14	49	40.14178	39.05790	12.8	-6.05	6.8	26
201	NGC1023EO-15	108	40.08364	39.04846	14.2	-6.02	3.9	26
202	NGC4546EO-1	NGC4546-UCD1	188.86958	-3.78919	25.5	-12.94	1.2	27
203	NGC4660EO-1	1300	191.13953	11.21640	14.3	-8.34	6.9	28
204	IC3652EO-1	1861_1	190.25600	11.15118	21.5	-11.95	9.2	29
205	NGC4278EO-1	127	185.04356	29.25819	10.1	-9.93	6.9	28
206	NGC4486BEO-1	1297_1	187.63925	12.49838	36.5	-11.98	2.7	29
207	M89EO-1	1632_1	188.90877	12.55032	39.4	-11.60	2.5	29
208	M89EO-2	1632_2	188.89642	12.56203	10.1	-10.96	5.5	29
209	M89EO-3	905	188.90874	12.55033	13.8	-10.44	2.5	28
210	M59EO-1	M59cO	190.48054	11.66769	32.0	-13.30	9.7	30
211	M49EO-1	1226_1	187.45142	8.01172	18.9	-10.47	3.6	29
212	M86EO-1	469	186.57520	12.95977	14.6	-9.66	8.2	28
213	M86EO-2	423	186.54214	12.95353	12.1	-9.08	2.9	28
214	NGC4476EO-1	1250_1	187.48619	12.32541	11.1	-10.89	7.2	29
215	M60EO-01	D68	190.91044	11.50765	47.4	-10.74	13.1	52
216	M60EO-02	A32	190.93851	11.55510	36.5	-10.53	6.2	52
217	M60EO-03	C28	190.93384	11.58893	13.6	-9.86	11.5	52
218	M60EO-04	C42	190.89172	11.60050	14.9	-9.64	15.4	52
219	M60EO-05	E86	190.83444	11.58470	15.3	-8.98	24.9	52
220	M60EO-06	A78	190.96050	11.57642	19.3	-8.86	14.2	52
221	M60EO-07	A51	190.95406	11.57855	13.8	-8.83	12.9	52
222	M60EO-08	A155	190.93540	11.56335	39.5	-8.78	6.1	52
223	M60EO-09	B139	190.95322	11.52758	11.2	-8.71	12.6	52
224	M60EO-10	A98	190.97622	11.58127	15.1	-8.69	18.7	52
225	M60EO-11	C84	190.92504	11.58225	15.0	-8.52	8.8	52
226	M60EO-12	A122	190.94838	11.55112	14.7	-8.25	9.0	52
227	M60EO-13	E91	190.88530	11.56337	16.1	-8.03	9.3	52
228	M60EO-14	A209	190.97510	11.58856	16.2	-8.03	19.5	52
229	M60EO-15	A225	190.93870	11.56310	16.1	-7.90	6.9	52
230	M60EO-16	A205	190.99612	11.55534	12.9	-7.80	22.5	52
231	M60EO-17	E161	190.88659	11.56913	10.1	-7.70	9.7	52
232	M60EO-18	A221	190.97657	11.57877	14.1	-7.68	18.5	52
233	M60EO-19	E123	190.87078	11.55612	13.9	-7.66	13.0	52
234	M60EO-20	D312	190.89790	11.49049	15.7	-7.64	18.7	52
235	M60EO-21	D243	190.90484	11.51923	13.1	-7.50	10.2	52
236	M60EO-22	A701	190.93746	11.55946	11.9	-7.42	6.2	52
237	M87EO-01	VUCD7	187.97040	12.26641	93.2	-13.42	83.5	31
238	M87EO-02	VUCD3	187.73917	12.42911	20.0	-12.65	14.6	31
239	M87EO-03	S547	187.73910	12.42903	21.6	-12.30	14.5	32

TABLE A.1— A catalog of EOs – continued

Nr.	Name	alt. Name	RA (deg)	Dec (deg)	r_{eff} (pc)	M_V (mag)	R_{proj} (kpc)	Ref.
240	M87EO-04	VUCD5	187.79950	12.68364	19.2	-12.20	89.2	32
241	M87EO-05	VUCD1	187.53155	12.60861	12.1	-12.20	80.4	32
242	M87EO-06	VUCD2	187.70085	12.58636	14.1	-12.10	56.8	32
243	M87EO-07	VUCD4	187.76865	11.94347	25.1	-12.00	131.5	32
244	M87EO-08	VUCD8	188.06088	12.05150	23.5	-11.96	141.2	31
245	M87EO-09	VUCD6	187.86816	12.41766	18.8	-11.90	46.8	32
246	M87EO-10	S417	187.75616	12.32351	14.7	-11.70	24.3	29;32
247	M87EO-11	H55930	187.63929	12.49845	28.9	-11.70	36.5	32
248	M87EO-12	VUCD9	188.06074	12.05149	25.4	-11.70	141.2	32
249	M87EO-13	S928	187.69875	12.40845	36.3	-11.30	5.4	29;32
250	M87EO-14	H36612	187.48603	12.32538	14.5	-11.20	65.4	32
251	M87EO-15	S5065	187.70854	12.40248	26.1	-11.10	3.4	32
252	M87EO-16	S477	187.74961	12.30030	33.5	-11.10	29.2	32
253	M87EO-17	1316_6	187.70854	12.40254	13.9	-11.05	3.4	29
254	M87EO-18	S999	187.69130	12.41709	33.7	-10.90	8.6	29;32
255	M87EO-19	H8005	187.69254	12.40647	28.7	-10.83	5.9	29
256	M87EO-20	1316_4	187.69439	12.40622	21.6	-10.82	5.5	29
257	M87EO-21	S1629	187.61066	12.34572	26.4	-10.80	30.1	32
258	M87EO-22	S8006	187.69436	12.40616	31.7	-10.70	5.5	32
259	M87EO-23	H30772	187.74191	12.26728	10.0	-10.70	37.5	32
260	M87EO-24	S686	187.72421	12.47187	21.2	-10.70	24.1	32
261	M87EO-25	S8005	187.69252	12.40641	36.9	-10.60	5.9	32
262	M87EO-26	S796	187.71563	12.34815	15.3	-10.50	12.8	32
263	M87EO-27	S672	187.72804	12.36065	25.9	-10.40	10.9	32
264	M87EO-28	H46823	187.73054	12.41109	17.0	-10.40	9.1	32
265	M87EO-29	S887	187.70389	12.36544	10.0	-10.20	7.5	32
266	M87EO-30	S731	187.72452	12.28682	24.8	-10.20	30.8	32
267	M87EO-31	H27916	187.71521	12.23610	13.7	-10.20	45.2	32
268	M87EO-32	761	187.69281	12.40584	11.1	-10.15	5.7	28
269	M87EO-33	S1201	187.67423	12.39478	29.9	-10.10	9.1	32
270	M87EO-34	532	187.70389	12.36553	14.2	-9.91	7.5	28
271	M87EO-35	S682	187.72775	12.33962	23.7	-9.90	16.2	32
272	M87EO-36	S6004	187.79259	12.26697	40.3	-9.80	43.7	32
273	M87EO-37	601	187.68594	12.38174	14.7	-9.71	6.3	28
274	M87EO-38	H30401	187.82795	12.26247	10.7	-9.70	51.0	32
275	M87EO-39	777	187.70682	12.40792	10.3	-9.69	4.9	28
276	M87EO-40	S825	187.71263	12.35542	13.3	-9.60	10.6	32
277	M87EO-41	S723	187.72399	12.33940	16.9	-9.60	15.9	32
278	M87EO-42	543	187.69012	12.37016	10.7	-9.57	7.6	28
279	M87EO-43	H44905	187.73785	12.39440	40.0	-9.40	9.1	32
280	M87EO-44	H46017	187.72083	12.40476	31.5	-9.40	5.8	32
281	M87EO-45	H42003	187.74030	12.37334	34.3	-9.20	11.1	32
282	M87EO-46	H46484	187.69745	12.40857	39.1	-9.20	5.6	32
283	M87EO-47	S1508	187.63087	12.42356	42.4	-9.10	23.3	32
284	M87EO-48	H41821	187.69752	12.37159	29.4	-8.90	6.2	32
285	M87EO-49	568	187.71568	12.37620	13.3	-8.59	5.2	28
286	M87EO-50	H39168	188.15205	12.34920	11.0	-8.30	127.4	32
287	M87EO-51	B1	187.70503	12.40549	34.0	-8.10	4.2	32

TABLE A.1— A catalog of EOs – continued

Nr.	Name	alt. Name	RA (deg)	Dec (deg)	r_{eff} (pc)	M_V (mag)	R_{proj} (kpc)	Ref.
288	M85EO-1	798_2	186.35841	18.19665	19.0	-11.46	2.9	29
289	M85EO-2	798_1	186.33742	18.17016	14.5	-10.40	7.3	29
290	M85EO-3	384	186.35210	18.17757	14.8	-9.87	4.1	28
291	M85EO-4	392	186.33609	18.17072	10.7	-8.50	7.4	28
292	M84EO-1	285	186.28130	12.88212	11.3	-9.75	4.9	28
293	NGC1380EO-01	185	54.11132	-34.96907	14.9	-9.45	2.5	34
294	NGC1380EO-02	129	54.11729	-34.96428	10.4	-8.11	3.9	34
295	NGC1380EO-03	8	54.10075	-34.93829	10.3	-7.48	12.6	34
296	NGC1380EO-04	125	54.12065	-34.96491	11.3	-6.76	3.9	34
297	NGC1380EO-05	26	54.11092	-34.93517	12.3	-6.55	13.1	34
298	NGC1380EO-06	122	54.11232	-34.96009	11.7	-6.20	5.2	34
299	NGC1380EO-07	53	54.11759	-34.94131	12.3	-6.06	11.2	34
300	NGC1380EO-08	27	54.11335	-34.93612	10.1	-5.96	12.8	34
301	NGC1380EO-09	15	54.10905	-34.93829	12.8	-5.85	12.2	34
302	NGC1380EO-10	7	54.10049	-34.93837	13.5	-5.73	12.6	34
303	NGC1380EO-11	28	54.11308	-34.93562	11.5	-5.68	12.9	34
304	NGC1380EO-12	47	54.10708	-34.92143	11.6	-5.30	17.6	34
305	NGC1380EO-13	29	54.09843	-34.92817	11.2	-5.14	15.9	34
306	NGC1399EO-01	F-19(UCD3)	54.72542	-35.55933	89.7	-13.40	45.6	35
307	NGC1399EO-02	UCD6	54.52121	-35.40267	10.3	-12.58	31.4	31;33
308	NGC1399EO-03	F-24(UCD4)	54.89958	-35.47350	29.5	-12.30	75.1	35
309	NGC1399EO-04	F-1(UCD2)	54.52625	-35.48300	23.1	-12.20	28.0	35
310	NGC1399EO-05	UCD1	54.26375	-35.63461	22.4	-12.19	114.2	36
311	NGC1399EO-06	UCD5	54.96908	-35.07336	31.2	-11.97	155.8	36
312	NGC1399EO-07	91:93	54.52613	-35.48297	16.0	-11.63	28.1	37
313	NGC1399EO-08	F-12	54.62083	-35.38231	10.3	-11.50	22.4	35
314	NGC1399EO-09	F2	54.52708	-35.38444	14.0	-11.35	33.6	38
315	NGC1399EO-10	UCD50	54.89492	-35.89561	10.9	-11.24	164.6	31;33
316	NGC1399EO-11	F-7	54.57333	-35.55067	14.9	-11.10	35.7	35
317	NGC1399EO-12	F-22	54.82375	-35.42503	10.0	-11.10	55.0	35
318	NGC1399EO-13	UCD33	54.57337	-35.55078	11.4	-11.08	35.8	31;33
319	NGC1399EO-14	UCD17	54.21533	-35.51081	11.8	-10.86	111.4	31;33
320	NGC1399EO-15	89:22	54.57304	-35.55069	11.0	-10.71	35.8	37
321	NGC1399EO-16	78:12	54.74371	-35.44114	11.0	-10.66	32.9	37
322	NGC1399EO-17	FCOS1-063	54.73392	-35.41364	11.0	-10.66	32.4	37
323	NGC1399EO-18	90:12	54.56167	-35.56097	27.0	-10.02	40.1	37
324	NGC1533EO-1	2101	62.48020	-56.12503	12.6	-7.52	3.5	39
325	NGC1533EO-2	5754	62.46387	-56.10909	11.3	-7.26	3.2	39
326	NGC1533EO-3	5271	62.44848	-56.12190	12.7	-7.04	3.5	39
327	NGC3923EO-1	NGC3923-UCD1	177.76708	-28.80550	12.3	-12.43	3.2	27
328	NGC3923EO-2	NGC3923-UCD2	177.73292	-28.80511	13.0	-11.93	8.0	27
329	NGC3923EO-3	NGC3923-UCD3c	177.77167	-28.81636	14.1	-11.29	6.0	27
330	NGC1316EO-01	20	50.67486	-37.21958	13.6	-9.26	4.0	40
331	NGC1316EO-02	50	50.65591	-37.21779	16.2	-8.35	6.1	40
332	NGC1316EO-03	62	50.63268	-37.21603	11.7	-8.10	12.5	40
333	NGC1316EO-04	86	50.68407	-37.22403	19.4	-7.79	6.6	40
334	NGC1316EO-05	88	50.69759	-37.21027	20.0	-7.78	7.5	40
335	NGC1316EO-06	96	50.65909	-37.19480	19.2	-7.67	7.0	40

TABLE A.1— A catalog of EOs – continued

Nr.	Name	alt. Name	RA (deg)	Dec (deg)	r_{eff} (pc)	M_V (mag)	R_{proj} (kpc)	Ref.
336	NGC1316EO-07	98	50.69050	-37.18807	11.5	-7.66	9.7	40
337	NGC1316EO-08	104	50.63670	-37.20435	10.7	-7.61	11.2	40
338	NGC1316EO-09	110	50.64670	-37.22981	16.7	-7.54	11.2	40
339	NGC1316EO-10	128	50.67939	-37.19871	11.6	-7.43	4.5	40
340	NGC1316EO-11	129	50.64779	-37.20978	16.5	-7.43	7.7	40
341	NGC1316EO-12	149	50.66958	-37.19126	10.5	-7.27	7.0	40
342	NGC1316EO-13	153	50.68898	-37.21884	11.0	-7.24	6.1	40
343	NGC1316EO-14	189	50.68246	-37.21916	19.2	-6.97	4.7	40
344	NGC1316EO-15	196	50.68986	-37.18891	14.0	-6.93	9.3	40
345	NGC1316EO-16	199	50.66734	-37.22761	13.9	-6.90	7.2	40
346	NGC1316EO-17	211	50.64998	-37.21487	11.3	-6.83	7.3	40
347	NGC1316EO-18	217	50.63753	-37.21259	11.5	-6.79	10.9	40
348	NGC1316EO-19	232	50.66797	-37.22720	10.4	-6.72	7.0	40
349	NGC1316EO-20	241	50.64326	-37.19348	11.6	-6.68	10.9	40
350	NGC1316EO-21	244	50.64377	-37.19612	10.7	-6.67	10.2	40
351	NGC1316EO-22	257	50.67602	-37.18819	10.2	-6.58	8.1	40
352	NGC1316EO-23	274	50.63443	-37.21121	11.1	-6.49	11.8	40
353	NGC1316EO-24	287	50.70333	-37.20490	10.3	-6.44	9.4	40
354	NGC1316EO-25	290	50.65323	-37.21544	11.9	-6.43	6.5	40
355	NGC1316EO-26	296	50.65016	-37.21022	13.7	-6.40	7.0	40
356	NGC1316EO-27	316	50.69166	-37.19541	10.2	-6.31	7.8	40
357	NGC1316EO-28	318	50.64011	-37.20197	11.0	-6.31	10.4	40
358	NGC1316EO-29	327	50.64893	-37.20247	10.4	-6.27	7.8	40
359	NGC1316EO-30	336	50.64086	-37.22588	10.1	-6.25	11.7	40
360	NGC1316EO-31	349	50.70297	-37.20909	12.6	-6.21	9.1	40
361	NGC1316EO-32	354	50.67533	-37.22200	10.6	-6.18	4.9	40
362	NGC1316EO-33	362	50.69967	-37.22729	11.4	-6.15	10.6	40
363	NGC1316EO-34	372	50.67495	-37.19259	10.7	-6.12	6.4	40
364	NGC1316EO-35	376	50.66970	-37.19023	11.9	-6.10	7.4	40
365	NGC1316EO-36	384	50.64157	-37.20097	13.3	-6.08	10.1	40
366	NGC1316EO-37	386	50.63718	-37.22845	14.0	-6.08	13.1	40
367	NGC1316EO-38	404	50.70050	-37.21723	10.0	-5.99	8.9	40
368	NGC1316EO-39	417	50.64606	-37.22926	11.9	-5.90	11.2	40
369	NGC1316EO-40	419	50.63990	-37.19841	15.1	-5.87	10.9	40
370	NGC1316EO-41	426	50.69515	-37.19237	12.0	-5.86	9.3	40
371	NGC1316EO-42	429	50.68904	-37.22781	10.6	-5.84	8.6	40
372	NGC1316EO-43	438	50.70344	-37.20465	11.7	-5.81	9.4	40
373	NGC1316EO-44	441	50.64781	-37.19575	10.6	-5.80	9.3	40
374	NGC1316EO-45	475	50.67326	-37.18386	12.0	-5.65	9.7	40
375	NGC4365EO-001	30383	186.10868	7.23861	17.6	-11.84	32.0	41
376	NGC4365EO-002	30273	186.12327	7.28679	18.4	-10.89	12.6	41
377	NGC4365EO-003	20128	186.06631	7.30659	12.2	-10.66	21.0	41
378	NGC4365EO-004	2081	186.04534	7.28115	10.9	-10.51	32.4	41
379	NGC4365EO-005	60346	186.15156	7.37799	15.2	-10.45	27.9	41
380	NGC4365EO-006	354	186.11364	7.30963	20.7	-9.73	3.6	41
381	NGC4365EO-007	10241	186.08400	7.32993	11.3	-9.16	14.3	41
382	NGC4365EO-008	20297	186.07873	7.28603	11.2	-9.12	20.1	41
383	NGC4365EO-009	10238	186.08466	7.33185	12.1	-9.06	14.4	41

TABLE A.1— A catalog of EOs – continued

Nr.	Name	alt. Name	RA (deg)	Dec (deg)	r_{eff} (pc)	M_V (mag)	R_{proj} (kpc)	Ref.
384	NGC4365EO-010	50367	186.19582	7.35330	21.3	-8.80	34.4	41
385	NGC4365EO-011	6076	186.10823	7.36437	10.2	-8.70	19.3	41
386	NGC4365EO-012	1024	186.12451	7.34152	11.8	-8.65	10.1	41
387	NGC4365EO-013	8041	186.04033	7.22457	19.9	-8.64	48.6	41
388	NGC4365EO-014	736	186.10959	7.33443	17.3	-8.50	7.5	41
389	NGC4365EO-015	40413	186.16258	7.28170	21.2	-8.43	23.1	41
390	NGC4365EO-016	50259	186.17889	7.35586	22.4	-8.37	29.0	41
391	NGC4365EO-017	614	186.10031	7.33587	18.9	-8.33	10.1	41
392	NGC4365EO-018	50231	186.16464	7.33479	10.5	-8.32	20.1	41
393	NGC4365EO-019	2068	186.06214	7.32031	17.4	-8.23	22.2	41
394	NGC4365EO-020	50154	186.15684	7.33743	14.7	-8.10	17.6	41
395	NGC4365EO-021	50365	186.19398	7.34996	10.4	-8.09	33.2	41
396	NGC4365EO-022	472	186.10188	7.32569	22.4	-8.08	7.1	41
397	NGC4365EO-023	5056	186.15808	7.36643	14.2	-8.08	25.5	41
398	NGC4365EO-024	50330	186.16949	7.31110	11.8	-8.07	20.9	41
399	NGC4365EO-025	80123	186.05812	7.20208	10.8	-7.95	52.3	41
400	NGC4365EO-026	30247	186.09816	7.25621	12.5	-7.92	25.9	41
401	NGC4365EO-027	30453	186.12455	7.23854	13.0	-7.89	32.0	41
402	NGC4365EO-028	50172	186.15351	7.32651	13.6	-7.88	14.8	41
403	NGC4365EO-029	30133	186.09367	7.27034	10.9	-7.87	21.3	41
404	NGC4365EO-030	40374	186.15703	7.28848	12.5	-7.79	19.6	41
405	NGC4365EO-031	6012	186.10758	7.38573	14.4	-7.79	27.8	41
406	NGC4365EO-032	40263	186.14497	7.29515	10.8	-7.78	14.2	41
407	NGC4365EO-033	819	186.10570	7.34283	10.2	-7.74	11.3	41
408	NGC4365EO-034	50384	186.18577	7.32999	15.6	-7.74	27.7	41
409	NGC4365EO-035	50312	186.18280	7.34655	11.3	-7.70	28.6	41
410	NGC4365EO-036	50183	186.15119	7.32022	16.2	-7.70	13.5	41
411	NGC4365EO-037	50254	186.16812	7.33427	10.2	-7.69	21.3	41
412	NGC4365EO-038	6035	186.11640	7.39604	11.0	-7.68	31.7	41
413	NGC4365EO-039	6078	186.10849	7.36424	15.2	-7.65	19.2	41
414	NGC4365EO-040	80144	186.03704	7.21006	13.2	-7.57	54.0	41
415	NGC4365EO-041	50328	186.16825	7.30894	21.3	-7.56	20.5	41
416	NGC4365EO-042	40411	186.15169	7.25936	16.1	-7.54	27.1	41
417	NGC4365EO-043	80301	186.01287	7.20223	11.1	-7.53	62.6	41
418	NGC4365EO-044	80207	186.01247	7.21515	11.9	-7.49	58.9	41
419	NGC4365EO-045	30170	186.09349	7.26344	18.0	-7.49	23.9	41
420	NGC4365EO-046	8	186.08301	7.30985	10.8	-7.49	14.2	41
421	NGC4365EO-047	2077	186.04744	7.28671	13.6	-7.47	30.7	41
422	NGC4365EO-048	10101	186.06190	7.34671	11.1	-7.44	25.2	41
423	NGC4365EO-049	80392	186.03579	7.17184	13.6	-7.44	67.2	41
424	NGC4365EO-050	40266	186.13964	7.28317	15.6	-7.44	16.4	41
425	NGC4365EO-051	20117	186.04824	7.27513	11.3	-7.42	32.6	41
426	NGC4365EO-052	20316	186.07990	7.28348	15.1	-7.41	20.4	41
427	NGC4365EO-053	30182	186.11390	7.28966	13.9	-7.40	11.3	41
428	NGC4365EO-054	205	186.04533	7.31194	17.3	-7.40	29.0	41
429	NGC4365EO-055	20254	186.08369	7.30717	15.7	-7.39	14.2	41
430	NGC4365EO-056	60415	186.15822	7.37873	20.9	-7.37	29.5	41
431	NGC4365EO-057	80179	186.04452	7.19847	11.1	-7.35	56.2	41

TABLE A.1— A catalog of EOs – continued

Nr.	Name	alt. Name	RA (deg)	Dec (deg)	r_{eff} (pc)	M_V (mag)	R_{proj} (kpc)	Ref.
432	NGC4365EO-058	30218	186.10685	7.27304	13.2	-7.35	18.4	41
433	NGC4365EO-059	60360	186.14911	7.37116	18.9	-7.30	25.0	41
434	NGC4365EO-060	60477	186.14661	7.33909	16.1	-7.27	14.5	41
435	NGC4365EO-061	50213	186.15640	7.32254	14.0	-7.27	15.6	41
436	NGC4365EO-062	5077	186.14785	7.34165	10.6	-7.27	15.5	41
437	NGC4365EO-063	40478	186.18236	7.29492	15.8	-7.25	27.4	41
438	NGC4365EO-064	876	186.13044	7.32537	13.4	-7.24	6.0	41
439	NGC4365EO-065	50170	186.15546	7.33081	18.4	-7.24	16.1	41
440	NGC4365EO-066	30224	186.11455	7.28259	10.1	-7.23	14.1	41
441	NGC4365EO-067	5087	186.16287	7.36911	10.8	-7.22	27.6	41
442	NGC4365EO-068	40453	186.17282	7.28715	13.6	-7.21	25.2	41
443	NGC4365EO-069	50326	186.17321	7.32097	11.3	-7.20	22.3	41
444	NGC4365EO-070	50161	186.15983	7.34131	15.2	-7.18	19.4	41
445	NGC4365EO-071	30227	186.11502	7.28249	10.9	-7.14	14.2	41
446	NGC4365EO-072	2095	186.06467	7.31652	14.2	-7.14	21.2	41
447	NGC4365EO-073	40408	186.15697	7.27318	15.0	-7.14	23.8	41
448	NGC4365EO-074	20110	186.05886	7.30015	16.1	-7.13	24.5	41
449	NGC4365EO-075	30258	186.12059	7.28526	17.3	-7.13	13.1	41
450	NGC4365EO-076	50202	186.16845	7.34987	10.4	-7.12	24.1	41
451	NGC4365EO-077	20216	186.06803	7.28454	12.0	-7.12	23.9	41
452	NGC4365EO-078	30190	186.10498	7.27597	16.5	-7.09	17.5	41
453	NGC4365EO-079	50122	186.14777	7.32681	11.7	-7.09	12.6	41
454	NGC4365EO-080	20171	186.05525	7.27246	11.5	-7.09	30.9	41
455	NGC4365EO-081	40315	186.14487	7.28200	15.2	-7.09	18.0	41
456	NGC4365EO-082	40379	186.16842	7.31066	21.5	-7.08	20.5	41
457	NGC4365EO-083	50415	186.20153	7.35241	10.4	-7.06	36.4	41
458	NGC4365EO-084	30439	186.13661	7.25948	14.4	-7.06	24.6	41
459	NGC4365EO-085	797	186.12633	7.32425	12.0	-7.05	4.4	41
460	NGC4365EO-086	451	186.09610	7.32933	16.0	-7.05	9.8	41
461	NGC4365EO-087	80243	186.03373	7.19736	21.7	-7.04	58.9	41
462	NGC4365EO-088	8021	186.02294	7.23736	13.0	-7.03	49.8	41
463	NGC4365EO-089	5018	186.15601	7.36878	10.3	-7.00	25.7	41
464	NGC4365EO-090	3069	186.10783	7.29889	11.3	-7.00	8.5	41
465	NGC4365EO-091	50333	186.18465	7.34168	10.5	-6.99	28.5	41
466	NGC4365EO-092	20108	186.05366	7.29028	19.6	-6.97	27.8	41
467	NGC4365EO-093	1066	186.05787	7.35428	21.4	-6.96	28.1	41
468	NGC4365EO-094	50340	186.17669	7.32329	11.1	-6.92	23.7	41
469	NGC4365EO-095	60473	186.15457	7.35672	15.4	-6.90	21.6	41
470	NGC4365EO-096	30393	186.10538	7.23149	17.4	-6.90	35.0	41
471	NGC4365EO-097	112	186.11834	7.28898	10.6	-6.88	11.5	41
472	NGC4365EO-098	10309	186.09277	7.33361	13.7	-6.84	11.9	41
473	NGC4365EO-099	10245	186.08595	7.33272	15.4	-6.84	14.1	41
474	NGC4365EO-100	1047	186.05146	7.35106	11.1	-6.84	29.7	41
475	NGC4365EO-101	80374	186.03736	7.17479	22.3	-6.81	65.9	41
476	NGC4365EO-102	6011	186.09727	7.36451	14.8	-6.79	20.6	41
477	NGC4365EO-103	1075	186.12255	7.34726	12.0	-6.79	12.2	41
478	NGC4365EO-104	40131	186.13542	7.30320	18.8	-6.77	9.2	41
479	NGC4365EO-105	992	186.14597	7.32143	13.9	-6.76	11.4	41

TABLE A.1— A catalog of EOs – continued

Nr.	Name	alt. Name	RA (deg)	Dec (deg)	r_{eff} (pc)	M_V (mag)	R_{proj} (kpc)	Ref.
480	NGC4365EO-106	40311	186.14724	7.28737	14.6	-6.74	17.0	41
481	NGC4365EO-107	2083	186.04635	7.28241	12.3	-6.73	31.8	41
482	NGC4365EO-108	40158	186.14030	7.30612	10.3	-6.73	10.2	41
483	NGC4365EO-109	30196	186.10416	7.27385	13.6	-6.71	18.4	41
484	NGC4365EO-110	222	186.10693	7.30649	11.0	-6.71	6.2	41
485	NGC4365EO-111	50307	186.18824	7.35949	14.4	-6.69	32.9	41
486	NGC4365EO-112	5070	186.15856	7.36461	15.4	-6.68	25.1	41
487	NGC4365EO-113	1044	186.06052	7.37221	14.6	-6.68	31.7	41
488	NGC4365EO-114	30285	186.10301	7.25691	20.8	-6.67	25.1	41
489	NGC4365EO-115	1062	186.04801	7.33532	20.8	-6.66	28.8	41
490	NGC4365EO-116	10226	186.09726	7.36450	14.8	-6.65	20.6	41
491	NGC4365EO-117	340	186.11893	7.30381	11.1	-6.64	5.6	41
492	NGC4365EO-118	50345	186.19264	7.35485	16.2	-6.63	33.6	41
493	NGC4365EO-119	80249	186.04526	7.18989	12.0	-6.61	59.0	41
494	NGC4365EO-120	80266	186.02636	7.19814	16.5	-6.61	60.4	41
495	NGC4365EO-121	10262	186.10276	7.36384	11.0	-6.60	19.6	41
496	NGC4365EO-122	50403	186.19855	7.35024	14.2	-6.60	35.0	41
497	NGC4365EO-123	10310	186.08517	7.31770	20.1	-6.57	13.0	41
498	NGC4365EO-124	20377	186.07873	7.26562	14.6	-6.57	26.1	41
499	NGC4365EO-125	6091	186.11867	7.38117	11.0	-6.57	25.7	41
500	NGC4365EO-126	80316	186.02947	7.19117	13.9	-6.56	62.0	41
501	NGC4365EO-127	60303	186.14333	7.37357	18.0	-6.55	24.8	41
502	NGC4365EO-128	30348	186.10272	7.24001	19.6	-6.54	31.8	41
503	NGC4365EO-129	50240	186.15946	7.31997	16.2	-6.53	16.8	41
504	NGC4365EO-130	60163	186.11356	7.34936	11.8	-6.53	12.9	41
505	NGC4365EO-131	10143	186.07178	7.35016	10.6	-6.50	22.6	41
506	NGC4365EO-132	60466	186.14558	7.34120	18.3	-6.49	14.7	41
507	NGC4365EO-133	181	186.09584	7.31266	13.1	-6.48	8.9	41
508	NGC4365EO-134	115	186.09817	7.30624	20.7	-6.46	9.0	41
509	NGC4365EO-135	30449	186.13625	7.25586	17.3	-6.45	26.0	41
510	NGC4365EO-136	50437	186.18687	7.30539	16.7	-6.45	28.1	41
511	NGC4365EO-137	30424	186.11731	7.23644	20.9	-6.45	32.7	41
512	NGC4365EO-138	10154	186.08702	7.37517	15.4	-6.43	26.3	41
513	NGC4365EO-139	80330	186.04147	7.18001	17.8	-6.43	63.3	41
514	NGC4365EO-140	10189	186.07319	7.32952	12.0	-6.41	18.4	41
515	NGC4365EO-141	856	186.11976	7.33311	11.4	-6.40	6.3	41
516	NGC4365EO-142	10129	186.07526	7.36324	10.8	-6.39	25.0	41
517	NGC4365EO-143	53	186.10028	7.29939	21.9	-6.39	10.1	41
518	NGC4365EO-144	92	186.11221	7.29320	11.3	-6.39	10.0	41
519	NGC4365EO-145	8033	186.03307	7.22943	20.3	-6.36	49.0	41
520	NGC4365EO-146	30250	186.10713	7.26796	15.8	-6.33	20.4	41
521	NGC4365EO-147	30354	186.12621	7.27089	11.1	-6.33	19.1	41
522	NGC4365EO-148	60316	186.14188	7.36708	11.0	-6.31	22.2	41
523	NGC4365EO-149	146	186.09938	7.30768	21.7	-6.30	8.3	41
524	NGC4365EO-150	50422	186.20283	7.34916	11.4	-6.30	36.4	41
525	NGC4365EO-151	60290	186.12878	7.34785	13.3	-6.29	13.0	41
526	NGC4365EO-152	20315	186.09114	7.30699	13.9	-6.27	11.4	41
527	NGC4365EO-153	30451	186.11981	7.23213	10.4	-6.23	34.4	41

TABLE A.1— A catalog of EOs – continued

Nr.	Name	alt. Name	RA (deg)	Dec (deg)	r_{eff} (pc)	M_V (mag)	R_{proj} (kpc)	Ref.
528	NGC4365EO-154	60342	186.13685	7.34896	14.9	-6.18	14.8	41
529	NGC4365EO-155	20176	186.06018	7.27974	10.3	-6.18	27.6	41
530	NGC4365EO-156	10206	186.07404	7.32329	16.2	-6.18	17.6	41
531	NGC4365EO-157	52	186.09110	7.30700	21.3	-6.18	11.4	41
532	NGC4365EO-158	80219	186.04460	7.19515	10.5	-6.16	57.3	41
533	NGC4365EO-159	30110	186.08092	7.25630	20.3	-6.16	28.7	41
534	NGC4365EO-160	60209	186.11890	7.34674	11.7	-6.15	11.8	41
535	NGC4365EO-161	50397	186.18950	7.33362	14.6	-6.15	29.5	41
536	NGC4365EO-162	10317	186.08889	7.32379	16.7	-6.15	11.8	41
537	NGC4365EO-163	60385	186.15344	7.37554	10.6	-6.14	27.4	41
538	NGC4365EO-164	30404	186.11739	7.24400	18.5	-6.14	29.6	41
539	NGC4365EO-165	20219	186.06587	7.27823	10.8	-6.13	26.1	41
540	NGC4365EO-166	40141	186.13926	7.30917	17.1	-6.11	9.3	41
541	NGC4365EO-167	40234	186.14416	7.29996	17.4	-6.09	12.8	41
542	NGC4365EO-168	80263	186.01331	7.20604	14.6	-6.09	61.3	41
543	NGC4365EO-169	50190	186.15184	7.31874	21.5	-6.08	13.7	41
544	NGC4365EO-170	6069	186.11069	7.37107	13.2	-6.05	21.8	41
545	NGC4365EO-171	10194	186.07847	7.33939	18.4	-6.02	18.0	41
546	NGC4365EO-172	80339	185.99671	7.20477	18.3	-6.00	66.4	41
547	NGC4365EO-173	60363	186.15516	7.38316	11.2	-6.00	30.4	41
548	NGC4365EO-174	60117	186.12497	7.38431	18.6	-5.98	27.1	41
549	NGC4365EO-175	80298	186.00222	7.20885	20.5	-5.97	63.6	41
550	NGC4365EO-176	341	186.09136	7.32685	21.6	-5.97	11.2	41
551	NGC4365EO-177	80169	186.03332	7.20743	19.9	-5.97	55.7	41
552	NGC4365EO-178	30326	186.09686	7.23647	17.4	-5.96	33.7	41
553	NGC4365EO-179	40143	186.14546	7.32092	20.8	-5.95	11.2	41
554	NGC4365EO-180	40467	186.16478	7.26357	12.0	-5.93	28.8	41
555	NGC4365EO-181	20330	186.09008	7.30138	19.1	-5.93	12.8	41
556	NGC4365EO-182	6066	186.10910	7.36861	11.8	-5.93	20.9	41
557	NGC4365EO-183	20356	186.08577	7.28531	11.3	-5.93	18.2	41
558	NGC4365EO-184	80155	186.03041	7.21251	19.8	-5.92	54.9	41
559	NGC4365EO-185	60403	186.15571	7.37734	10.2	-5.91	28.5	41
560	NGC4365EO-186	8024	186.02221	7.23735	19.9	-5.90	50.0	41
561	NGC4365EO-187	902	186.10262	7.35057	13.1	-5.89	14.6	41
562	NGC4365EO-188	2010	186.03709	7.29222	11.0	-5.87	33.8	41
563	NGC4365EO-189	80135	186.01885	7.22334	17.1	-5.84	54.8	41
564	NGC4365EO-190	20112	186.06690	7.31647	11.9	-5.82	20.3	41
565	NGC4365EO-191	40359	186.14937	7.27717	10.8	-5.80	20.6	41
566	NGC4365EO-192	50206	186.16898	7.35075	11.5	-5.80	24.5	41
567	NGC4365EO-193	40308	186.15555	7.30525	14.9	-5.78	16.0	41
568	NGC4365EO-194	8048	186.03389	7.22768	12.9	-5.78	49.3	41
569	NGC4365EO-195	1088	186.14934	7.32613	16.7	-5.78	13.2	41
570	NGC4365EO-196	8063	186.04476	7.21938	10.4	-5.73	49.1	41
571	NGC4365EO-197	80214	186.03385	7.20190	11.3	-5.73	57.4	41
572	NGC4365EO-198	60244	186.12709	7.35641	17.4	-5.68	16.1	41
573	NGC4365EO-199	40355	186.15575	7.29154	17.6	-5.67	18.5	41
574	NGC4365EO-200	60341	186.14770	7.37217	21.9	-5.65	25.1	41
575	NGC4365EO-201	227	186.09675	7.31521	19.6	-5.63	8.4	41

TABLE A.1— A catalog of EOs – continued

Nr.	Name	alt. Name	RA (deg)	Dec (deg)	r_{eff} (pc)	M_V (mag)	R_{proj} (kpc)	Ref.
576	NGC4365EO-202	40417	186.15376	7.26255	14.9	-5.62	26.5	41
577	NGC4365EO-203	678	186.09803	7.34107	14.6	-5.57	12.3	41
578	NGC4365EO-204	60367	186.13544	7.34125	11.4	-5.57	11.9	41
579	NGC4365EO-205	50143	186.16118	7.35064	12.0	-5.54	21.9	41
580	NGC4365EO-206	50118	186.15944	7.35225	17.4	-5.53	21.8	41
581	NGC4365EO-207	10249	186.09828	7.35768	13.1	-5.53	17.9	41
582	NGC4365EO-208	1016	186.14558	7.32328	12.9	-5.47	11.4	41
583	NGC4365EO-209	1005	186.12589	7.33889	20.6	-5.47	9.2	41
584	NGC4365EO-210	20212	186.06686	7.28357	16.1	-5.44	24.5	41
585	NGC4365EO-211	80220	186.04052	7.19744	11.9	-5.44	57.4	41
586	NGC4365EO-212	2058	186.05060	7.30040	17.1	-5.43	27.7	41
587	NGC4365EO-213	830	186.10383	7.34508	20.7	-5.42	12.4	41
588	NGC4365EO-214	30266	186.10036	7.25658	18.3	-5.40	25.5	41
589	NGC4365EO-215	8081	186.01701	7.23194	22.3	-4.98	53.0	41
590	NGC4365EO-216	8030	186.02057	7.23684	10.4	-4.93	50.6	41
591	NGC4365EO-217	80210	186.01038	7.21593	12.3	-4.66	59.3	41
592	NGC5846EO-01	31	226.63982	1.58661	35.8	-9.32	12.2	42
593	NGC5846EO-02	23	226.64918	1.60707	44.2	-8.93	12.7	42
594	NGC5846EO-03	35	226.61362	1.64200	13.8	-8.81	17.4	42
595	NGC5846EO-04	43	226.64252	1.62224	21.3	-8.01	12.4	42
596	NGC5846EO-05	33	226.62210	1.63770	34.1	-7.92	14.9	42
597	NGC5846EO-06	29	226.63496	1.59199	13.8	-7.71	8.8	42
598	NGC5846EO-07	24	226.63895	1.61803	18.2	-7.68	9.8	42
599	NGC5846EO-08	13	226.62708	1.60820	12.9	-7.52	2.7	42
600	NGC5846EO-09	36	226.60770	1.64942	13.8	-7.47	21.4	42
601	NGC5846EO-10	46	226.63206	1.57597	11.8	-7.36	14.6	42
602	NGC5846EO-11	47	226.63502	1.58229	29.7	-7.33	12.5	42
603	NGC5846EO-12	51	226.64378	1.56278	13.2	-7.14	22.4	42
604	NGC5846EO-13	25	226.63968	1.61330	19.2	-6.89	9.0	42
605	NGC3370EO-01	5	161.75560	17.29800	13.7	-7.61	12.7	43
606	NGC3370EO-02	193	161.77750	17.28220	14.6	-7.61	6.3	43
607	NGC3370EO-03	205	161.79290	17.28840	13.8	-7.39	13.8	43
608	NGC3370EO-04	235	161.78080	17.27640	13.3	-7.37	6.5	43
609	NGC3370EO-05	32	161.75290	17.27510	16.9	-7.36	6.4	43
610	NGC3370EO-06	258	161.77160	17.25820	10.9	-7.32	7.7	43
611	NGC3370EO-07	243	161.77250	17.25380	15.0	-7.20	9.8	43
612	NGC3370EO-08	71	161.76370	17.28660	10.4	-6.85	6.3	43
613	NGC3370EO-09	55	161.75660	17.27270	12.1	-6.83	4.7	43
614	NGC3370EO-10	267	161.80860	17.28600	11.2	-6.76	19.9	43
615	NGC3370EO-11	197	161.77720	17.27840	10.5	-6.64	5.2	43
616	NGC3370EO-12	201	161.78960	17.27580	11.5	-6.50	10.4	43
617	NGC3370EO-13	220	161.78970	17.29560	11.8	-6.50	14.8	43
618	NGC3370EO-14	270	161.79550	17.27680	15.8	-6.47	13.2	43
619	NGC3370EO-15	277	161.78300	17.25620	10.6	-6.34	11.2	43
620	NGC3370EO-16	26	161.74810	17.26410	11.7	-6.24	9.7	43
621	NGC3370EO-17	105	161.75970	17.26270	11.7	-6.06	6.2	43
622	NGC3370EO-18	14	161.75500	17.28950	13.2	-6.01	9.3	43
623	NGC3370EO-19	48	161.75810	17.27790	11.3	-5.69	4.5	43

TABLE A.1— A catalog of EOs – continued

Nr.	Name	alt. Name	RA (deg)	Dec (deg)	r_{eff} (pc)	M_V (mag)	R_{proj} (kpc)	Ref.
624	NGC3370EO-20	37	161.74850	17.25950	12.9	-5.56	10.8	43
625	NGC3370EO-21	109	161.75900	17.25940	11.9	-5.51	7.7	43
626	NGC3370EO-22	260	161.77860	17.27910	12.4	-5.51	6.0	43
627	NGC1199EO-1	HCG22UCD001	45.89358	-15.61272	10.1	-12.15	9.1	44
628	NGC1199EO-2	HCG22UCD002	45.90100	-15.62022	20.7	-11.97	6.3	44
629	NGC4696EO-1	CCOS J1248.74-4118.58	192.18625	-41.30973	29.5	-11.52	9.4	45
630	NGC4696EO-2	CCOS J1248.70-4118.23	192.17496	-41.30383	10.2	-11.10	15.7	45
631	NGC3311EO-01	HUCD1	159.17708	-27.54803	25.4	-13.35	16.3	46
632	NGC3311EO-02	HUCD8	159.18250	-27.53950	18.5	-12.03	9.7	46
633	NGC3311EO-03	HUCD14	159.13084	-27.50714	25.6	-11.89	38.9	46
634	NGC3311EO-04	HUCD35	159.13208	-27.50889	10.1	-11.69	37.5	46
635	NGC3311EO-05	HUCD21	159.19750	-27.51850	11.9	-11.67	16.1	46
636	NGC3311EO-06	HUCD30	159.20834	-27.53192	13.1	-11.36	22.1	46
637	NGC3311EO-07	HUCD18	159.18124	-27.53039	13.5	-11.33	2.7	46
638	NGC3311EO-08	HUCD54	159.18542	-27.51242	10.5	-10.83	14.1	46
639	NGC3311EO-09	HUCD66	159.16292	-27.52225	11.5	-10.79	12.4	46
640	NGC3311EO-10	HUCD59	159.15958	-27.53928	11.0	-10.77	16.5	46
641	NGC3311EO-11	HUCD46	159.13834	-27.51522	14.0	-10.75	31.2	46
642	NGC3311EO-12	HUCD69	159.17166	-27.54631	11.2	-10.37	15.6	46
643	NGC3311EO-13	HUCD61	159.20834	-27.54306	10.8	-10.27	25.0	46
644	NGC3311EO-14	HUCD99	159.20124	-27.53308	11.5	-9.99	17.1	46
645	NGC3311EO-15	HUCD94	159.12500	-27.51719	11.5	-9.91	40.1	46
646	NGC3311EO-16	HUCD101	159.15708	-27.53494	13.3	-9.81	16.5	46
647	NGC3311EO-17	HUCD110	159.18626	-27.54875	12.8	-9.65	17.8	46
648	NGC3311EO-18	HUCD114	159.13292	-27.51031	14.4	-9.60	36.4	46
649	NGC3311EO-19	HUCD115	159.12334	-27.52022	11.2	-9.29	40.8	46
650	NGC1275EO-01	UCD79	49.95679	41.47650	27.4	-13.33	44.0	47
651	NGC1275EO-02	UCD45	49.78363	41.48797	33.8	-12.87	157.8	47
652	NGC1275EO-03	UCD13	49.93804	41.53500	57.0	-12.80	31.2	47
653	NGC1275EO-04	UCD52	49.82183	41.54233	22.6	-12.42	125.4	47
654	NGC1275EO-05	UCD5	49.91967	41.51483	24.8	-12.40	29.0	47
655	NGC1275EO-06	UCD54	49.83350	41.48108	18.1	-12.37	115.2	47
656	NGC1275EO-07	UCD27	49.96583	41.49567	16.3	-12.24	24.3	47
657	NGC1275EO-08	UCD20	49.95817	41.50286	15.7	-12.21	13.0	47
658	NGC1275EO-09	UCD19	49.95817	41.52267	13.1	-12.09	15.3	47
659	NGC1275EO-10	UCD39	49.99200	41.54433	22.1	-11.96	55.7	47
660	NGC1275EO-11	UCD51	49.82113	41.49000	14.4	-11.95	123.2	47
661	NGC1275EO-12	UCD60	49.86792	41.57500	49.0	-11.95	109.8	47
662	NGC1275EO-13	UCD69	49.91192	41.46167	22.1	-11.95	71.7	47
663	NGC1275EO-14	UCD25	49.96429	41.50481	11.5	-11.94	15.3	47
664	NGC1275EO-15	UCD22	49.95892	41.51108	13.1	-11.92	7.7	47
665	NGC1275EO-16	UCD14	49.93983	41.51217	13.1	-11.91	10.1	47
666	NGC1275EO-17	UCD78	49.94829	41.49028	23.4	-11.91	26.6	47
667	NGC1275EO-18	UCD17	49.95233	41.52161	18.4	-11.89	12.4	47
668	NGC1275EO-19	UCD64	49.88679	41.57608	13.3	-11.87	99.4	47
669	NGC1275EO-20	UCD81	49.97300	41.46778	46.1	-11.84	58.2	47
670	NGC1275EO-21	UCD34	49.97304	41.50567	16.8	-11.82	22.1	47
671	NGC1275EO-22	UCD21	49.95854	41.53581	31.2	-11.81	30.8	47

TABLE A.1— A catalog of EOs – continued

Nr.	Name	alt. Name	RA (deg)	Dec (deg)	r_{eff} (pc)	M_V (mag)	R_{proj} (kpc)	Ref.
672	NGC1275EO-23	UCD29	49.96996	41.50444	22.4	-11.80	20.0	47
673	NGC1275EO-24	UCD80	49.96088	41.46161	16.0	-11.77	62.8	47
674	NGC1275EO-25	UCD70	49.91862	41.46925	20.0	-11.74	60.4	47
675	NGC1275EO-26	UCD7	49.92096	41.53642	12.5	-11.69	41.2	47
676	NGC1275EO-27	UCD43	49.76263	41.51525	33.3	-11.69	174.5	47
677	NGC1275EO-28	UCD11	49.93483	41.51786	13.1	-11.66	16.6	47
678	NGC1275EO-29	UCD16	49.95025	41.53111	15.2	-11.63	24.1	47
679	NGC1275EO-30	UCD41	49.75158	41.52489	19.2	-11.60	185.5	47
680	NGC1275EO-31	UCD31	49.97067	41.50128	10.7	-11.55	22.6	47
681	NGC1275EO-32	UCD40	49.99475	41.49864	13.9	-11.55	44.0	47
682	NGC1275EO-33	UCD76	49.94092	41.47939	24.5	-11.47	41.0	47
683	NGC1275EO-34	UCD49	49.80554	41.53197	16.0	-11.46	137.0	47
684	NGC1275EO-35	UCD71	49.92033	41.46769	26.1	-11.46	61.4	47
685	NGC1275EO-36	UCD56	49.85650	41.51378	11.2	-11.44	87.4	47
686	NGC1275EO-37	UCD10	49.92358	41.50619	17.6	-11.39	26.1	47
687	NGC1275EO-38	UCD59	49.86725	41.48219	18.6	-11.38	85.6	47
688	NGC1275EO-39	UCD23	49.95896	41.48731	11.5	-11.37	31.2	47
689	NGC1275EO-40	UCD48	49.80537	41.54647	14.1	-11.36	141.6	47
690	NGC1275EO-41	UCD57	49.85896	41.57472	13.3	-11.35	115.5	47
691	NGC1275EO-42	UCD84	49.98112	41.46500	10.9	-11.35	64.4	47
692	NGC1275EO-43	UCD75	49.92962	41.48489	12.3	-11.32	38.5	47
693	NGC1275EO-44	UCD82	49.97308	41.47019	17.0	-11.32	55.5	47
694	NGC1275EO-45	UCD83	49.97417	41.48267	11.2	-11.32	42.1	47
695	NGC1275EO-46	UCD66	49.89533	41.54131	15.7	-11.29	63.1	47
696	NGC1275EO-47	UCD12	49.93600	41.48322	20.8	-11.28	37.8	47
697	NGC1275EO-48	UCD62	49.87233	41.54847	20.0	-11.26	85.8	47
698	NGC1275EO-49	UCD65	49.88879	41.57619	13.6	-11.24	98.4	47
699	NGC1275EO-50	UCD24	49.96383	41.51242	19.2	-11.23	12.2	47
700	NGC1275EO-51	UCD15	49.94146	41.50925	13.6	-11.21	9.1	47
701	NGC1275EO-52	UCD58	49.86487	41.54553	13.3	-11.21	90.0	47
702	NGC1275EO-53	UCD1	49.90683	41.49550	11.7	-11.15	45.4	47
703	NGC1275EO-54	UCD35	49.97533	41.49058	18.6	-11.13	34.8	47
704	NGC1275EO-55	UCD61	49.86821	41.48647	24.8	-11.13	82.7	47
705	NGC1275EO-56	UCD9	49.92333	41.53553	14.4	-11.03	38.9	47
706	NGC1275EO-57	UCD8	49.92154	41.51367	13.9	-11.00	27.1	47
707	NGC1275EO-58	UCD50	49.80708	41.57300	11.2	-10.99	153.4	47
708	NGC1275EO-59	UCD72	49.92579	41.56653	10.1	-10.89	71.8	47
709	NGC1275EO-60	UCD28	49.96779	41.49508	11.7	-10.87	26.0	47
710	NGC1275EO-61	UCD36	49.97908	41.50631	39.7	-10.86	27.2	47
711	NGC1275EO-62	UCD73	49.92608	41.47847	21.8	-10.85	47.1	47
712	NGC1275EO-63	UCD63	49.88087	41.50608	10.9	-10.84	65.1	47
713	NGC1275EO-64	UCD67	49.90812	41.53467	14.7	-10.84	48.7	47
714	NGC1275EO-65	UCD46	49.79054	41.48247	11.7	-10.83	152.9	47
715	NGC1275EO-66	UCD44	49.76954	41.53439	10.4	-10.82	170.4	47
716	NGC1275EO-67	UCD32	49.97087	41.54050	29.8	-10.81	40.3	47
717	NGC1275EO-68	UCD77	49.94208	41.44958	11.7	-10.81	77.4	47
718	NGC1275EO-69	UCD2	49.91579	41.50478	26.9	-10.80	33.5	47
719	NGC1275EO-70	UCD47	49.79692	41.51650	14.7	-10.78	142.8	47

TABLE A.1— A catalog of EOs – continued

Nr.	Name	alt. Name	RA (deg)	Dec (deg)	r_{eff} (pc)	M_V (mag)	R_{proj} (kpc)	Ref.
720	NGC1275EO-71	UCD4	49.91733	41.50922	18.9	-10.77	31.1	47
721	NGC1275EO-72	UCD42	49.75717	41.55711	22.9	-10.67	188.2	47
722	NGC1275EO-73	UCD53	49.83342	41.52739	15.7	-10.67	110.5	47
723	NGC1275EO-74	UCD55	49.85504	41.52706	18.4	-10.67	90.8	47
724	NGC1275EO-75	UCD33	49.97125	41.50442	10.4	-10.66	21.1	47
725	NGC1275EO-76	UCD26	49.96583	41.52608	13.9	-10.64	22.7	47
726	NGC1275EO-77	UCD74	49.92692	41.45986	21.0	-10.63	67.9	47
727	NGC1275EO-78	UCD68	49.90975	41.44533	17.3	-10.53	90.6	47
728	NGC1275EO-79	UCD6	49.92038	41.49981	10.4	-10.50	31.7	47
729	NGC1275EO-80	UCD37	49.98829	41.51975	25.3	-10.49	36.3	47
730	NGC1275EO-81	UCD18	49.95463	41.49525	33.0	-10.48	20.7	47
731	NGC1275EO-82	UCD38	49.98846	41.48867	11.5	-10.48	45.2	47
732	NGC1275EO-83	UCD30	49.97013	41.48786	14.9	-10.27	34.6	47
733	NGC1275EO-84	UCD3	49.91667	41.48297	11.2	-9.98	47.6	47
734	NGC4889EO-1	242857	195.04836	27.92300	24.8	-11.34	91.5	48
735	NGC4889EO-2	1.04323E6	194.98637	27.99943	13.0	-11.11	78.2	48
736	IC3998EO-1	1.04283E6	195.00751	27.99481	15.2	-11.79	102.0	48
737	IC4030EO-1	163341	195.12248	27.95551	19.5	-11.41	9.0	48
739	IC4030EO-2	150880	195.15168	27.97341	11.0	-11.07	61.4	48
738	IC4030EO-3	163400	195.12877	27.97444	54.4	-10.70	36.9	48
740	IC4041EO-1	150000	195.16649	27.99672	24.3	-11.31	5.4	48
741	IC4041EO-2	163575	195.13586	27.98630	12.8	-11.11	55.0	48
742	IC4041EO-3	81669	195.18616	28.02906	17.7	-10.77	61.3	48
743	NGC4874EO-01	1	194.91342	27.99853	40.5	-14.03	71.2	49
744	NGC4874EO-02	2	194.91917	27.96900	28.7	-12.68	35.2	49
745	NGC4874EO-03	6	194.91417	27.97781	11.2	-12.28	39.5	49
746	NGC4874EO-04	5	194.90700	27.97711	14.4	-12.18	33.1	49
747	NGC4874EO-05	8	194.92171	27.95303	10.6	-12.12	36.6	49
748	NGC4874EO-06	4	194.91342	27.96292	15.4	-12.10	23.1	49
749	NGC4874EO-07	10	194.91933	27.97786	11.3	-11.96	44.7	49
750	NGC4874EO-08	13	194.90829	27.97244	21.9	-11.91	26.8	49
751	NGC4874EO-09	11	194.92462	27.98025	11.1	-11.89	53.4	49
752	NGC4874EO-10	195526	194.91829	27.95858	32.5	-11.88	29.8	48
753	NGC4874EO-11	12	194.90025	27.96817	18.2	-11.75	15.3	49
754	NGC4874EO-12	121666	194.91318	28.01979	38.3	-11.68	106.6	48
755	NGC4874EO-13	196790	194.93714	27.98170	22.6	-11.55	70.0	48
756	NGC4874EO-14	15	194.89712	27.97081	64.7	-11.51	19.9	49
757	NGC4874EO-15	16	194.88471	27.96900	10.6	-11.32	27.1	49
758	NGC4874EO-16	20	194.91375	27.97222	20.4	-11.29	31.8	49
759	NGC4874EO-17	120985	194.90078	28.02008	42.8	-11.20	104.9	48
760	NGC4874EO-18	21	194.89000	27.95467	10.6	-11.03	15.7	49
761	NGC4874EO-19	26	194.90912	27.96047	13.2	-11.03	15.9	49
762	NGC4874EO-20	28	194.92300	27.99367	29.4	-11.00	69.8	49
763	NGC4874EO-21	1.04151E6	194.92938	27.97935	14.4	-10.98	58.0	48
764	NGC4874EO-22	29	194.91137	27.99381	19.1	-10.98	62.5	49
765	NGC4874EO-23	35	194.88012	27.97664	10.8	-10.71	41.2	49
766	NGC4874EO-24	30	194.90500	27.95581	12.2	-10.62	11.3	49
767	NGC4874EO-25	38	194.91829	27.95011	10.2	-10.47	33.8	49

TABLE A.1— A catalog of EOs – continued

Nr.	Name	alt. Name	RA (deg)	Dec (deg)	r_{eff} (pc)	M_V (mag)	R_{proj} (kpc)	Ref.
768	NGC4874EO-26	41	194.91017	27.96039	27.7	-10.46	17.4	49
769	NGC4874EO-27	39	194.89950	27.97142	11.5	-10.38	20.8	49
770	NGC4874EO-28	37	194.88492	28.00197	50.6	-10.33	76.5	49
771	NGC4874EO-29	43	194.91950	27.97553	16.6	-10.19	42.1	49
772	NGC4874EO-30	42	194.86771	27.95372	11.6	-10.11	48.4	49
773	NGC4874EO-31	47	194.90571	27.96511	18.0	-10.10	14.5	49
774	NGC4874EO-32	45	194.90717	27.96733	49.4	-10.09	18.8	49
775	NGC4874EO-33	48	194.90225	27.98094	12.3	-10.07	37.6	49
776	NGC4874EO-34	46	194.91871	27.97483	24.9	-10.03	40.4	49
777	NGC4874EO-35	51	194.91246	27.98358	11.2	-9.91	46.7	49
778	NGC4874EO-36	52	194.91046	27.97433	11.0	-9.85	31.4	49
779	NGC1132EO-01		43.21250	-1.27194	79.1	-14.80	8.1	50
780	NGC1132EO-02				18.9	-13.03	21.5	50
781	NGC1132EO-03				12.8	-12.42	37.7	50
782	NGC1132EO-04				18.6	-12.06	68.7	50
783	NGC1132EO-05				18.6	-12.01	22.7	50
784	NGC1132EO-06				10.6	-11.83	7.8	50
785	NGC1132EO-07				10.4	-11.68	23.1	50
786	NGC1132EO-08				12.8	-11.66	33.9	50
787	NGC1132EO-09				11.1	-11.41	12.6	50
788	NGC1132EO-10				17.1	-11.29	12.3	50
789	NGC1132EO-11				10.4	-11.20	10.8	50
790	NGC1132EO-12				10.8	-11.17	26.2	50
791	NGC1132EO-13				11.4	-11.06	8.7	50
792	NGC1132EO-14				10.8	-11.02	39.5	50
793	NGC1132EO-15				11.3	-11.00	36.1	50
794	NGC1132EO-16				23.0	-10.97	39.8	50
795	NGC1132EO-17				10.2	-10.72	21.0	50
796	NGC1132EO-18				14.0	-10.70	20.4	50
797	NGC1132EO-19				15.9	-10.66	21.2	50
798	NGC1132EO-20				15.9	-10.63	16.6	50
799	NGC1132EO-21				13.1	-10.55	59.1	50
800	NGC1132EO-22				11.9	-10.52	8.2	50
801	NGC1132EO-23				16.9	-10.48	20.8	50
802	NGC1132EO-24				11.6	-10.45	17.6	50
803	NGC1132EO-25				56.3	-10.32	11.8	50
804	NGC1132EO-26				12.6	-10.29	39.5	50
805	NGC1132EO-27				16.6	-10.25	41.0	50
806	NGC1132EO-28				26.1	-10.23	26.7	50
807	NGC1132EO-29				25.8	-10.21	61.0	50
808	NGC1132EO-30				12.1	-10.13	25.9	50
809	NGC1132EO-31				10.1	-10.01	35.5	50
810	NGC1132EO-32				33.8	-9.96	29.5	50
811	NGC1132EO-33				11.1	-9.95	26.1	50
812	NGC1132EO-34				11.3	-9.87	44.2	50
813	NGC1132EO-35				11.9	-9.73	57.3	50
814	NGC1132EO-36				38.4	-9.66	26.9	50
815	NGC1132EO-37				54.2	-9.51	19.6	50

TABLE A.1— A catalog of EOs – continued

Nr.	Name	alt. Name	RA (deg)	Dec (deg)	r_{eff} (pc)	M_V (mag)	R_{proj} (kpc)	Ref.
816	NGC1132EO-38				12.6	-9.50	58.6	50
817	NGC1132EO-39				30.7	-9.24	23.2	50
818	NGC4908EO-1	151072	195.15761	27.97795	68.1	-12.47	145.2	48
819	NGC4908EO-2	1.04425E6	195.20955	28.01042	32.6	-11.31	57.8	48
820	NGC4908EO-3	92415	195.13438	28.00352	22.0	-11.08	143.3	48
821	ESO325-G004EO-01	211	205.86130	-38.18323	81.3	-12.74	55.9	51
822	ESO325-G004EO-02	4579	205.91782	-38.16729	80.2	-12.48	61.9	51
823	ESO325-G004EO-03	3688	205.89787	-38.17786	90.2	-12.06	19.3	51
824	ESO325-G004EO-04	4755	205.91962	-38.17162	76.4	-11.89	62.5	51
825	ESO325-G004EO-05	1318	205.89067	-38.15035	11.2	-11.60	64.3	51
826	ESO325-G004EO-06	5097	205.91919	-38.18841	85.9	-11.31	68.0	51
827	ESO325-G004EO-07	1659	205.88557	-38.16813	90.3	-11.27	20.4	51
828	ESO325-G004EO-08	2626	205.89274	-38.16961	40.0	-11.23	18.3	51
829	ESO325-G004EO-09	2253	205.87746	-38.19469	16.9	-11.23	51.2	51
830	ESO325-G004EO-10	5396	205.92415	-38.19283	83.9	-11.15	81.9	51
831	ESO325-G004EO-11	267	205.86669	-38.17410	61.6	-11.13	42.6	51
832	ESO325-G004EO-12	1201	205.88024	-38.16939	60.8	-11.00	22.9	51
833	ESO325-G004EO-13	4507	205.90258	-38.19380	44.1	-10.83	52.5	51
834	ESO325-G004EO-14	1990	205.88631	-38.17262	12.3	-10.79	9.4	51
835	ESO325-G004EO-15	2317	205.89302	-38.16406	67.1	-10.63	31.3	51

TABLE A.2— Catalog of the 66 galaxies containing EOs

Galaxy	Type	$M_{V,gal}$ (mag)	D_{gal} (kpc)	Pix_{HST} (pc)	N_{EO}	$M_{V,EO,min}$ (mag)	$M_{V,EO,max}$ (mag)	N_{GC}	Ref
Milky Way	LT	-20.5	0		11	-4.73	-9.42	142	1
SAGdSph	LT	-13.8	27		2	-5.41	-5.68	2	2
LMC	LT	-18.34	50		4	-4.37	-7.25	12	3
Fornax	ET	-13.3	138		1	-5.32	-5.32	4	3
NGC6822	LT	-16	470	0.1	3	-6.06	-7.7	3	4
M31	LT	-21.8	780	0.2	20	-4.4	-7.68	232	5;6;7
M33	LT	-19.4	870	0.2	2	-5.9	-6.6	4	8;9
UGCA86	LT	-13.55	2728	0.7	1	-7.58	-7.58	11	10
UGC8638	LT	-13.8	3285	0.8	1	-6.57	-6.57	2	10
NGC247	LT	-19.4	3636	0.9	2	-6.59	-7.42	0	10
NGC5128	ET	-21.4	3676	0.9	26	-5.2	-11.17	194	11;12;13;14;15
M81	LT	-21.2	3692	0.9	44	-4.53	-8.59	369	16
NGC4449	LT	-18.28	3693	0.9	7	-5.35	-7.14	99	17
IKN	ET	-11.5	3680	0.9	1	-6.76	-6.76	4	10
NGC5237	LT	-15.7	3794	0.9	1	-6.85	-6.85	2	10
ESO269-58	LT	-16.3	3825	0.9	2	-6.62	-6.86	6	10
UGC7605	LT	-13.8	4177	1.0	1	-6.44	-6.44	0	18;19
Scl-dE1	ET	-11.1	4300	1.0	1	-6.7	-6.7	0	20
KK065	LT	-13.32	4510	1.1	1	-6.75	-6.75	0	18;19
NGC784	LT	-17.6	4560	1.1	2	-6.4	-6.62	5	10
M83	LT	-21	4659	1.1	1	-8.24	-8.24	20	21
NGC4605	LT	-18.5	4730	1.1	2	-6.34	-8.26	9	10
UGC3974	LT	-15.2	4897	1.2	1	-8.72	-8.72	4	10

TABLE A.2— Catalog of the 66 galaxies containing EOs - continued

Galaxy	Type	$M_{V,gal}$ (mag)	D_{gal} (kpc)	Pix_{HST} (pc)	N_{EO}	$M_{V,EO,min}$ (mag)	$M_{V,EO,max}$ (mag)	N_{GC}	Ref
UGC3755	LT	-15	5166	1.3	2	-6.09	-7.54	30	18;19
KK112	LT	-12.28	5220	1.3	2	-6.21	-6.77	1	18;19
NGC1311	LT	-16.3	5252	1.3	1	-7.33	-7.33	5	10
UGC4115	LT	-14.12	5508	1.3	1	-6.0	-6.0	2	18;19
M51	LT	-21.4	8031	1.9	21	-6.91	-8.86	2203	22
M104	LT	-22.45	9000	2.2	10	-6.05	-12.3	184	23;24
NGC891	LT	-21.2	9700	2.4	6	-5.16	-7.3	37	25
KK84	ET	-14.4	10069	2.4	6	-6.64	-9.68	1	18;19
NGC1023	ET	-21.2	11791	2.9	15	-6.02	-7.13	14	26
NGC4546	ET	-20.9	13060	3.2	1	-12.94	-12.94	0	27
NGC4660	ET	-19.69	14875	3.6	1	-8.34	-8.34	50	28
IC3652	ET	-18.7	14960	3.6	1	-11.95	-11.95	0	29
NGC4278	ET	-20.78	15154	3.7	1	-9.93	-9.93	66	28
NGC4486B	ET	-17.64	15450	3.7	1	-11.98	-11.98	0	29
M89	ET	-21.32	15574	3.8	3	-10.44	-11.6	104	28;29
M59	ET	-21.38	15821	3.8	1	-13.3	-13.3	0	30
M49	ET	-22.63	16052	3.9	1	-10.47	-10.47	0	29
M86	ET	-22.21	16321	4.0	2	-9.08	-9.66	74	28
NGC4476	ET	-18.97	16450	4.0	1	-10.89	-10.89	0	29
M60	ET	-22.34	16500	4.0	22	-7.42	-10.74	1102	52
M87	ET	-22.54	16675	4.0	51	-8.1	-13.42	301	28;29;31;32
M85	ET	-21.98	17382	4.2	4	-8.5	-11.46	55	28;29
M84	ET	-22.12	17422	4.2	1	-9.75	-9.75	92	28
NGC1380	ET	-21.3	18221	4.4	13	-5.14	-9.45	174	34
NGC1399	ET	-21.88	18950	4.6	18	-10.02	-13.4	18	31;33;35;36;37;38
NGC1533	ET	-20.7	19400	4.7	3	-7.04	-7.52	136	39
NGC3923	ET	-21.9	21280	5.2	3	-11.29	-12.43	0	27
NGC1316	ET	-22.91	21900	5.3	45	-5.65	-9.26	433	40
NGC4365	ET	-22.13	23100	5.6	217	-4.66	-11.84	2038	41
NGC5846	ET	-22.18	26709	6.5	13	-6.89	-9.32	41	42
NGC3370	LT	-20	27376	6.6	22	-5.51	-7.61	255	43
NGC1199	ET	-21.25	33100	8.0	2	-11.97	-12.15	8	44
NGC4696	ET	-22.81	37582	9.1	2	-11.1	-11.52	6	45
NGC3311	ET	-22.2	47200	11.4	19	-9.29	-13.35	7	46
NGC1275	ET	-22.72	71000	17.2	84	-9.98	-13.33	0	47
NGC4889	ET	-23.51	94400	22.9	2	-11.11	-11.34	2	48
IC4041	ET	-20.74	98950	22.9	3	-10.77	-11.31	0	48
IC3998	ET	-20.43	98950	24.0	1	-11.79	-11.79	0	48
IC4030	ET	-19.6	98950	24.0	3	-10.7	-11.41	0	48
NGC4874	ET	-23.25	98950	24.0	36	-9.85	-14.03	2	48;49
NGC1132	ET	-22.65	99500	24.1	39	-9.24	-14.8	11	50
NGC4908	ET	-21.82	101114	24.5	3	-11.08	-12.47	0	48
ESO325-G004	ET	-23.2	143000	34.7	15	-11.34	-13.51	0	51

B

A Manual for Merging Star Cluster Simulations

The merging star cluster simulations were all performed with the PM code SUPERBOX described in detail in Sect. 2.2. This short manual provides the basic knowledge required to use SUPERBOX for simulations of merging star clusters (SCs). SUPERBOX was initially implemented in the programming language Fortran (Bien et al. 1990, 1991; Fellhauer et al. 2000) and can be executed on standard desktop computers. A later version developed at the AIfA was implemented in the C++ programming language and makes use of modern multi-core processor technologies (Metz 2008).

The setup programs for the CCs are all written in the programming language Fortran. They are interactive except for the programs **mcluster.f** and **newgrid.f** which require modifications of the Fortran code. In this manual I use the following conventions:

- Interactive programs and commands entered in a terminal window are displayed in typewriter style. The user entries are highlighted using bold face type.
- Fortran programs that need to be modified are displayed in a different sans-serif typeface than typewriter style. The user modifications are again highlighted using bold face type.

B.1 Setup of a Cluster Complex on an Orbit Around a Galaxy

The manual explains the setup procedure of a CC orbiting in an analytical galactic potential (disk+bulge+halo). It basically consists of three steps:

1. create a single SC (Sect. B.1.1),
2. generate the distribution of SCs in the CC (Sect. B.1.2),
3. put the SCs into the CC distribution and concatenate the CC with the orbit (Sect. B.1.3).

The theoretical background is described in Chapter 2. The physical units used by the programs are kpc, km s^{-1}, $M_\odot$ and Myr.

B.1.1 Creation of a Star Cluster

The SCs are modelled as Plummer spheres. The initial positions and velocities of the particles of a SC are obtained with the Fortran program **plummer.f**. The setup procedure is outlined in

Sect. 2.1.1. The compiled program **plummer.exe**[1] is an interactive program which successively reads the data entered by the user. An example setup is presented below.
Example of the setup procedure of a SC with a Plummer radius of $R_{\rm pl}^{\rm SC} = 4$ pc and a mass of $M^{\rm SC} = 3.125 \cdot 10^5$ M$_\odot$:

$>$ **./plummer.exe**

```
model units = 1; physical units = 0                    0
input number of particles                              100000
input plummer radius [kpc]                             0.004
input cutoff radius [kpc]                              0.02
input total mass [Msun] 0 for defining crossing time   3.125e5
input radius grid 1 [kpc] :                            0.08
input radius grid 2 [kpc] :                            0.8
input radius grid 3 [kpc] :                            70.0
input model name (no extension)                        SC_name
initialize random number generator                     12345
do you want normal velocities (1)
do you want zero velocities (0)
do you want rotating velocities (-1)                   1
```

Besides the basic parameters of the Plummer sphere all grid sizes for the entire CC simulation need to be defined already in the SC setup. More information on the choice of grid sizes for the three different grids in CC simulations is given in Sect. 2.2.3. To generate the initial configuration of a SC a user-defined number is required to initialize the random number generator. A given number always produces the same initial configuration and therefore makes a simulation repeatable. The program **plummer.f** creates two files, SC_name.CONT (binary data) and SC_name.LOG (ASCII data). The CONT-file[2] contains all information on the SC required to run a simulation with SUPERBOX. Besides the initial particle distribution (positions and velocities of all particles) the CONT-file also stores general information about the dataset called header data. The header data consist of an *integer array* with general information about the run and a *real array* with data concerning the SC. The LOG-file allows to check the SC parameter values chosen for the simulation.

The particle distribution generated by the program **plummer.exe** needs to be integrated for about 10 to 20 SC crossing times in SUPERBOX to adapt to the grids and the time step. The SC crossing time, $T_{\rm cross}^{\rm SC}$, can be estimated via

$$
\begin{aligned}
& T_{\rm cross}^{\rm SC} = \left(\tfrac{3\pi}{32}\right)^{-\frac{3}{2}} \sqrt{\frac{\left(R_{pl}^{SC}\right)^3}{G\,M_{SC}}}, \\
\Leftrightarrow \quad & T_{\rm cross}^{\rm SC} = \left(\tfrac{3\pi}{32}\right)^{-\frac{3}{2}} \sqrt{\frac{(0.004\,{\rm kpc})^3}{4.47\cdot10^{-12}\,\frac{\rm kpc^3}{\rm M_\odot\,Myr^2}\cdot 3.125\cdot10^5\,{\rm M_\odot}}}, \\
\Leftrightarrow \quad & T_{\rm cross}^{\rm SC} \approx 1.3\ {\rm Myr}.
\end{aligned}
$$

In this example, I chose an integration time of $t_{\rm int} = 20$ Myr. As a rule of thumb the time step should be smaller than the crossing time of a SC divided by 10. I chose a time step of

[1] To compile the program **plummer.f** enter the command: $>$ **gfortran plummer.f -o plummer.exe**
To start the program enter $>$ **./plummer.exe**
Note that the ">" sign only marks the prompt. Do not type it.

[2] The C++-version of Superbox requires all extensions in lower-case letters. When using the C++-version, the CONT-files need to be renamed.

$\Delta t = 0.1$ Myr which is well below this rule of thumb estimation. The number of integration steps is given by the fraction $t_{\rm int}/\Delta t$.
The parameters for the time integration are set with the Fortran program **define.f**. The program **define.f** modifies the header data of the CONT-file.
Example of the setup of integration parameters with **define.exe**:

```
> ./define.exe
file name?                                  SC_name

1)change number of integration steps        5)set analytical potential flag
2)change timestep (and variability)         6)set additional backup flag
3)change focus of grid                      7)set cosmology flag
4)change autosave                           8)set periodic boundary flag
9)show parameter of galaxy                  10)reset time to zero
99)save changes and quit                    11)add black hole
100)quit without saving

expecting your command :                    1
input number of integration steps :         200
expecting your command :                    2
input time step :                           0.1
Do you want variable timestep (yes=1) :     0
expecting your command :                    3
1 = center of mass
2 = center of density
select 1 or 2 :                             2
expecting your command :                    99
```

SUPERBOX needs a separate file "name", which contains the name of the created CONT-file (without the extension). As SUPERBOX overwrites the initial CONT-file it is useful to copy and rename the file to be able to restart a simulation. SUPERBOX++ also requires a file named "gridsize" specifying the number of grid cells (32, 64, 128, 256). It also contains a file "staticpotential.param" for an external tidal field consisting of a bulge, disk, and a dark matter halo (Sect. 2.1.4.1). Make sure that the external tidal field is turned off, i.e. remove the file "staticpotential.param" from the directory.

```
> echo SC_name > name
> echo 128 > gridsize
> cp SC_name.cont SC_name.start
> ./sb++.float-0.2c
```

SUPERBOX++ overwrites the initial file SC_name.cont (binary data) with the final values and creates the binary file **SC_name.head**. The file **SC_name.head** stores some physical quantities calculated during runtime for each time step like for example the center of mass and the Lagrange radii. The information can be transformed into plain ASCII files with the program **header.f**.

To check whether the SC has adapted to the grids its Lagrange radii are retrieved from the binary file **SC_name.head** and stored in the ASCII file **radb.g01**. The file **radb.g01** consists of

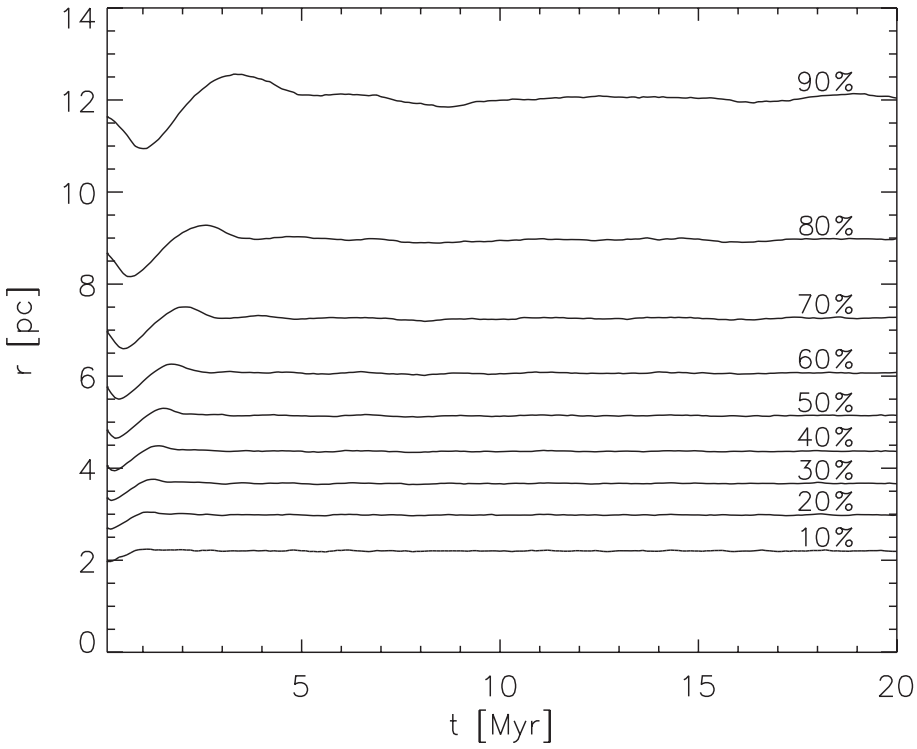

FIGURE B.1— Lagrange radii during the relaxation process of the SC. With increasing time the Lagrange radii become almost flat indicating that the SC is close to dynamical equilibrium.

ten columns. The first column displays the time and the remaining columns the Lagrange radii of the mass shells containing 10%, 20%, ... , 90% of all bound particles. The data can be easily visualized with any plotting program like Gnuplot, IDL etc. (Fig. B.1).

Example of generating the file radb.g01 from the binary file SC_name.HEAD with the program **header.exe**:

```
> ./header.exe
input filename without extension :        SC_name

1) energy
2) rad(t) 10% 20% .....  90%
3) angular momentum
4) center of mass & velocity
5) center of density
6) center of simulation
7) particles left/bound
8) cosmology data
9) rad(t) 10-90 % bound particles
99) exit program

expecting your command :                  9
writing data in file radb.g01....  done.
expecting your command :                  99
```

B.1.2 Generation of a Cluster Complex Model

The distribution of SCs in a CC is created with the program **pluascii.f**. It produces an ASCII file with positions and velocities according to a Plummer distribution.

Example of a CC consisting of $N_0^{\rm CC} = 32$ SCs. The CC has a Plummer radius of $R_{\rm pl}^{\rm CC} = 40$ pc and a mass of $M^{\rm CC} = 32\ M^{\rm SC} = 1.0 \cdot 10^7$ $M_\odot$:

$>$ **./pluascii.exe**

```
input number of particles                                  32
input plummer radius [kpc]                                 0.04
input cutoff radius [kpc]                                  0.2
input total mass [Msun] 0 for defining crossing time       1.e7
input radius grid 1 [kpc] :                                0.08
input radius grid 2 [kpc] :                                0.8
input radius grid 3 [kpc] :                                70.0
initialize random number :                                 12345
ordinary 0 rotating 1 :                                    0
input model name (no extension)                            CC_name
generating galaxy....done
```

The program **pluascii.exe** generates an ASCII file with the name CC_name.CONT. The file consists of header data and particle data. The header data is for information only and has to be removed by hand before continuing with the last step described in the next section.

B.1.3 Concatenation of the CC Distribution, the Individual SCs, and the Orbit

To concatenate the SC created in Sect. B.1.1 with the CC distribution of Sect. B.1.2 and to put the CC on an orbit the programs **mcluster.f** and **aconc3.f** are used. The file **mcluster.f** has to be edited by hand in a text editor.

Example of the program mcluster.f to generate the CC and to place it on a circular polar orbit at a distance of 60 kpc (for the Milky Way potential of Sect. 4.3.2.1.1):

$>$ **emacs mcluster.f &**

```
program mcluster

integer igal                    number of SCs building the CC, N_0^CC
parameter (igal = 32)

integer i,j
real cluster(6,igal),cms(6)

cms(1) = 60.0                   x[kpc]
cms(2) = 0.0                    y[kpc]
cms(3) = 0.0                    z[kpc]
```

```
cms(4) = 0.0                                          v_x[km/s]
cms(5) = 0.0                                          v_y[km/s]
cms(6) = 206.6                                        v_z[km/s]

open (1,file='CC_name.CONT',form='formatted')         open the CC model
open (2,file='aconc3.inp')
write (2,'(i2)') igal
do i = 1,igal
    read (1,'(6f15.9)') (cluster(j,i),j=1,6)
   do j = 1,6
      cluster(j,i) = cluster(j,i) + cms(j)
   enddo
   write (2,'(a)') 'SC_name'                          define the SCs which build up the CC
   write (2,'(3f20.10)') (cluster(j,i),j=1,3)
   write (2,'(3f20.10)') (cluster(j,i),j=4,6)
enddo
close (1)
close (2)
stop
end
```

After editing the file **mcluster.f** it needs to be compiled. The program **mcluster.exe** generates a file named **aconc3.inp** which is needed by the program **aconc3.exe** to concatenate all the objects and place the CC on the orbit. The file **aconc3.inp** is an ASCII file with all necessary information about the objects to be concatenated.

Structure of an exemplary file **aconc3.inp** with $N_0^{\rm CC} = 32$ SCs:

32	*number of SCs to be concatenated*
SC_name	*name of SC 1*
$x_{1,0}$,$y_{1,0}$,$z_{1,0}$	*intial position of SC 1*
$v_{x,1,0}$,$v_{y,1,0}$,$v_{z,1,0}$	*initial velocity of SC 1*
SC_name	*name of SC 2*
$x_{2,0}$,$y_{2,0}$,$z_{2,0}$	*intial position of SC 2*
$v_{x,2,0}$,$v_{y,2,0}$,$v_{z,2,0}$	*initial velocity of SC 2*
...	

In my simulations I used CCs with SCs of equal mass and size. As the SCs are identical, the file names for the initial SCs are all the same. The program **aconc3.exe** places the 32 objects specified in the ASCII file **aconc3.inp** on their destined positions and finally asks the user for the new name (without extension) of the final CC CONT-file.

B.2 Running the Simulations

A CC computation can be roughly divided into two phases: a merging phase in the first 1–2 Gyr followed by an evolution phase of the merger object. In the first part of a CC simulation, the simulations are stopped every 10 CC crossing times to look for mergers. The merged SCs are

determined and combined to a new object – the merger object – with an own set of grids. This procedure reduces the computing time significantly and improves the accuracy of the force calculation due to a higher number of particles in the individual grid cells. When it becomes apparent that no further SCs will merge into the merger object, the simulation can be run continuously to the end. The CC crossing time is estimated via

$$
\begin{aligned}
& T_{\text{cross}}^{\text{CC}} = \left(\tfrac{3\pi}{32}\right)^{-\frac{3}{2}} \sqrt{\frac{\left(R_{pl}^{CC}\right)^3}{G\,M_{CC}}}, \\
\Leftrightarrow \quad & T_{\text{cross}}^{\text{CC}} = \left(\tfrac{3\pi}{32}\right)^{-\frac{3}{2}} \sqrt{\frac{(0.04\,\text{kpc})^3}{4.47{\cdot}10^{-12}\,\frac{\text{kpc}^3}{\text{M}_\odot\,\text{Myr}^2}{\cdot}1.0{\cdot}10^7\,\text{M}_\odot}}, \\
\Leftrightarrow \quad & T_{\text{cross}}^{\text{CC}} \approx 7.5\ \text{Myr}.
\end{aligned}
$$

I stopped the simulation every 75 Myr. The time step of the simulation is already fixed by the time step of the simulation of an individual SC as described in Sect. B.1.1 ($\Delta t = 0.1$ Myr).

The parameters for the time integration are again set with the Fortran program **define.f**. The program **define.f** modifies the header data of the CC CONT-file.

Example of the setup of integration parameters with **define.exe**:

```
> ./define.exe
file name?                                  CC_name

1)change number of integration steps        5)set analytical potential flag
2)change timestep (and variability)         6)set additional backup flag
3)change focus of grid                      7)set cosmology flag
4)change autosave                           8)set periodic boundary flag
9)show parameter of galaxy #n (1..32)       10)reset time to zero
99)save changes and quit                    11)add black hole
100)quit without saving

expecting your command :                    1
input number of integration steps :         750
expecting your command :                    2
input time step :                           0.1
Do you want variable timestep (yes=1) :     0
expecting your command :                    3
1 = center of mass
2 = center of density
select 1 or 2 :                             2
expecting your command :                    9
which galaxy?                               1
 1) change parameter for save
 2) change parameter for itens
 3) change parameter for dtens
 4) change size of grid 1
 5) change size of grid 2
```

```
 6) change size of grid 3 (of all galaxies)
 7) change parameter for save for all galaxies
 8) change parameter for itens for all galaxies
 9) change parameter for dtens for all galaxies
 99) go back to main menu
expecting your command :                7
frequence                               100
number of first star to save            1
number of last star to save             100000
expecting your command :                99

1)change number of integration steps   5)set analytical potential flag
2)change timestep (and variability)    6)set additional backup flag
3)change focus of grid                 7)set cosmology flag
4)change autosave                      8)set periodic boundary flag
9)show parameter of galaxy #n (1..32)  10)reset time to zero
99)save changes and quit               11)add black hole
100)quit without saving

expecting your command :                99
```

The part typesetted in italic is only needed for intermediate files that can be used for snapshots. The positions and velocities of the stars in the SCs are saved every 100th integration step.
Before starting the CC simulation with SUPERBOX++ make sure that the external tidal field is turned on again, i.e. copy the file "staticpotential.param" into the directory. The external tidal field specified in the file "staticpotential.param" consists of a bulge, disk, and a dark matter halo (Sect. 2.1.4.1). In case of my Milky Way potential (Sect. 4.3.2.1.1) the file "staticpotential.param" looks as follows:

```
> more staticpotential.param
186.0 12.0
1.0e+11 6.5 0.26
3.4e+10 0.7
```

Starting the CC simulation:

```
> echo CC_name > name
> cp CC_name.cont CC_name.start
> sb++.float-0.2c
```

B.2.1 Determination of Merged Star Clusters

In the first part of a CC simulation, the simulations are stopped every 10 CC crossing times to look for mergers. The SCs are regarded to be merged if their mutual distance is below a certain value specified in the program **merger.exe** for more than three crossing times of the CC. To determine the number of merged SCs the time evolution of the center of densities of all SCs is needed. The positions of the SCs for every time step are stored in the file **CC_name**.head. The head-file can be accessed with the program **header.f**.

Example of retrieving the dcms-files of all SCs with the program **header.exe**:

```
> ./header.exe
input filename without extension :        CC_name
which galaxy (0 = all) :                  0
1) energy
2) rad(t) 10% 20% .....  90%
3) angular momentum
4) center of mass & velocity
5) center of density
6) center of simulation
7) particles left/bound
8) cosmology data
9) rad(t) 10-90 % bound particles
99) exit program
expecting your command :                  5
writing data in file dcms.g01....  done.
writing data in file dcms.g02....  done.
...
writing data in file dcms.g32....  done.
which galaxy (0 = all) :                  0
expecting your command :                  99
```

The program generates 32 dcms-files (dcms.g01 – dcms.g32). These files are needed by the program **merger.f** to determine the SCs that have merged. The program **merger.exe** creates an ASCII file **merger.dat** listing all merger events.

Example to determine the merged SCs with the program **merger.exe**:

```
number of galaxies:                32
interval of steps:                 5
timestep [Myr]:                    0.1
merger distance [kpc]:             0.02
Crossing time super-cluster [Myr]: 7.5
```

The number of galaxies corresponds to the number of SCs. The program looks every 5 time steps for merged SCs (interval of steps = 5). The merging criterion is a simple distance criterion: Two objects are considered as merged if their mutual distance stays below a given distance for more than three crossing times of the CC ($\equiv$ crossing time of the super-cluster). In this example a merger distance of 20 pc is chosen. A typical value for the merger distance is five Plummer radii of a single SC (Fellhauer et al. 2002).

The merged SCs are combined to a new object – the merger object – with an own set of grids. It is also possible that some minor merger events occur, i.e. additional mergers of 2 or 3 SCs. As an example, I assume a major merger event of SCs, one minor merger event (e.g. SCs 6 and 18) and only 5 unmerged SCs (e.g. SCs 3, 7, 8, 15, 29). Thus the number of SCs after the

merging events amounts to 7. The new CONT-file is created with the program **newgrid.f**. It has to be edited by hand in a text editor.

```
> emacs newgrid.f &
program newgrid

integer igal,jgal,istar,maxstar
parameter (igal = 32 , istar = 100000 , maxstar = 3200000)   igal: number of SCs before merging
                                                              maxstar = N_0^CC N_0^SC = 32 · 100000
parameter (jgal = 7)                                          jgal: number of SCs after merging

real fh(60,igal),nfh(60,jgal),hfh(60),star(6,maxstar),hs(6)
real cms(6),scm,scl,scv,sct
integer ih(60),iconc(jgal,igal)
integer i,j,k
character fname*20,lfname*20

fname = 'CC_name_old'                                         name of old CONT-file
lfname = 'CC_name_new'                                        name of new CONT-file
do i = 1,igal
    do j = 1,jgal
        iconc(j,i) = 0
    enddo
enddo
iconc(01,01) = 01                                             Major merger of 25 SCs
iconc(01,02) = 02
iconc(01,03) = 04
...
iconc(01,25) = 32
iconc(02,01) = 06                                             Minor merger of 2 SCs
iconc(02,02) = 18
iconc(03,01) = 03                                             Unmerged SCs
iconc(04,01) = 07
iconc(05,01) = 08
iconc(06,01) = 15
iconc(07,01) = 29

open (1,file=fname,access='direct',recl=240)
...
end
```

The two-dimensional array **iconc(j,i)** reads as follows: **iconc(j,i) = z**
j: object number of new object after merging, $j = 1, \ldots, N^{\text{CC}}_{\text{after\_merging}}$
i: running number of sub-objects of merger object, $i = 1, \ldots, N_{\text{merged\_SCs}}$
z: old object number

For the new CONT-file the integration time, $t_{\rm int}$, has to be defined and in case the grids of the merger object are too small the sizes of the high resolution grid, $R_{\rm hres}$, and/or intermediate resolution grid, $R_{\rm mres}$, have to be adjusted.

Example of setting the new number of integration steps with the program **define.exe**:

```
> ./define.exe
file name?                                  CC_name_new

1)change number of integration steps        5)set analytical potential flag
2)change timestep (and variability)         6)set additional backup flag
3)change focus of grid                      7)set cosmology flag
4)change autosave                           8)set periodic boundary flag
9)show parameter of galaxy #n (1..32)       10)reset time to zero
99)save changes and quit                    11)add black hole
100)quit without saving

expecting your command :                    1
input number of integration steps :         1500
expecting your command :                    9
which galaxy?                               1
 1) change parameter for save
 2) change parameter for itens
 3) change parameter for dtens
 4) change size of grid 1
 5) change size of grid 2
 6) change size of grid 3 (of all galaxies)
 7) change parameter for save for all galaxies
 8) change parameter for itens for all galaxies
 9) change parameter for dtens for all galaxies
 99) go back to main menu

expecting your command :                    4
input size of grid 1 :                      new size of inner grid
expecting your command :                    5
input size of grid 2 :                      new size of middle grid
expecting your command :                    99

1)change number of integration steps        5)set analytical potential flag
2)change timestep (and variability)         6)set additional backup flag
3)change focus of grid                      7)set cosmology flag
4)change autosave                           8)set periodic boundary flag
9)show parameter of galaxy #n (1..32)       10)reset time to zero
99)save changes and quit                    11)add black hole
100)quit without saving

expecting your command :                    99
```

Restart the simulation for another 75 Myr and redo the procedure described in this section again until it becomes apparent that no further SCs will merge into the merger object. In case the merging process is completely terminated the simulation can be run continuously until the integration time, $t_{\rm int}$, is reached.

C

Summary Tables of the Simulation Results

This appendix contains parameters of the final merger objects obtained from the various simulations presented in this thesis. It consists of 8 tables.

Section C.1 presents the results of the parameter study of FFs in the disk of the galaxy NGC 1023. For different points on the Bastian mass-radius relation, the orbit, the number of star clusters, and the initial configuration was varied (see Sect 4.2).

Section C.2 shows the parameters of the models obtained for the Milky Way cluster NGC 2419. For a fixed orbit, the CC mass and size as well as the initial distribution of star clusters in the CC was varied (see Sect. 4.3).

Section C.3 explains the nomenclature of the models used in the general study of EOs covered by Chapter 5.

Section C.4 shows two tables with the parameters of the merger objects resulting from CCs with different initial masses and sizes for a fixed eccentric orbit for two different inclinations. The results from a polar orbit are summarized in Table C.4 and those of an inclined orbit in Table C.5. The impact of the initial CC parameters on the resulting merger objects is discussed in Sect 5.2.

Section C.5 contains two tables with the parameters of merger objects evolving from low-mass CCs on different circular (Table C.6) and eccentric (Table C.7) orbits and without a tidal field (Table C.6). The impact of the orbit on the resulting merger objects is studied in Sect 5.3.

Section C.6 shows the results of simulations performed to discuss the formation of extremely extended EOs and the possible formation of UFOs in the Gilmore gap as pointed out in Sect 5.4.

C.1 Results of the Study of Faint Fuzzies in NGC 1023

TABLE C.1— Results of the 25 FF computations after 5 Gyr

Model	R_{gal} [a]	N_M [b]	M_{encl} [c]	M_{encl} [d]	V [e]	r_h [f]	r_{eff} [g]	r_t^{MO} [h]
	(kpc)		($M_\odot$)	(%)	(mag)	(pc)	(pc)	(pc)
CC_H_2_20	2	10	77923.6	20	23.5	8.6	7.2	37.6
CC_H_3_20	3	12	94180.2	24	23.3	9.5	7.8	41.7
CC_H_5_20	5	12	116021.0	29	23.0	12.3	10.1	52.0
CC_H_8_20	8	14	178244.0	45	22.6	15.3	12.4	64.3
CC_H_12_20	12	15	207737.0	52	22.4	17.1	13.4	88.9
CC_H_ecc_20	3-8	12	85120.6	21	23.4	9.3	7.4	38.2
CC_H_inf_20	∞	19	362804.0	91	21.8	29.6	22.5	—
CC_H_5_80	5	32	35565.1	9	24.3	10.6	8.5	39.2
CC_H_inf_80	∞	79	390052.0	98	21.7	60.8	45.6	—
CC_M_2_20	2	12	24366.5	24	24.7	5.7	4.7	24.4
CC_M_3_20	3	12	23297.8	23	24.8	6.0	4.9	26.4
CC_M_5_20	5	13	34793.1	35	24.4	8.3	6.8	35.3
CC_M_8_20	8	15	50045.4	50	24.0	10.0	8.3	43.5
CC_M_12_20	12	16	58413.3	58	23.8	10.5	8.3	58.6
CC_M_ecc_20	3-8	12	23198.6	23	24.8	6.2	4.9	26.1
CC_M_5_c2_20	5	16	24507.4	25	24.7	6.9	5.5	29.7
CC_M_5_c3_20	5	13	28668.2	29	24.6	6.9	5.6	30.4
CC_M_inf_20	∞	19	90740.5	91	23.3	16.6	12.7	—
CC_L_2_20	2	13	11360.3	28	25.6	4.4	3.6	18.8
CC_L_3_20	3	13	11879.8	30	25.5	4.9	4.1	20.9
CC_L_5_20	5	14	16422.8	41	25.2	6.3	5.1	25.8
CC_L_8_20	8	14	20470.2	51	24.9	6.5	5.1	30.3
CC_L_12_20	12	16	24679.0	62	24.7	7.7	6.1	43.9
CC_L_ecc_20	3-8	13	12491.0	31	25.5	4.8	3.9	21.1
CC_L_inf_20	∞	20	37643.0	94	24.3	11.7	9.0	—

[a] Distance to the center of galaxy NGC 1023.
[b] Number of merged star clusters.
[c] Enclosed mass of merger object.
[d] Percentage of enclosed mass compared to the initial CC mass.
[e] V-magnitudes (Eq. 4.1).
[f] Half-mass radius of merger object.
[g] Effective radius, i.e. the projected half-mass radius of the merger object.
[h] Tidal radius of merger object obtained from King fit.

C.2 Results of the Study of the Milky Way EO NGC 2419

TABLE C.2— Parameters of the 27 computed NGC 2419 models

Model [a]	$N_{\rm M}$ [b]	$M_{\rm encl}$ [c] (10^6 $M_\odot$)	$M_{\rm V}$ [d] (mag)	$r_{\rm h}$ [e] (pc)	$r_{\rm eff}$ [f] (pc)	$r_{\rm c}$ [g] (pc)	$\mu_{\rm V}$ [h] (mag arcsec^{-2})	σ [i] (km s^{-1})
M_1_1.0_25	20	0.93	–9.31	18.8	14.2	6.6	18.99	4.88
M_1_1.0_50	20	0.85	–9.21	25.8	19.2	5.7	19.36	4.13
M_1_1.0_75	20	0.77	–9.11	29.8	21.8	5.1	19.41	3.80
M_1_1.0_100	19	0.64	–8.91	24.9	19.1	5.5	19.51	3.59
M_1_1.0_125	16	0.54	–8.72	22.1	16.6	5.0	19.47	3.51
M_1_1.0_150	14	0.46	–8.55	19.6	14.4	4.5	19.39	3.47
M_1_1.5_25	20	1.38	–9.74	19.9	14.9	6.7	18.65	5.85
M_1_1.5_50	20	1.29	–9.67	26.6	20.0	6.2	19.04	4.99
M_1_1.5_75	20	1.17	–9.56	30.1	22.5	5.6	19.12	4.57
M_1_1.5_100	19	1.05	–9.44	31.8	23.5	4.9	19.08	4.34
M_1_1.5_125	17	0.92	–9.30	28.8	21.3	5.3	19.15	4.21
M_1_1.5_150	15	0.80	–9.15	25.1	18.8	4.8	19.09	4.10
M_1_2.0_25	20	1.84	–10.05	21.1	15.9	7.2	18.47	6.55
M_1_2.0_50	20	1.75	–10.00	28.4	21.2	6.4	18.83	5.65
M_1_2.0_75	20	1.61	–9.91	32.0	23.7	6.0	18.88	5.26
M_1_2.0_100	19	1.48	–9.82	35.2	25.6	5.3	18.87	4.99
M_1_2.0_125	16	1.26	–9.64	31.5	23.2	5.4	19.01	4.76
M_1_2.0_150	18	1.17	–9.56	28.9	21.2	5.1	18.81	4.81
M_1_2.0_200	14	0.99	–9.38	26.4	18.6	4.7	18.85	4.64
M_1_2.0_300	10	0.62	–8.87	17.6	13.2	4.8	19.03	4.18
M_1_3.0_100	19	2.40	–10.34	39.6	28.8	5.3	18.45	6.08
M_2_1.5_100	19	1.17	–9.56	37.2	27.5	5.8	19.34	4.24
M_3_1.5_100	19	1.07	–9.46	31.9	23.7	5.3	19.21	4.33
M_4_1.5_100	18	0.80	–9.15	22.7	17.9	5.8	19.23	4.10
M_5_1.5_100	19	0.87	–9.24	31.3	24.5	5.4	19.35	3.84
M_6_1.5_100	15	0.76	–9.09	33.4	25.5	5.2	19.58	3.53
M_7_1.5_200	19	0.93	–9.31	30.1	21.9	5.1	19.12	4.22

[a] Model__Configuration__$M^{\rm CC}$__$R_{\rm pl}^{\rm CC}$.
[b] Number of merged star clusters.
[c] Enclosed mass of merger object within 800 pc.
[d] Absolute V-magnitude of merger object.
[e] Half-mass radius of merger object.
[f] Effective radius, i.e. the projected half-mass radius of the merger object.
[g] Core radius of merger object obtained from a King fit.
[h] Central surface brightness μ_V of merger object obtained from a King fit. An extinction of $A_{\rm V}$ = 0.25 has been applied.
[i] Velocity dispersion within a projected radius of 100 pc.

C.3 Nomenclature of the Simulations of the General EO Study

TABLE C.3— Nomenclature of the simulations

$R_{\rm pl}^{\rm CC}$ [pc] [a] \ $M^{\rm CC}$ [$M_\odot$] [b]	10^5	$10^{5.5}$	10^6	$10^{6.5}$	10^7	$10^{7.5}$	10^8
10	10	11	12	13	14	15	16
20	20	21	22	23	24	25	26
40	30	31	32	33	34	35	36
80	40	41	42	43	44	45	46
160	50	51	52	53	54	55	56
240	60	61	62	63	64	65	66
320	70	71	72	73	74	75	76

[a] Initial CC Plummer radius.
[b] Initial CC mass.

The names of the resulting merger objects contain information on the parameters of the initial CC model and the orbit. The CC parameters size and mass constitute a matrix shown in Table C.3. The row index represents the initial CC Plummer radius and the column index the initial CC mass. For example CC_34 denotes a CC with an initial CC Plummer radius of $R_{\rm pl}^{\rm CC} = 40$ pc and an initial CC mass of $M^{\rm CC} = 10^7\,{\rm M}_\odot$. The simulations were performed on different circular (CIRC_$R_{\rm gal}$) and eccentric (ECC_$R_{\rm p}$_$R_{\rm a}$ or ECC_$R_{\rm a}$_$R_{\rm p}$) orbits and without a tidal field (INF).

The merger object names are constructed in the following way: CC_Model–Orbit. For example a CC model with an initial CC Plummer radius of $R_{\rm pl}^{\rm CC} = 160$ pc and an initial CC mass of $M^{\rm CC} = 10^6\,{\rm M}_\odot$ on a circular orbit at a galactic distance of $R_{\rm gal} = 60$ kpc is denoted by CC_52-CIRC_60. The same CC model on an eccentric orbit between peri- and apogalactic distances of 20 and 60 kpc leads to the name CC_52-ECC_20_60 (when starting at pericenter) or CC_52-ECC_60_20 (when starting at apocenter). Performing the simulation without an external tidal field is denoted by CC_52-INF.

C.4 Results of the Study with Varied Initial CC Parameters Mass and Size

TABLE C.4— Parameters of merger objects on a polar eccentric orbit between 20 and 60 kpc

Model [a]	M_{CC} [b] ($M_\odot$)	$R_{CC,pl}$ [c] (pc)	N_M [d]	M_{encl} [e] ($M_\odot$)	M_{encl} [f] (%)	r_h [g] (pc)	r_{eff} [h] (pc)	σ [i] (km s^{-1})	β [j]
CC_11-ECC_20_60	$10^{5.5}$	10.0	31	$2.98{\cdot}10^5$	94	14.3	11.6	3.24	0.27
CC_21-ECC_20_60	$10^{5.5}$	20.0	32	$2.92{\cdot}10^5$	92	20.4	15.7	2.83	0.55
CC_31-ECC_20_60	$10^{5.5}$	40.0	30	$2.54{\cdot}10^5$	80	25.5	19.2	2.41	1.11
CC_41-ECC_20_60	$10^{5.5}$	80.0	25	$1.85{\cdot}10^5$	59	30.3	22.4	1.92	2.40
CC_51-ECC_20_60	$10^{5.5}$	160.0	13	$0.85{\cdot}10^5$	27	19.6	13.9	1.63	7.29
CC_12-ECC_20_60	10^6	10.0	32	$9.48{\cdot}10^5$	95	15.9	12.7	5.52	0.19
CC_22-ECC_20_60	10^6	20.0	32	$8.81{\cdot}10^5$	88	28.0	21.6	4.16	0.38
CC_32-ECC_20_60	10^6	40.0	31	$8.70{\cdot}10^5$	87	33.0	25.2	3.87	0.77
CC_42-ECC_20_60	10^6	80.0	28	$6.63{\cdot}10^5$	66	34.4	25.4	3.39	1.59
CC_52-ECC_20_60	10^6	160.0	22	$4.37{\cdot}10^5$	44	30.3	23.1	2.85	3.75
CC_13-ECC_20_60	$10^{6.5}$	10.0	32	$3.04{\cdot}10^6$	96	16.1	12.8	9.80	0.13
CC_23-ECC_20_60	$10^{6.5}$	20.0	32	$2.92{\cdot}10^6$	92	27.7	21.8	7.51	0.26
CC_33-ECC_20_60	$10^{6.5}$	40.0	31	$2.88{\cdot}10^6$	91	33.2	25.6	6.93	0.53
CC_43-ECC_20_60	$10^{6.5}$	80.0	30	$2.38{\cdot}10^6$	75	37.5	28.1	6.01	1.07
CC_53-ECC_20_60	$10^{6.5}$	160.0	27	$1.75{\cdot}10^6$	55	42.1	31.3	4.99	2.30
CC_63-ECC_20_60	$10^{6.5}$	240.0	21	$1.36{\cdot}10^6$	43	35.6	26.0	4.83	4.00
CC_73-ECC_20_60	$10^{6.5}$	320.0	15	$1.00{\cdot}10^6$	32	27.3	19.4	5.01	7.16
CC_14-ECC_20_60	10^7	10.0	32	$9.67{\cdot}10^6$	97	16.3	13.1	17.21	0.09
CC_24-ECC_20_60	10^7	20.0	32	$9.48{\cdot}10^6$	95	26.3	20.7	13.78	0.18
CC_34-ECC_20_60	10^7	40.0	32	$9.48{\cdot}10^6$	95	33.4	26.5	12.10	0.36
CC_44-ECC_20_60	10^7	80.0	31	$8.55{\cdot}10^6$	86	46.4	34.9	10.35	0.73
CC_54-ECC_20_60	10^7	160.0	29	$6.20{\cdot}10^6$	62	51.3	38.8	8.52	1.51
CC_15-ECC_20_60	$10^{7.5}$	10.0	32	$3.06{\cdot}10^7$	97	17.2	13.9	29.84	0.06
CC_25-ECC_20_60	$10^{7.5}$	20.0	32	$2.87{\cdot}10^7$	91	33.7	26.7	21.00	0.12
CC_35-ECC_20_60	$10^{7.5}$	40.0	32	$2.98{\cdot}10^7$	94	40.5	31.9	19.57	0.24
CC_45-ECC_20_60	$10^{7.5}$	80.0	31	$2.82{\cdot}10^7$	89	52.1	39.0	17.80	0.50
CC_55-ECC_20_60	$10^{7.5}$	160.0	30	$2.16{\cdot}10^7$	68	65.0	46.4	15.15	1.02
CC_65-ECC_20_60	$10^{7.5}$	240.0	24	$1.59{\cdot}10^7$	50	46.1	34.7	14.21	1.56
CC_75-ECC_20_60	$10^{7.5}$	320.0	24	$1.33{\cdot}10^7$	42	38.6	31.0	13.02	2.16
CC_16-ECC_20_60	10^8	10.0	32	$9.64{\cdot}10^7$	96	18.6	14.9	51.11	0.04
CC_26-ECC_20_60	10^8	20.0	32	$9.16{\cdot}10^7$	92	31.9	25.2	38.78	0.09
CC_36-ECC_20_60	10^8	40.0	32	$9.50{\cdot}10^7$	95	38.2	29.9	36.06	0.17
CC_46-ECC_20_60	10^8	80.0	32	$9.11{\cdot}10^7$	91	53.9	40.4	31.26	0.34
CC_56-ECC_20_60	10^8	160.0	31	$7.74{\cdot}10^7$	77	72.4	53.8	26.06	0.69

[a] Nomenclature as defined in Sect. C.3
[b] Initial CC Mass.
[c] Initial CC Plummer radius.
[d] Number of merged star clusters.
[e] Enclosed mass of merger object.
[f] Percentage of enclosed mass compared to the initial CC mass.
[g] Half-mass radius of merger object.
[h] Effective radius, i.e. the projected half-mass radius of the merger object.
[i] Overall line-of-sight velocity dispersion.
[j] β-parameter (see Sect. 2.1.4.2)

TABLE C.5— Parameters of merger objects on an inclined eccentric orbit between 20 and 60 kpc

Model [a]	M_{CC} [b] ($M_\odot$)	$R_{CC,pl}$ [c] (pc)	N_M [d]	M_{encl} [e] ($M_\odot$)	M_{encl} [f] (%)	r_h [g] (pc)	r_{eff} [h] (pc)	σ [i] (km s^{-1})	β [j]
CC_21-ECC_i_20_60	$10^{5.5}$	20.0	32	$2.92{\cdot}10^5$	92	20.4	14.7	2.96	0.55
CC_31-ECC_i_20_60	$10^{5.5}$	40.0	30	$2.60{\cdot}10^5$	82	26.7	19.7	2.43	1.11
CC_41-ECC_i_20_60	$10^{5.5}$	80.0	25	$1.76{\cdot}10^5$	56	27.3	20.3	1.95	2.40
CC_51-ECC_i_20_60	$10^{5.5}$	160.0	18	$0.95{\cdot}10^5$	30	17.8	13.2	1.75	7.29
CC_22-ECC_i_20_60	10^6	20.0	32	$8.87{\cdot}10^5$	89	28.1	20.9	4.31	0.38
CC_32-ECC_i_20_60	10^6	40.0	30	$8.58{\cdot}10^5$	86	32.6	24.2	3.98	0.77
CC_42-ECC_i_20_60	10^6	80.0	29	$7.12{\cdot}10^5$	71	37.3	27.7	3.36	1.59
CC_52-ECC_i_20_60	10^6	160.0	19	$3.79{\cdot}10^5$	38	23.9	17.6	3.01	3.75
CC_33-ECC_i_20_60	$10^{6.5}$	40.0	32	$2.95{\cdot}10^6$	93	34.1	25.1	7.22	0.53
CC_43-ECC_i_20_60	$10^{6.5}$	80.0	30	$2.54{\cdot}10^6$	80	42.2	31.2	6.00	1.07
CC_53-ECC_i_20_60	$10^{6.5}$	160.0	22	$1.40{\cdot}10^6$	44	29.1	21.0	5.35	2.30
CC_34-ECC_i_20_60	10^7	40.0	32	$9.50{\cdot}10^6$	95	33.6	25.1	12.79	0.36
CC_44-ECC_i_20_60	10^7	80.0	30	$8.36{\cdot}10^6$	84	46.0	34.5	10.29	0.73
CC_54-ECC_i_20_60	10^7	160.0	29	$6.16{\cdot}10^6$	62	57.9	42.2	8.39	1.51
CC_45-ECC_i_20_60	$10^{7.5}$	80.0	30	$2.77{\cdot}10^7$	88	50.8	38.2	17.75	0.50
CC_55-ECC_i_20_60	$10^{7.5}$	160.0	30	$2.23{\cdot}10^7$	71	73.5	53.1	14.61	1.02
CC_46-ECC_i_20_60	10^8	80.0	31	$8.99{\cdot}10^7$	90	52.7	39.0	31.91	0.34
CC_56-ECC_i_20_60	10^8	160.0	30	$7.09{\cdot}10^7$	71	70.2	51.5	26.10	0.69

[a-j] see Table C.4

C.5 Results of the Study with Varied Orbital Parameters

TABLE C.6— Parameters of merger objects on different circular orbits and without tidal field

Model [a]	M^{CC} [b] ($M_\odot$)	R_{pl}^{CC} [c] (pc)	N_M [d]	M_{encl} [e] ($M_\odot$)	M_{encl} [f] (%)	r_h [g] (pc)	r_{eff} [h] (pc)	σ [i] (km s^{-1})	β [j]
CC_21-CIRC_20	$10^{5.5}$	20.0	31	$2.78{\cdot}10^5$	88	19.3	14.5	2.90	0.55
CC_21-CIRC_40	$10^{5.5}$	20.0	31	$2.92{\cdot}10^5$	92	20.4	15.2	2.89	0.34
CC_21-CIRC_60	$10^{5.5}$	20.0	32	$3.01{\cdot}10^5$	95	21.1	16.3	2.81	0.26
CC_21-CIRC_120	$10^{5.5}$	20.0	32	$3.07{\cdot}10^5$	97	21.6	16.5	2.80	0.16
CC_21-INF	$10^{5.5}$	20.0	32	$3.11{\cdot}10^5$	98	21.9	16.7	2.81	—
CC_31-CIRC_20	$10^{5.5}$	40.0	29	$2.31{\cdot}10^5$	73	23.4	17.3	2.46	1.11
CC_31-CIRC_40	$10^{5.5}$	40.0	30	$2.70{\cdot}10^5$	85	27.7	20.8	2.39	0.69
CC_31-CIRC_60	$10^{5.5}$	40.0	31	$2.88{\cdot}10^5$	91	29.9	22.6	2.37	0.52
CC_31-CIRC_120	$10^{5.5}$	40.0	31	$2.95{\cdot}10^5$	93	30.8	23.6	2.31	0.32
CC_31-INF	$10^{5.5}$	40.0	31	$3.10{\cdot}10^5$	98	32.8	25.2	2.30	—
CC_41-CIRC_20	$10^{5.5}$	80.0	22	$1.40{\cdot}10^5$	44	21.8	16.6	1.94	2.40
CC_41-CIRC_40	$10^{5.5}$	80.0	22	$1.90{\cdot}10^5$	60	29.5	21.6	2.00	1.41
CC_41-CIRC_60	$10^{5.5}$	80.0	27	$2.17{\cdot}10^5$	69	33.2	24.6	1.97	1.05
CC_41-CIRC_120	$10^{5.5}$	80.0	29	$2.72{\cdot}10^5$	86	46.0	32.2	1.87	0.63
CC_41-INF	$10^{5.5}$	80.0	30	$3.06{\cdot}10^5$	97	59.1	44.5	1.83	—
CC_51-CIRC_20	$10^{5.5}$	160.0	10	$0.64{\cdot}10^5$	20	13.9	10.5	1.57	7.29
CC_51-CIRC_40	$10^{5.5}$	160.0	21	$1.24{\cdot}10^5$	39	24.6	18.4	1.70	3.21
CC_51-CIRC_50*	$10^{5.5}$	160.0	22	$1.38{\cdot}10^5$	44	31.5	23.7	1.65	2.62
CC_51-CIRC_60	$10^{5.5}$	160.0	22	$1.57{\cdot}10^5$	50	38.5	28.9	1.57	2.24
CC_51-CIRC_70*	$10^{5.5}$	160.0	25	$1.80{\cdot}10^5$	57	46.0	35.6	1.52	1.97
CC_51-CIRC_120	$10^{5.5}$	160.0	24	$2.25{\cdot}10^5$	71	65.7	48.9	1.59	1.30
CC_51-INF	$10^{5.5}$	160.0	26	$3.06{\cdot}10^5$	97	122.1	93.2	1.45	—

[a-j] see Table C.4

[*] Additional simulations needed for the discussion of extremely extended star clusters and of UFOs in the Gilmore gap (see Sect. 5.4).

TABLE C.7— Parameters of merger objects on different eccentric orbits

Model [a]	M^{CC} [b] ($M_\odot$)	R_{pl}^{CC} [c] (pc)	N_M [d]	$M_{encl,Peri}$ [e] ($M_\odot$)	$M_{encl,Peri}$ [f] (%)	$r_{h,Peri}$ [g] (pc)	$r_{eff,Peri}$ [h] (pc)	σ_{Peri} [i] (km s^{-1})	β_{start} [j]
CC_31-ECC_20_60	$10^{5.5}$	40.0	30	$2.54{\cdot}10^5$	80	25.4	19.1	2.42	1.11
CC_51-ECC_20_60	$10^{5.5}$	160.0	13	$0.85{\cdot}10^5$	27	19.4	13.8	1.65	7.29
CC_51-ECC_60_20	$10^{5.5}$	160.0	17	$1.00{\cdot}10^5$	32	22.4	17.0	1.62	2.24
CC_31-ECC_20_120	$10^{5.5}$	40.0	31	$2.75{\cdot}10^5$	87	27.6	21.5	2.35	1.11
CC_51-ECC_20_120	$10^{5.5}$	160.0	16	$1.11{\cdot}10^5$	35	23.3	17.2	1.72	7.29
CC_51-ECC_120_20	$10^{5.5}$	160.0	20	$1.30{\cdot}10^5$	41	27.4	20.2	1.71	1.30
CC_31-ECC_40_60	$10^{5.5}$	40.0	31	$2.80{\cdot}10^5$	89	29.0	22.4	2.32	0.69
CC_51-ECC_40_60	$10^{5.5}$	160.0	19	$1.30{\cdot}10^5$	41	29.5	22.0	1.61	3.21
CC_51-ECC_40_90*	$10^{5.5}$	160.0	21	$1.55{\cdot}10^5$	49	35.3	26.4	1.63	3.21
CC_31-ECC_40_120	$10^{5.5}$	40.0	31	$2.89{\cdot}10^5$	91	29.9	23.1	2.32	0.69
CC_51-ECC_40_120	$10^{5.5}$	160.0	21	$1.65{\cdot}10^5$	52	40.8	30.6	1.62	3.21

[a-j, *] see Table C.6

C.6 Results of the Study on the Formation of Extremely Extended EOs and UFOs in the Gilmore Gap

TABLE C.8— Parameters of merger objects on circular orbits at 60 and 120 kpc and without tidal field

Model [a]	M^{CC} [b] ($M_\odot$)	$R_{\mathrm{pl}}^{\mathrm{CC}}$ [c] (pc)	N_{M} [d]	M_{encl} [e] ($M_\odot$)	M_{encl} [f] (%)	r_{h} [g] (pc)	r_{eff} [h] (pc)	σ [i] (km s^{-1})	β [j]
CC_30-CIRC_60	$10^{5.0}$	40.0	30	$8.49{\cdot}10^4$	85	27.2	20.4	1.35	0.75
CC_30-CIRC_120	$10^{5.0}$	40.0	31	$9.25{\cdot}10^4$	93	30.3	23.3	1.30	0.46
CC_40-CIRC_60	$10^{5.0}$	80.0	21	$5.66{\cdot}10^4$	57	28.0	21.0	1.09	1.54
CC_40-CIRC_120	$10^{5.0}$	80.0	26	$7.90{\cdot}10^4$	79	39.5	28.9	1.05	0.93
CC_50-CIRC_60	$10^{5.0}$	160.0	18	$3.94{\cdot}10^4$	39	29.9	21.5	0.91	3.58
CC_50-CIRC_120	$10^{5.0}$	160.0	22	$5.91{\cdot}10^4$	59	54.5	41.4	0.82	1.95
CC_21-CIRC_60	$10^{5.5}$	20.0	32	$3.01{\cdot}10^5$	95	21.1	16.3	2.81	0.26
CC_21-CIRC_120	$10^{5.5}$	20.0	32	$3.07{\cdot}10^5$	97	21.6	16.5	2.80	0.16
CC_31-CIRC_60	$10^{5.5}$	40.0	31	$2.88{\cdot}10^5$	91	29.9	22.6	2.37	0.52
CC_31-CIRC_120	$10^{5.5}$	40.0	31	$2.95{\cdot}10^5$	93	30.8	23.6	2.31	0.32
CC_41-CIRC_60	$10^{5.5}$	80.0	27	$2.17{\cdot}10^5$	69	33.2	24.6	1.97	1.05
CC_41-CIRC_120	$10^{5.5}$	80.0	29	$2.72{\cdot}10^5$	86	46.0	32.2	1.87	0.63
CC_51-CIRC_60	$10^{5.5}$	160.0	22	$1.57{\cdot}10^5$	50	38.5	28.9	1.57	2.24
CC_51-CIRC_120	$10^{5.5}$	160.0	24	$2.25{\cdot}10^5$	71	65.7	48.9	1.59	1.30
CC_32-CIRC_60	$10^{6.0}$	40.0	32	$9.40\cdot10^5$	94	35.6	27.9	3.73	0.35
CC_32-CIRC_120	$10^{6.0}$	40.0	31	$9.63\cdot10^5$	96	37.3	28.4	3.83	0.22
CC_42-CIRC_60	$10^{6.0}$	80.0	30	$8.11{\cdot}10^5$	81	43.5	32.2	3.34	0.71
CC_42-CIRC_120	$10^{6.0}$	80.0	31	$9.10{\cdot}10^5$	91	52.9	38.8	3.29	0.43
CC_52-CIRC_60	$10^{6.0}$	160.0	26	$6.17{\cdot}10^5$	62	51.9	38.6	2.72	1.47
CC_52-CIRC_120	$10^{6.0}$	160.0	30	$7.96{\cdot}10^5$	80	81.4	58.9	2.69	0.88
CC_53-CIRC_60	$10^{6.5}$	160.0	29	$2.18{\cdot}10^6$	69	62.4	45.9	4.82	0.99
CC_53-CIRC_120	$10^{6.5}$	160.0	30	$2.50{\cdot}10^6$	79	93.9	68.4	4.59	0.60
CC_54-CIRC_60	$10^{7.0}$	160.0	29	$7.43{\cdot}10^6$	74	77.5	57.6	8.02	0.67
CC_54-CIRC_120	$10^{7.0}$	160.0	31	$7.97{\cdot}10^6$	80	105.0	75.5	7.98	0.41
CC_55-CIRC_60	$10^{7.5}$	160.0	31	$2.52{\cdot}10^7$	80	91.3	66.6	14.05	0.46
CC_56-CIRC_60	$10^{8.0}$	160.0	32	$8.15{\cdot}10^7$	82	116.0	82.1	24.85	0.31
CC_56-INF	$10^{8.0}$	160.0	31	$8.64{\cdot}10^7$	86	117.4	98.7	24.88	—-

[a-j] see Table C.4

Bibliography

Aarseth, S. J., Henon, M., & Wielen, R. 1974, A&A, 37, 183

Al Sufi, A. A. 964, Book of Fixed Stars

Ashman, K. M. & Zepf, S. E. 1998, Globular Cluster Systems

Balbinot, E., Santiago, B. X., da Costa, L., et al. 2013, ApJ, 767, 101

Barnes, J. & Hut, P. 1986, Nature, 324, 446

Bastian, N., Emsellem, E., Kissler-Patig, M., & Maraston, C. 2006a, A&A, 445, 471

Bastian, N., Gieles, M., Efremov, Y. N., & Lamers, H. J. G. L. M. 2005, A&A, 443, 79

Bastian, N., Saglia, R. P., Goudfrooij, P., et al. 2006b, A&A, 448, 881

Bastian, N., Schweizer, F., Goudfrooij, P., Larsen, S. S., & Kissler-Patig, M. 2013, MNRAS, 431, 1252

Bastian, N., Trancho, G., Konstantopoulos, I. S., & Miller, B. W. 2009, ApJ, 701, 607

Baumgardt, H., Côté, P., Hilker, M., et al. 2009, MNRAS, 396, 2051

Bekki, K., Couch, W. J., & Drinkwater, M. J. 2001, ApJ, 552, L105

Bekki, K., Couch, W. J., Drinkwater, M. J., & Shioya, Y. 2003, MNRAS, 344, 399

Bekki, K., Couch, W. J., Drinkwater, M. J., & Shioya, Y. 2004, ApJ, 610, L13

Bell, E. F., Slater, C. T., & Martin, N. F. 2011, ApJ, 742, L15

Bellazzini, M. 2007, A&A, 473, 171

Bellazzini, M., Ferraro, F. R., & Ibata, R. 2002, AJ, 124, 915

Belokurov, V., Walker, M. G., Evans, N. W., et al. 2010, ApJ, 712, L103

Belokurov, V., Zucker, D. B., Evans, N. W., et al. 2006, ApJ, 642, L137

Bien, R., Brandt, T., & Just, A. 2013, MNRAS, 428, 1631

Bien, R., Fuchs, B., & Wielen, R. 1990, A simplified numerical treatment of encounters between galaxies, ed. R. Wielen, 212

Bien, R., Fuchs, B., & Wielen, R. 1991, in CP90 Europhysics Conference on Computational Physics, ed. A. G. Tenner, 3–13

Blakeslee, J. P. & Barber DeGraaff, R. 2008, AJ, 136, 2295

Blom, C., Spitler, L. R., & Forbes, D. A. 2012, MNRAS, 420, 37

Boselli, A., Lequeux, J., & Gavazzi, G. 2002, Ap&SS, 281, 127

Bournaud, F., Bois, M., Emsellem, E., & Duc, P.-A. 2008a, Astronomische Nachrichten, 329, 1025

Bournaud, F., Duc, P.-A., & Emsellem, E. 2008b, MNRAS, 389, L8

Brasseur, C. M., Martin, N. F., Macciò, A. V., Rix, H.-W., & Kang, X. 2011, ApJ, 743, 179

Brodie, J. P. & Larsen, S. S. 2002, AJ, 124, 1410

Brodie, J. P., Romanowsky, A. J., Strader, J., & Forbes, D. A. 2011, AJ, 142, 199

Brodie, J. P. & Strader, J. 2006, ARA&A, 44, 193

Brüns, R. C. & Kroupa, P. 2011, ApJ, 729, 69

Brüns, R. C. & Kroupa, P. 2012, A&A, 547, A65

Brüns, R. C., Kroupa, P., & Fellhauer, M. 2009, ApJ, 702, 1268

Brüns, R. C., Kroupa, P., Fellhauer, M., Metz, M., & Assmann, P. 2011, A&A, 529, A138

Bruzual, G. & Charlot, S. 2003, MNRAS, 344, 1000

Burkert, A., Brodie, J., & Larsen, S. 2005, ApJ, 628, 231

Burstein, D., Li, Y., Freeman, K. C., et al. 2004, ApJ, 614, 158

Cantiello, M., Brocato, E., & Blakeslee, J. P. 2009, A&A, 503, 87

Cao, C. & Wu, H. 2007, AJ, 133, 1710

Cappellari, M., Bacon, R., Bureau, M., et al. 2006, MNRAS, 366, 1126

Casetti-Dinescu, D. I., Girard, T. M., Majewski, S. R., et al. 2009, ApJ, 701, L29

Catelan, M. 2009, Ap&SS, 320, 261

Cezario, E., Coelho, P. R. T., Alves-Brito, A., Forbes, D. A., & Brodie, J. P. 2013, A&A, 549, A60

Chandar, R., Bianchi, L., & Ford, H. C. 2000, AJ, 120, 3088

Chandar, R., Whitmore, B., & Lee, M. G. 2004, ApJ, 611, 220

Chattopadhyay, A. K., Chattopadhyay, T., Davoust, E., Mondal, S., & Sharina, M. 2009, ApJ, 705, 1533

Chiboucas, K., Tully, R. B., Marzke, R. O., et al. 2011, ApJ, 737, 86

Chies-Santos, A. L., Larsen, S. S., Wehner, E. M., et al. 2011, A&A, 525, A19

Chies-Santos, A. L., Pastoriza, M. G., Santiago, B. X., & Forbes, D. A. 2006, A&A, 455, 453

Chies-Santos, A. L., Santiago, B. X., & Pastoriza, M. G. 2007, A&A, 467, 1003

Chilingarian, I. V. & Mamon, G. A. 2008, MNRAS, 385, L83

Chilingarian, I. V., Mieske, S., Hilker, M., & Infante, L. 2011, MNRAS, 412, 1627

Chou, M.-Y., Majewski, S. R., Cunha, K., et al. 2007, ApJ, 670, 346

Christian, C. A. & Schommer, R. A. 1982, ApJS, 49, 405

Chun, M. S. 1978, AJ, 83, 1062

Ciardullo, R., Feldmeier, J. J., Jacoby, G. H., et al. 2002, ApJ, 577, 31

Cockcroft, R., Harris, W. E., Ferguson, A. M. N., et al. 2011, ApJ, 730, 112

Cohen, J. G. 2004, AJ, 127, 1545

Cohen, J. G., Persson, S. E., & Searle, L. 1984, ApJ, 281, 141

Conn, A. R., Lewis, G. F., Ibata, R. A., et al. 2013, ApJ, 766, 120

da Costa, G. S. 2002, in IAU Symposium, Vol. 207, Extragalactic Star Clusters, ed. D. P. Geisler, E. K. Grebel, & D. Minniti, 83

Da Costa, G. S. & Armandroff, T. E. 1995, AJ, 109, 2533

Da Costa, G. S., Grebel, E. K., Jerjen, H., Rejkuba, M., & Sharina, M. E. 2009, AJ, 137, 4361

Da Rocha, C., Mieske, S., Georgiev, I. Y., et al. 2011, A&A, 525, A86

Dabringhausen, J., Hilker, M., & Kroupa, P. 2008, MNRAS, 386, 864

Dabringhausen, J. & Kroupa, P. 2013, MNRAS, 429, 1858

Dabringhausen, J., Kroupa, P., & Baumgardt, H. 2009, MNRAS, 394, 1529

Dame, T. M. 1993, in American Institute of Physics Conference Series, Vol. 278, Back to the Galaxy, ed. S. S. Holt & F. Verter, 267–278

de Grijs, R., Anders, P., Bastian, N., et al. 2003, MNRAS, 343, 1285

Debattista, V. P., Corsini, E. M., & Aguerri, J. A. L. 2002, MNRAS, 332, 65

DeGraaff, R. B., Blakeslee, J. P., Meurer, G. R., & Putman, M. E. 2007, ApJ, 671, 1624

Dinescu, D. I., Majewski, S. R., Girard, T. M., & Cudworth, K. M. 2000, AJ, 120, 1892

Dotter, A., Sarajedini, A., Anderson, J., et al. 2010, ApJ, 708, 698

Drinkwater, M. J., Gregg, M. D., Hilker, M., et al. 2003, Nature, 423, 519

Drinkwater, M. J., Jones, J. B., Gregg, M. D., & Phillipps, S. 2000, PASA, 17, 227

Duffau, S., Zinn, R., Vivas, A. K., et al. 2006, ApJ, 636, L97

Elmegreen, D. M. 2007, in IAU Symposium, Vol. 235, IAU Symposium, ed. F. Combes & J. Palous, 376–380

Elmegreen, D. M. & Elmegreen, B. G. 1982, MNRAS, 201, 1021

Evstigneeva, E. A., Drinkwater, M. J., Peng, C. Y., et al. 2008, AJ, 136, 461

Evstigneeva, E. A., Gregg, M. D., Drinkwater, M. J., & Hilker, M. 2007, AJ, 133, 1722

Fadely, R., Willman, B., Geha, M., et al. 2011, AJ, 142, 88

Fellhauer, M. 2001, PhD thesis, Naturwissenschaftlich-Mathematische Gesamtfakultät der Universität Heidelberg, Germany. Berichte aus der Astronomie, Aachen: Shaker Verlag. ISBN 3-8265-8658-1, 114 pp. (2001)

Fellhauer, M. 2004, in Reviews in Modern Astronomy, Vol. 17, Reviews in Modern Astronomy, ed. R. E. Schielicke, 209

Fellhauer, M., Baumgardt, H., Kroupa, P., & Spurzem, R. 2002, Celestial Mechanics and Dynamical Astronomy, 82, 113

Fellhauer, M. & Kroupa, P. 2002a, MNRAS, 330, 642

Fellhauer, M. & Kroupa, P. 2002b, AJ, 124, 2006

Fellhauer, M. & Kroupa, P. 2005a, MNRAS, 359, 223

Fellhauer, M. & Kroupa, P. 2005b, ApJ, 630, 879

Fellhauer, M., Kroupa, P., Baumgardt, H., et al. 2000, New A, 5, 305

Fellhauer, M., Kroupa, P., & Evans, N. W. 2006, MNRAS, 372, 338

Flynn, C., Holmberg, J., Portinari, L., Fuchs, B., & Jahreiß, H. 2006, MNRAS, 372, 1149

Forbes, D. A. & Bridges, T. 2010, MNRAS, 404, 1203

Forbes, D. A. & Kroupa, P. 2011, PASA, 28, 77

Forbes, D. A., Lasky, P., Graham, A. W., & Spitler, L. 2008, MNRAS, 389, 1924

Galleti, S., Federici, L., Bellazzini, M., Fusi Pecci, F., & Macrina, S. 2004, A&A, 416, 917

Geehan, J. J., Fardal, M. A., Babul, A., & Guhathakurta, P. 2006, MNRAS, 366, 996

Geha, M., van der Marel, R. P., Guhathakurta, P., et al. 2010, ApJ, 711, 361

Georgiev, I. Y., Puzia, T. H., Hilker, M., & Goudfrooij, P. 2009, MNRAS, 392, 879

Georgiev, L., Borissova, J., Rosado, M., et al. 1999, A&AS, 134, 21

Gieles, M., Athanassoula, E., & Portegies Zwart, S. F. 2007, MNRAS, 376, 809

Gieles, M., Portegies Zwart, S. F., Baumgardt, H., et al. 2006, MNRAS, 371, 793

Gilmore, G., Wilkinson, M. I., Wyse, R. F. G., et al. 2007, ApJ, 663, 948

Glatt, K., Gallagher, III, J. S., Grebel, E. K., et al. 2008, AJ, 135, 1106

Goerdt, T., Moore, B., Kazantzidis, S., et al. 2008, MNRAS, 385, 2136

Gómez, M., Geisler, D., Harris, W. E., et al. 2006, A&A, 447, 877

Goudfrooij, P. 2012, ApJ, 750, 140

Grillmair, C. J. 2006, ApJ, 645, L37

Haşegan, M., Jordán, A., Côté, P., et al. 2005, ApJ, 627, 203

Harris, G. L. H., Gómez, M., Harris, W. E., et al. 2012, AJ, 143, 84

Harris, G. L. H., Rejkuba, M., & Harris, W. E. 2010, PASA, 27, 457

Harris, W. E. 1996, AJ, 112, 1487

Harris, W. E. 2001, Globular Cluster Systems, 223

Harris, W. E., Mouhcine, M., Rejkuba, M., & Ibata, R. 2009, MNRAS, 395, 436

Hau, G. K. T., Spitler, L. R., Forbes, D. A., et al. 2009, MNRAS, 394, L97

Hernquist, L. 1990, ApJ, 356, 359

Hilker, M., Baumgardt, H., Infante, L., et al. 2007, A&A, 463, 119

Hilker, M., Infante, L., Vieira, G., Kissler-Patig, M., & Richtler, T. 1999, A&AS, 134, 75

Hodge, P. W. 1961a, ApJ, 133, 413

Hodge, P. W. 1961b, AJ, 66, 83

Hubble, E. 1932, ApJ, 76, 44

Hubble, E. P. 1936, Realm of the Nebulae

Hurley, J. R. & Mackey, A. D. 2010, MNRAS, 408, 2353

Hut, P. & Makino, J. 2003, The Art of Computational Science, http://www.artcompsci.org

Huxor, A., Ferguson, A. M. N., Barker, M. K., et al. 2009, ApJ, 698, L77

Huxor, A. P., Ferguson, A. M. N., Tanvir, N. R., et al. 2011a, MNRAS, 414, 770

Huxor, A. P., Ferguson, A. M. N., Veljanoski, J., Mackey, A. D., & Tanvir, N. R. 2013, MNRAS, 429, 1039

Huxor, A. P., Phillipps, S., Price, J., & Harniman, R. 2011b, MNRAS, 414, 3557

Huxor, A. P., Tanvir, N. R., Ferguson, A. M. N., et al. 2008, MNRAS, 385, 1989

Huxor, A. P., Tanvir, N. R., Irwin, M. J., et al. 2005, MNRAS, 360, 1007

Hwang, N. & Lee, M. G. 2008, AJ, 135, 1567

Hwang, N., Lee, M. G., Lee, J. C., et al. 2011, ApJ, 738, 58

Ibata, R., Sollima, A., Nipoti, C., et al. 2011, ApJ, 738, 186

Jarrett, T. H., Polletta, M., Fournon, I. P., et al. 2006, AJ, 131, 261

Jordán, A., Côté, P., Blakeslee, J. P., et al. 2005, ApJ, 634, 1002

King, I. 1962, AJ, 67, 471

King, I. R. 1966, AJ, 71, 276

Kissler-Patig, M. 2004, in Astronomical Society of the Pacific Conference Series, Vol. 322, The Formation and Evolution of Massive Young Star Clusters, ed. H. J. G. L. M. Lamers, L. J. Smith, & A. Nota, 535

Klessen, R. S. & Kroupa, P. 1998, ApJ, 498, 143

Kroupa, P. 1998, MNRAS, 300, 200

Kroupa, P. 2001, MNRAS, 322, 231

Kroupa, P. 2008, in Lecture Notes in Physics, Berlin Springer Verlag, Vol. 760, The Cambridge N-Body Lectures, ed. S. J. Aarseth, C. A. Tout, & R. A. Mardling, 181

Kroupa, P., Famaey, B., de Boer, K. S., et al. 2010, A&A, 523, A32

Kroupa, P., Theis, C., & Boily, C. M. 2005, A&A, 431, 517

Küpper, A. H. W., Kroupa, P., Baumgardt, H., & Heggie, D. C. 2010, MNRAS, 407, 2241

Lagos, P., Telles, E., Nigoche-Netro, A., & Carrasco, E. R. 2011, AJ, 142, 162

Larsen, S. S. 2004, A&A, 416, 537

Larsen, S. S. & Brodie, J. P. 2000, AJ, 120, 2938

Larsen, S. S., Brodie, J. P., Huchra, J. P., Forbes, D. A., & Grillmair, C. J. 2001a, AJ, 121, 2974

Larsen, S. S., Efremov, Y. N., Elmegreen, B. G., et al. 2002, ApJ, 567, 896

Larsen, S. S., Forbes, D. A., & Brodie, J. P. 2001b, MNRAS, 327, 1116

Larsen, S. S. & Richtler, T. 1999, A&A, 345, 59

Lee, M. G., Chandar, R., & Whitmore, B. C. 2005, AJ, 130, 2128

Lieder, S., Lisker, T., Hilker, M., Misgeld, I., & Durrell, P. 2012, A&A, 538, A69

Mackey, A. D. & Gilmore, G. F. 2004, MNRAS, 352, 153

Mackey, A. D., Huxor, A., Ferguson, A. M. N., et al. 2006, ApJ, 653, L105

Madore, B. F. & Arp, H. C. 1979, ApJ, 227, L103

Madrid, J. P. 2011, ApJ, 737, L13

Madrid, J. P. & Donzelli, C. J. 2013, ApJ, 770, 158

Madrid, J. P., Graham, A. W., Harris, W. E., et al. 2010, ApJ, 722, 1707

Makino, J. & Saitoh, T. 2012, PTEP, 303, 27

Makino, J. & Taiji, M. 1998, Scientific Simulations with Special-Purpose Computers–the GRAPE Systems

Maraston, C., Bastian, N., Saglia, R. P., et al. 2004, A&A, 416, 467

Marks, M., Kroupa, P., Dabringhausen, J., & Pawlowski, M. S. 2012, MNRAS, 422, 2246

Martin, N. F., de Jong, J. T. A., & Rix, H.-W. 2008, ApJ, 684, 1075

Masters, K. L., Jordán, A., Côté, P., et al. 2010, ApJ, 715, 1419

McConnachie, A. W. 2012, AJ, 144, 4

McConnachie, A. W. & Irwin, M. J. 2006, MNRAS, 365, 1263

McConnachie, A. W., Irwin, M. J., Ferguson, A. M. N., et al. 2005, MNRAS, 356, 979

McLaughlin, D. E., Barmby, P., Harris, W. E., Forbes, D. A., & Harris, G. L. H. 2008, MNRAS, 384, 563

McLaughlin, D. E. & van der Marel, R. P. 2005, ApJS, 161, 304

Mengel, S., Lehnert, M. D., Thatte, N. A., et al. 2008, A&A, 489, 1091

Metz, M. 2008, PhD thesis, Mathematisch-Naturwissenschaftlichen Fakultät der Rheinischen Friedrich-Wilhelms-Universität Bonn, Germany

Mieske, S., Hilker, M., & Infante, L. 2002, A&A, 383, 823

Mieske, S., Hilker, M., Jordán, A., Infante, L., & Kissler-Patig, M. 2007, A&A, 472, 111

Mieske, S., Hilker, M., Jordán, A., et al. 2008, A&A, 487, 921

Mieske, S., Hilker, M., & Misgeld, I. 2012, A&A, 537, A3

Mieske, S., Infante, L., Hilker, M., et al. 2005, A&A, 430, L25

Mieske, S. & Kroupa, P. 2008, ApJ, 677, 276

Miocchi, P. & Capuzzo-Dolcetta, R. 2002, A&A, 382, 758

Miocchi, P., Dolcetta, R. C., & Matteo, P. D. 2009, Simulations of Globular Clusters Merging in Galactic Nuclear Regions, ed. T. Richtler & S. Larsen, 407

Misgeld, I. & Hilker, M. 2011, MNRAS, 414, 3699

Misgeld, I., Mieske, S., Hilker, M., et al. 2011, A&A, 531, A4

Miyamoto, M. & Nagai, R. 1975, PASJ, 27, 533

Mouhcine, M., Harris, W. E., Ibata, R., & Rejkuba, M. 2010, MNRAS, 404, 1157

Muñoz, R. R., Geha, M., Côté, P., et al. 2012, ApJ, 753, L15

Murray, N. 2009, ApJ, 691, 946

Nantais, J. B., Huchra, J. P., Zezas, A., Gazeas, K., & Strader, J. 2011, AJ, 142, 183

Newberg, H. J., Willett, B. A., Yanny, B., & Xu, Y. 2010, ApJ, 711, 32

Newberg, H. J., Yanny, B., Grebel, E. K., et al. 2003, ApJ, 596, L191

Newberg, H. J., Yanny, B., & Willett, B. A. 2009, ApJ, 700, L61

Noordermeer, E., Merrifield, M. R., Coccato, L., et al. 2008, MNRAS, 384, 943

Norris, M. A. & Kannappan, S. J. 2011, MNRAS, 414, 739

Pawlowski, M. S., Kroupa, P., & Jerjen, H. 2013, MNRAS

Peacock, M. B., Maccarone, T. J., Waters, C. Z., et al. 2009, MNRAS, 392, L55

Peebles, P. J. E. & Dicke, R. H. 1968, ApJ, 154, 891

Pellerin, A., Meurer, G. R., Bekki, K., et al. 2010, AJ, 139, 1369

Peng, E. W., Côté, P., Jordán, A., et al. 2006, ApJ, 639, 838

Penny, S. J., Forbes, D. A., & Conselice, C. J. 2012, MNRAS, 422, 885

Pfalzner, S. & Gibbon, P. 2005, Many-Body Tree Methods in Physics

Pfeffer, J. & Baumgardt, H. 2013, MNRAS, 433, 1997

Phillipps, S., Drinkwater, M. J., Gregg, M. D., & Jones, J. B. 2001, ApJ, 560, 201

Plummer, H. C. 1911, MNRAS, 71, 460

Price, J., Phillipps, S., Huxor, A., et al. 2009, MNRAS, 397, 1816

Pryor, C. & Meylan, G. 1993, in Astronomical Society of the Pacific Conference Series, Vol. 50, Structure and Dynamics of Globular Clusters, ed. S. G. Djorgovski & G. Meylan, 357

Puzia, T. H., Perrett, K. M., & Bridges, T. J. 2005, A&A, 434, 909

Rejkuba, M. 2012, Ap&SS, 341, 195

Richtler, T., Dirsch, B., Larsen, S., Hilker, M., & Infante, L. 2005, A&A, 439, 533

Ripepi, V., Clementini, G., Di Criscienzo, M., et al. 2007, ApJ, 667, L61

Salaris, M. & Weiss, A. 2002, A&A, 388, 492

Salinas, R., Jílková, L., Carraro, G., Catelan, M., & Amigo, P. 2012, MNRAS, 421, 960

Salpeter, E. E. 1955, ApJ, 121, 161

Sarajedini, A. & Mancone, C. L. 2007, AJ, 134, 447

Schommer, R. A., Christian, C. A., Caldwell, N., Bothun, G. D., & Huchra, J. 1991, AJ, 101, 873

Secker, J. 1992, AJ, 104, 1472

Sharina, M. E., Karachentsev, I. D., Dolphin, A. E., et al. 2008, MNRAS, 384, 1544

Sharina, M. E., Puzia, T. H., & Makarov, D. I. 2005, A&A, 442, 85

Simien, F. & Prugniel, P. 1997, A&AS, 126, 519

Slater, C. T., Bell, E. F., & Martin, N. F. 2011, ApJ, 742, L14

Smith Castelli, A. V., Cellone, S. A., Faifer, F. R., et al. 2012, MNRAS, 419, 2472

Smith Castelli, A. V., Faifer, F. R., Richtler, T., & Bassino, L. P. 2008, MNRAS, 391, 685

Spinnato, P. F., Fellhauer, M., & Portegies Zwart, S. F. 2003, MNRAS, 344, 22

Spitzer, L. 1987, Dynamical evolution of globular clusters

Spitzer, Jr., L. & Hart, M. H. 1971, ApJ, 164, 399

Stonkutė, R., Vansevičius, V., Arimoto, N., et al. 2008, AJ, 135, 1482

Strader, J., Fabbiano, G., Luo, B., et al. 2012a, ApJ, 760, 87

Strader, J., Seth, A. C., & Caldwell, N. 2012b, AJ, 143, 52

Sugimoto, D., Chikada, Y., Makino, J., et al. 1990, Nature, 345, 33

Taylor, M. A., Puzia, T. H., Harris, G. L., et al. 2010, ApJ, 712, 1191

Tran, H. D., Sirianni, M., Ford, H. C., et al. 2003, ApJ, 585, 750

Trancho, G., Bastian, N., Miller, B. W., & Schweizer, F. 2007, ApJ, 664, 284

Trancho, G., Konstantopoulos, I. S., Bastian, N., et al. 2012, ApJ, 748, 102

van den Bergh, S. 1995, AJ, 110, 1171

van den Bergh, S. 2006, AJ, 131, 304

van den Bergh, S. & Mackey, A. D. 2004, MNRAS, 354, 713

Warnick, K. 2004, Diploma Thesis, Faculty of Physics and Astronomy, Astronomisches Rechen-Institut Heidelberg, Germany

Whitmore, B. C. 2003, in A Decade of Hubble Space Telescope Science, ed. M. Livio, K. Noll, & M. Stiavelli, 153–178

Whitmore, B. C., Chandar, R., Schweizer, F., et al. 2010, AJ, 140, 75

Whitmore, B. C., Gilmore, D., Leitherer, C., et al. 2005, AJ, 130, 2104

Whitmore, B. C. & Schweizer, F. 1995, AJ, 109, 960

Whitmore, B. C., Zhang, Q., Leitherer, C., et al. 1999, AJ, 118, 1551

Willman, B. & Strader, J. 2012, AJ, 144, 76

Wilson, C. D., Harris, W. E., Longden, R., & Scoville, N. Z. 2006, ApJ, 641, 763

Wilson, C. D., Scoville, N., Madden, S. C., & Charmandaris, V. 2003, ApJ, 599, 1049

Wyder, T. K., Hodge, P. W., & Cole, A. 2000, PASP, 112, 594

Zepf, S. E., Geisler, D., & Ashman, K. M. 1994, ApJ, 435, L117

Acknowledgements

First of all, I would like to thank my supervisors *Pavel Kroupa* and *Michael Fellhauer* for providing this very interesting and "hot" thesis topic and for stimulating discussions. It is very fascinating to witness the growing interest of the astronomical globular cluster and dwarf galaxy community in EOs and to be able to contribute to make these objects more popular. I am deeply grateful to *Pavel Kroupa* to encourage me to pursue my own scientific ideas. I would also like to thank him for his considerable efforts to improve the computational infrastructure at the AIfA.

I am very grateful to *Ulrich Klein* volunteering to be the second referee of my thesis and for the excellent collaboration on webpages and other issues.

A big thank you goes to *Manual Metz* who developed a new parallelized version of the PM code SUPERBOX which lead to a significant speed-up of the simulations and made the large parameter studies of this thesis possible on an acceptable timescale.

I further wish to thank *Søren Larsen* and *Juan Madrid* for kindly providing additional data on faint fuzzies, ECs and UCDs and *Michael Hilker* for valuable discussions on the EO catalog and future observational projects.

I would also like to thank *Nadya Ben Behkti*, *Lucia Klarmann*, *Marcel Pawlowski* and *Ylva Schuberth* for carefully reading parts of this thesis. Thank you for your time and effort!

I am indebted to *Nadya Ben Behkti* for her excellent moral support and to *Christina Stein-Schmitz* for her help and good advice in all kind of issues.

I would also like to thank the *computer department* for taking good care of the dynamix machines and for repairing my good old aibn39 quickly whenever it broke down again.

I enjoyed the exchange on SUPERBOX and SUPERBOX projects with *Kristin Warnick* and *Paulina Assmann* during their visits at the AIfA.

I would like to thank all members of the *SPODYR group* for the friendly, open and cooperative atmosphere. Besides the scientific part, I learned a lot about different cultures and their fascinating bowling techniques.

Finally, I am deeply grateful to my *husband* who was a major driving force during good and bad times and provided excellent moral support during all these years. I am also very grateful for his critical and thorough reading of numerous drafts of the entire thesis.

Last but not least, I would like to thank all participating extended clusters for not being slim ...